UNIVERSITÀ DEGLI STUDI DI PALERMO

Dottorato di ricerca in Information and Communication Technologies

Dipartimento di Ingegneria

Design of perfusion bioreactors and PLLA-based scaffolds for *in vitro* tissue engineering

DOTTORESSA

ING. ELISA CAPUANA

COORDINATRICE

PROF. SSA ILENIA TINNIRELLO

TUTOR

PROF. VINCENZO LA CARRUBBA

CICLO XXXIV

ANNO CONSEGUIMENTO TITOLO 2022

Abstract

Tissue engineering (TE) represents a novel approach that uses cells integrated with matrices to achieve the formation of new tissues. In this strategy, three essential components constitute the so-called triad of Tissue Engineering: regulatory signals, cells, and three-dimensional (3D) biodegradable porous scaffolds. They are combined to develop an organized 3D functional tissue that mimics the extracellular matrix (ECM) of tissue to be regenerated. The tissue-specific functions of native tissues are linked to complex environments that can be replicated outside the body by using special devices called bioreactors. These systems provide an environment where specific parameters can be controlled to match desired biological conditions.

In this thesis, all these components are accounted for developing *in vitro* models for various applications in the field of Tissue Engineering. Specifically, poly-(L-lactic acid) (PLLA)-based scaffold, scaffold fabrication via phase separation, static cell cultures, and dynamic cell cultures using perfusion bioreactors are analyzed and discussed.

Two main sections compose this thesis: several experimental setups using PLLA-based scaffolds for various *in vitro* systems; and the design and modeling of a custom perfusion bioreactor using computational fluid dynamics (CFD) and mathematical equations. A rigorous theoretical framework is developed to study the properties of PLLA biomaterial, the use of perfusion bioreactor for regenerative medicine, and models developed for investigating cells growth on 3D matrices cultured within a dynamic system. In the experiments, the morphology of different PLLA scaffolds produced through different protocols of the thermally induced phase separation technique (TIPS) is analyzed according to the targeted properties of TE scaffolds, i.e., porosity, pore interconnectivity, and pore size. Cell cultures are performed in these constructs to create a 3D environment so that seeded cells can grow both in static 3D culture and the perfusion bioreactor. Cell proliferation and adhesion are observed up to 7 days of *in vitro* culture, demonstrating that scaffold morphology can induce cell growth under both static and dynamic conditions.

For the second part, a combined modeling and experimental approach is followed. The custom-made perfusion apparatus is an existing airlift bioreactor that provides a low-shear environment with good mixing, resolving mass transport limitations and providing physical stimuli beneficial for overall cells proliferation and differentiation. The hydrodynamics (gas holdup, superficial liquid velocity, and shear rate) and mass transfer (kLa and the volumetric mass transfer coefficient) are modeled and determined by CFD to examine the influence of

these features on cell and tissue growth. The simulation results indicate that the hydrodynamics matched the mathematical data and experimental validation. Then, osteoblast cells are cultured on a support in the bioreactor perfused with culture medium at 10mL/min for up to 6 days. An evaluation combining proliferation results and statistical analysis allows the quantification of cell growth as a function of the space inside the system. Given the hierarchical nature of the bioreactor-scaffold system, its multi-scale nature will be considered, ranging from the extracellular matrix scale to the bioreactor scale. The flow-dependent properties of an engineered matrix cultured within a perfusion bioreactor are studied theoretically and evaluated experimentally, emphasizing the influence of inter-scale dependencies.

Perfusion bioreactors are *in vitro* systems beneficial for drug screening because they mimic the *in vivo* environment. For this purpose, an optimized design of the airlift bioreactor that can induce a double-flow on a hollow scaffold is theoretically and experimentally validated. Specifically, the system is tested for carriers diffusion and air-liquid-interface (ALI) model to reproduce the nasal mucosa environment. The rationale is to combine an internal and an external flow of independent fluids for either diffusing the carriers throughout the engineered matrix for drug prescreening or redirecting the culture medium to feed the cells seeded into the channel of the hollow scaffold. In conclusion, this thesis project focuses on the major aspects of tissue engineering and regenerative medicine, varying from *in vitro* tests for growing cells on scaffolds toward models to study the multi-scale nature of a tissue-like system or recreate the physiology of a native tissue.

Sommario

L'ingegneria tissutale rappresenta un nuovo approccio che integra cellule e matrici ingegnerizzate per la formazione di nuovi tessuti. In questa strategia, tre componenti essenziali costituiscono la cosiddetta triade della Tissue Engineering: segnali regolatori, cellule e scaffold tridimensionali (3D) biodegradabili e porosi. Tali elementi sono combinati per sviluppare un tessuto funzionale organizzato e 3D che simula la matrice extracellulare (ECM) del tessuto da rigenerare. Le funzioni specifiche dei tessuti nativi sono correlate agli ambienti complessi che, all'esterno del corpo, possono essere imitati usando degli strumenti chiamati bioreattori. Questi sistemi forniscono un ambiente in cui i parametri specifici possono essere controllati per raggiungere le condizioni biologiche desiderate.
In questa tesi, tutti questi componenti sono stati impiegati per lo sviluppo di modelli *in vitro* in diverse applicazioni dell'ingegneria tissutale. In particolare, sono stati analizzati e discussi i temi relativi a: scaffold a base di poli-(acido L-lattico) (PLLA), fabbricazione di scaffold tramite separazione di fase, colture cellulari statiche e colture cellulari dinamiche utilizzando bioreattori di perfusione. Due sezioni principali compongono questa tesi: diverse configurazioni sperimentali che utilizzano scaffold a base di PLLA per vari sistemi *in vitro*; e la progettazione e la modellazione di un bioreattore di perfusione utilizzando fluidodinamica computazionale (CFD) ed equazioni matematiche. In primis, un rigoroso quadro teorico è stato investigato per studiare le proprietà del biomateriale PLLA, l'uso di bioreattori a perfusione per la medicina rigenerativa e i modelli sviluppati per studiare la crescita delle cellule su matrici 3D coltivate all'interno di un sistema dinamico. Negli esperimenti, la morfologia di diversi scaffold in PLLA prodotti attraverso vari protocolli della tecnica di separazione di fase indotta termicamente (TIPS) è stata analizzata in base alle proprietà desiderate per scaffold adatti agli scopi dell'ingegneria tissutale, in termini di porosità, interconnessione dei pori e dimensione dei pori. Le colture cellulari sono state eseguite in questi costrutti per creare un ambiente 3D in modo che le cellule seminate potessero crescere sia in coltura statica 3D che nel bioreattore a perfusione. La proliferazione e l'adesione delle cellule sono state osservate fino a 7 giorni di coltura *in vitro*, dimostrando che la morfologia degli scaffold può indurre la crescita delle cellule sia in condizioni statiche che dinamiche. Per la seconda parte, si è seguito un approccio combinato di modellazione e sperimentazione. Il sistema di perfusione usato è un bioreattore airlift (precedentemente progettato dal mio gruppo di ricerca) che fornisce un ambiente a basso sforzo di taglio e una buona miscelazione, risolvendo i limiti del trasporto di massa e fornendo stimoli fisici

vantaggiosi per la proliferazione e la differenziazione delle cellule. L'idrodinamica (gas holdup, velocità superficiale del liquido e sforzo di taglio) e il trasferimento di massa (in termini di coefficiente di trasferimento di massa) sono stati modellati e determinati da analisi CFD per esaminare l'influenza di questi parametri sulla crescita delle cellule e dei tessuti. I risultati della simulazione hanno indicato che l'idrodinamica, i dati matematici e la validazione sperimentale erano in linea tra di loro. In seguito, cellule osteoblastiche sono state coltivate su scaffold posti su un supporto all'interno del bioreattore perfuso con terreno di coltura a 10ml/ min per un massimo di 6 giorni. Combinando i risultati della proliferazione e l'analisi statistica, è stata quantificata e analizzata la crescita cellulare in funzione dello spazio all'interno del sistema bioreattore. Data la natura gerarchica del sistema bioreattore-scaffold, tale sistema è stato considerato dalla scala della matrice extracellulare alla scala del bioreattore. Le proprietà dipendenti dal flusso di una matrice ingegnerizzata e coltivata all'interno di un bioreattore a perfusione sono state studiate teoricamente e valutate sperimentalmente, sottolineando l'influenza delle dipendenze inter-scala.

I bioreattori a perfusione sono sistemi *in vitro* utili per testare famaci poiché imitano l'ambiente *in vivo*. A questo scopo, è stato modellato e validato sperimentalmente un sistema ottimizzato del bioreattore airlift in grado di indurre un doppio flusso su uno scaffold fabbricato con un canale al suo interno. In particolare, il sistema è stato testato per la diffusione di carriers e per simulare un sistema aria-liquido-interfaccia (ALI) tale da riprodurre l'ambiente della mucosa nasale. Il razionale di tale sistema è il potenziale legato alla combinazione di un flusso interno ed uno esterno di fluidi indipendenti al fine di diffondere i carriers in tutta la matrice ingegnerizzata per pre-screening di farmaci o reindirizzare il mezzo di coltura nel canale dello scaffold per alimentare le cellule seminate. In conclusione, questo progetto di tesi si è concentrato sui principali aspetti dell'ingegneria tissutale e della medicina rigenerativa, spaziando da test *in vitro* per la crescita delle cellule su scaffold, a modelli per studiare sia le caratteristiche multi-scala di un sistema atto a replicare un tessuto sia l'efficacia della fluidodinamica di un sistema nuovo destinato a validare test farmacologici o mimare al meglio la fisiologia di un tessuto.

Publications

1. F. Lopresti, A. Liga, E. Capuana, D. Gulfi, C. Zanca, R. Inguanta, V. Brucato, V. La Carrubba, F. Carfi Pavia. Effect of polyhydroxyalcanoate (PHA) concentration on polymeric scaffolds based on blends of poly-L-lactic acid (PLLA) and PHA prepared via thermally induced phase separation (TIPS). *Polymers.* 2022

2. E. Capuana, F. Lopresti, M. Ceraulo, and V. La Carrubba. Poly-L-lactic acid (PLLA)-based biomaterials for regenerative medicine: a review on processing and applications. *Polymers.* 2022

3. E. Capuana, A. Fucarino, S. Burgio, G. Intili, O. M. Manna, A. Pitruzzella, V. Brucato, V. La Carrubba, and F. Carfì Pavia. A dynamic Air Liquid Interface system for in vitro mimicking of the nasal mucosa. *Biotechnology and Bioengineering.* 2022

4. E. Capuana, F. Carfì Pavia, M. E. Lombardo, S. Rigogliuso,G. Ghersi, V. La Carrubba, and V. Brucato. Mathematical and numerical modeling of an airlift perfusion bioreactor for tissue engineering applications. *Biochemical Engineering Journal.* 2021

5. M. E. Lombardo, F. Carfì Pavia, E. F. Craparo, E. Capuana, G. Cavallaro, V. Brucato, and V. La Carrubba. Novel dual-flow perfusion bioreactor for in vitro pre-screening of nanoparticles delivery: design, characterization and testing. *Bioprocess and Biosystems Engineering.* 2021

6. E. Capuana, F. Lopresti, F. Carfì Pavia, V. Brucato, and V. La Carrubba. Solution-Based Processing for Scaffold Fabrication in Tissue Engineering Applications: A Brief Review. *Polymers.* 2021

7. F.Lopresti, S. Campora, G. Tirri, E. Capuana, F. Carfì Pavia, V. Brucato, G. Ghersi, V. La Carrubba. Core-shell PLA/Kef hybrid scaffolds for skin tissue engineering applications prepared by direct Kefiran coating on PLA electrospun fibers optimized via air-plasma treatment. *Materials Science and Engineering: C.* 2021

8. F. Lopresti, F. Carfì Pavia, M.Ceraulo, E. Capuana, V. Brucato, G. Ghersi, L. Botta, and V. La Carrubba. Physical and biological properties of electrospun poly(d,l-lactide)/nanoclay and poly(d,l-lactide)/nanosilica nanofibrous scaffold for bone tissue engineering. *Journal of Biomedical Material Researc: Part A.* 2021

9. E. Capuana, D. Marino, R. Di Gesù, V. La Carrubba, V. Brucato, R.S. Tuan, R. Gottardi R. High-Throughput Mechanical Activator for Cartilage Engineering Enables Rapid Screening of in vitro Response of Tissue Models to Physiological and Supra-Physiological Loads. *Cells Tissues Organs.* 2021

10. C. Zanca, I. Mendolia, E. Capuana, G. Blanda, F. Carfì Pavia, V. Brucato, G. Ghersi, V. La Carrubba, S. Piazza, C. Sunseri, R. Inguanta. Co-Deposition and Characterization of Hydroxyapatite-Chitosan and Hydroxyapatite-Polyvinylacetate Coatings on 304 SS for Biomedical Devices. *Key Engineering Materials.* 2019

National Conferences:

C. Zanca, G. Cordaro, E. Capuana, V. Brucato, F. Carfì Pavia, V. La Carrubba, G. Ghersi, R. Inguanta. Galvanic Deposition of Hydroxyapatite/chitosan/collagen Coatings on 304 Stainless Steel. *ICheaP15, Naples (Italy).* June 2021

International Conferences:

E. Capuana, D. Marino, R. Di Gesù, V. La Carrubba, V. Brucato, R.S. Tuan, R. Gottardi R. High-Throughput Mechanical Activator for Cartilage Engineering Enables Rapid Screening of in vitro Response of Tissue Models to Physiological and Supra-Physiological Loads. *ORS 2019 Annual Meeting - Orthopaedic Research Society, Austin (TX, USA).* February 2019 – Speaker: R. Gottardi

K. W. Smith, S. Ali Akbari Ghavimi, S. Logterman, P. M. Gehret, E. Capuana, G. Conoscenti, V. Brucato, V. La Carrubba, J. T. Lawrence, R. Gottardi. *In Vivo* Validation Of A Continuous Gradient Porous Scaffold For Osteochondral Defect Repair In A Rabbit Model. *TERMIS – AM 2022, Toronto (Canada).* July 2022 – Speaker: K. W. Smith

Acknowledgments

The Ph.D. course has been a path that has allowed me to grow from a professional and personal point of view, enriching my treasure of social and scientific experience. Thanks to this journey, I understood my path, which is to work in the world of research to make progress in the world of medicine and health.

I want to thank my colleagues Dr. Francesco Carfì Pavia and Ing. Francesco Lopresti, and my supervisors Prof. Vincenzo La Carrubba and Prof. Valerio Brucato, for their guidance and support during these three years, transmitting me their experience and love for research. Among these, I particularly thank Francesco Carfì Pavia for cheering the long working days.

I also want to express my gratitude to the colleagues of the Biology Department Simona Campora and Silvia Rigogliuso and of the I.R.C.C.S Rizzoli Institute Angela De Luca, for accepting me into their research group and collaborating with enthusiasm and mutual respect.

Finally, I genuinely thank my family and friends for their support and encouragement, especially during some of the more difficult times that occurred during this journey.

Table of contents

List of figures

List of Tables

Chapter 1

General introduction

1.1 Tissue engineering (TE)

By definition, the term "Tissue Engineering" refers to "the application of life sciences and engineering to develop a basic understanding of the functional and structural relationships of natural and pathologic mammalian tissues and the development of bio-substitutes that can be utilized to restore, maintain, or improve tissues damaged or lost by various disease conditions" (Vacanti and Langer, 1999; Meyer et al., 2016). Tissue engineering is an interdisciplinary field that combines the knowledge gained in cell and stem cell biology, biochemistry, and molecular biology, with advances in materials science, chemical engineering, and bioengineering, resulting in engineering principles applied to living systems.

The field of Tissue Engineering was established in the United States in the past decades as one possible solution for the tissue and organ deficiencies affecting an enormous number of patients and claiming transplantation as the only hope for survival. However, transplantation has the common problems of the demand for viable organs or tissue from donors that significantly exceeds the supply and the chronic rejection produced by the immune system over time (Wu and Hsu, 2015). On the other hand, Tissue engineering aims to construct organ or tissue substitutes in the laboratory by combining cells with artificial components and subsequently introducing them into a patient.

According to Saltzman (Saltzman, 2004), the field of tissue engineering can be organized in two ways: by organ system (which concerns the engineering replacements for tissues function, i.e., vascular TE or bone TE), and by general objective (involving the metabolic function or structural function of the tissue replacement). Different approaches have been defined to guide tissue regeneration, including to use only living cells, cells and a matrix or scaffold as a template and scaffolds alone. (Shafiee and Atala, 2017). Moreover, the advent of precision medicine has opened new perspectives in stem cell biology to produce tissue, leading to a new term, i.e., regenerative medicine, which is often used as TE synonym (Gomes et al., 2017). Most investigators in tissue engineering believe that the use of cells integrated with matrices offers an advantage over the use of cells alone to achieve new tissue formation (Lanza et al., 2007). In this strategy, regulatory signals, cells, and porous

biodegradable 3-dimensional (3D) scaffolds are combined to develop organized 3D functional tissue simulating the extracellular matrix (ECM) of the tissue to regenerate. These three essential components make up the well-known Tissue Engineering triad (Fig. 1.1).

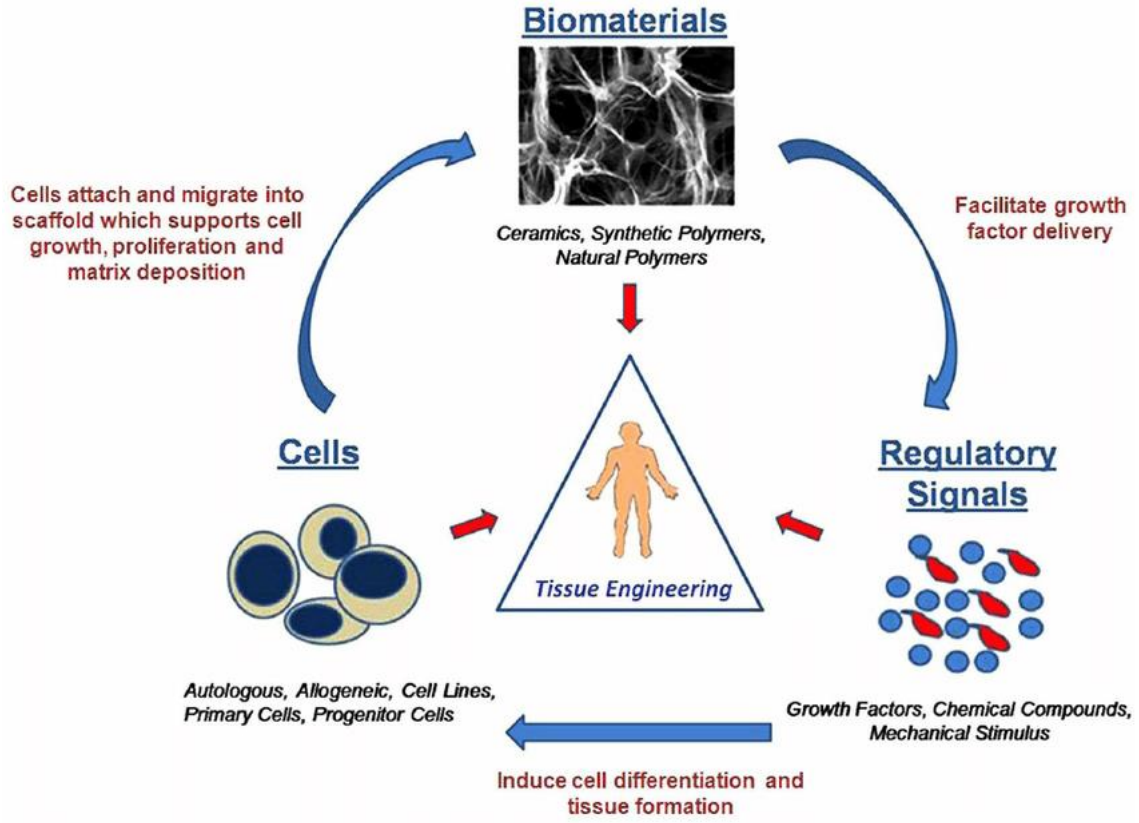

Figure 1.1 Schematic of the Tissue Engineering triad: cells, signals, and biomaterials are the main components for specific TE applications (Murphy et al., 2013).

Regulatory signals consist of the components to which cells are exposed in their microenvironment. They can be biological cues, physicochemical signals, mechanical stimuli, or even combinations of each other. These biochemical signals include growth and differentiation factors, specific receptors, and soluble molecules. Physical forces and chemical and mechanical stimuli can be applied using a bioreactor. The latter is a system containing cultures where the environmental conditions can be optimized and carefully controlled to influence cell behavior (Eberli, 2011).

Cells are the principal source for creating functional structures. In tissue engineering, some approaches use the patient's cells, either from another individual (genetically non-identical) or a nonhuman animal species; other applications use stem and progenitor cells which respond to signals to differentiate into differing lineages (Li and Yang, 2001). Nevertheless, harvested cells are placed into cell culture, where they proliferate and then are transferred to templates, such as scaffolds.

Scaffolds are biodegradable materials with an appropriate porous structure that provides 3D templates and a synthetic extracellular matrix environment to guide cell growth while mimicking the complex architecture of native tissues (Patel et al., 2011). Various fabrication technologies can be applied using synthetic or natural materials according to the structural and mechanical performance expected to replace the tissue.

1.2 Cells for Tissue Engineering applications

The need for living cells in the TE field rises from their ability to create functional tissues using preprogrammed information and signaling. Cells are fundamental for reaching the TE/regenerative medicine principle: collected cells are introduced directly into the damaged tissue or in a porous 3D material where the physicochemical and mechanical parameters of the environment allow cells homeostasis and stability (Stoltz et al., 2012). Mechanical cues can be intracellular or extracellular and are exerted in the cytoskeleton, transmitting them to long distances. Additional intercellular forces that may be direct or biochemically transformed are essential for tissue development.

There are three cell strategies for treating diseased or injured tissues during therapy: (1) implantation of isolated cells, (2) implantation of a tissue substitute composed of cells and scaffolds, or (3) *in situ* tissue regeneration by native cells through gene therapy (Murphy et al., 2013). Hence, the starting point to engineering a tissue or organ substitute is to choose the source of the cells to be employed, which can be autologous, allogeneic, or xenogeneic, as described in Tab. 1.1.

Table 1.1 List of the three traditional sources of cells for organ and tissue substitute (Lanza et al., 2007)

Type	*Comments*
Autologous	Patient's own cells; immune acceptable, but does not lend itself to off-the-shelf availability unless recruited from the host
Allogeneic	Cells from other human sources; lends itself to off-the-shelf availability, but may require engineering immune acceptance
Xenogeneic	From different species; not only requires engineering immune acceptance, but must be concerned with animal virus transmission

Among these sources, the better choice is an autologous cell, i.e., differentiated cells or adult stem/progenitor cells. For collecting cells, a tissue sample is obtained from the patient's biopsy, and then individual cell types are isolated from these biopsies and selectively expanded for implantation (Yamzon et al., 2008). Concerning autologous cells, these cells are not simply available and are frequently in a pathological state. This fact explains the increasing interest in allogenic and xenogeneic cells. Xenogeneic tissues induce more vigorous rejection than allogeneic tissues, thus requiring a high dosage of immunosuppressants to prevent graft rejection (Eberli, 2011).

The difference between cell types relies on their degree of differentiation. Stem cells, derived from adult or embryonic tissue, have unlimited self-renewal and the potential to differentiate. Embryonic stem cells are totipotent in that they can differentiate into any tissue in the organism under micro-environment manipulation or specific culture conditions. Besides, they can undergo limitless undifferentiated proliferation *in vitro*, making them a potential source for large-scale production of cell lines (Chimutengwende-Gordon and Khan, 2012). However, embryonic stem cells have disadvantages associated with their immunogenicity, tumor formation *in vivo*, and ethical concerns. Adult mesenchymal stem cells (MSC) are multipotent, meaning they can differentiate into numerous cell lineages, such as bone, cartilage, adipose tissue, muscle, tendon, ligament, and nerve. They have received significant attention in regenerative medicine for their regenerative capabilities of injured tissue.

Progenitor cells have a limited or no capacity for self-renewal and are classified as unipotent cells since they can differentiate into one target tissue. They are frequently used in bone tissue engineering, where tissue regeneration is biologically driven by progenitor cells that can form new osteoblasts (Murphy et al., 2013). Likewise, primary cells, which are mechanically or enzymatically isolated from tissue explants, are commonly used in bone TE since they provide cells more comparable to endogenous progenitors.

Recently, a new type of cell has been developed: Induced pluripotent stem cells (iPS). They result from the addition of transcription factors that lead to *in vitro* reprogramming of an adult cell. This point is likewise necessary to underline that the iPS are exposed to a significant risk of malignant transformations (Stoltz et al., 2012).

In Tissue Engineering and Regenerative Medicine, once one has selected the cell type to be employed, cells are induced to differentiate and proliferate in static or dynamic culture by using a scaffold and/or in a bioreactor. During culture, cells initially undergo growth and subsequent changes or development. Firstly, cells produce proteins inside their structure; after their development, proteins are produced outside cells. In tissue formation, cells

initially differentiate and organize and then produce molecules to form the ECM. The driving force of this process relies on cell proliferation, gene reprogramming, and energy supply (i.e., blood and oxygen). In addition, the development of different tissue types and cell differentiation depend on the specific site of cell migration. While culturing cells, the culture media needs a specific composition, with growth factors compatible with targeted cells lines. Generally, adding growth factors during cell culture induces lower proliferation and higher differentiation. Also, molecules concentration needs to be monitored since it affects information sent to cells. Indeed, the environment affects cell behavior and triggers morphogenesis under different chemical cues (i.e., soluble factors) and physical cues (i.e., traction/shear forces, contact, or intermediate cells). In this process, the cytoskeleton of cells mainly interacts with the environment and decides cells' fate. Several biological assays that analyze morphology, viability, and gene/protein expression are used to assess cell activity, proliferation, and differentiation *in vitro*. Specifically, to examine the cell differentiation and phenotypic expression, well-defined proteins that affect proliferation induction and the synthesis of extracellular by the cells are investigated (Lin et al., 2014). Among them, the transforming growth factor TGF-β, insulin-like growth factor (IGF-1), bone morphogenetic proteins (BMPs), fibroblast growth factors (FGFs), and epidermal growth factor (EGF) are the molecules that are mostly considered for TE studies (Nerem and Sambanis, 1995).

1.3 Scaffolds for Tissue Engineering

The development of biological substitutes to replace, repair, and improve the functions of tissues is one of the main purposes of Tissue Engineering (Martin et al., 2004; Lanza et al., 2007; Zhao et al., 2018b). Scaffolds play a crucial role in providing functional support to enhance extracellular matrix deposition and cellular growth while temporarily replacing the mechanical function of the tissue (Scaffaro et al., 2016). An ideal scaffold should mimic the native extracellular matrix, an endogenous substance that surrounds cells providing mechanical signals that aid cellular development and morphogenesis (Patel et al., 2011). Biocompatibility, sterilizability, appropriate mechanical properties, and high surface-to-volume ratio are some of the essential characteristics of materials suitable for TE applications (Cruz, 2010; Gupta et al., 2018; Bisht et al., 2021). Moreover, scaffolds need to be biodegradable materials whose degradation must be compatible with the production of the ECM by the cells (Eberli, 2011; Shafiee and Atala, 2017). It is possible to control their biodegradation by changing the composition of materials. Therefore, the actual challenge of

TE is to fabricate scaffolds that enhance the adherence of cells and ensure that the mechanical properties of the engineered tissue are appropriate for the *in vivo* environment (O'Dea et al., 2013). For instance, modifying a scaffolding material with reinforcing components is a commonly adopted strategy to improve its degradation and mechanical properties, cell proliferation, and absorption (Ciapetti et al., 2012; Pandey and Sakurai, 2021).

The scaffold architecture and morphology also influence the cell-matrix interaction during cell culture on templates. Depending on the fabrication technique used, two types of structures can be obtained: foam-like scaffold or fibrous scaffold. Foams can be fabricated by freeze-drying and phase separation by finely tuning porosity, pore size, and shape while having a fully interconnected pore network. Fiber scaffolds can be produced by electrospinning, creating fibers deposited on top of each other in a random or aligned manner (Eberli, 2011).

Recently, many studies have focused on the effect of the pore structure on cell organization and tissue regeneration (Li and Yang, 2001; Fu et al., 2017). Compared to low porosity and small average pore size matrices, high porosity and larger pore size enhance the formation of 3D large cells aggregate among the fibers/pores (Keeney and Pandit, 2009). In scaffolds with low porosity and small pore dimension, cells are inclined to spread as individual cells on a single fiber surface or bridged across several fibers/pores (Oh et al., 2010).

3D functional scaffolds can be produced using both natural-based and synthetic-based materials (Vacanti and Langer, 1999). In addition, ceramic materials have also been used in tissue engineering applications due to their high resilience and suitability for mineralized tissues, such as bone (Zeinali et al., 2021). While processed, ceramics cannot be easily transformed into interconnected porous structures because of their brittle nature (Patel et al., 2011). When combining ceramic and polymer materials, it is possible to produce scaffolds with mechanical properties that match the ones of load-bearing tissues (Yang et al., 2001). Natural biomaterials support cell attachment, growth, and differentiation. This feature occurs because these materials induce a positive response of the host tissue and do not produce harmful degradation products, thus enhancing the integration within the body (Serbo and Gerecht, 2013). The major limitation of natural polymers is their low mechanical strength affecting the process of scaffold fabrication. As compared to natural-based polymeric scaffolds, scaffolds developed with synthetic materials can be easily modifiable and manufactured (Solchaga et al., 2005; Siddiqui et al., 2018) since they present more tunable properties, such as molecular weight, crystallinity, and transition temperatures (Chen et al.,

2020a). Synthetic-based scaffolds can be reproducible and readily available and are cheap to fabricate, offering control over many critical properties, such as the degradation rate and mechanical properties. However, their hydrophobic nature limits the cell-material interactions and the biological recognition on the material surface. Surface treatments can be exploited to improve the surface bioactivity of synthetic polymers, thus providing an ideal environment for promoting cell adhesion (Patel et al., 2011). The deposition of bioactive molecules is the most commonly used surface treatment. However, surface modifications may alter surface chemistry so that protein absorption and chemical reactions dramatically change, thus affecting the in vivo response. Hence, composite scaffolds have been produced to improve the properties of the pure biomaterial while overcoming the issues related to surface modifications. Specifically, natural and synthetic polymers, together with ceramic materials, can be combined to formulate composite scaffolds with desired physical, mechanical, and biological properties (Yang et al., 2001; Liang et al., 2018; Ou et al., 2020). The biopolymers that are most commonly used in TE are polycaprolactone (PCL), polylactide (PLA), and its homopolymers (PLLA and PDLA), poly(lactide-co-glycolide (PLGA), poly(vinyl) alcohol (PVA), gelatin, chitosan, and collagen. The most common bioceramics used in the TE field are hydroxyapatite, bioactive glasses, and calcium phosphate, that are bioactive, biocompatible materials used as fillers for bone defect repair (Bružauskaitė et al., 2016). Hence, several combinations of scaffold, cells, and bioactive molecules can be tested to facilitate the regeneration of damaged tissues.

Due to the structural and mechanical performance required for tissue replacement, different fabrication methods have been developed, such as freeze-drying, Thermally or Diffusion Induced Phase Separation (TIPS or DIPS), electrospinning, 3D printing, particulate leaching, or a valuable combination of them.

1.3.1 Scaffolds fabrication technologies

A key for suitable scaffold production is a guaranteed interconnected porous structure that allows the cells to grow as in native tissue. The fabrication techniques should meet the appropriate requirements, including feasible reproducibility and time- and cost-effective assets (Capuana et al., 2021a). Here, general information on the most widely adopted technologies, including freeze-drying, thermally or diffusion induced phase separation (TIPS or DIPS), electrospinning, and additive manufacturing, are presented. Table 1.2 represents an overview of these manufacturing processes, with their advantages and

disadvantages.

Table 1.2 Techniques for scaffold fabrication with pros and cons

Technique	***Description***	***Advantages***	***Disadvantages***
Phase Separation (TIPS) and (DIPS)	The system becomes thermodynamically unstable, being induced to separate into two distinct phases. The solvent is subsequently eliminated forming a porous network characterized by appropriate pore geometry and interconnectivity	Low production cost, simple experimental procedure, capability to produce highly porous scaffolds with controllable architecture	Use of organic solvents, limited material selection
Particulate leaching	Porogens are dispersed in a polymeric solution. After solvent evaporation, leaching of the porogen leaves open-cell porous foams	Controlled pore size and porosity, low production cost, large material selection	Use of organic solvents, poor interconnection of pores
Electrospinning	It produces polymer fibers by inducing the polymer solution to travel through a small needle towards the collector thanks to high voltage	High porosity, nano-sized fibers, high surface area	Inhomogeneous distribution of pores, high-voltage and conducting materials required
Freeze drying	As porogen leaching, but using ice crystals to form porous structures	Controlled pore size, easy to operate, use of water instead of organic solvents	Slow production, difficult to produce hierarchical structures
Additive manufacturing	Technology to fabricate complex models' layer by layer, regardless of the shape geometry	Manufacturing of complex topology structures, no toxic solvents, reproducibility	micro-sized fibers and large-sized pores, difficult to handle

Freeze-drying

Freeze-drying (or lyophilization) is a conventional technique for 3D scaffold fabrication, creating a complex scaffold geometry while achieving a uniform pore morphology (Siddiqui et al., 2018). This method converts solutions into solids through four steps: pretreatment, freezing, primary drying, and secondary drying (Fereshteh, 2018) (Fig. 1.2).

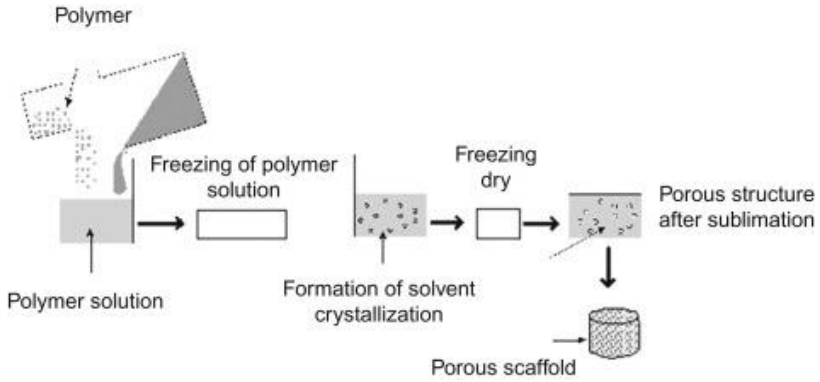

Figure 1.2 Schematic of the freeze-drying steps for scaffold fabrication (Ghalia and Dahman, 2016)

In the first stage, treatments are applied to improve the stability of the precursors during the formation process so that the prepared precursors are ready for the freezing stage. In this latter, the solution is cooled down to a temperature below the triple point of the solvent; so that solvent crystals sublimate, and the polymer creates an arranged network within the interstitial spaces (Ranganathan et al., 2019). The final drying phase is divided into two steps in which the solvent in frozen and unfrozen components is removed by sublimation and evaporation, respectively (Brougham et al., 2017). Temperature and pressure cycles are accurately adjusted during the whole process to avoid structural damage of produced scaffolds and achieve a controlled interconnected porous architecture.

Overall, freeze-drying can produce pore structures that can be effectively controlled by modifying the freeze-drying cycle, hence fabricating a variety of scaffolds with a wide range of mean pore dimensions (Haugh et al., 2010). Moreover, by circumventing the dissolution in organic solvents, both natural-based and synthetic polymers with a high hydrosolubility are used to produce porous structures that are functionally robust and potentially non-cytotoxic. Moreover, this technique was demonstrated to be effective in fabricating multi-layered scaffolds, which also exhibit widespread applications in biomimetic TE, i.e., scaffolds with a nano-scaled architecture. However, this technique presents the disadvantage of being significantly energy- and time- consuming; and the resulting pore sizes are substantially smaller than would be expected for supporting penetration and differentiation of certain types of cells (Izquierdo-Barba, 2014; Dattola et al., 2019; Liu et al., 2020).

Phase separation

Phase separation is a widely explored scaffold fabrication technique with the advantage of tailoring mechanical properties and pore size of the foams produced for tissue engineering purposes (Liu et al., 2020). A phase separation process takes advantage of the thermodynamic demixing of a homogeneous polymer–solvent (binary) or polymer-solvent-

nonsolvent (ternary) solution to obtain a polymer-rich (with a high polymer concentration) and a polymer-lean phase (with a low polymer concentration) (Zeng et al., 2016). As a result, a solid matrix forms after the solidification of the polymer-rich phase, while the polymer-lean phase generates pores after solvent removal (Lu et al., 2013). The phase separation can occur as a consequence of the diffusion between the solvent and a nonsolvent (immiscible or partially miscible solvent) or by reaching a demixing temperature (Fig. 1.3) (Wang et al., 2013). The first process is called either diffusion induced phase separation (DIPS) or nonsolvent induced phase separation (NIPS), and the second one is known as thermally induced phase separation (TIPS). In the DIPS method, the first step is the molding of a thin layer of the polymer solution onto a solid support (i.e., tube, fibers), followed by immersion in a nonsolvent bath to induce the demixing (La Carrubba et al., 2010). The TIPS process consists of changes in temperature onto the homogenous polymer solution, creating two different phases in equilibrium (Conoscenti et al., 2017). Both processes are usually followed by extracting the obtained foams from the mold, a washing step in distilled water, and a desiccation stage to ensure the removal of any solvent trace (Guillen et al., 2011; Thavornyutikarn et al., 2014; Geven et al., 2021).

Using the DIPS technique, the average size and pore size distribution, together with the size and shape of the scaffolds, can be easily adjusted by choosing a few key process parameters (Figoli et al.). Some limitations of this technique concern the evaporation-induced shrinkage of the produced scaffolds and the formation of macro voids that could weaken the mechanical properties of the constructs (Figoli et al.; Jung et al., 2016).

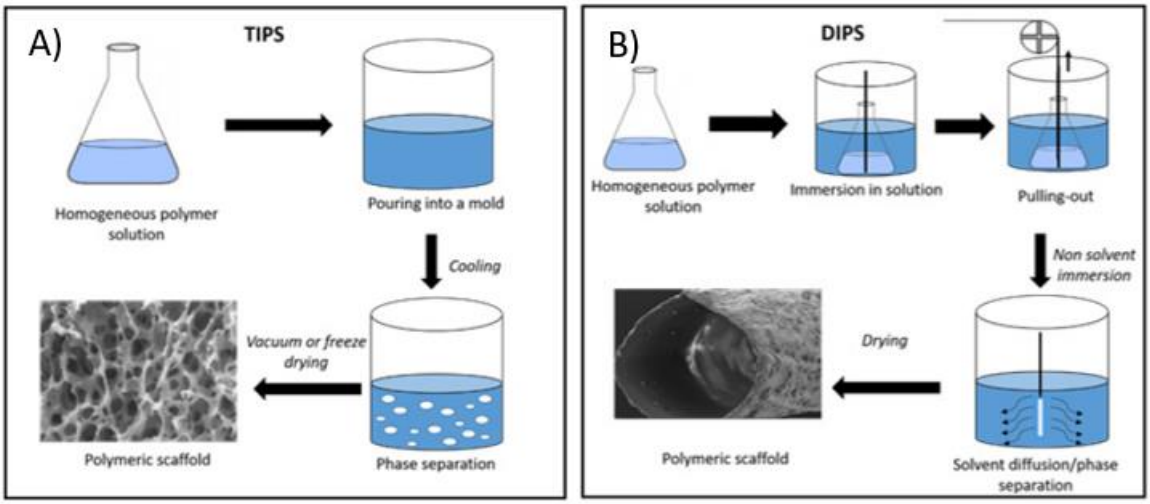

Figure 1.3 Schematic of the two main phase separation-based techniques for scaffold fabrication: (A) the thermally induced phase separation (TIPS) and (B) the diffusion induced phase separation (DIPS) (Capuana et al., 2021a)

TIPS

In thermally induced phase separation, the porous scaffold morphology is significantly affected by changing the parameters, such as types of polymer, polymer concentration, solvent/nonsolvent ratio, and thermal history (i.e., temperature versus time path) (Yang et al., 2001). The fabrication of polymeric scaffold was carried out by Lombardo et al. (Lombardo et al., 2019) via TIPS by using PLLA to assess the morphology of scaffolds prepared by varying demixing temperatures, times, and immersion conditions, as shown in Fig. 1.4. According to their findings, by keeping the cooling pathway constant, longer demixing time results in larger pore size.

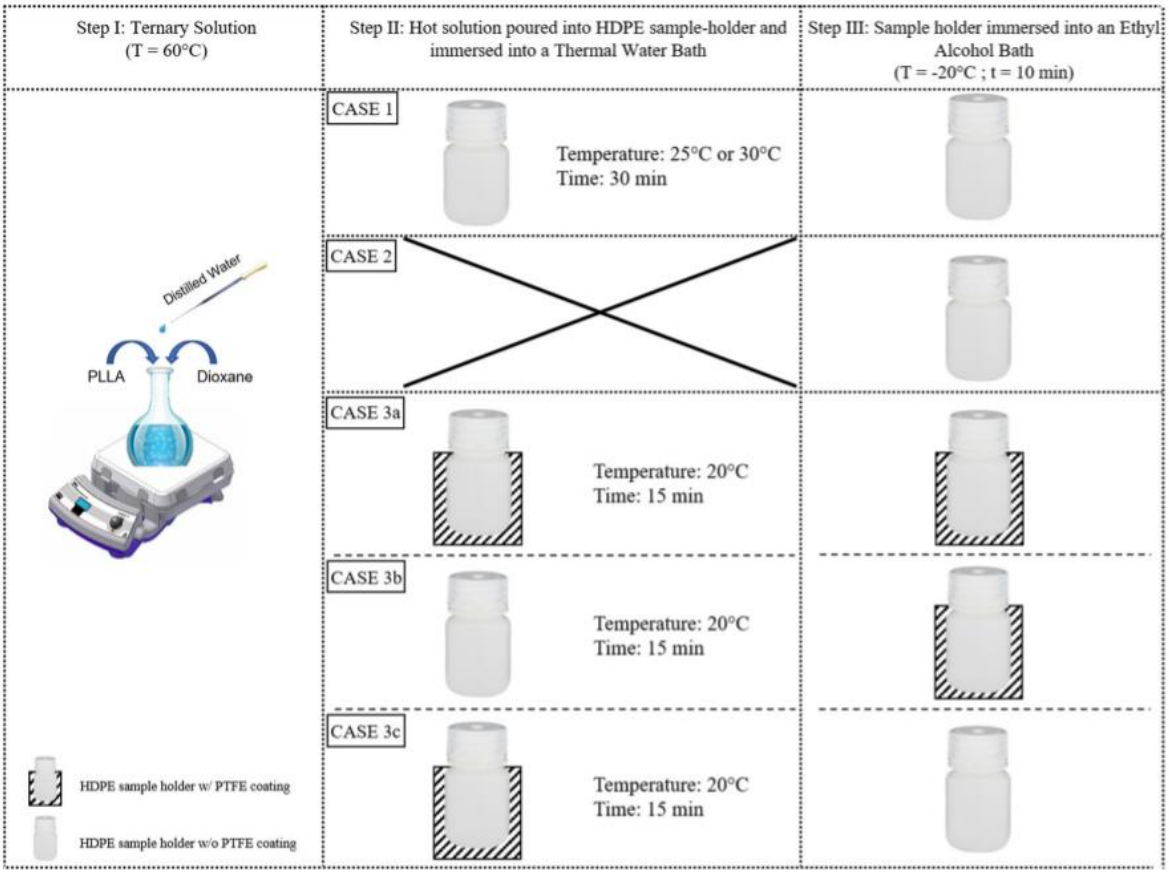

Figure 1.4 Schematic representation of scaffold preparation steps. A ternary solution (PLLA/dioxane/water) was prepared and kept at T = 60 °C, and hot poured into HDPE cylindrical sample-holders. Case 1: the sample holder was maintained at the demixing temperature of 25 °C (or 30 °C) for 30 min; thereafter, the system was suddenly quenched by pool immersion in an ethyl alcohol bath (EAB) at a temperature of −20 °C for at least 10 min to freeze the as-obtained structure. Case 2: the sample-holder was placed directly at −20 °C for 20 min being subjected to the so-called Direct Quench (DQ). Case 3 a,b,c: the sample holder was kept uncoated or embedded in a PTFE coating before immersion in the thermostatic water bath (TWB) and then maintained at the demixing temperature of 20 °C for 15 min; thereafter, the system was suddenly quenched by pool immersion in an ethyl alcohol bath (EAB) or at a temperature of −20 °C for at least 10 min to freeze the as-obtained structure (Lombardo et al., 2019).

Moreover, as the polymer concentration increases, pore dimension and porosity decrease accordingly while obtaining a well-interconnected macroporous structure (Sabzi et al., 2020).

Overall, the TIPS technique is an effective conventional fabrication technology for tissue engineering scaffolds that allows one to generate porous matrices with an interconnected pore network while offering low production cost and relatively easy processability (Zeinali et al., 2021). Moreover, it is one of the most effective methods for producing polymeric foams with porosity over 95% (Lou et al., 2016). Despite the presence of organic solvents, a literature review confirms that the TIPS process ensures the achievement of a final structure without any remaining solvent trace, thus preserving biocompatibility. However, this phase separation method suffers from some disadvantages, such as limited material selection, reduced reproducibility, and unspecific resolution (Nikolova and Chavali, 2019).

Electrospinning

Electrospinning involves the production of continuous fibers from inducing the charged filaments of polymer solutions by using an electric force directed by a high-voltage system equipped with a syringe connected to a metallic needle, a pressure pump, and a grounded stationary or rotating collector (Fig. 1.5) (Das et al., 2021; Lopresti et al., 2021a).

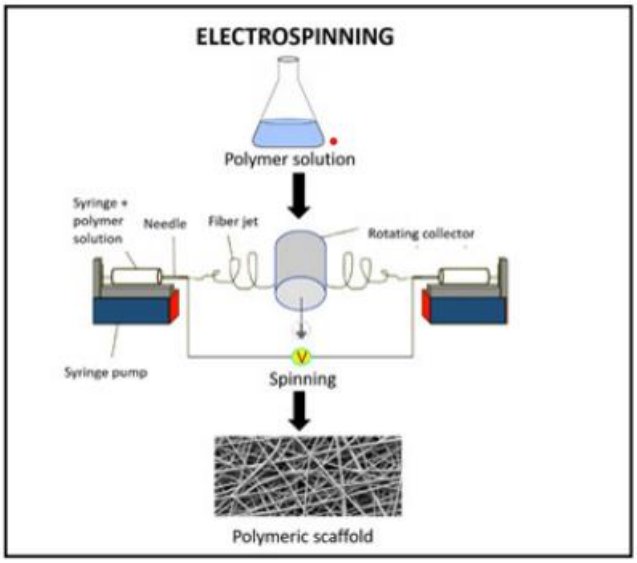

Figure 1.5 Schematic of the electrospinning technique for scaffold fabrication (Capuana et al., 2021a)

As the liquid solution is pumped into the syringe, it flows upward on a dangling droplet suspended at the tip of the needle. This droplet is then stretched continuously to form a conical structure, called a Taylor cone, increasing the applied tension. Successive jet initiates from the tip of the Taylor cone, and then it is continuously stretched and thinned down by

the electrostatic force overcoming the liquid surface tension (Das et al., 2021). The electrospinning process requires particular attention to factors influencing the structure and size of electrospun fibers and preventing the break-up of the fibers during the process, such as solution concentration, polymer average molecular weight and distribution, viscosity, electric field, solution feed rate, and voltage (Koyyada and Orsu, 2020).

The fabrication of nanofiber scaffold mainly occurs by the electrospinning method, which better supports a fine-tuning of surface area and aspect ratio in a fast and effective manner. Moreover, this technique allows the control over porosity, pore size, and diameter of fibers and a high degree of flexibility in creating the final form of scaffolds. Some disadvantages rely on the limited thickness of nanofibrous scaffolds produced through conventional electrospinning and limitations in cell penetration within the fibrous network (Tan and Zhou, 2019; Christy et al., 2020).

Additive manufacturing

Additive manufacturing (AM) technologies involve the process of creating a three-dimensional object through repetitive deposition and processing of material layers using a computer-aided design (CAD) model (Zhao et al., 2018b). This approach can offer a solution for fabricating structures with specifically required internal and external geometry (Swieszkowski et al., 2007). Nevertheless, cell seeding/encapsulation and growth in these scaffolding structures seem to be still inefficient (Di Luca et al., 2016).

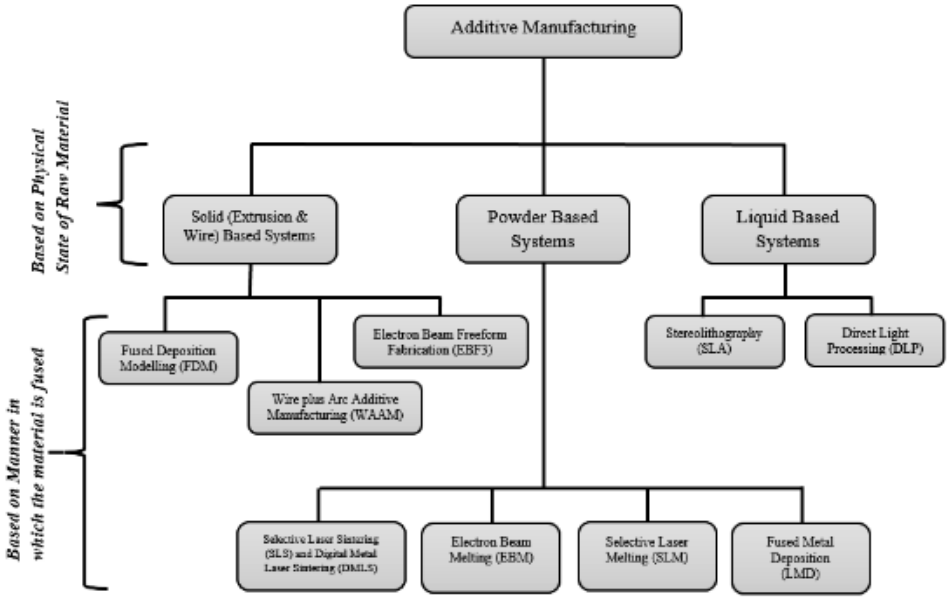

Figure 1.6 Classification of different AM processes (Joshi and Sheikh, 2015)

Various additive manufacturing techniques have been applied in tissue engineering (Fig. 1.6), such as 3D printing, fused deposition modeling (FSM), stereolithography (SLA), and selective laser sintering (SLS). Among the latter, inkjet-based three-dimensional printing was the first used in tissue engineering applications (Lanza et al., 2007). This technique involves an inkjet printing system directed by the CAD program, a thin layer of polymer powder spread over a piston surface, and a binding liquid dispensed by the inkjet (Fig. 1.7). The inkjet is the polymer solvent and acts as a binder for compacting the powder according to the desired geometry. Biological agents, such as growth factors, can also be incorporated into the printed scaffolds to improve biocompatibility (Wang et al., 2021).

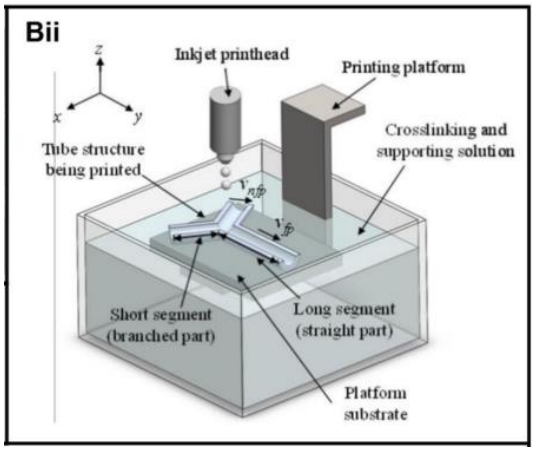

Figure 1.7 Inkjet printing system to form scaffold with the desired geometry designed in a CAD program (Wang et al., 2021)

FDM is a heat-using technique consisting of the extrusion from a nozzle and deposition layer by layer of the filament of the desired material, which is previously fed and melted in a liquefier by heat (Fig. 1.8A) (Wu and Hsu, 2015). SLA is a high-precision, high-resolution process that uses a photoreactive resin that is selectively cured while a platform moves the construct after each new layer is deposited (Fig. 1.8B) (Nikolova and Chavali, 2019). SLS involves small particles, particularly ceramics or glass, which are fused using a high-power laser to form a 3D structure and 3D CAD data to guide the tracing laser, thus providing the final geometry (Fig. 1.8C) (Shivalkar and Singh, 2017).

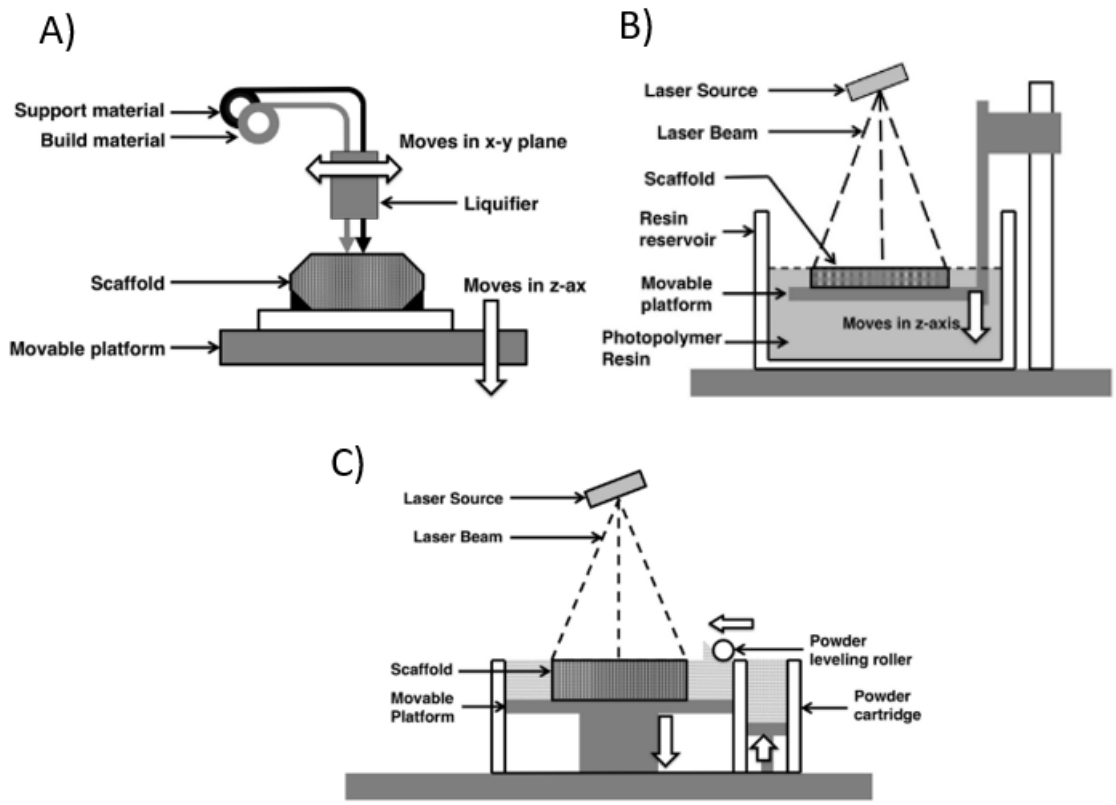

Figure 1.8 Schematic of the equipment and features concerning (A) Fused deposition modeling (FSM), (B) stereolithography (SLA), and (C) selective laser sintering (SLS) (A) (Wu and Hsu, 2015)

Recently, 3D biofabrication technologies, relying on the simultaneous deposition of cells and biomaterials, have been developed in the TE field as an innovative approach to form 3D well-organized living heterogeneous structures (Groll et al., 2016). This strategy is the first in which cells are included in the 3D structure from the beginning, thus overcoming the issue related to 3D culture efficiency after seeding. However, this technique requires an enormous cell number (up to 180 million) that may change their phenotype during their long-time expansion in 2D flasks.

The advantage of additive manufacturing technologies is their design-dependent characteristic for scaffold fabrication, whereas conventional scaffold fabrication techniques are highly process-dependent. Moreover, highly reproducible scaffolds with size, geometry, and porosity that can be precisely controlled can be manufactured according to a patient's specification (Wu and Hsu, 2015). On the other hand, complex, high-precision scaffolds require higher resolution than these technologies offer, especially for nano- and micro-sized porous structures. To meet these requirements, 3D printing can be integrated with other technologies, such as solvent casting, electrospinning, or post-processing technologies (Wang et al., 2021).

Particulate leaching

The particulate leaching, or solvent casting, technique is the fabrication technique that best enhances control over porosity and pore diameters. This method uses particulate porogen to form sponge/foam-like scaffolds by dispersing the particles (i.e., sodium chloride, sodium citrate) into a polymer solution to form a homogeneous mix. This dispersion is then treated by casting or freeze-drying to evaporate the solvent and finally porogen leaching to leave the rest (Sivashanmugam et al., 2015). Fig. 1.9 shows the sequence of the described steps concerning the particulate leaching process.

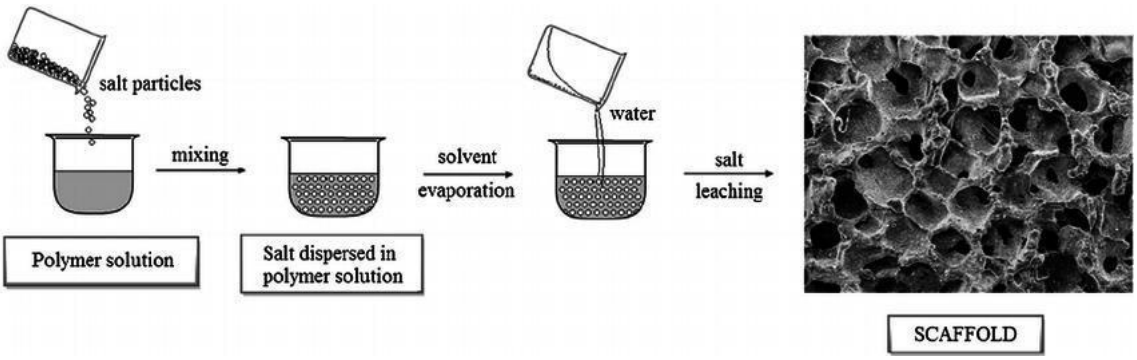

Figure 1.9 Steps for the fabrication of porous scaffold using particulate leaching process (Hua et al., 2015)

The scaffold porosity can be controlled by the amount of added particulate, while the pore size is dependent on the size of the crystal (Patel et al., 2011). Disadvantages include the time-consuming leaching step, the decreasing bioactivity or the removal of molecules for polymers preloaded with bioactive molecules due to salt leaching, and the poor interconnection of pores (Lanza et al., 2007; Patel et al., 2011; Huang et al., 2014).

1.3.2 PLLA-based scaffolds for Tissue Engineering

Among biodegradable polymers used for tissue engineering, poly-L-lactic acid (PLLA) has been investigated thanks to its high mechanical properties, tailorable biodegradability with time, and good biocompatibility (Ciapetti et al., 2012). PLLA can maintain mechanical and structural integrity during *in vitro* and *in vivo* applications while supporting tissue formation. PLLA possesses versatile properties, as its crystallinity, thermal and mechanical resistance, and solubility can be modified in several ways (Casalini et al., 2019). In addition, PLLA is a biomaterial approved by FDA for its non-cytotoxicity, which indicates that the scaffold could promote tissue regeneration. However, PLLA is a polyester that can degrade by hydrolysis into acid by-products which could alter the local pH, thus affecting the differentiation of cells seeded into the scaffolds (Solchaga et al., 2005; Lee et al., 2021).

Surface modifications can be operated by biochemical or physical procedures to manipulate PLLA hydrophobicity and augment cell adhesion and adsorption (Siddiqui et al., 2018; Bisht et al., 2021). Moreover, PLLA is commonly combined with other biomaterials, such as natural and synthetic polymers and bioceramics, to produce TE scaffolds (Fig. 1.10).

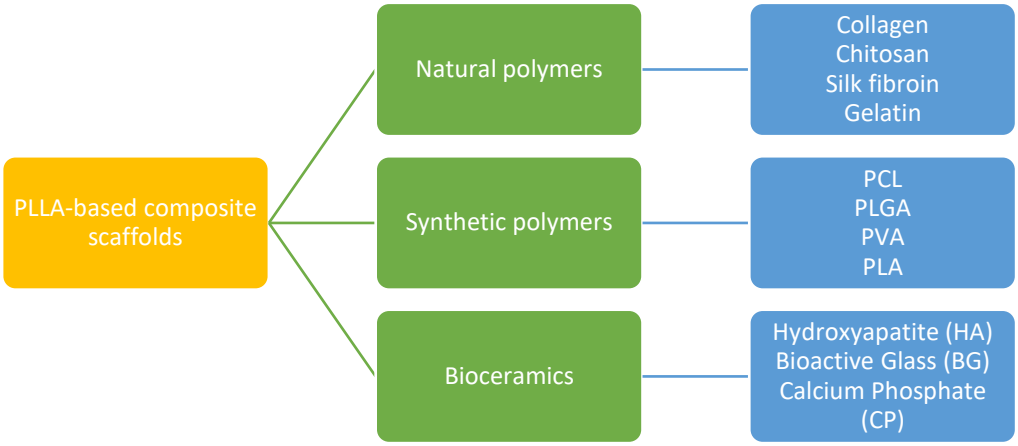

Figure 1.10 Biomaterials that are commonly combined with PLLA to produce PLLA-based scaffolds.

Different fabrication technologies have been reported for PLLA-based scaffold manufacturing. Pisanti et al. (Pisanti et al., 2012) produced PLLA scaffolds using supercritical carbon dioxide gel drying (SC-CO_2) and combining this technique with porogen leaching. Respectively from the two processes, they obtained nanoporous and microporous structures. Their research showed that the produced scaffolds with larger pore sizes induced a higher proliferation of hMCSs cells. La Carrubba et al. (Montesanto et al., 2015, 2019; Carfì Pavia et al., 2017; Conoscenti et al., 2017; Lombardo et al., 2019) have extensively studied PLLA scaffolds produced via phase separation techniques and have found that these methods allow to improve scaffold morphology and enhance cells growth. They investigated TIPS and DIPS techniques and optimized operating parameters to obtain porous matrices with porosities and pore sizes adequate to host various cells. The TIPS technique has also been combined with the sugar template method to produce PLLA matrices with precisely regulated porous architecture (Ge et al., 2016). Additionally, another central feature of PLLA scaffolds produced by phase separation is the capability to control their biodegradability (Zeinali et al., 2021). Electrospinning is another technique to produce pure PLLA scaffolds for tissue engineering (Huang et al., 2003; Ramakrishna et al., 2005; Pham et al., 2006). Electrospun PLLA has a nanofibrous structure whose porosity and thickness depend on the initial concentration of the polymer solution (Chen et al., 2020b). The electrospinning process may be used to fabricate piezoelectric PLLA scaffolds for sensing applications by stretching the randomly orientated chains and aligning molecular dipoles to induce

polarization (Sultana et al., 2017). Researchers have shown how it is possible to fabricate 3D scaffolds from PLLA powder through a rapid prototype technique (Patel et al., 2011). However, 3D-printed PLLA scaffolds seemed to exhibit large-sized pores that cannot support cell adhesion (Zeinali et al., 2021).

Since the mechanical properties and degradation behavior of PLLA are influenced by its crystallinity degree (which is associated with the scaffold fabrication techniques), researchers must consider all the technical parameters during scaffold fabrication when they aim to improve the properties of scaffolds (Lin et al., 2020). Several studies have shown that PLLA-based scaffolds can promote tissue ingrowth and the development of functional substitutes, both *in vitro* and *in vivo*, for specific TE applications, such as bone, skin, cartilage, and vascular repair.

1.4 Regulatory signals in Tissue Engineering applications

Regulatory signals are the third component of the tissue engineering triad. They include biochemical, biophysical, and biomechanical stimuli that strongly influence cell behavior. The ECM plays a relevant role in this activity by encoding molecular, biochemical, and physical information that the surrounding environment provides (Murphy et al., 2013). This feature means that ECM molecules alter cell growth via biochemical and biomechanical signaling mechanisms. In addition, the timing and mode of application of these stimuli change cellular behavior.

Biochemical stimulation is generally referred to as the presence of growth factors and cell-signaling molecules (i.e., cytokines and receptors). Also, culture conditions and cellular interactions play a positive role in modulating tissue growth and development (Stoltz et al., 2012). On the other hand, tissue culture bioreactors represent a controllable system for providing biophysical (i.e., pH, pressure, and temperature) and biomechanical (i.e., mechanical forces) signals, thus allowing to improve the understanding of the *in vivo* phenomena by means of a reproducible *in vitro* culture environment (Anderson and Johnstone, 2017).

1.4.1 Biochemical stimuli: growth factors

At the *in vivo* level, the local cellular environment is responsible for biochemical signaling pathways affecting cellular processes such as differentiation, proliferation, migration, and death. Hence, the biochemical environment of cells should have the optimal nutrient/oxygen delivery and the provision of growth factors and other cell-signaling molecules.

Growth factors are soluble, small, and stable polypeptides of ECM secreted by cells and acting as mediators between cells and ECM. When cells experience a defined stimulus, the production of specific growth factors, which bind to receptors on the cell surface, activates defined signaling pathways that govern gene expression for tissue growth and function. Hence, growth factors can be used to change patterns of gene expression in target cells, as well as to up-regulate and down-regulate the synthesis of other growth factors and receptors (Murphy et al., 2013).

In tissue engineering, growth factors have been widely adopted to control cell attachment, viability, protein adsorption, and differentiation of stem cells (Naqvi and McNamara, 2020). Nowadays, growth factors can be produced in the genetic engineering laboratory and used in biological therapy. The *in vitro* growth factor studies have been performed by simply adding a soluble growth factor to the medium and have shown that an appropriate combination of growth factors and scaffolds has great potential to promote tissue repair effectively. Nevertheless, the use of localized slow release of growth factors is one approach that is being tested for the fabrication of synthetic, large tissue, and whole organs. For this purpose, tissue-engineered devices involve controlled drug-delivery methods to release growth factors that may increase angiogenesis or facilitate new tissue formation (Vacanti and Langer, 1999).

During *in vivo* conditions, the growth factors incorporated into scaffolds can spread out of the scaffolds and degrade rapidly (Chen et al., 2020a). Additional studies are required to clarify the optimal strategy for tissue regeneration *in vivo* when growth factor incorporation is adopted.

Since growth factors are polypeptides, their sequence of amino acids allows the classification into families, suggesting that they evolved from a single protein. The most investigated families are (Gooch et al., 2001; Masszi et al., 2010; Wengst and Reichl, 2010; Van Caam et al., 2016; Zhang et al., 2018):

- The insulin family comprises insulin-like growth factors (IGF-1 and IGF-2) constitutively produced in large amounts in the liver and locally in many other tissues, such as kidney, heart, lung, fat tissues, and various glandular tissues. For therapy purposes, local application of IGF-1 is of interest for degenerative joint diseases due to its ability to stimulate osteoblast activity and collagen production. Besides, IGF-1 promotes insulin actions, thus improving relative insulin sensitivity in metabolic diseases associated with insulin resistance.

- The Transforming growth factors (TGFs) family comprises the alpha and beta forms. TGF-α is upregulated in certain human cancers while it also induces epithelial development. TGF-β exists in three subtypes that are TGF-β1, TGF-β2, and TGFβ-3. These are upregulated in several human cancers, but they also play a crucial role in tissue regeneration, embryonic development, cell differentiation, and and immune system regulation.
- Fibroblast growth factors (FGF) have a role in angiogenesis (where new blood cells are created), healing wounds, embryonic development, maintenance of the brain, and endocrine signaling pathways. FGF1 and FGF2 promote endothelial cell proliferation and the growth of new blood vessels, whereas FGF7 and FGF10 help repair injured and damaged skin/mucosal tissues.
- The Hepatocyte growth factors (HGF) family has various roles in tissue regeneration, angiogenesis, and wound healing thanks to their regulatory function, which improves cell growth and motility. HGF largely deals with both epithelial and endothelial cells.
- Keratinocyte growth factor (KGF) has been linked to proliferation, DNA repair, cell survival, and tumor growth. KGF is a potent epithelial cell-specific growth factor whose upregulation after epithelial injury suggests tissue repair within the body.

1.4.2 Biomechanical-biophysical stimuli: bioreactors

Once cells attach to the scaffold, they sense and respond to mechanical and physical stimuli by converting them to biochemical signals: a combination of receptor-mediated, physical-mediated, and mechanical-mediated signals will regulate their phenotype and function, with a process defined as mechanotransduction (Almouemen et al., 2019). Concerning the biophysical signals, pH, temperature, external magnetic field, pressure, nutrient concentration, and oxygen tension are the microenvironmental parameters that affect cell migration, proliferation, and differentiation (Brady et al., 2014). On the other hand, biomechanical stimuli, such as hydrostatic pressure, shear stress, tensile and compressive forces, and dynamic loadings, also influence the ECM properties directing cells activity and tissue-specific gene expression (Issa et al., 2018).

Standard 2D static culture lacks most biological, mechanical, and topographical complexity proper of the physiological tissues. On the other hand, 3D culture systems can recapitulate more complex cell-cell interactions, improving tissue architecture and experimental reproducibility. A TE bioreactor is one device used to facilitate, monitor, and strictly control

fluid flow and well-determined environmental conditions during dynamic culture (Martin et al., 2004). Hence, bioreactor systems are projected to enhance the mass transport of nutrients and oxygen and to efficiently provide biological, biochemical, and biophysical stimuli for optimizing cell proliferation, differentiation, and matrix deposition. When using bioreactors, hydrodynamic cultures can be operated through specific medium flow conditions, thus addressing mass transport limitations and applying mechanical stimuli to the cells.

Table 1.3 Description of the main bioreactor types used in the TE field (Salehi-Nik et al., 2013)

Bioreactor type	General descriptions	Mass transfer mechanism	Shear stress	Special usage	Tissue	Considerations
Static culture	Batch culture with no flow of nutrient	Diffusion (high)	Very low	Cell proliferation	—	Homogeneous structure of cell constructs and nutrient diffusion limitations
Stirred flasks 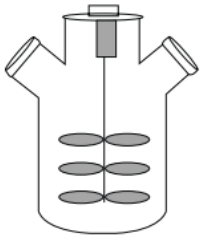	Magnetically stirring of medium	Convection (high)	High	Dynamic seeding of scaffolds	Cartilage	Appropriate scaffold and balance between increasing mass transfer and modulating shear stresses
Rotating wall 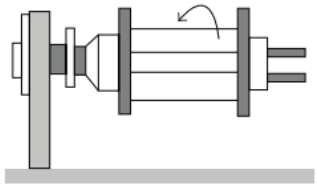	Rotating at a speed so the constructs in the reactor are maintained "stationary" in a state of continuous free fall	Convection (high)	Low	Tissue constructs which need dynamic laminar flow	Cartilage, bone and skin	Operating conditions (e.g., speed of rotating) especially for growing large tissue mass
Perfusion 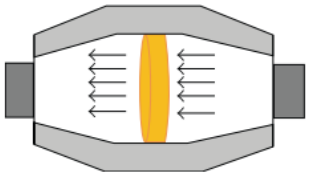	Flow of medium over or through a cell population or bed of cells	Convection (moderate) and diffusion (high)	Moderate	Tissues physico-chemicaly and environ-mentally relevant to human tissues	Epithelial cells, intestinal, bone, cartilage, and arteries	Seeding and attachment of human cells especially within the scaffold body

Therefore, bioreactors have the potential to mimic the complex *in vivo* environment in an *in vitro* setting. Hence, they can provide more reliable results in predicting human diseases and drug response compared to the traditional approach of *in vitro* cell culture combined with the animal *in vivo* testing (Lombardo et al., 2021).

Many types of bioreactors are frequently mentioned in cell cultivation for tissue engineering applications to provide hydrodynamic culture environments for culturing a specific cell lineage. Among them, spinner flask bioreactors, rotating-wall vessels, and perfusion bioreactors are the most adopted in the TE strategy (Tab. 1.3) (Yamada et al., 2021).

Other bioreactor systems, such as airlift and hollow-fibers bioreactors, have shown promising outcomes compared to static culture conditions.

Spinner flask bioreactors

In spinner flasks bioreactors, a magnetic stir bar or an internal rotating plate moves the medium, thus enhancing the external mass transport through the seeded scaffolds and facilitating waste removal. In this system, the scaffolds are connected by a needle to the flask lid to maintain their position fixed (Fig. 1.11). The top of the flasks presents apertures with a filter to allow gas exchange between the bioreactor and the incubator without any contamination risk (Martin et al., 2004).

During culture, nutrients and oxygen are transported to and into the scaffold by convection, thus overcoming the typical diffusion limit of 100-200 μm. Hence, the ideal stirred medium should provide a homogenous mass transfer, uniform pH gradient, and shear gradients that avoid cell damage (Correia et al., 2012). The shear stress is dependent on stirring speed which is at a maximum of 50 rpm for 120 ml flasks (Eberli, 2011).

One limitation of spinning bioreactors is the possibility of the formation of a dense superficial cell layer, resulting in a lack of oxygen and nutrients reaching the middle of the constructs. Other disadvantages are the inhomogeneous velocity profile within the bioreactor (producing stimuli that change with the scaffold) and the weak reproducibility during experiments (Goldstein et al., 2001).

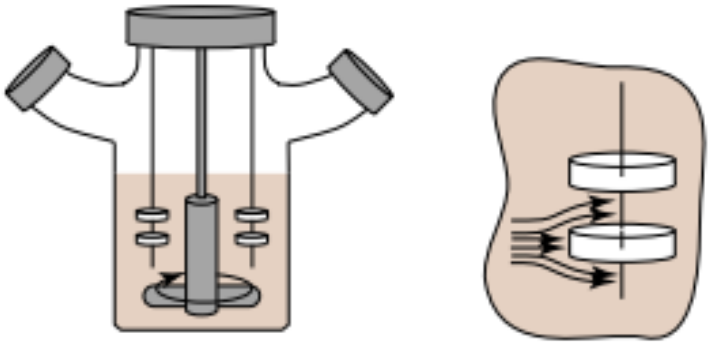

Figure 1.11 Spinner flask bioreactor (Martin et al., 2004)

Rotating-wall vessels

In rotating-wall bioreactors, the vessel wall rotates along its axis at a rate that enables the

balance of all three forces - drag, centrifugal, and net gravitational forces – on the constructs inside the bioreactor (Fig. 1.12). Hence, these vessels provide a dynamic culture environment where scaffolds in suspension remain in a state of free-fall through the culture medium, with low shear stresses and high mass-transfer rates (Martin et al., 2004). The vessel is typically cylindrical and horizontally positioned, put in rotation by an external motor at a speed calibrated to the mass of the cell carrier constructs (Eberli, 2011). Indeed, the material density of the scaffold influence the way the construct is moved by the fluid: if densities of the scaffold and the culture medium are similar, the construct will stay in suspension; if the two densities are different, the construct may have turbulent movements within the vessel, increasing the probability of collision with the wall and other constructs (Rúnarsson, 2019). Moreover, the construct size has a similar effect on the suspension conditions. Therefore, control systems are required to vary the rotation speed of the vessel in the function of tissue size. Specifically, while the tissue is growing inside the vessel, its terminal free-fall velocity increases; hence, if the rotation velocity is maintained constant, the tissue will hit the bottom region of the vessel, potentially limiting the nutrient transfer. For this reason, these reactors are of limited use for growing large tissue mass (Martin and Vermette, 2005).

Overall, rotation of the vessel induces laminar flow by inertial effects, inducing levels of shear stress that remain very low, probably because the constructs follow the movement of the fluid (Yamada et al., 2021).

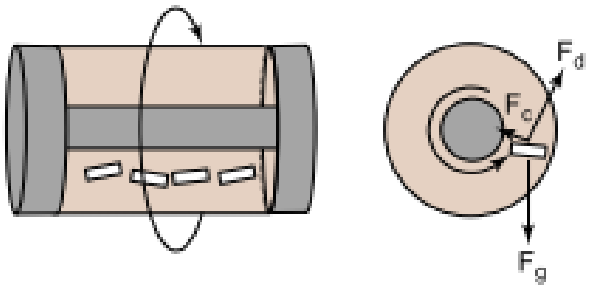

Figure 1.12 Rotating-wall vessel (Martin et al., 2004)

Perfusion bioreactors

Perfusion bioreactors mediate flow through the pores of the scaffolds during seeding or 3D cultures. As a result, these systems have the advantage of a highly uniform cell distribution during seeding, enhanced mass transfer within the internal pores, and distribute shear stress

in the whole construct under laminar flow conditions (Martin et al., 2004). This feature improves tissue architecture and gives cells a suitable flux of media throughout time.

Perfusion systems are usually constituted of a chamber containing cells or scaffolds, and through which the culture medium is perfused by using a pump with a tubing system. The flow of the culture medium can either work as a recirculating system or go from a reservoir to a waste container. Perfusion bioreactors can provide oscillatory, pulsed, or continuous flow, and additional equipment can be coupled to induce mechanical stimulation on the seeded scaffolds (Jasuja et al., 2021).

Perfusion bioreactors are classified into two categories: the direct perfusion system (where the culture medium is directly forced through the construct) (Fig. 1.13A) and the indirect perfusion system (allowing the culture medium to flow at the surrounding of the scaffold) (Fig. 1.13B) (Burova et al., 2019).

In indirect perfusion systems, the medium takes the path of least resistance through the chamber, resulting in preferential cell proliferation around the construct and starving and hypoxic conditions at the center of the scaffold (Campolo and Curcio, 2013). On the other hand, bioreactors with direct perfusion ensure uniform shear stress and velocity field distribution within the whole construct, giving the most homogeneous cell arrangement in the volume of the scaffolds (Salehi-Nik et al., 2013).

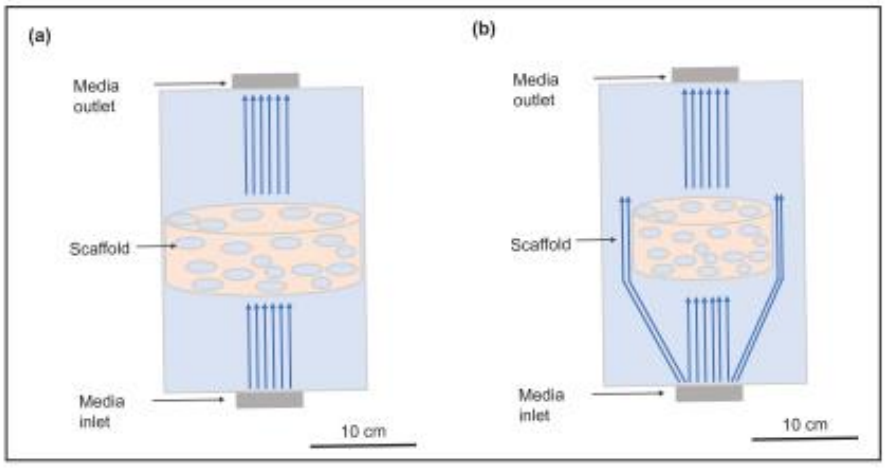

Figure 1.13 Perfusion bioreactor: (A) the direct perfusion system (where the culture medium is directly forced through the construct) and (B) the indirect perfusion system (allowing the culture medium to flow at the surrounding of the scaffold) (Burova et al., 2019)

During bioreactor setup, it is crucial to choose the optimal medium flow rate since its increase may cause an increase in the shear stress, inducing detachment or damage of cells. Recently, these devices have been miniaturized, leading to a new scientific field for *in vitro*

cell modeling miniaturized technology, called organ-on-a-chip (Lee et al., 2018). These systems are perfused miniaturized bioreactors that allow cell culturing in single chambers, promoting their communication through milli- or micro-fluidic channels and controlling spatial and temporal distribution of their micro-environment. The miniaturization reduces the reagent volumes, while the integration of electronic sensors allows measuring biological and physical parameters

1.5 Aims of the PhD thesis and structure

The main objective of this study is to design specific perfusion bioreactors to perform dynamic cell cultures on PLLA scaffolds in the perspective of future application for *in vitro* tissue modeling or tissue engineering for regenerative purposes. By combining experimental tests, and mathematical and numerical models, bioreactor design (using modeling tools), scaffold fabrication and characterization, and *in vitro* cell cultures were performed with the goal of a uniform distribution of cells in the final construct and improved nutrient supply to the inner region of the scaffold.

Overall, the thesis has an extensive and comprehensive introduction that provides the reader with a general and comprehensive overview of the subject matter. Specifically, starting with a general introduction to tissue engineering (Chapter 1), it then goes into more detail with PLLA-based scaffolds (Chapter 2), bioreactors (Chapter 3), and their modeling (Chapter 4). Since some of the experimental work is found in Chapter 2 (thus breaking the introduction into two parts), this section invites the reader to accept this subdivision. The latter was chosen because the remaining experimental parts involved a bioreactor, unlike the tests in Chapter 2. The properties of poly-L-lactic acid (PLLA) as a scaffold biomaterial are presented in Chapter 2, comparing the various applications of this synthetic polymer in the re-construction of different tissues, such as bone, cartilage, the skin, and the vascular system. Bone tissue engineering is chosen as the context of a case study presented in the same chapter. In scaffolds, the porosity, the pore size, and the interconnection regulate cellular activity. We assume that, by producing scaffolds by thermally induced phase separation (TIPS), the scaffold porosity is not variable in a spatial sense, although varying in morphology. We use morphological (micro-CT) and biological analysis techniques to find the response of cells to the analyzed morphologies in static conditions. The results are presented for particular morphological choices for which there is a similarity with bone tissue while assessing cell proliferation and degree of mineralization. We show a comparison of morphological and biological results in static conditions.

In Chapter 3, we present an overview of the use of perfusion bioreactors, coupling the theory of fluid flow, nutrient concentration, and cell growth in the perfusion bioreactor. We analyze the literature, mainly studying the design of two types of perfusion bioreactors: the airlift and the dual flow. These two types are then used in the following chapters for modeling and testing scaffolds in PLLA. We conclude that these two perfusion bioreactor designs are advantageous for mass transfer and particular fluid dynamic conditions.

In Chapter 4, we further extend the theoretical analysis of perfusion bioreactors presented in Chapter 3 to analyze the models for studying and evaluating hydrodynamic and mass transport profiles in these devices. In this study, mathematical equations are presented as a method of the global resolution, not delineated in space, but which allows for quantifying the average quantities of the system. On the other hand, computational modeling allows the punctual resolution in space and time, although assumptions and/or the verification of the solution with experimental or analytical results is necessary.

Chapter 5 consists of the modeling and experimental validation of a custom-made dual flow bioreactor. This device has the peculiarity of allowing two independent flows of fluid (liquid or gas), i.e., one external and one internal of a scaffold with a channel. Thus, by exploiting the dynamics of the system, it is possible to control the direction and value of a radial flow that, crossing the pores of the scaffold, has the potential to deliver particles through the construct or to bring the culture media into the internal channel of the scaffold. These two properties can be exploited for drug delivery purposes and replication of an air-fluid interlocking tissue, such as the nasal mucosa. Both these applications were tested and discussed in the same chapter.

The main objective of Chapter 6 is to develop a method that combines a mathematical and numerical model of fluid flow, nutrient concentration, and cell growth in an airlift perfusion bioreactor. From experimental evidence, we assume that the flow regime is a turbulent bubbly flow. This hypothesis makes it possible to mathematically find hydrodynamic quantities, such as the size of the bubble and its terminal velocity. The convection equation is used to model the distribution of nutrients. The flow field to steady-state can be determined locally by numerical modeling. The model is solved numerically with the finite element solver COMSOL. The numerical results are validated while analytically solving the model with some simplifying hypotheses. We compare the analytical and numerical results, finding a good agreement. We also verify that the bioreactor system obeys the results relating to the oxygen concentration (from equations) and, therefore, cell viability. Such verification is done experimentally with cell culture in dynamic conditions on scaffolds in PLLA produced

via TIPS.

One of the challenges facing tissue engineering is nutrient intake in the inner region of the construct. For the nutrient to feed the cells, the culture medium must reach them optimally, thanks to an adequate flow profile. In Chapter 7, using a numerical method, we present the results of the flow regime within the pores of the scaffold in PLLA produced via TIPS within the airlift bioreactor presented in Chapter 6. This analysis is performed using the geometry of the construct without geometric simplifications, exploiting the reconstruction of the scaffold by the micro-CT technique. The promising numerical results are experimentally verified by a dynamic culture of 24 scaffolds placed simultaneously inside the airlift bioreactor, using specific support, which does not alter the uniform fluid dynamics found in the results of Chapter 6. We conclude that the custom-made airlift bioreactor system is suitable for tissue Engineering applications at a multi-scale level, i.e., bioreactor-scaffold-pores.

In Chapter 8, we summarize the main conclusions of the thesis and outline possible extensions of the presented devices and models. In conclusion, this dissertation has the novelty of describing in a combined manner the design of perfusion bioreactors, the optimization of TIPS scaffolds in PLLA, and their proof of use in cell cultures under both static and dynamic conditions, with a view to a future application for in vitro tissue modeling or tissue engineering for regenerative purposes.

References

Almouemen, N., Kelly, H. M., and O'Leary, C. (2019). Tissue Engineering: Understanding the Role of Biomaterials and Biophysical Forces on Cell Functionality Through Computational and Structural Biotechnology Analytical Methods. *Comput. Struct. Biotechnol. J.* 17, 591. doi:10.1016/J.CSBJ.2019.04.008.

Anderson, D. E., and Johnstone, B. (2017). Dynamic Mechanical Compression of Chondrocytes for Tissue Engineering: A Critical Review. *Front. Bioeng. Biotechnol.* 5, 76. doi:10.3389/fbioe.2017.00076.

Bisht, B., Hope, A., Mukherjee, A., and Paul, M. K. (2021). Advances in the Fabrication of Scaffold and 3D Printing of Biomimetic Bone Graft. *Ann. Biomed. Eng.* 49, 1129–1150. doi:10.1007/s10439-021-02752-9.

Brady, M. A., Vaze, R., Amin, H. D., Overby, D. R., and Ethier, C. R. (2014). The Design and Development of a High-Throughput Magneto-Mechanostimulation Device for Cartilage Tissue Engineering. doi:10.1089/ten.tec.2013.0225.

Brougham, C. M., Levingstone, T. J., Shen, N., Cooney, G. M., Jockenhoevel, S., Flanagan, T. C., et al. (2017). Freeze-Drying as a Novel Biofabrication Method for Achieving a Controlled Microarchitecture within Large, Complex Natural Biomaterial Scaffolds. *Adv. Healthc. Mater.* 6, 1700598. doi:10.1002/adhm.201700598.

Bružauskaitė, I., Bironaitė, D., Bagdonas, E., and Bernotienė, E. (2016). Scaffolds and cells for tissue regeneration: different scaffold pore sizes—different cell effects. *Cytotechnology* 68, 355–369. doi:10.1007/s10616-015-9895-4.

Burova, I., Wall, I., and Shipley, R. J. (2019). Mathematical and computational models for bone tissue engineering in bioreactor systems. *J. Tissue Eng.* 10. doi:10.1177/2041731419827922.

Campolo, M., and Curcio, F. (2013). Minimal Perfusion Flow for Osteogenic Growth of Mesenchymal Stem Cells on Lattice Scaffolds in Wiley Online Library. *Am. Inst. Chem. Eng. AIChE J* 59, 3131–3144. doi:10.1002/aic.14084.

Capuana, E., Lopresti, F., Pavia, F. C., Brucato, V., and Carrubba, V. La (2021). Solution-Based Processing for Scaffold Fabrication in Tissue Engineering Applications: A Brief Review. *Polym. 2021, Vol. 13, Page 2041* 13, 2041. doi:10.3390/POLYM13132041.

Carfì Pavia, F., La Carrubba, V., Ghersi, G., Greco, S., and Brucato, V. (2017). Double flow bioreactor for in vitro test of drug delivery. *Curr. Drug Deliv.* 14, 239–245. doi:10.2174/1567201813666160527141538.

Casalini, T., Rossi, F., Castrovinci, A., and Perale, G. (2019). A Perspective on Polylactic Acid-Based Polymers Use for Nanoparticles Synthesis and Applications. *Front. Bioeng. Biotechnol.* 7, 259. doi:10.3389/FBIOE.2019.00259.

Chen, L., Liu, J., Guan, M., Zhou, T., Duan, X., and Xiang, Z. (2020a). Growth Factor and Its Polymer Scaffold-Based Delivery System for Cartilage Tissue Engineering. *Int. J. Nanomedicine* 15, 6097–6111. doi:10.2147/IJN.S249829.

Chen, Y., Shafiq, M., Liu, M., Morsi, Y., and Mo, X. (2020b). Advanced fabrication for electrospun three-dimensional nanofiber aerogels and scaffolds. *Bioact. Mater.* 5, 963–979. doi:10.1016/j.bioactmat.2020.06.023.

Chimutengwende-Gordon, M., and Khan, W. (2012). Advances in the use of stem cells and tissue engineering applications in bone repair. *Curr. Stem Cell Res. Ther.* 7, 122–126. doi:10.2174/157488812799219036.

Christy, P. N., Basha, S. K., Kumari, V. S., Bashir, A. K. H., Maaza, M., Kaviyarasu, K., et al. (2020). Biopolymeric nanocomposite scaffolds for bone tissue engineering applications – A

review. *J. Drug Deliv. Sci. Technol.* 55, 101452. doi:10.1016/j.jddst.2019.101452.

Ciapetti, G., Granchi, D., Devescovi, V., Baglio, S. R., Leonardi, E., Martini, E., et al. (2012). Enhancing osteoconduction of PLLA-based nanocomposite scaffolds for bone regeneration using different biomimetic signals to MSCs. *Int. J. Mol. Sci.* 13, 2439–2458. doi:10.3390/IJMS13022439.

Conoscenti, G., Schneider, T., Stoelzel, K., Carfì Pavia, F., Brucato, V., Goegele, C., et al. (2017). PLLA scaffolds produced by thermally induced phase separation (TIPS) allow human chondrocyte growth and extracellular matrix formation dependent on pore size. *Mater. Sci. Eng. C* 80, 449–459. doi:10.1016/j.msec.2017.06.011.

Correia, C., Pereira, A. L., Duarte, A. R., Frias, A. M., Pedro, A. J., Oliveira, J. T., et al. (2012). Dynamic Culturing of Cartilage Tissue: The Significance of Hydrostatic Pressure. doi:10.1089/ten.tea.2012.0083.

Cruz, F. (2010). "Fabrication of HA/PLLA Composite Scaffolds for Bone Tissue Engineering Using Additive Manufacturing Technologies," in *Biopolymers*, ed. E. Magdy (InTech), 227–242. doi:10.5772/10264.

Das, A., Balakrishnan, N. T. M., Joyner, J. D., Medhavi, N., Manaf, O., Jabeen Fatima, M. J., et al. (2021). "Electrospinning: The State of Art Technique for the Production of Nanofibers and Nanofibrous Membranes for Advanced Engineering Applications," in (Springer, Singapore), 23–71. doi:10.1007/978-981-15-8844-0_2.

Dattola, E., Parrotta, E. I., Scalise, S., Perozziello, G., Limongi, T., Candeloro, P., et al. (2019). Development of 3D PVA scaffolds for cardiac tissue engineering and cell screening applications. *RSC Adv.* 9, 4246–4257. doi:10.1039/C8RA08187E.

Di Luca, A., Ostrowska, B., Lorenzo-Moldero, I., Lepedda, A., Swieszkowski, W., Van Blitterswijk, C., et al. (2016). Gradients in pore size enhance the osteogenic differentiation of human mesenchymal stromal cells in three-dimensional scaffolds. *Sci. Reports 2016 61* 6, 1–13. doi:10.1038/srep22898.

Eberli, D. (2011). *Tissue Engineering for tissue and organ regeneration*. Rijeka, Croatia: InTech.

Fereshteh, Z. (2018). "Freeze-drying technologies for 3D scaffold engineering," in *Functional 3D Tissue Engineering Scaffolds: Materials, Technologies, and Applications* (Elsevier), 151–174. doi:10.1016/B978-0-08-100979-6.00007-0.

Figoli, A., De Luca, G., Longavita, E., and Drioli, E. PEEKWC capsules prepared by phase inversion technique: A morphological and dimensional study.

Fu, N., Zhang, X., Sui, L., Liu, M., and Lin, Y. (2017). "Application of Scaffold Materials in Cartilage Tissue Engineering," in *Cartilage Regeneration, Stem Cell Biology and Regenerative Medicine*, ed. Y. Lin (Humana Press, Cham), 21–39. doi:10.1007/978-3-319-51617-2_2.

Ge, M., Xue, L., Nie, T., Ma, H., and Zhang, J. (2016). The precision structural regulation of PLLA porous scaffold and its influence on the proliferation and differentiation of MC3T3-E1 cells. *J. Biomater. Sci. Polym. Ed.* 27, 1685–1697. doi:10.1080/09205063.2016.1229901.

Geven, M. A., Lapomarda, A., Guillaume, O., Sprecher, C. M., Eglin, D., Vozzi, G., et al. (2021). Osteogenic differentiation of hBMSCs on porous photo-crosslinked poly(trimethylene carbonate) and nano-hydroxyapatite composites. *Eur. Polym. J.*, 110335. doi:10.1016/j.eurpolymj.2021.110335.

Ghalia, M. A., and Dahman, Y. (2016). Advanced nanobiomaterials in tissue engineering: Synthesis, properties, and applications. *Nanobiomaterials Soft Tissue Eng. Appl. Nanobiomaterials*, 141–172. doi:10.1016/B978-0-323-42865-1.00006-4.

Goldstein, A. S., Juarez, T. M., Helmke, C. D., Gustin, M. C., and Mikos, A. G. (2001). Effect of convection on osteoblastic cell growth and function in biodegradable polymer foam scaffolds. *Biomaterials* 22, 1279–1288. doi:10.1016/S0142-9612(00)00280-5.

Gomes, M. E., Rcia, M., Rodrigues, T., Domingues, R. M. A., and Reis, R. L. (2017). Tissue Engineering and Regenerative Medicine: New Trends and Directions—A Year in Review. *TISSUE Eng. Part B* 23. doi:10.1089/ten.teb.2017.0081.

Gooch, K. J., Blunk, T., Courter, D. L., Sieminski, A. L., Bursac, P. M., Vunjak-Novakovic, G., et al. (2001). IGF-I and mechanical environment interact to modulate engineered cartilage development. *Biochem. Biophys. Res. Commun.* 286, 909–915. doi:10.1006/bbrc.2001.5486.

Groll, J., Boland, T., Blunk, T., Burdick, J., Cho, D., Dalton, P., et al. (2016). Biofabrication: reappraising the definition of an evolving field. *Biofabrication* 8. doi:10.1088/1758-5090/8/1/013001.

Guillen, G. R., Pan, Y., Li, M., and Hoek, E. M. V. (2011). Preparation and characterization of membranes formed by nonsolvent induced phase separation: A review. *Ind. Eng. Chem. Res.* 50, 3798–3817. doi:10.1021/ie101928r.

Gupta, S., Bissoyi, A., and Bit, A. (2018). A Review on 3D Printable Techniques for Tissue Engineering. *Bionanoscience* 8, 868–883. doi:10.1007/s12668-018-0525-4.

Haugh, M. G., Murphy, C. M., and O'Brien, F. J. (2010). Novel freeze-drying methods to produce a range of collagen- glycosaminoglycan scaffolds with tailored mean pore sizes. *Tissue Eng. - Part C Methods* 16, 887–894. doi:10.1089/ten.tec.2009.0422.

Hua, F., Zhang, P., Zhang, F., Zhao, Y., Li, C., Sun, C., et al. (2015). Development and evaluation of an up-converting phosphor technology-based lateral flow assay for rapid detection of Francisella tularensis. *Sci. Rep.* 5, 17178. doi:10.1038/SREP17178).

Huang, R., Zhu, X., Tu, H., and Wan, A. (2014). The Crystallization Behavior of Porous PLA Prepared by Modified Solvent Casting/Particulate Leaching Technique for Potential Use of Tissue Engineering Scaffold. doi:10.1016/j.matlet.2014.08.044.

Huang, Z. M., Zhang, Y. Z., Kotaki, M., and Ramakrishna, S. (2003). A review on polymer nanofibers by electrospinning and their applications in nanocomposites. *Compos. Sci. Technol.* 63, 2223–2253. doi:10.1016/S0266-3538(03)00178-7.

Issa, R., Boeving, M., Kinter, M., and Griffin, T. M. (2018). Effect of biomechanical stress on endogenous antioxidant networks in bovine articular cartilage. *J. Orthop. Res.* 36, 760–769. doi:10.1002/jor.23728.

Izquierdo-Barba, I. (2014). "Scaffold Designing," in *Bio-Ceramics with Clinical Applications* (Chichester, UK: John Wiley & Sons, Ltd), 291–313. doi:10.1002/9781118406748.ch10.

Jasuja, H., Kar, S., Katti, D. R., and Katti, K. S. (2021). Perfusion bioreactor enabled fluid-derived shear stress conditions for novel bone metastatic prostate cancer testbed. *Biofabrication* 13. doi:10.1088/1758-5090/abd9d6.

Joshi, S. C., and Sheikh, A. A. (2015). 3D printing in aerospace and its long-term sustainability. *Virtual Phys. Prototyp.* 10, 175–185. doi:10.1080/17452759.2015.1111519.

Jung, J. T., Kim, J. F., Wang, H. H., Di Nicolo, E., Drioli, E., and Lee, Y. M. (2016). Understanding the non-solvent induced phase separation (NIPS) effect during the fabrication of microporous PVDF membranes via thermally induced phase separation (TIPS). *J. Memb. Sci.* 514, 250–263. doi:10.1016/j.memsci.2016.04.069.

Keeney, M., and Pandit, A. (2009). The osteochondral junction and its repair via bi-phasic tissue engineering scaffolds. *Tissue Eng. Part B. Rev.* 15, 55–73. doi:10.1089/ten.teb.2008.0388.

Koyyada, A., and Orsu, P. (2020). Recent Advancements and Associated Challenges of Scaffold Fabrication Techniques in Tissue Engineering Applications. *Regen. Eng. Transl. Med.*, 1–13. doi:10.1007/s40883-020-00166-y.

La Carrubba, V., Pavia, F. C., and Brucato, V. (2010). Tubular scaffold for vascular tissue engineering application. *Int. J. Mater. Form.* 3, 567–570. doi:10.1007/s12289-010-0833-x.

Lanza, R., Langer, R., and Vacanti, J. P. (2007). *Principles of Tissue Engineering*. Third Edit.

Lee, H. I., Heo, Y., Baek, S. W., Kim, D. S., Song, D. H., and Han, D. K. (2021). Multifunctional Biodegradable Vascular PLLA Scaffold with Improved X-ray Opacity, Anti-Inflammation, and Re-Endothelization. *Polym. 2021, Vol. 13, Page 1979* 13, 1979. doi:10.3390/POLYM13121979.

Lee, P. H., Kim, J. S., Lee, S. W., Shao, C., and Chung, H. (2018). Experimental investigation on a hybrid manufacturing process of micro-scale mold for biomimetic intestinal villi's scaffold. *J. Mech. Sci. Technol.* 32, 4283–4289. doi:10.1007/s12206-018-0826-0.

Li, Y., and Yang, S. T. (2001). Effects of three-dimensional scaffolds on cell organization and tissue development. *Biotechnol. Bioprocess Eng.* 6, 311–325. doi:10.1007/BF02932999.

Liang, C., Luo, Y., Yang, G., Xia, D., Liu, L., Zhang, X., et al. (2018). Graphene Oxide Hybridized nHAC/PLGA Scaffolds Facilitate the Proliferation of MC3T3-E1 Cells. *Nanoscale Res. Lett.* 13, 1–10. doi:10.1186/s11671-018-2432-6.

Lin, H., Lozito, T. P., Alexander, P. G., Gottardi, R., and Tuan, R. S. (2014). Stem Cell-Based Microphysiological Osteochondral System to Model Tissue Response to Interleukin-1β. doi:10.1021/mp500136b.

Lin, S., Dong, P., Zhou, C., Dallan, L. A. P., Zimin, V. N., Pereira, G. T. R., et al. (2020). Degradation modeling of poly-l-lactide acid (PLLA) bioresorbable vascular scaffold within a coronary artery. *Nanotechnol. Rev.* 9, 1217–1226. doi:10.1515/NTREV-2020-0093.

Liu, S., Zheng, Y., Hu, J., Wu, Z., and Chen, H. (2020). Fabrication and characterization of polylactic acid/polycaprolactone composite macroporous micro-nanofiber scaffolds by phase separation. *New J. Chem.* 44, 17382–17390. doi:10.1039/d0nj03176c.

Lombardo, M., Carfì Pavia, F., Craparo, E., Capuana, E., Cavallaro, G., Brucato, V., et al. (2021). Novel dual-flow perfusion bioreactor for in vitro pre-screening of nanoparticles delivery: design, characterization and testing. *Bioprocess Biosyst. Eng.* 44, 2361–2374. doi:10.1007/S00449-021-02609-4.

Lombardo, M. E., Carfì Pavia, F., Vitrano, I., Ghersi, G., Brucato, V., Rosei, F., et al. (2019). PLLA scaffolds with controlled architecture as potential microenvironment for in vitro tumor model. *Tissue Cell* 58, 33–41. doi:10.1016/j.tice.2019.04.004.

Lopresti, F., Pavia, F. C., Ceraulo, M., Capuana, E., Brucato, V., Ghersi, G., et al. (2021). Physical and biological properties of electrospun poly(d,l-lactide)/nanoclay and poly(d,l-lactide)/nanosilica nanofibrous scaffold for bone tissue engineering. *J. Biomed. Mater. Res. - Part A* In Press. doi:10.1002/jbm.a.37199.

Lou, T., Wang, X., Yan, X., Miao, Y., Long, Y. Z., Yin, H. L., et al. (2016). Fabrication and biocompatibility of poly(l-lactic acid) and chitosan composite scaffolds with hierarchical microstructures. *Mater. Sci. Eng. C* 64, 341–345. doi:10.1016/j.msec.2016.03.107.

Lu, T., Li, Y., and Chen, T. (2013). Techniques for fabrication and construction of three-dimensional scaffolds for tissue engineering. *Int. J. Nanomedicine* 8, 337–50. doi:10.2147/IJN.S38635.

Martin, I., Wendt, D., and Heberer, M. (2004). The role of bioreactors in tissue engineering. *Trends Biotechnol.* 22, 80–86. doi:10.1016/j.tibtech.2003.12.001.

Martin, Y., and Vermette, P. (2005). Bioreactors for tissue mass culture: Design, characterization, and recent advances. *Biomaterials* 26, 7481–7503. doi:10.1016/j.biomaterials.2005.05.057.

Masszi, A., Speight, P., Charbonney, E., Lodyga, M., Nakano, H., Szászi, K., et al. (2010). Fate-determining mechanisms in epithelial-myofibroblast transition: major inhibitory role for Smad3. *J. Cell Biol.* 188, 383–99. doi:10.1083/jcb.200906155.

Meyer, U., Meyer, T., Handschel, J., and Wiesmann, H. P. (2016). *Fundamentals of tissue engineering and regenerative medicine.* SPRINGER-VERLAG BERLIN AN.

Montesanto, S., Mannella, G. A., Carfì Pavia, F., La Carrubba, V., and Brucato, V. (2015). Coagulation bath composition and desiccation environment as tuning parameters to prepare skinless membranes via diffusion induced phase separation. *J. Appl. Polym. Sci.* 132, 132. doi:10.1002/app.42151.

Montesanto, S., Smithers, N. P., Bucchieri, F., Brucato, V., La Carrubba, V., Davies, D. E., et al. (2019). Establishment of a pulmonary epithelial barrier on biodegradable poly-L-lactic-acid membranes. *PLoS One* 14, e0210830. doi:10.1371/journal.pone.0210830.

Murphy, C. M., O'Brien, F. J., Little, D. G., and Schindeler, A. (2013). Cell-scaffold interactions in the bone tissue engineering triad. *Eur. Cells Mater.* 26, 120–132. doi:10.22203/ECM.V026A09.

Naqvi, S. M., and McNamara, L. M. (2020). Stem Cell Mechanobiology and the Role of Biomaterials in Governing Mechanotransduction and Matrix Production for Tissue Regeneration. *Front. Bioeng. Biotechnol.* 0, 1375. doi:10.3389/FBIOE.2020.597661.

Nerem, R. M., and Sambanis, A. (1995). Tissue Engineering: From Biology to Biological Substitutes. *Tissue Eng.* 1, 3–13. doi:10.1089/ten.1995.1.3.

Nikolova, M. P., and Chavali, M. S. (2019). Recent advances in biomaterials for 3D scaffolds: A review. *Bioact. Mater.* 4, 271–292. doi:10.1016/j.bioactmat.2019.10.005.

O'Dea, R. D., Osborne, J. M., El Haj, A. J., Byrne, H. M., and Waters, S. L. (2013). The interplay between tissue growth and scaffold degradation in engineered tissue constructs. *J. Math. Biol.* 67, 1199–1225. doi:10.1007/s00285-012-0587-9.

Oh, S. H., Kim, T. H., Im, G. Il, and Lee, J. H. (2010). Investigation of pore size effect on chondrogenic differentiation of adipose stem cells using a pore size gradient scaffold. *Biomacromolecules* 11, 1948–1955. doi:10.1021/bm100199m.

Ou, S.-F., Tsao, Y.-L., Lin, W.-C., Wang, Y.-T., Wang, L., and Fan, F.-Y. (2020). Novel Epigallocatechin-3-Gallate (EGCG)-Loaded Mesoporous Bioglass Scaffolds for Bone Recruitment Applications. *Appl. Sci.* 11, 243. doi:10.3390/app11010243.

Pandey, A. K., and Sakurai, S. (2021). Recent Developments in the Crystallization of PLLA-Based Blends, Block Copolymers, and Nanocomposites. in *Crystallization* (Rijeka, Croatia: IntechOpen). doi:10.5772/INTECHOPEN.97088.

Patel, H., Bonde, M., Srinivasan, G., and others (2011). Biodegradable polymer scaffold for tissue engineering. *Trends Biomater Artif Organs* 25, 20–29. Available at: http://medind.nic.in/taa/t11/i1sji/taat11i1sjip20.pdf.

Pham, Q., Sharma, U., and Mikos, A. (2006). Electrospinning of polymeric nanofibers for tissue engineering applications: a review. *Tissue Eng.* 12, 1197–1211. doi:10.1089/TEN.2006.12.1197.

Pisanti, P., Yeatts, A. B., Cardea, S., Fisher, J. P., and Reverchon, E. (2012). Tubular perfusion system culture of human mesenchymal stem cells on poly- L- Lactic acid scaffolds produced using a supercritical carbon dioxide-assisted process. *J. Biomed. Mater. Res. - Part A* 100 A, 2563–2572. doi:10.1002/jbm.a.34191.

Ramakrishna, S., Fujihara, K., Teo, W. E., Lim, T. C., and Ma, Z. (2005). An introduction to electrospinning and nanofibers. *An Introd. to Electrospinning Nanofibers*, 1–382. doi:10.1142/5894.

Ranganathan, N., Mugeshwaran, A., Bensingh, R. J., Kader, M. A., and Nayak, S. K. (2019). "Biopolymeric scaffolds for tissue engineering application," in *Biomedical Engineering and its Applications in Healthcare* (Springer Singapore), 249–274. doi:10.1007/978-981-13-3705-5_11.

Rúnarsson, S. R. (2019). Designing and constructing a prototype standalone bioreactor using 3D printing and finite element analysis: A tool to define osteogenic differentiation in a 3D mechanical environment.

Sabzi, E., Abbasi, F., and Ghaleh, H. (2020). Interconnected porous nanofibrous gelatin scaffolds prepared via a combined thermally induced phase separation/particulate leaching method. *J. Biomater. Sci. Polym. Ed.* doi:10.1080/09205063.2020.1845921.

Salehi-Nik, N., Amoabediny, G., Pouran, B., Tabesh, H., Shokrgozar, M. A., Haghighipour, N., et al. (2013). Engineering parameters in bioreactor's design: A critical aspect in tissue engineering. *Biomed Res. Int.* 2013. doi:10.1155/2013/762132.

Saltzman, W. M. (2004). *Tissue engineering: engineering principles for the design of replacement organs and tissues*. Oxford, UK: Oxford University Press Available at: http://books.google.com/books?id=KorDMxtkZ_wC&pgis=1.

Scaffaro, R., Lopresti, F., Botta, L., Rigogliuso, S., and Ghersi, G. (2016). Integration of PCL and PLA in a monolithic porous scaffold for interface tissue engineering. *J. Mech. Behav. Biomed. Mater.* 63, 303–313. doi:10.1016/j.jmbbm.2016.06.021.

Serbo, J. V., and Gerecht, S. (2013). Vascular tissue engineering: Biodegradable scaffold platforms to promote angiogenesis. *Stem Cell Res. Ther.* 4, 8. doi:10.1186/scrt156.

Shafiee, A., and Atala, A. (2017). Tissue Engineering: Toward a New Era of Medicine. *Annu. Rev. Med.* 68, 29–40. doi:10.1146/annurev-med-102715-092331.

Shivalkar, S., and Singh, S. (2017). Solid Freeform Techniques Application in Bone Tissue Engineering for Scaffold Fabrication. *Tissue Eng. Regen. Med.* 14, 187–200. doi:10.1007/s13770-016-0002-5.

Siddiqui, N., Asawa, S., Birru, B., Baadhe, R., and Rao, S. (2018). PCL-Based Composite Scaffold Matrices for Tissue Engineering Applications. *Mol. Biotechnol.* 60, 506–532. doi:10.1007/s12033-018-0084-5.

Sivashanmugam, A., Arun Kumar, R., Vishnu Priya, M., Nair, S. V., and Jayakumar, R. (2015). An overview of injectable polymeric hydrogels for tissue engineering. *Eur. Polym. J.* 72, 543–565. doi:10.1016/j.eurpolymj.2015.05.014.

Solchaga, L. A., Temenoff, J. S., Gao, J., Mikos, A. G., Caplan, A. I., and Goldberg, V. M. (2005). Repair of osteochondral defects with hyaluronan- and polyester-based scaffolds. *Osteoarthr. Cartil.* 13, 297–309. doi:10.1016/J.JOCA.2004.12.016.

Stoltz, J., Decot, V., Huseltein, C., He, X., Zhang, L., Magdalou, J., et al. (2012). Introduction to regenerative medicine and tissue engineering. *Biomed. Mater. Eng.* 22, 3–16. doi:10.3233/BME-2012-0684.

Sultana, A., Ghosh, S. K., Sencadas, V., Zheng, T., Higgins, M. J., Middya, T. R., et al. (2017). Human skin interactive self-powered wearable piezoelectric bio-e-skin by electrospun poly-L-lactic acid nanofibers for non-invasive physiological signal monitoring. *J. Mater. Chem. B* 5, 7352–7359. doi:10.1039/C7TB01439B.

Swieszkowski, W., Tuan, B., Kurzydlowski, K., and Hutmacher, D. (2007). Repair and

regeneration of osteochondral defects in the articular joints. *Biomol. Eng.* 24, 489–495. doi:10.1016/J.BIOENG.2007.07.014.

Tan, G. Z., and Zhou, Y. (2019). Electrospinning of biomimetic fibrous scaffolds for tissue engineering: a review. *Int. J. Polym. Mater. Polym. Biomater.*, 1–14. doi:10.1080/00914037.2019.1636248.

Thavornyutikarn, B., Chantarapanich, N., Sitthiseripratip, K., Thouas, G. A., and Chen, Q. (2014). Bone tissue engineering scaffolding: computer-aided scaffolding techniques. *Prog. Biomater.* 3, 61–102. doi:10.1007/s40204-014-0026-7.

Vacanti, J. P., and Langer, R. (1999). Tissue engineering: the design and fabrication of living replacement devices for surgical reconstruction and transplantation. *Lancet* 354, S32–S34. doi:10.1016/S0140-6736(99)90247-7.

Van Caam, A., Madej, W., Thijssen, E., Garcia de Vinuesa, A., Van den Berg, W., Goumans, M.-J., et al. (2016). Expression of TGFβ-family signalling components in ageing cartilage: age-related loss of TGFβ and BMP receptors. *Osteoarthr. Cartil.* 24, 1235–1245. doi:10.1016/j.joca.2016.02.008.

Wang, L., Abedalwafa, M., Wang, F., and Li, C. (2013). Biodegradable poly-epsilon-caprolactone (PCL) for tissue engineering applications: a review. *Rev. Adv. Mater. Sci* 34, 123–140. Available at: https://pdfs.semanticscholar.org/f393/80a9d2ecac8005a7ab2aee0f3eb1fc6cbe01.pdf [Accessed June 27, 2018].

Wang, P., Sun, Y., Shi, X., Shen, H., Ning, H., and Liu, H. (2021). 3D printing of tissue engineering scaffolds: a focus on vascular regeneration. *Bio-Design Manuf.* 4, 344–378. doi:10.1007/s42242-020-00109-0.

Wengst, A., and Reichl, S. (2010). RPMI 2650 epithelial model and three-dimensional reconstructed human nasal mucosa as in vitro models for nasal permeation studies. *Eur. J. Pharm. Biopharm.* 74, 290–297. doi:10.1016/j.ejpb.2009.08.008.

Wu, G. H., and Hsu, S. H. (2015). Review: Polymeric-based 3D printing for tissue engineering. *J. Med. Biol. Eng.* 35, 285–292. doi:10.1007/s40846-015-0038-3.

Yamada, S., Yassin, M. A., Schwarz, T., Hansmann, J., and Mustafa, K. (2021). Induction of osteogenic differentiation of bone marrow stromal cells on 3D polyester-based scaffolds solely by subphysiological fluidic stimulation in a laminar flow bioreactor: *https://doi.org/10.1177/20417314211019375* 12, 204173142110193. doi:10.1177/20417314211019375.

Yamzon, J. L., Kokorowski, P., and Koh, C. J. (2008). Stem Cells and Tissue Engineering Applications of the Genitourinary Tract. *Pediatr. Res. 2008 635* 63, 472–477. doi:10.1203/pdr.0b013e31816a704a.

Yang, S., Leong, K.-F. E., Du, Z. M. E., and Chua, C.-K. (2001). The Design of Scaffolds for Use in Tissue Engineering. Part I. Traditional Factors. *TISSUE Eng.* 7, 679–89. doi:10.1089/107632701753337645.

Zeinali, R., Del Valle, L. J., Torras, J., and Puiggalí, J. (2021). Recent progress on biodegradable tissue engineering scaffolds prepared by thermally-induced phase separation (Tips). *Int. J. Mol. Sci.* 22, 3504. doi:10.3390/ijms22073504.

Zeng, S., Cui, Z., Yang, Z., Si, J., Wang, Q., Wang, X., et al. (2016). Characterization of highly interconnected porous poly(lactic acid) and chitosan-coated poly(lactic acid) scaffold fabricated by vacuum-assisted resin transfer molding and particle leaching. *J. Mater. Sci.* 51, 9958–9970. doi:10.1007/s10853-016-0203-2.

Zhang, D., Wu, X., Chen, J., and Lin, K. (2018). The development of collagen based composite scaffolds for bone regeneration. *Bioact. Mater.* 3, 129–138. doi:10.1016/J.BIOACTMAT.2017.08.004.

Zhao, P., Gu, H., Mi, H., Rao, C., Fu, J., and Turng, L. S. (2018). Fabrication of scaffolds in tissue engineering: A review. *Front. Mech. Eng.* 13, 107–119. doi:10.1007/s11465-018-0496-8.

Chapter 2

Tissue Engineering Applications of PLLA-based Scaffolds: state of the art and proof of concept results

This chapter investigates the potential of PLLA-based scaffold for Tissue Engineering (TE) applications. Specifically, bone, cartilage, skin tissues, and blood vessels are deeply investigated to remark the wide use of this material as biocompatible support for tissue development. Moreover, a case study is also presented as an application of PLLA scaffolds in the field of bone tissue engineering. This work aims to evaluate, *in vitro*, the biological interactions of various morphologies of PLLA scaffolds with SaOS-2 (osteoblast-like cells). This study allows us to investigate the cellular behavior of this osteogenic cell line in terms of cell proliferation, attachment, and mineralization. Moreover, a Micro-CT analysis was assessed to study the mean porosity and pore spatial distribution in the fabricated scaffolds. Hence, the optimum morphology of PLLA matrices has been determined based on the observed cellular activity of the 3D scaffolds and structural analysis of the samples.

2.1 PLLA-Based Scaffolds

PLLA is one of the first synthetic polymers that has been extensively recognized as an attractive material for tissue engineering due to its excellent degradation and biocompatibility. In this context, PLLA properties have been tailored to produce PLLA-based scaffolds for specific TE applications.

2.1.1 Bone tissue

Bone tissue is a dynamic and complex organization of blood vessels and different types of active cells, including osteoblasts, osteoclasts, and osteogenic cells. Depending on the microbiologic conditions, osteogenic cells, which are undifferentiated, may become osteoblasts or osteoclasts. In this way, they actively regulate bone homeostasis (Thavornyutikarn et al., 2014; Abdal-hay et al., 2017; Teixeira et al., 2020). Bone is a self-healing tissue when a small defect occurs. However, treating critical defects, such as pathological fractures and complex breaks, is still a big challenge (Zeng et al., 2018; Bigham et al., 2020). PLLA-based scaffolds could provide functional support for bone tissue repair. PLLA-based scaffolds fabricated by phase separation technique were widely studied *in vitro* as potential matrices for bone regeneration by Ciapetti et al. (Ciapetti et al., 2012). They

analyzed the morphological, biochemical, and gene expression of human MCSs seeded on PLLA-based scaffolds, including single-walled carbon nanotubes (CNT), micro-hydroxyapatite particles (HA), and bone morphogenetic protein 2 (BMP2) molecules. Their findings revealed that the addition of HA and BMP2 to the composite enhanced the number of cells on the scaffolds and the collagen production during the mineralization phase, respectively. On the other hand, the CNT-added PLLA scaffold had a low osteoconductive ability. Recently, a series of composite PLLA/HA foams produced by TIPS with different hydroxyapatite contents (10, 25, 50, 75, and 90 wt.% of the HA) were deeply analyzed for bone TE (Huang et al., 2020). This research revealed that the compressive properties and proliferation rate of osteoblast cells were proportional to the HA content of the foam, reaching optimal properties in PLLA/HA 25/75 scaffolds. *In vivo* studies using PLLA-based scaffolds fabricated by phase separation technique indicated their suitability for bone regeneration. Weng. et al (Weng et al., 2014) compared the *in vivo* regeneration of a 15mm-ulna bone defect in a rabbit using PLLA and PLLA/PCL scaffolds. They found a slow degradation rate and low bone mineral density for both PLLA and PLLA/PCL scaffolds, whereas the callus formation of PLLA/PCL was better than PLLA. As a fact, PCL does not produce acidic degradation products, hence obviating the disadvantages of PLLA.

In the context of bone TE, electrospinning has been widely used to produce nanofibrous scaffolds with a structure close to the nanoscale collagen fibers of bone (Lopresti et al., 2021b). Electrospun PLLA scaffolds were produced using a surface modification to direct cellular differentiation to the bone lineage and achieve optimal bone regenerative performances. In a recent study by Fu et al. (Fu et al., 2018), electrospun PLLA nanofibers were successfully modified via surface deposition of osteogenic ECM (secreted by MC3T3-E1 cells). Then, these scaffolds were used to examine the Mouse bone marrow stromal cells (mBMSCs) response on seeded scaffolds. The results indicated that mineral growth, ALP activity, and cell morphology were at optimum conditions in the modified constructs compared to pure PLLA nanofibers. Electrospun PLLA nanofiber scaffolds were even examined for *in vivo* bone formation using a critical-size rat calvarial defect model (Schofer et al., 2011).

In addition, the direct incorporation of BMP2 into nanofibers was analyzed in terms of enhanced osteoinductivity of the scaffolds (Fig. 2.1).

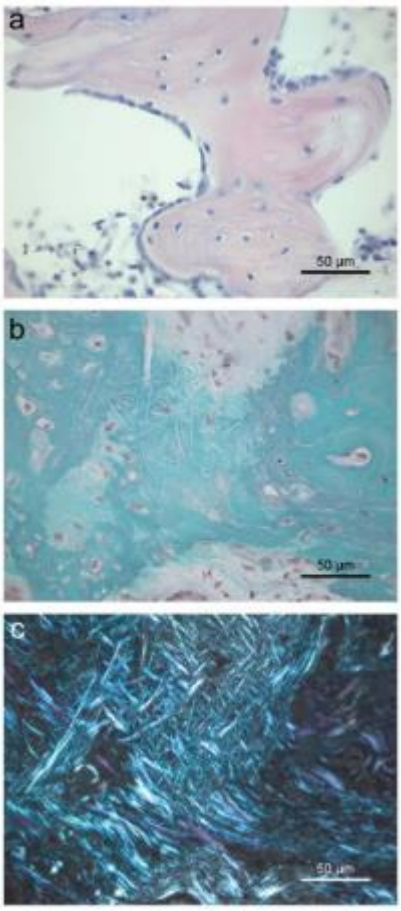

Figure 2.1 Histological analysis of a defect filled with PLLA/BMP- 2. (a) New bone ossicle with active osteoblasts on the upper right edge and lining cells on the opposite edge in a defect implanted with PLLA/ BMP-2 after 8 weeks (Hematoxylin-Eosin, BF). (b) New bone formation in a defect filled with PLLA/BMP-2 after 12 weeks, viewed under visible light, showing the remains of PLLA nanofibers (Masson-Goldner, BF). (c) The same micrograph as in 'b' under polarized light microscopy, revealing the full extent of bone incorporation through the nanofiber scaffold as well as some loose collagen fibers at the top. Reprinted with permission from PLOS ONE (Schofer et al., 2011)

After implantation, PLLA scaffolds showed marginal ossification than PLLA/BMP2 scaffolds, which induced faster bone regeneration during the first eight weeks. However, no significant differences between the two types of scaffolds were observed after twelve weeks of the *in vivo* experiment. The ability of electrospun PLLA-based scaffolds to promote bone repair in a rabbit model was also investigated in PLLA/HA nanofibers by simply interposing the biomaterial at the fracture site while being exposed to bone marrow, which is a rich source of stem cells (Rainer et al., 2011). This research did not consider the use of autologous cells, but it studied the endogenous repair by direct interaction of the endogenous cells with a scaffold. Whether newly formed bone trabeculae were between the scaffold fibers was assessed through histological evaluation and analysis of osteoinductive signaling during the *in vivo* response.

Functional PLLA-based scaffolds to promote bone tissue repair have also been produced by additive manufacturing technologies, specifically in combination with bioceramic materials. Since the main limitation of bioceramics is their inability to fuse in the presence of thermoplastic polymers (Shivalkar and Singh, 2017), low-temperature deposition manufacturing (LDM) has been developed to produce PLLA/ceramics composite scaffolds (Thavornyutikarn et al., 2014; Wu and Hsu, 2015; Bisht et al., 2021). All these produced scaffolds had high porosity and mechanical strength close to those of spongy human bone, supporting bone-like cell proliferation and *in vivo* bone conductivity.

2.1.2 Cartilage tissue

Cartilage is a load-bearing connective tissue containing chondrocytes as cells and a surrounding extracellular matrix, which is a complex network of water, collagen, proteoglycans, and other noncollagenous proteins (Luo et al., 2017). Progressive aging and injury can cause cartilage damages, thus leading to different types of diseases, such as osteoarthritis. The self-repair capacity of cartilage is extremely limited because of the absence of progenitors cells and vascularization in the tissue (Mallick et al., 2017). Recent tissue-engineering biotechnologies examined plenty of scaffolds architectures and different MSC sources, as well as combinations of synthetic polymers and living cells, to build an implantable replacement for the regeneration of cartilage (Bružauskaitė et al., 2016). Synthetic polymers and high-modulus hydrogels are the most often used materials as scaffolds for tissue-engineered cartilage (Saltzman, 2004).

For instance, PLLA nanofibrous scaffolds fabricated by phase separation combined with porogen leaching have been demonstrated to be excellent candidates for a wide variety of *in vivo* and *in vitro* cartilage repair strategies. This feature is due to the highly porous, interconnected, and degradable properties of these scaffolds (Chen et al., 2020a). He et al. used a combination of TIPS and salt-leaching methods to produce PCL/PLLA hybrid nanofibrous scaffolds for chondrocytes culture (He et al., 2009). After 12 days, chondrocytes exhibited a rounded shape, enhanced viability, and an induced expression of collagen II and aggrecan, which are cartilage-specific ECM genes. These results indicated that these scaffolds could serve as a favorable environment for maintaining the chondrocyte phenotype. Gupte et al. (Gupte et al., 2018) prepared PLLA nanofibrous scaffolds with different pore sizes via the TIPS technique. Then, they studied the relationship between pore size and chondrogenesis both *in vitro* and *in vivo* (Fig. 2.2).

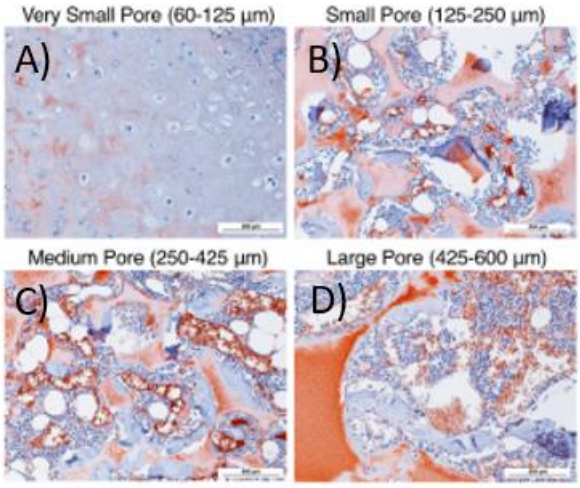

Figure 2.2 H&E histological analysis after 8 weeks subcutaneous implantation at 100x magnification. A very small pore scaffold (60-125 µm, A) contained cartilage with typical morphology in the center of the scaffold. Small (125-250 µm, B), medium (250-425 µm, C), and large-pore (425-600 µm, D) scaffold supported bone formation on pore walls, shown by pink staining of bone matrix, with bone marrow-like tissue within the pores. n=3 for each group. Scale bars = 200 µm. Reprinted with permission from Acta Materialia Inc. (Gupte et al., 2018).

Results showed that scaffolds with a small pore size (125-250 µm) significantly induced the *in vitro* chondrogenic differentiation of human BMSCs and better supported the *in vivo* cartilage formation than large pore size (425-600 µm) constructs.

However, although nanofibrous PLLA-based scaffolds have shown beneficial effects on cartilage repair, their fibrous nature leads to limited load-bearing properties (Fu et al., 2017). Highly porous scaffolds have been extensively studied in terms of mechanical properties and chondrogenesis support for cartilage TE. Recently, Rajzer et al. (Rajzer et al., 2018) fabricated a layered Gelatin/PLLA scaffold by electrospinning and 3D printing for nasal cartilage reconstruction. Fabricated scaffolds had nanofibrous gelatin membranes on the surface of porous 3D printed PLLA scaffolds. Researchers tested the influence of the internal architecture of the porous 3D printed scaffolds on their mechanical properties, resulting in maximum tensile strength of 18 MPa, in line with the range of 0.8-25 MPa that commonly occurs for cartilage tissue (Wu et al., 2020). The mechanical properties of sponge-like PLLA-based scaffolds for cartilage TE were also investigated by Mallick et al. (Mallick et al., 2016), that developed hybrid chitosan/PLLA scaffolds at different compositions by freeze-drying method. From their findings, the mechanical properties of the scaffolds decreased as the proportion of PLLA increased, however, reaching mechanical stability when the ratio of chitosan: PLLA was 70:30, which also showed the most enhanced support for the proliferation and attachment of cells. The effect of porous PLLA scaffolds and their

pore dimensions on the proliferation and differentiation of chondrocytes was also studied by Conoscenti et al. (Conoscenti et al., 2017). They produced highly porous scaffolds with controlled pore sizes by the TIPS technique. From a gene expression analysis, scaffolds with an average pore size of 100 μm seemed to promote higher expression of the chondrogenic genes than PLLA with a pore size of 200 μm. This aspect occurred both for articular cartilage and nasoseptal chondrocytes. Additionally, these scaffolds were tested for the chondrogenesis of MSCs. Results revealed a higher expression of cartilaginous genes in scaffolds with 100 μm-pore size.

All the above research indicated that suitable pore size of scaffolds improves functional properties of cartilage, hence providing an effective strategy for regeneration and repair of this tissue.

2.1.3 Blood vessels

Nowadays, the most common clinical solution for a heart attack caused by atherosclerosis is vascular bypass grafting. However, this kind of surgery only bypasses a blocked and damaged vessel without repairing the damage caused to heart tissue (Serbo and Gerecht, 2013). Hence, Tissue Engineering has focused on the fabrication of vascular networks through the utilization of scaffolds that could resemble the natural vascular tissue structure and function. Artery vessels have a three-layered structure: the external layer (the adventitia) is made of connective tissue; the middle layer, called the media, is constituted by smooth muscle cells and extracellular matrix (collagen, elastin, and proteoglycans); the inner layer, called the intima, supports a monolayer of endothelial cells (Bilodeau et al., 2005a). Hence, the fabrication of a functional substitute for such a complex structure is still a challenge. In the conventional studies of vascular TE, monolayer scaffolds were investigated to mimic only one of the three layers of blood vessels. Hu et al. (Hu et al., 2010) evaluated the effect of tubular nanofibrous PLLA scaffolds on the phenotype control of human aortic smooth muscle cells (HASMCs) for regenerating the tunica media layer. They performed *in vitro* culture and *in vivo* implantations, showing that PLLA scaffolds supported the contractile phenotype of HASMCs *in vitro* and the HASMCs differentiation *in vivo*. The reconstruction of tunica media for vascular tissue engineering was also evaluated on PLLA/PLGA/PCL hybrid scaffolds (Wang et al., 2018) (Fig. 2.3).

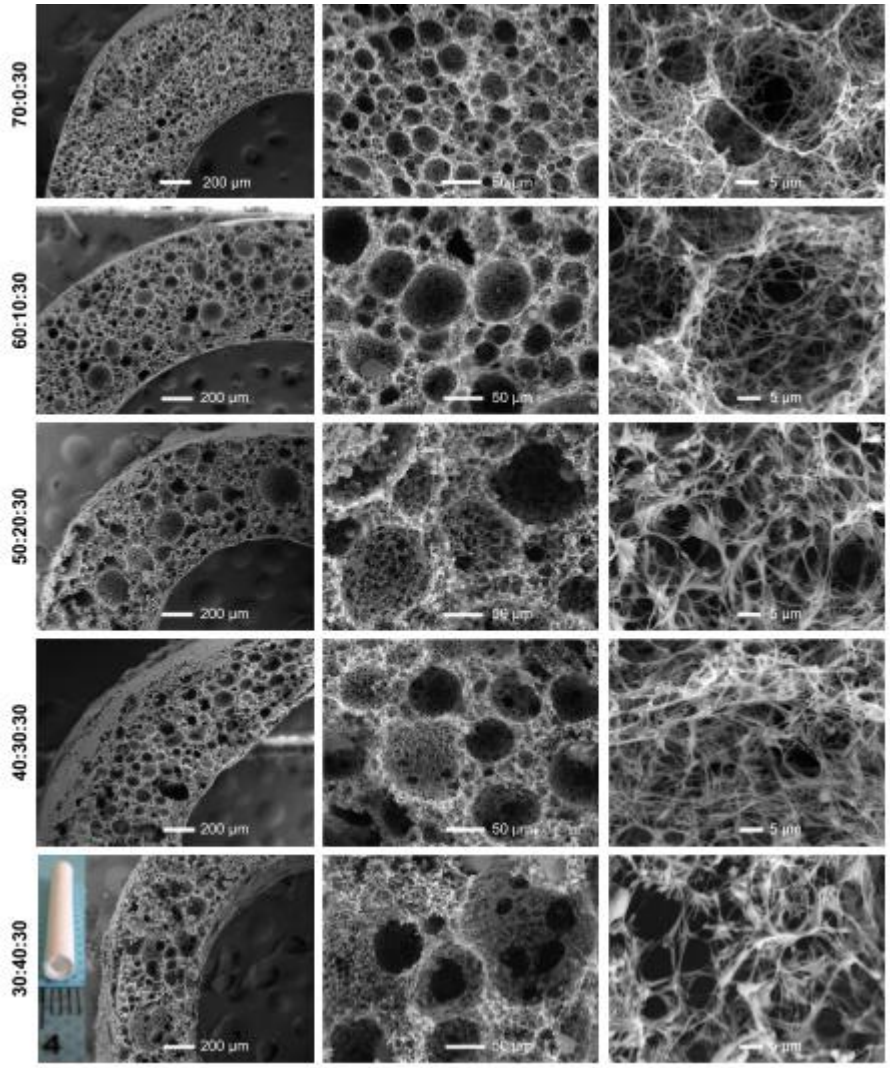

Figure 2.3 The SEM images and pore diameter distributions of PLLA/PLGA/PCL composite scaffolds with various weight ratios. Reprinted with permission from Dove Press (Wang et al., 2018).

The latter were seeded with human vascular SMCs (HVSMCs) and investigated in terms of cells growth and infiltration capacity. HVSMCs gradually spread on the scaffold surface and proliferate with the increase in culture time. Additionally, after seven days of culture, infiltration of HVSMCs was detected into the interior of the PLLA/PLGA/PCL scaffold, and the expression of the marker protein α-smooth muscle actin (α-SMA) resulted highly induced. Tubular scaffolds based on PLLA/PLA blends were produced and cultured with endothelial cells to develop a homogeneous "vessel-like" monolayer (La Carrubba et al., 2010; Bardone et al., 2012), showing a good level of cells adhesion and absence of apoptotic cell morphology.

Recently, multi-layer scaffolds have been produced for blood vessel TE. For instance, PCL, collagen, and PLLA nanofibers were used to mimic the tunica intima, tunica media, and tunica adventitia, respectively. For this purpose, these nanofibers were fabricated by

sequential electrospinning to form a three-layered tubular scaffold (Haghjooy Javanmard et al., 2016). Both endothelial cells and smooth muscle cells were cultured for bioactivity evaluation, showing that the collagen in the middle layer significantly improved attachment and proliferation of SMCs and that endothelial cell proliferation considerably increased with culture, indicating the non-cytotoxicity of the constructs.

Future research directions should focus on the implantation into bigger mammalian models, such as canine or porcine models, and the scaffold seeding by using cells from the patient's own body.

2.1.4 Skin tissue

Skin ECM is constituted by fibrous proteins, polysaccharides, two dense tissue layers (i.e. dermis and epidermis), and cells (mainly epithelial cells, keratinocytes, and fibroblasts). When skin incurs severe damages, such as in cases of exposure to high heat or pressure, it cannot self-repair (Eberli, 2011; Jeong et al., 2017). Since the supply of functional, transplantable skin is inadequate, significant efforts have been made in the TE field for the development of engineered constructs that allow facilitating skin repair. In this context, PLLA-based scaffolds have been fabricated and used with cells to form human skin equivalents. Lu et al. (Lu et al., 2012) took advantage of the mechanical strength of PLLA woven mesh to produce hybrid scaffolds with funnel-like collagen or gelatin sponge. The *in vitro* dermal fibroblast culture showed that hybrid scaffolds induced high cell seeding efficiency and improved fibroblast adhesion and proliferation compared to control collagen sponge. On the other hand, the *in vivo* wound healing assessment indicated that the healing occurred faster and more efficiently in the hybrid scaffolds than in the control collagen ones. Mostly, PLLA, collagen, and gelatin have been frequently combined to fabricate nanofibrous scaffolds, showing physical properties and biological characteristics that match those found in skin substitutes (He et al., 2019; Bacakova et al., 2020).

PLLA has also been used to fabricate a multi-layer scaffold closely mimicking the native skin structure. Lou et al. (Lou et al., 2014) developed a novel bi-layer scaffold composed of a superficial chitosan/PCL nanofibrous mat (CP-nano mat) and an underlying PLLA microporous disc (PLLA-micro disc). Hence, keratinocytes and fibroblasts were co-cultured as an epidermal equivalent and a dermal equivalent, respectively. Results showed that the cell proliferation was higher in bi-layer scaffolds compared to single CP-nano mats and PLLA-micro discs. Besides, the gene and protein expression assessments indicated an active

wound healing state, further confirming that the bi-layer scaffold could provide a suitable micro-environment for stimulating skin regeneration.

Extra research should be made to generate three-dimensional tissues meeting the requirements for clinical application.

2.2 A case study: *In vitro* evaluation of the interaction of various morphologies of PLLA scaffolds with osteoblast-like cells

2.2.1 Bone biology

Bone is a mineralized connective tissue histologically characterized by a gradient structure in which porous cancellous (trabecular) bone (density 0.1–1 g/cm^3) is surrounded by the relatively dense cortical (compact) bone (1.8–2 g/cm^3) (Bigham et al., 2020). The latter mainly provides strength, whereas the cancellous bone is the vascularized internal tissue that is porous and spongy (50–90% volume porosity) as compared to the cortical bone (5– 15% porosity) (Figure 2.4) (Wang et al., 2014).

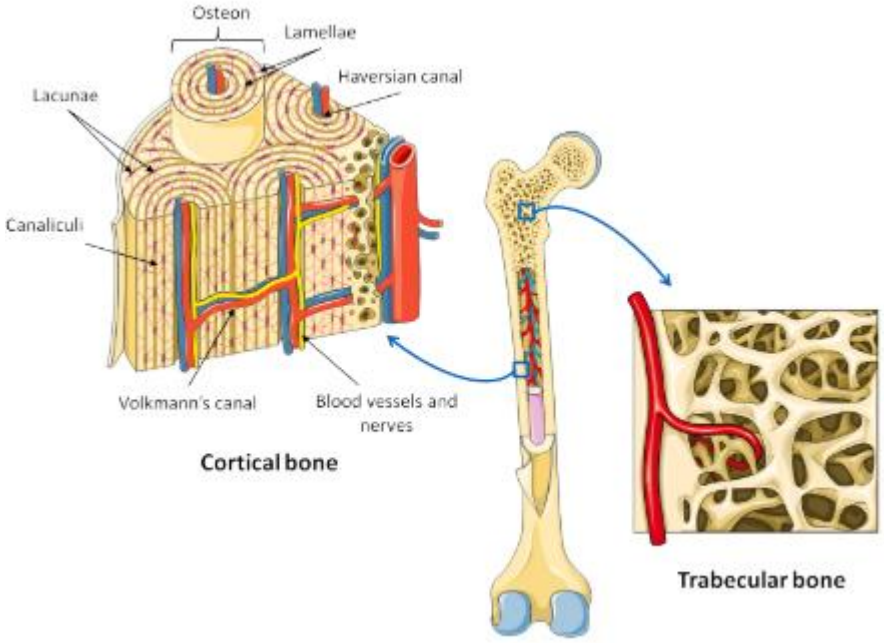

Figure 2.4 Illustration of cortical and trabecular bone structure (Wang et al., 2014)

Briefly, the functionally graded structure has an outer porosity gradually increasing from cortical to cancellous bone, particularly at the end of long bones. However, the porosity of bone is promoted to change in response to altered loading, disease, and the aging process (Bahraminasab, 2020).

The macro and microarchitecture of cortical and cancellous bones can be differentiated, leading to differences in functional bone strength and mechanical properties (Bigham et al., 2020). Specifically, cortical bone is more compressive and stiffer (compressive strength 130–230 MPa and Young's modulus 0.02–0.5 GPa) compared to cancellous bone (compressive strength 2–12 MPa and Young's modulus 7–30 GPa) (Donate et al., 2020). Despite this difference, the same minerals (calcium mineral crystals) and organic materials (type I collagen, glycosaminoglycans, osteocalcin, osteonectin, bone sialoprotein) constitute the two types of bone (Bisht et al., 2021).

The bone tissue has multiple tissue types, including the periosteum, the nervous system, blood vessels, and structural units called osteons. The periosteum is a functional fibrous tissue containing blood vessels and nerves covering cortical and cancellous bones. Osteons are grouped parallel to the long axis of the cortical bone and contain mineralized matrix and concentrically arranged osteocytes. These units have a central conduit called the Haversian Canal, i.e., a conduit for blood vessels and nerve fibers that nourish bones. The osteon matrix consists of collagen fibers that can resist bending or fracture (Bahraminasab, 2020).

After an injury, the bones undergo a dynamic remodeling through a cycle of maturation, differentiation, and resorption. The interaction of bone cells (osteoblast, osteocyte, and osteoclast cells), extracellular matrix proteins (collagen and non-collagen proteins), growth factors, and calcium contributes to this complex process. This cycle begins with bone resorption induced by osteoclasts, followed by the formation of new bones (neo-osteogenesis) by osteoblasts. However, an imbalance in bone formation vs. resorption can result in several bone diseases, including osteoporosis (Bisht et al., 2021).

2.2.2 Fabrication of PLLA scaffolds

PLLA scaffolds were fabricated using the TIPS method. Briefly, a 4% PLLA solution (dioxane/water ratio of 87/13) was kept at a constant demixing temperature for a defined time. One method of controlling the mean pore size is setting the temperature and/or the demixing time. Moreover, to fabricate a construct with a uniform distribution of pore size, an insulating material (such as Teflon) can be used as a shirt covering the sample holder, creating a homogeneous heat transfer throughout the construct. For this study, the Teflon-coated sample holder was kept at a temperature of 30°C for either 15 min or 45 min, inducing the formation of larger pore sizes, respectively. A method of creating a gradient in the mean pore size of the scaffolds is by suppressing the additional insulating shirt during the fabrication process. To achieve a gradient scaffold with the desired pore distribution, the

solution was kept at 32°C for 40 min. The distinct methods are summarized in Table 2.1. After the demixing step, the scaffolds were frozen using a glycol bath at -20°C for 15 min, dried, and cut into slices for sample preparation.

2.2.2.1 Sample preparation

Scaffold cylinders were prepared, sized 5 mm diameter × 5 mm height for *in vitro* experiments. A bilayer scaffold was arranged by attaching two subsamples of 5 mm diameter × 2.5 mm height obtained from the 30°C-15min and 30°C-45min groups, thus forming a total thickness of 5 mm. Specifically, a laboratory brush was used to coat one of the two bases of the sub-scaffolds with pure dioxane; then, the bases of the two sub-units were brought into contact, immediately resulting in a strong attachment between the two parts. Overall, this attachment process takes advantage of the solvent properties of dioxane toward PLLA.

Four groups can be distinguished: 30°C-15min (80-100 µm); 30°C-45min (170-220 µm); 32°C-40min/grad (70-220 µm); attached/bilayer (80-220 µm). The scaffolds of all groups were sterilized by 70% ethanol infiltration under vacuum, as previously reported (Lu et al., 2012; Beşkardeş et al., 2017; Kim et al., 2017; Birru et al., 2018).

2.2.3 Structural analysis from Micro-CT

The 3D structure of the scaffolds was analyzed to evaluate its morphological details, including porosity and pore distribution. This analysis was carried out using a micro-CT scanner (micro-CT Skyscan 1272, Bruker). Each cylindrical sample in its entire structure (i.e., 5 mm in diameter and 5 mm in height) was placed on the rotating support of the apparatus, which allowed the acquisition of images while rotating with a rotation pitch of 0.100°. An energy level of 40 kV and an intensity of 250 mA were set for the X-ray beam to optimize the contrast for the scaffolds reconstruction and highlight the internal structure of the different morphologies. At the end of the scans, the images were obtained in TIFF format with a 16-bit color depth. Then, 3D reconstruction was performed using the N-Recon software (version 1.6.10.2 Bruker micro-CT, Kontich, Belgium), while data processing, including artifact elimination and noise reduction in each slice, was done via the CT-software Analyser (CT-An) (version 1.16.1, Bruker micro-CT, Kontich, Belgium). The latter allowed quantitative analysis by binarization of the raw images.

2.2.3.1 Quantitative analysis of porosity

Quantitative analysis of porosity and its distribution along the scaffold geometry was evaluated using *CTAn* software. Briefly, each cylindrical scaffold was divided into separate portions (N=3: Top, middle, and bottom) of 800 layers, and three *"Volume of Interest" (VOI)* of 3 mm^3 were selected for each of these regions. Then, raw images were arranged by choosing an appropriate threshold value to convert them from 8 bit to 1 bit. Following a binary transformation, a 3D analysis was performed to assess a study on sample porosity (vol.%).

2.2.3.2 Quantitative analysis of spatial porosity distribution

The spatial distribution of porosity along the height of the samples was evaluated in "gradient" and "bilayer" groups. In this way, the spatial distribution was compared in the two morphologies against a similar overall average. Practically, a cylindrical VOI was built with a diameter of 1 mm and the height of the sample itself. After processing by thresholding and despeckling, a 2D porosity analysis was carried out. The results for each slice were then plotted against the z- coordinate.

2.2.4 Evaluation of the biological activity of scaffolds

2.2.4.1 Cell culture of Saos-2 cells

As a way to study the interaction of the cells with the scaffolds, a human osteosarcoma cell line (SaOS-2) was seeded on the four PLLA groups at a density of 10^7 cells/ml and incubated for 30 minutes at 37 °C, 5% CO2 to allow the cells to attach to the pore surface. After this stage, this operation was repeated for the other base of the fabricated cylinders. Then, Dulbecco's modified Eagle's-high glucose medium (DMEM, Sigma Aldrich, Italy), 2 mM L-glutamine (Euroclone, Celbar, Italy) supplement with 10% (v/v) fetal bovine serum (FBS) and 1% antibiotic (50 μg/ml streptomycin, 50 U/ml penicillin) solution (both from Euroclone, Celbar, Italy) was added, and samples were incubated at 37 °C, 5% CO_2. Before seeding, the constructs (n = 6 for each group) were sterilized by soaking them in 70% ethanol for 30 min followed by three times immersion in sterile PBS for 5 min each time and a pre-wetting with supplemented DMEM.

2.2.4.2 Cell metabolism via Picogreen Assay

The metabolic activity of cultured SaOS-2 cells was monitored using the dsDNA content quantification performed by fluorimetric Quant-iT PicoGreen assay kit (Molecular Probes, Eugene, OR, USA). The lysis solution was prepared by diluting 0.01 ml Triton in 100 ml Tris EDTA buffer. At each time point (24 hrs and 7 days), the culture media was removed, and the lysis solution was added to each sample after washing with PBS. Hence, cell lysis was completed by three freezes-thaw cycles at -80 °C. The lysates were used for the calculation of DNA content by adding 100ml of fluorescent nucleic acid stain to each sample. dsDNA amount was calculated referring to a standard curve. The fluorescence was measured in triplicate at the fluorescent intensity at 490 nm (excitation) and 520 nm (emission) using GloMax multiwell plate reader (GloMax, Promega Corporation, Madison, WI, USA). Results were expressed as relative fluorescence units (RFU).

2.2.4.3 Bone mineralization

SaOS-2 cells bone mineralization was investigated at 7 days using the OsteoImage Mineralization Assay kit (Lonza) to stain calcium deposits, according to the manufacturer's instructions. Stained samples were observed using a fluorescent plate reader. The fluorescent signals from the HA portion were measured at 490 nm (excitation) and 520 nm (emission) (GloMax-Multi Detection System, Promega).

2.2.5 Statistical analysis

Statistically significant differences between three or more treatments were assessed by one-way analysis of variance with Tukey's post hoc analysis. Statistically significant differences between the two treatments were assessed by the Student's unpaired t-test. All results were reported as mean ± standard deviation. A probability value of 95% ($p < 0.05$) was used to determine significance.

2.2.6 Results

2.2.6.1 Images reconstruction

From the individual layers, the different samples were visualized in three-dimensional space. The images of the 3D reconstructions of the bilayer and gradient PLLA scaffolds are reported in Figures 2.5 and 2.6, respectively. In Figure 2.5A, the cylindrical bilayer PLLA sample is represented as a continuous structure, confirming the success in the attachment for the

manufacturing of a bone-like scaffold. The cross-section image shown in Figure 2.5B highlights the absence of discontinuity between the two different structures attached to form the bilayer construct.

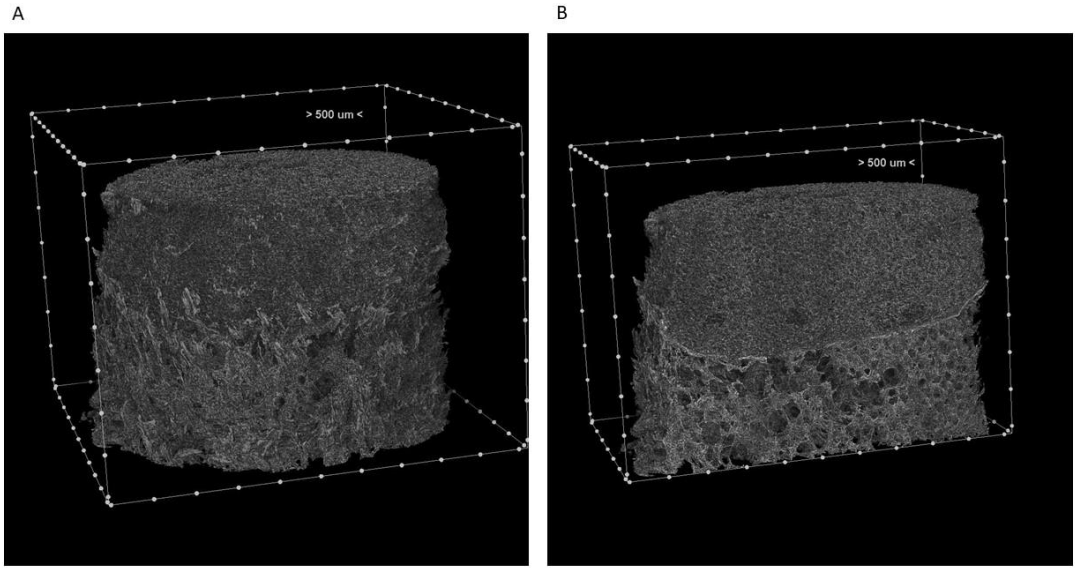

Figure 2.5 A) 3D reconstruction of the bilayer PLLA scaffold produced in a cylindrical shape by TIPS process; B) section of the 3D reconstruction of the bilayer scaffold by CTVox software.

The cross-section obtained from the 3D reconstruction of the gradient sample (Fig. 2.6B) reports a gradual increase in pore size throughout the height of the construct.

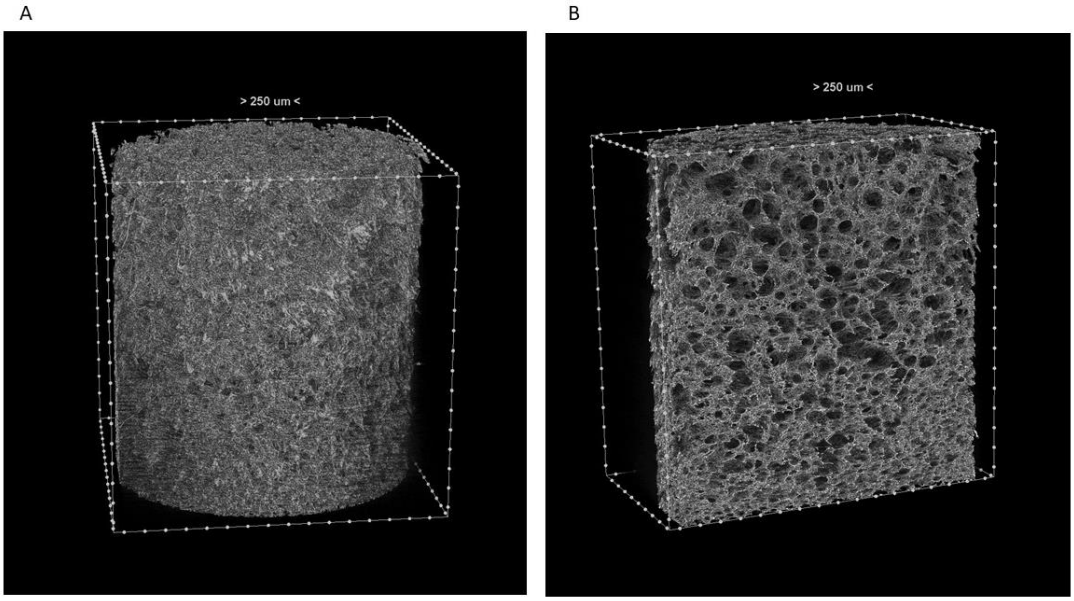

Figure 2.6 A) 3D reconstruction of the gradient PLLA scaffold produced in a cylindrical shape by TIPS process; B) section of the 3D reconstruction of the gradient scaffold by CTVox software.

Although the different manufacturers of the bilayer and gradient groups, both structures showed the same pore size range, i.e., 70-200 µm.

2.2.6.2 Quantitative analysis of porosity

In Table 2.1, 3D analysis results on porosity are compared for the different morphologies.

Table 2.1 Porosity of scaffolds with different morphologies expressed as mean value [%] ± Standard Deviation (SD).

Group	***Fabrication method***	***Mean value [%]***	***SD***
30°-15min	TIPS with a thermal path of 15 minutes at 30°C while using a Teflon holder	87.6	0.42
30°-45min	TIPS with a thermal path of 45 minutes at 30°C while using a Teflon holder	90.5	1.15
Gradient ***Gradient top*** ***Gradient middle*** ***Gradient bottom***	TIPS with a thermal path of 40 minutes at 32°C without using a Teflon holder	88.3 86.8 88.5 89.4	1.3 0.55 0.35 0.85
Bilayer ***Bilayer interface***	Bonding of the two sub-units 30°C-15min and 30°C-45min by brushing dioxane between the two contact surfaces.	87.9 85.6	2.22 0.17

The samples all have high porosity, ranging between 87 to 91%. Altogether, the groups named 30°C-15min and 30°C-45min had the smallest and the highest porosities, respectively. This result reflects the average size of the pores in the four groups, being the group 30°C-15min with small uniform pores and the 30°C-45min with large uniform pores. On the other hand, "gradient" and "bilayer" groups have a distribution of large and small pores, which altogether result in an average pore size intermediate between groups 30°C-15min and 30°C-45min. As expected, the "bilayer" group has a higher porosity deviation

due to the interface generated by the two attacked samples which, despite being continuous, results in a decrease in porosity. More details are discussed in the next paragraph.

2.2.6.3 Spatial distribution of porosity

The spatial distribution of porosity was evaluated only in the "gradient" and "bilayer" samples as the latter also contains the other two groups. Figure 2.7 shows the distributions obtained from the 2D analysis performed with the *Ctan* software.

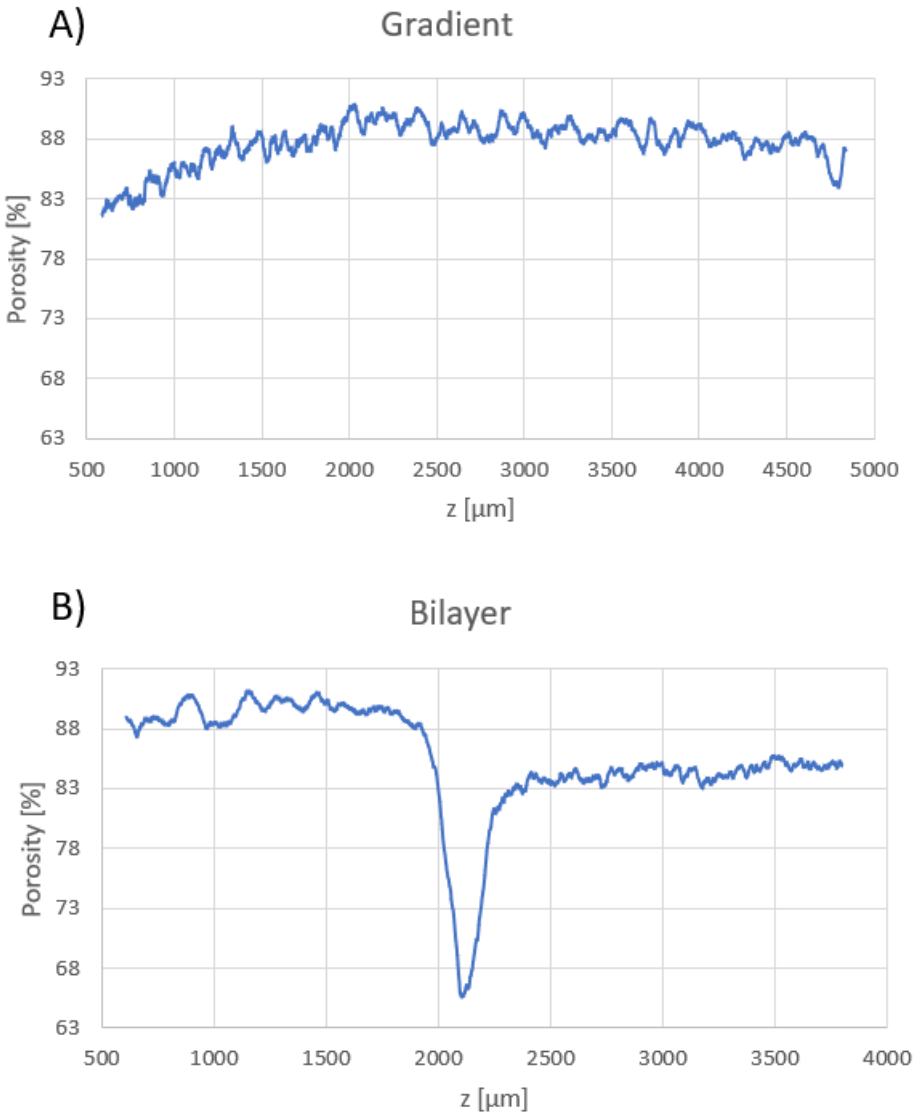

Figure 2.7 Porosity distribution along the z-coordinate of the samples “gradient” (A) and “bilayer” (B). While a uniform distribution is observed in the gradient sample, a drop in the porosity value resulted in the bilayer group

The gradient sample showed a uniform porosity distribution throughout the construct, with slightly greater porosity in the region with larger pores. In contrast, the distribution of the sample named "bilayer" is not uniform since the porosity drops at the interface (Fig. 2.8).

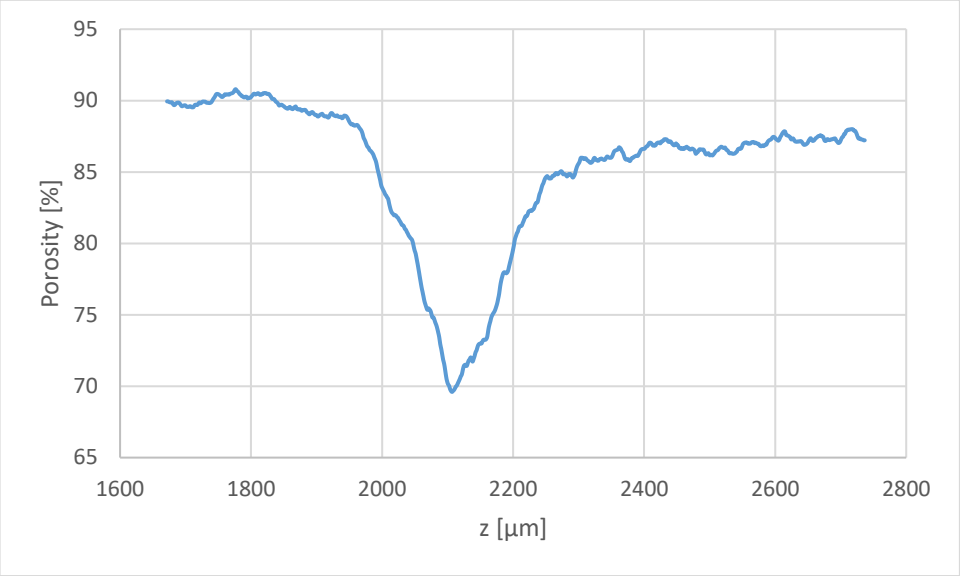

Figure 2.8 Porosity distribution in the region around the interface of the bilayer scaffold

However, despite a lower porosity in the latter area, the average value of porosity at the region around the interface is still high (85.6%, Tab.1). It is an acceptable value to confirm the continuity between the two attached parts.

2.2.6.4 SaOS-2 metabolic activity

The effect of scaffold morphology on cellular behavior was investigated by evaluating the viability, adhesion, and proliferation of Saos-2 cells seeded on the four groups. Adhesion of Saos-2 cells on the scaffolds was studied after 24h of incubation, and the number of adherent cells on bilayer scaffolds was found to be greater than the other groups (Figure 2.9).

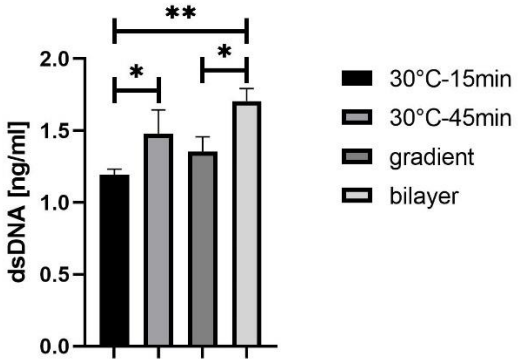

Figure 2.9 Picogreen assay results expressed as dsDNA concentration after 24 hr of static culture. Values represent mean ±SEM (**p<0.01, *p<0.05)

When proliferation profiles of cells were studied in different groups, the metabolic activity and the total number of adhered SaOS-2 cells significantly increased only on two scaffolds groups between 24 hrs and 7 days (Fig. 2.10) ($p < 0.05$).

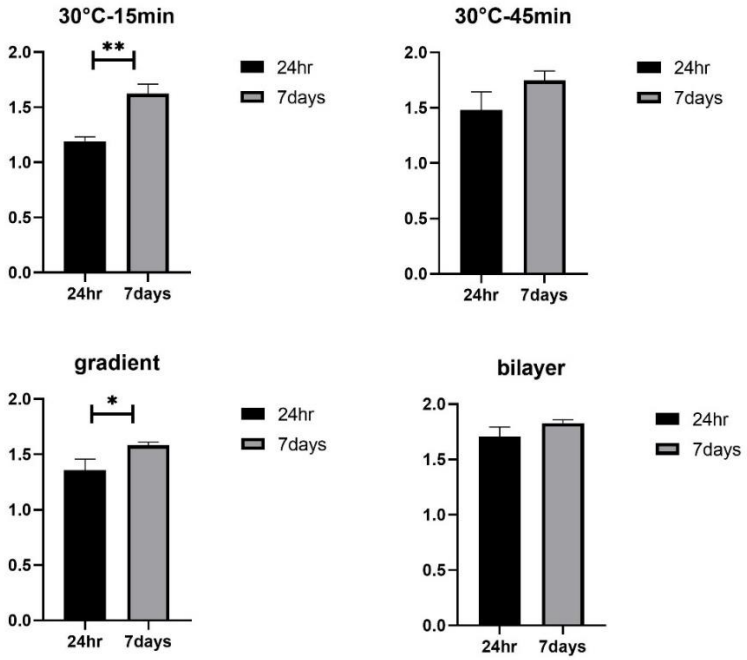

Figure 2.10 Cell viability measurements of adhered SaOS-2 cells from Picogreen Assay. Data are presented as mean ± SD, (**p<0.01, * p < 0.05)

As expected, cellular viability was significantly high on samples with natural gradient; however, the scaffolds fabricated at 30°C for 15mins showed the highest metabolic activity and total DNA on day 7 (Fig. 2.11). The latter group also showed the most significant increase in the proliferation rate compared to the other samples (Fig. 2.10).

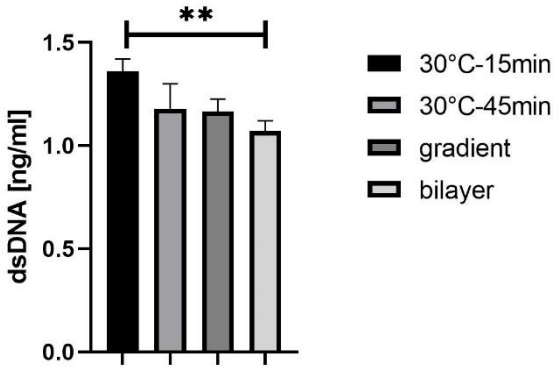

Figure 2.11 Picogreen assay results expressed as dsDNA concentration at 7 days of static culture normalized to values at 24 hr. Values represent mean ±SEM (**p<0.01, *p<0.05)

2.2.6.5 Bone mineralization

Osteoimage Assay showed bone mineralization by SaOS-2 cells on samples after 1 week of cell culture (Fig. 2.12A,B). A higher density of bone mineralization was observed on the natural gradient scaffolds and those fabricated at 30°C for 15 minutes compared with the other groups, suggesting that a smaller pore size promotes increased calcium and hydroxyapatite deposition.

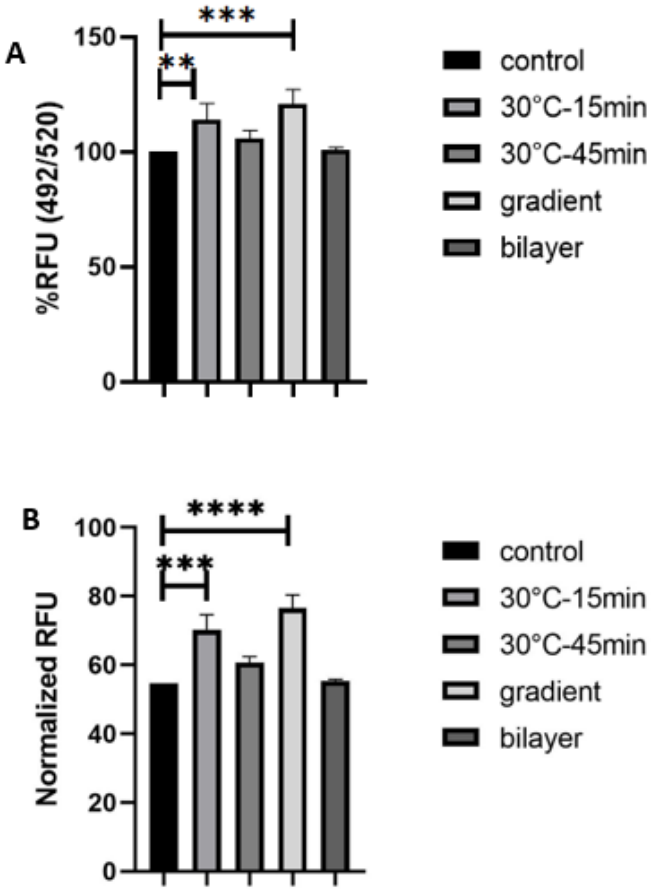

Figure 2.12 Osteoimage results after 7 days of static culture expressed as %RFU (A) and normalized (B) to dsDNA content from Picogreen assay at 7 days. Data are presented as mean ± SD, (****p<0.0001, ***p<0.001, **p<0.01, * p < 0.05)

Results were also normalized to the cell viability at 7 days to account for the loss of cells during cell culture and to preclude any potential influence of initial seeding density.

2.2.7 Discussion

The overall goal of this study was to investigate the effects of scaffold morphology on osteoblast-like cells (Saos-2) initial attachment, proliferation, and calcium matrix deposition. When designing the scaffold for this *in vitro* application, the physical properties of

the bone, as composed of two layers of cancellous and cortical bones, were considered. Moreover, the scaffold should present similar mechanical and structural properties to the local bone. Literature has shown that ceramic-based scaffold is appropriate to replace cortical bone, while polymers are more suitable for cancellous bone (Abbasi et al., 2020). Interestingly, the gradient scaffold architecture is similar to the natural structure of native bone tissue that represents different densities from cancellous bone to cortical bone (Bahraminasab, 2020). Besides the composition, other important parameters for scaffold design are the pore size of the final structure, pore interconnectivity, and porosity.

In this study, by altering the thermal protocol used in the TIPS technique, PLLA scaffolds were fabricated with four distinct morphologies that possessed increasing porosity with increasing mean pore size. Specifically, the fabricated morphologies were: uniform pore size distribution with either 90 or 200 μm, gradient distribution ranging from 80 to 220 μm, and two uniform samples attached to form a bilayer scaffold with 90 and 200 μm of pore size on each side. The high interconnectivity of the pores is another important geometric parameter that characterizes the fabricated scaffolds, as it directly influences the diffusion of nutrients and the removal of metabolic waste and ensures continuous bone tissue ingrowth (Link et al., 2013). The obtained morphologies have been analyzed structurally (by micro-CT technique) and biologically. Micro-CT is a non-destructive and reproducible tool that can provide 3D representations of morphological characteristics of complex structures (Bansalyz et al., 2010; Vissers et al., 2015). When samples are characterized by a structure with interconnected pores and a high level of porosity, micro-CT is applied to obtain reliable quantitative data about their features, such as porosity and pore size distribution. However, as discussed by Freire-Gormaly et al. (Freire-Gormaly et al., 2015)**,** in a scaffold with micro and macro porosity, micro-CT cannot estimate microporosity, which is highly dependent on imaging pixel size and threshold values. Although these drawbacks, the micro-CT morphometric analysis of PLLA scaffolds served as an assessment method for the structural investigation of fabricated scaffolds for the desired *in vitro* application.

From a quantitative analysis, a high porosity (87-91%) was obtained in all tested groups while considering the whole structure of the constructs. This result is in line with porosity levels higher than 50% generally needed to allow vascularization and even exceeding 85% for some bone scaffolds found in the literature (Fassina et al., 2008; Sultana and Wang, 2012; Gupta et al., 2019). The one-way variance with Tukey's post hoc analysis showed that the samples had no statistical differences between them. It confirms the high porosity achieved by the TIPS technique, regardless of the thermal path used. In addition, concerning the

bilayer scaffold, even the interface area showed a high porosity despite the attack line immediately decreasing in this value. In fact, in the region at the interface, 3D analysis in the three VOIs considered gave an average porosity value not affected by this decrease.

The results of this study demonstrated that, although altering the mean pore size did not affect the average porosity of scaffolds before cell seeding, there were distinct differences in the response of cells to the different scaffold variants. In particular, scaffolds with the two attached parts stimulated the lowest level of mineralization in comparison to the scaffolds with the smallest mean pore size as early as day 7. When cell attachment was assessed in the four distinct scaffolds at 24 h after seeding, it was evident that the morphology of the scaffold affected cells behavior. Bilayer scaffolds resulted in higher cell adhesion at 24hr after seeding than gradient scaffolds and those with smaller mean pore sizes. Indeed, porosity has been reported to affect cell attachment, as it changes the available surface area for the interaction with cells (Müller et al., 2015). From the 2D analysis of micro-CT concerning the porosity distribution, the present study found a porosity decrease of up to 63% in the bilayer scaffold at the interface region. Since the porosity of the native bone tissue has a spatial distribution, with lower levels in cortical than cancellous bone, it was hypothesized that cells found a higher affinity for adhesion in this bilayer structure with varying porosities in different regions, as required from the cell growth perspective (Müller et al., 2015). However, total porosity alone has no direct relationship to tissue ingrowth, whereas pore size and interconnectivity do. Scaffold pore size also influenced the number of cells after 7 days of culture, with some scaffold groups having different proliferation rates (Fig. 2.11). Gradient and 30-15 groups produced a significant difference in cells number at 24hr and 7 days after seeding. Interestingly, markedly higher mineralization was observed in these two groups compared to the unseeded control at 7 days of culture (Fig. 2.12 A,B), despite high levels of proliferation. It is consistent with other results stating that in vitro assays of Saos-2 cells show both good proliferative activity and a propensity for bio-mineralization (Adkisson et al., 2000; Wiens et al., 2010). These data provide evidence that, before hydroxyapatite (HA) formation, the cells undergo a high proliferation phase (Wang et al., 2014; Eren et al., 2018; Voltrova et al., 2019).

Overall, the results demonstrate the ability of the scaffold microarchitecture to elicit a distinct osteoblastic response in terms of adhesion, proliferation, and HA matrix production *in vitro*, thus highlighting the importance of this scaffold property in the development of biomaterials for the repair of bone defects.

2.2.8 Conclusions

PLLA has proven to be a synthetic polymer with excellent mechanical properties, good biocompatibility, and ease of processing, thus gaining great interest as a biomaterial for tissue engineering. Several examples of PLLA-based scaffolds for TE applications, such as bone, cartilage, vascular, and skin tissues, have been characterized by various research groups. Different fabrication technologies have been reported for PLLA-based scaffolds manufacturing, such as electrospinning, phase separation, salt leaching, and additive manufacturing. All these studies have shown that PLLA-based scaffolds can promote tissue ingrowth and the development of functional substitutes, both *in vitro* and *in vivo*.

In this chapter, a case study in the field of bone TE has been analyzed and discussed. A combination of scaffold fabrication features, material characterization, and biological evaluation was exploited to study an *in vitro* model for bone replacement. Different scaffold morphologies were investigated to mimic the natural bilayer structure of bone (composed of the cancellous and compact tissues). One of them includes a "gradient" porous scaffold, in which the pore size gradually increases from layer to layer, to overcome some of the individual limitations of small and large homogeneous pore scaffolds. The influence of scaffold microstructure was evaluated by quantitative micro-CT study on sample porosity or by assessing the proliferation and mineralization of osteoblastic cells up to 7 days of static culture.

References

Abbasi, N., Ivanovski, S., Gulati, K., Love, R. M., and Hamlet, S. (2020). Role of offset and gradient architectures of 3-D melt electrowritten scaffold on differentiation and mineralization of osteoblasts. *Biomater. Res. 2019 241* 24, 1–16. doi:10.1186/S40824-019-0180-Z.

Abdal-hay, A., Khalil, K. A., Hamdy, A. S., and Al-Jassir, F. F. (2017). Fabrication of highly porous biodegradable biomimetic nanocomposite as advanced bone tissue scaffold. *Arab. J. Chem.* 10, 240–252. doi:10.1016/j.arabjc.2016.09.021.

Adkisson, H. D., Strauss-Schoenberger, J., Gillis, M., Wilkins, R., Jackson, M., and Hruska, K. A. (2000). Rapid quantitative bioassay of osteoinduction. *J. Orthop. Res.* 18, 503–511. doi:10.1002/JOR.1100180326.

Bacakova, L., Zikmundova, M., Pajorova, J., Broz, A., Filova, E., Blanquer, A., et al. (2020). "Nanofibrous Scaffolds for Skin Tissue Engineering and Wound Healing Based on Synthetic Polymers," in *Applications of Nanobiotechnology*, eds. M. Stoytcheva and Z. Roumen (London: IntechOpen). doi:10.5772/intechopen.88744.

Bahraminasab, M. (2020). Challenges on optimization of 3D-printed bone scaffolds. *Biomed. Eng. Online* 19, 69. doi:10.1186/s12938-020-00810-2.

Bansalyz, P. N., Joshix, N. S., Entezariy, V., Grinstaffzx, M. W., and Snydery, B. D. (2010). Contrast Enhanced Computed Tomography can predict the glycosaminoglycan content and biomechanical properties of articular cartilage. *Osteoarthr. Cartil.* 18, 184–191. doi:10.1016/j.joca.2009.09.003.

Bardone, E., Brucato, A., Keshavarz, T., Carfì Pavia, F., Rigogliuso, S., La Carrubba, V., et al. (2012). Poly Lactic Acid Based Scaffolds for Vascular Tissue Engineering. 27, 409–414. Available at: www.aidic.it/cet [Accessed July 14, 2021].

Beşkardeş, I. G., Hayden, R. S., Glettig, D. L., Kaplan, D. L., and Gümüşderelioğlu, M. (2017). Bone tissue engineering with scaffold-supported perfusion co-cultures of human stem cell-derived osteoblasts and cell line-derived osteoclasts. *Process Biochem.* 59, 303–311. doi:10.1016/J.PROCBIO.2016.05.008.

Bigham, A., Foroughi, F., Rezvani Ghomi, E., Rafienia, M., Neisiany, R. E., and Ramakrishna, S. (2020). The journey of multifunctional bone scaffolds fabricated from traditional toward modern techniques. *Bio-Design Manuf.* 3, 281–306. doi:10.1007/s42242-020-00094-4.

Bilodeau, K., Couet, F., Boccafoschi, F., and Mantovani, D. (2005). Design of a perfusion bioreactor specific to the regeneration of vascular tissues under mechanical stresses. *Artif. Organs* 29, 906–912. doi:10.1111/j.1525-1594.2005.00154.x.

Birru, B., Mekala, N. K., and Parcha, S. R. (2018). Improved osteogenic differentiation of umbilical cord blood MSCs using custom made perfusion bioreactor. *Biomed. J.* 41, 290–297. doi:10.1016/J.BJ.2018.07.002.

Bisht, B., Hope, A., Mukherjee, A., and Paul, M. K. (2021). Advances in the Fabrication of Scaffold and 3D Printing of Biomimetic Bone Graft. *Ann. Biomed. Eng.* 49, 1129–1150. doi:10.1007/s10439-021-02752-9.

Bružauskaitė, I., Bironaitė, D., Bagdonas, E., and Bernotienė, E. (2016). Scaffolds and cells for tissue regeneration: different scaffold pore sizes—different cell effects. *Cytotechnology* 68, 355–369. doi:10.1007/s10616-015-9895-4.

Chen, L., Liu, J., Guan, M., Zhou, T., Duan, X., and Xiang, Z. (2020). Growth Factor and Its Polymer Scaffold-Based Delivery System for Cartilage Tissue Engineering. *Int. J. Nanomedicine* 15, 6097–6111. doi:10.2147/IJN.S249829.

Ciapetti, G., Granchi, D., Devescovi, V., Baglio, S. R., Leonardi, E., Martini, E., et al. (2012). Enhancing osteoconduction of PLLA-based nanocomposite scaffolds for bone regeneration using different biomimetic signals to MSCs. *Int. J. Mol. Sci.* 13, 2439–2458. doi:10.3390/IJMS13022439.

Conoscenti, G., Schneider, T., Stoelzel, K., Carfì Pavia, F., Brucato, V., Goegele, C., et al. (2017). PLLA scaffolds produced by thermally induced phase separation (TIPS) allow human chondrocyte growth and extracellular matrix formation dependent on pore size. *Mater. Sci. Eng. C* 80, 449–459. doi:10.1016/j.msec.2017.06.011.

Donate, R., Monzón, M., and Alemán-Domínguez, M. E. (2020). Additive manufacturing of PLA-based scaffolds intended for bone regeneration and strategies to improve their biological properties. *E-Polymers* 20, 571–599. doi:10.1515/epoly-2020-0046.

Eberli, D. (2011). *Tissue Engineering for tissue and organ regeneration*. Rijeka, Croatia: InTech.

Eren, E. D., Tansik, G., Tekinay, A. B., and Guler, M. O. (2018). Mineralized Peptide Nanofiber Gels for Enhanced Osteogenic Differentiation. *ChemNanoMat* 4, 837–845. doi:10.1002/CNMA.201700354.

Fassina, L., Saino, E., Visai, L., Silvani, G., De Angelis, M. G. C., Mazzini, G., et al. (2008). Electromagnetic enhancement of a culture of human SAOS-2 osteoblasts seeded onto titanium fiber-mesh scaffolds. *J. Biomed. Mater. Res. Part A* 87A, 750–759. doi:10.1002/JBM.A.31827.

Freire-Gormaly, M., Ellis, J. S., Bazylak, A., and MacLean, H. L. (2015). Comparing thresholding techniques for quantifying the dual porosity of Indiana Limestone and Pink Dolomite. *Microporous Mesoporous Mater.* 207, 84–89. doi:10.1016/j.micromeso.2015.01.002.

Fu, N., Zhang, X., Sui, L., Liu, M., and Lin, Y. (2017). "Application of Scaffold Materials in Cartilage Tissue Engineering," in *Cartilage Regeneration, Stem Cell Biology and Regenerative Medicine*, ed. Y. Lin (Humana Press, Cham), 21–39. doi:10.1007/978-3-319-51617-2_2.

Fu, Y., Liu, L., Cheng, R., and Cui, W. (2018). ECM Decorated Electrospun Nanofiber for Improving Bone Tissue Regeneration. *Polym. 2018, Vol. 10, Page 272* 10, 272. doi:10.3390/POLYM10030272.

Gupta, D., Singh, A. K., Dravid, A., and Bellare, J. (2019). Multiscale Porosity in Compressible Cryogenically 3D Printed Gels for Bone Tissue Engineering. *ACS Appl. Mater. Interfaces* 11, 20437–20452. doi:10.1021/ACSAMI.9B05460/SUPPL_FILE/AM9B05460_SI_002.MP4.

Gupte, M. J., Swanson, W. B., Hu, J., Jin, X., Ma, H., Zhang, Z., et al. (2018). Pore Size Directs Bone Marrow Stromal Cell Fate and Tissue Regeneration in Nanofibrous Macroporous Scaffolds by Mediating Vascularization. *Acta Biomater.* 82, 1–11. doi:10.1016/J.ACTBIO.2018.10.016.

Haghjooy Javanmard, S., Anari, J., Zargar Kharazi, A., and Vatankhah, E. (2016). In vitro hemocompatibility and cytocompatibility of a three-layered vascular scaffold fabricated by sequential electrospinning of PCL, collagen, and PLLA nanofibers. *J. Biomater. Appl.* 31, 438–449. doi:10.1177/0885328216652068.

He, L., Liu, B., Xipeng, G., Xie, G., Liao, S., Quan, D., et al. (2009). Microstructure and properties of nano-fibrous PCL-b-PLLA scaffolds for cartilage tissue engineering. *Eur. Cell. Mater.* 18, 63–74. doi:10.22203/ECM.V018A06.

He, R., Wang, K., Ren, J., Zhang, W., Wang, Z., Deng, K., et al. (2019). Efficacy of a synthetic biomimetic skin substitute of PLLA/gelatin nanofiber membrane in facilitating chronic cutaneous wound healing. *Mater. Technol.* 35, 872–880. doi:10.1080/10667857.2019.1709286.

Hu, J., Sun, X., Ma, H., Xie, C., Chen, Y. E., and Ma, P. X. (2010). Porous nanofibrous PLLA scaffolds for vascular tissue engineering. *Biomaterials* 31, 7971–7977. doi:10.1016/j.biomaterials.2010.07.028.

Huang, Q., Liu, Y., Ouyang, Z., and Feng, Q. (2020). Comparing the regeneration potential between PLLA/Aragonite and PLLA/Vaterite pearl composite scaffolds in rabbit radius segmental bone defects. *Bioact. Mater.* 5, 980–989. doi:10.1016/J.BIOACTMAT.2020.06.018.

Jeong, K. H., Park, D., and Lee, Y. C. (2017). Polymer-based hydrogel scaffolds for skin tissue engineering applications: a mini-review. *J. Polym. Res.* 24, 112. doi:10.1007/s10965-017-1278-4.

Kim, J.-W., Shin, K.-H., Koh, Y.-H., Hah, M. J., Moon, J., and Kim, H.-E. (2017). Production of Poly(ε-Caprolactone)/Hydroxyapatite Composite Scaffolds with a Tailored Macro/Micro-Porous Structure, High Mechanical Properties, and Excellent Bioactivity. *Materials (Basel).* 10, 1123. doi:10.3390/ma10101123.

La Carrubba, V., Pavia, F. C., and Brucato, V. (2010). Tubular scaffold for vascular tissue engineering application. *Int. J. Mater. Form.* 3, 567–570. doi:10.1007/s12289-010-0833-x.

Link, T., Wang, X., Schloßmacher, U., Feng, Q., Schröder, H. C., and Müller, W. E. G. (2013). An approach to a biomimetic bone scaffold: Increased expression of BMP-2 and of osteoprotegerin in SaOS-2 cells grown onto silica-biologized 3D printed scaffolds. *RSC Adv.* 3, 11140–11147. doi:10.1039/C2RA22352J.

Lopresti, F., Pavia, F. C., Ceraulo, M., Capuana, E., Brucato, V., Ghersi, G., et al. (2021). Physical and biological properties of electrospun poly(d,l-lactide)/nanoclay and poly(d,l-lactide)/nanosilica nanofibrous scaffold for bone tissue engineering. *J. Biomed. Mater. Res. - Part A* 109, 2120–2136. doi:10.1002/jbm.a.37199.

Lou, T., Leung, M., Wang, X., Chang, J. Y. F., Tsao, C. T., Sham, J. G. C., et al. (2014). Bi-layer scaffold of chitosan/PCL-nanofibrous mat and PLLA-microporous disc for skin tissue engineering. *J. Biomed. Nanotechnol.* 10, 1105–1113. doi:10.1166/JBN.2014.1793.

Lu, H., Oh, H. H., Kawazoe, N., Yamagishi, K., and Chen, G. (2012). PLLA-collagen and PLLA-gelatin hybrid scaffolds with funnel-like porous structure for skin tissue engineering. *STAdM* 13, 064210. doi:10.1088/1468-6996/13/6/064210.

Luo, Y., Sinkeviciute, D., He, Y., Karsdal, M., Henrotin, Y., Mobasheri, A., et al. (2017). The minor collagens in articular cartilage. *Protein Cell* 8, 560–572. doi:10.1007/s13238-017-0377-7.

Mallick, S. P., Pal, K., Rastogi, A., and Srivastava, P. (2016). Evaluation of poly(L-lactide) and chitosan composite scaffolds for cartilage tissue regeneration. *http://dx.doi.org/10.1080/15685551.2015.1136535* 19, 271–282. doi:10.1080/15685551.2015.1136535.

Mallick, S. P., Rastogi, A., Tripathi, S., and Srivastava, P. (2017). Strategies on process engineering of chondrocyte culture for cartilage tissue regeneration. *Bioprocess Biosyst. Eng.* 40, 601–610. doi:10.1007/s00449-016-1724-4.

Müller, W. E. G., Schröder, H. C., Feng, Q., Schlossmacher, U., Link, T., and Wang, X. (2015). Development of a morphogenetically active scaffold for three-dimensional growth of bone cells: biosilica–alginate hydrogel for SaOS-2 cell cultivation. *J. Tissue Eng. Regen. Med.* 9,

E39–E50. doi:10.1002/TERM.1745.

Rainer, A., Spadaccio, C., Sedati, P., De Marco, F., Carotti, S., Lusini, M., et al. (2011). Electrospun hydroxyapatite-functionalized PLLA scaffold: potential applications in sternal bone healing. *Ann. Biomed. Eng.* 39, 1882–1890. doi:10.1007/S10439-011-0289-2.

Rajzer, I., Kurowska, A., Jabłoński, A., Jatteau, S., Śliwka, M., Ziąbka, M., et al. (2018). Layered gelatin/PLLA scaffolds fabricated by electrospinning and 3D printing- for nasal cartilages and subchondral bone reconstruction. *Mater. Des.* 155, 297–306. doi:10.1016/J.MATDES.2018.06.012.

Saltzman, W. M. (2004). *Tissue engineering: engineering principles for the design of replacement organs and tissues*. Oxford, UK: Oxford University Press Available at: http://books.google.com/books?id=KorDMxtkZ_wC&pgis=1.

Schofer, M. D., Roessler, P. P., Schaefer, J., Theisen, C., Schlimme, S., Heverhagen, J. T., et al. (2011). Electrospun PLLA Nanofiber Scaffolds and Their Use in Combination with BMP-2 for Reconstruction of Bone Defects. *PLoS One* 6, e25462. doi:10.1371/JOURNAL.PONE.0025462.

Serbo, J. V., and Gerecht, S. (2013). Vascular tissue engineering: Biodegradable scaffold platforms to promote angiogenesis. *Stem Cell Res. Ther.* 4, 8. doi:10.1186/scrt156.

Shivalkar, S., and Singh, S. (2017). Solid Freeform Techniques Application in Bone Tissue Engineering for Scaffold Fabrication. *Tissue Eng. Regen. Med.* 14, 187–200. doi:10.1007/s13770-016-0002-5.

Sultana, N., and Wang, M. (2012). PHBV/PLLA-based composite scaffolds fabricated using an emulsion freezing/freeze-drying technique for bone tissue engineering: surface modification and in vitro biological evaluation. *Biofabrication* 4. doi:10.1088/1758-5082/4/1/015003.

Teixeira, M. A., Amorim, M. T. P., and Felgueiras, H. P. (2020). Poly(Vinyl Alcohol)-Based Nanofibrous Electrospun Scaffolds for Tissue Engineering Applications. *Polymers (Basel).* 12, 7. doi:10.3390/POLYM12010007.

Thavornyutikarn, B., Chantarapanich, N., Sitthiseripratip, K., Thouas, G. A., and Chen, Q. (2014). Bone tissue engineering scaffolding: computer-aided scaffolding techniques. *Prog. Biomater.* 3, 61–102. doi:10.1007/s40204-014-0026-7.

Vissers, C. A. B., Harvestine, J. N., and Leach, J. K. (2015). Pore size regulates mesenchymal stem cell response to Bioglass-loaded composite scaffolds. *J. Mater. Chem. B* 3, 8650–8658. doi:10.1039/c5tb00947b.

Voltrova, B., Hybasek, V., Blahnova, V., Sepitka, J., Lukasova, V., Vocetkova, K., et al. (2019). Different diameters of titanium dioxide nanotubes modulate Saos-2 osteoblast-like cell adhesion and osteogenic differentiation and nanomechanical properties of the surface. *RSC Adv.* 9, 11341–11355. doi:10.1039/C9RA00761J.

Wang, W., Nie, W., Liu, D., Du, H., Zhou, X., Chen, L., et al. (2018). Macroporous nanofibrous vascular scaffold with improved biodegradability and smooth muscle cells infiltration prepared by dual phase separation technique. *Int. J. Nanomedicine* 13, 7003–7018. doi:10.2147/IJN.S183463.

Wang, X., Tolba, E., Der, H. C. S., Neufurth, M., Feng, Q., Diehl-Seifert, B. R., et al. (2014). Effect of Bioglass on Growth and Biomineralization of SaOS-2 Cells in Hydrogel after 3D Cell Bioprinting. *PLoS One* 9, e112497. doi:10.1371/JOURNAL.PONE.0112497.

Weng, W., Song, S., Cao, L., Chen, X., Cai, Y., Li, H., et al. (2014). A comparative study of bioartificial bone tissue poly-l-lactic acid/polycaprolactone and PLLA scaffolds applied in bone regeneration. *J. Nanomater.* 2014, 236. doi:10.1155/2014/935149.

Wiens, M., Wang, X., Schlomacher, U., Lieberwirth, I., Glasser, G., Ushijima, H., et al. (2010). Osteogenic potential of biosilica on human osteoblast-like (SaOS-2) cells. *Calcif. Tissue Int.* 87, 513–524. doi:10.1007/S00223-010-9408-6/FIGURES/8.

Wu, G. H., and Hsu, S. H. (2015). Review: Polymeric-based 3D printing for tissue engineering. *J. Med. Biol. Eng.* 35, 285–292. doi:10.1007/s40846-015-0038-3.

Wu, J., Chen, Q., Deng, C., Xu, B., Zhang, Z., Yang, Y., et al. (2020). Exquisite design of injectable hydrogels in cartilage repair. *Theranostics* 10, 9843–9864. doi:10.7150/THNO.46450.

Zeng, J. H., Liu, S. W., Xiong, L., Qiu, P., Ding, L. H., Xiong, S. L., et al. (2018). Scaffolds for the repair of bone defects in clinical studies: A systematic review. *J. Orthop. Surg. Res.* 13, 33. doi:10.1186/s13018-018-0724-2.

Chapter 3

Perfusion bioreactors for TE applications

This chapter describes the role of perfusion bioreactors and their main design parameters for Tissue Engineering applications. Particular attention is given to airlift and double-flow perfusion systems, as they are the bioreactors adopted in this thesis work. For these devices, the effect of operational variables on cell viability and the development of 3D biological construct is also reviewed.

3.1 The role of perfusion bioreactors in TE

Bioreactors provide an environment with *in vitro* physiological tissue-specific properties allowing cells to mature. When using bioreactor systems, various functional tissues have been generated and cultured *in vitro* (Gomes et al., 2006; Pu et al., 2010; Sandino and Lacroix, 2011; Pisanti et al., 2012; Mitra et al., 2017).

Among the different types of bioreactor technologies, perfusion bioreactors aim to mimic *in vitro* the microscopic mechanical loading of the native tissue (Correia et al., 2012). Specifically, perfusion bioreactor systems pump culture medium through the pores network of the scaffolds located within the device in a continuous or non-continuous way (Fig. 3.1).

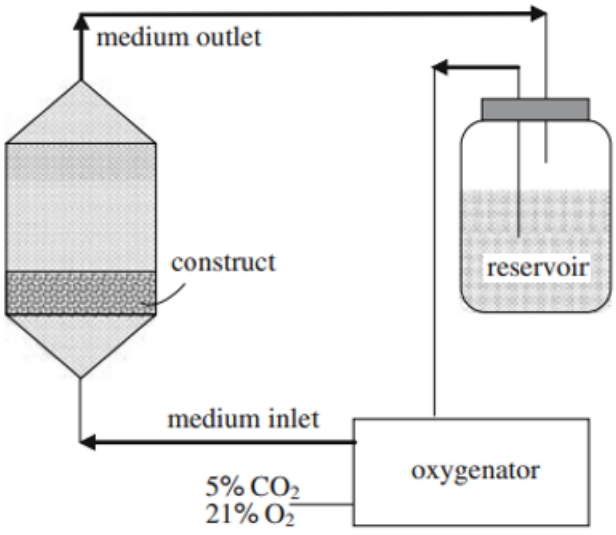

Figure 3.1 Example of a perfusion bioreactor system with a scaffold located within the device (Chen and Hu, 2014)

The basic design of perfusion bioreactors consists of a pump, a culture media reservoir, a tubing circuit, and chambers or columns that accommodate the scaffolds (Gaspar et al., 2012). These devices offer the advantage of supplying the areas with a high concentration of metabolic products with fresh cell culture media. Hence, the periodic exchange of the cell culture media does not alter the molecular composition of the media (Grayson et al., 2008). In addition to enhanced medium delivery, perfusion systems have been indicated as tools to exert mechanical forces that may potentially increase cell differentiation. Indeed, turbulent flow or perfusion generates hydrodynamic shear forces, which leads to altered gene expression profiles and functional changes by activating extracellular signal-regulated pathways that, in turn, affect the proliferation and differentiation of cells (Bilodeau et al., 2005a). For instance, this feature could be convenient for providing mechanical stimulation to bone and cartilage cells that are known to be regulated by mechanical signals (Jaasma et al., 2008; Grayson et al., 2011; Correia et al., 2012; Vetsch et al., 2017). For the engineering of these tissues, a different interstitial flow of medium provides diverse hydrodynamic shear stress, thus influencing the development and function of the perfused construct. Generally, the amount of shear stress experienced by cells can be varied by varying the flow rates of the perfusion system (Fig. 3.2) (Seddiqi et al., 2020). In this context, perfusion systems are more beneficial than static cultures in enhancing matrix production (Karande et al., 2004; Bilodeau et al., 2005b; Ru Choi et al., 2017; Vetsch et al., 2017).

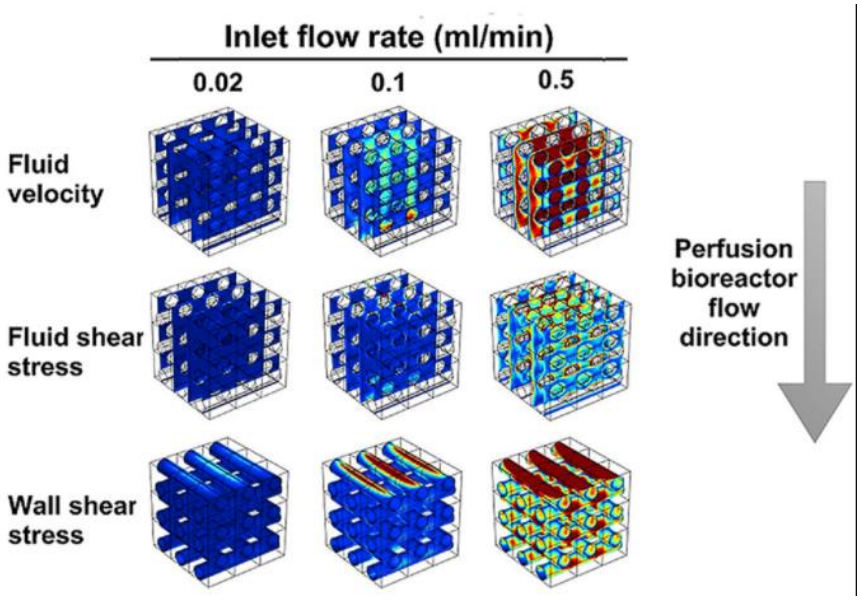

Figure 3.2 Varying inlet flow rate of perfusion bioreactors (0.02, 01, 0.5 ml/min) affects fluid velocity, fluid shear stress, and wall shear stress inside 3D-printed scaffolds, but does not gauge fluid pressure or oxygen concentration after 5 days using finite element modeling. (Seddiqi et al., 2020)

However, local internal shear stresses can be experienced by individual cells depending not only on medium flow but also on the viscosity of the medium and porous structure. This latter depends on the scaffold microarchitecture, in terms of porosity, dimensions, geometry of the scaffold, construction material, and degree of interconnectivity (Porter et al., 2005). Besides the benefit of flow-induced shear stress within the scaffold, perfusion bioreactors are the most used dynamic bioreactors that have been tested in different tissue engineering applications because of their consistent distribution of nutrients. The primary role of perfusion has been to increase the transport rates of nutrients, metabolites, and oxygen to and from the cells through the continuously perfused fluid that forces the medium through the internal porous network (Fig. 3.3). For achieving this condition, the fluid path must be ideally confined to ensure perfusion to the core architecture of the scaffold rather than around its edges, i.e., a direct perfusion configuration (Martin et al., 2004). However, in concrete systems, the tendency of flow to follow a preferential path through the construct remains a problem. This phenomenon commonly occurs for scaffolds with a wide pore size distribution, where some regions arise poorly nourished while others are appropriately perfused.

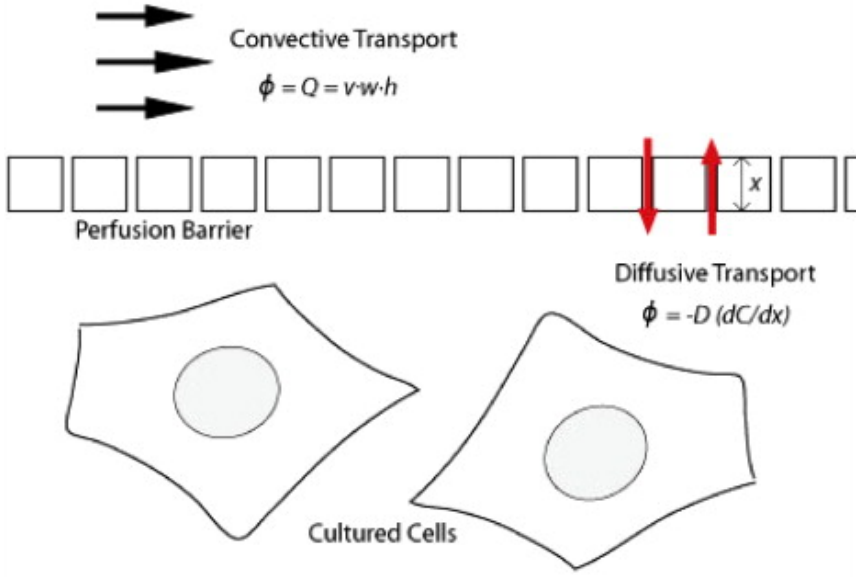

Figure 3.3 Flow perfusion culture overcomes the internal diffusion limitation on cultured cells, where D is the diffusion coefficient, C is the concentration, Q is the flow rate, and φ the flux.

Different bioreactor configurations and scaffold materials/preparations have been explored for various tissues, showing that they markedly increase mass transport compared to other bioreactor systems. Correspondingly, it induced better ECM distribution throughout the 3D scaffold, increased cell number, increased expression of the regulatory phenotype, and improved ECM deposition (Dvir et al., 2006; McCoy and O'Brien, 2010; Pham et al., 2012;

Gharravi et al., 2013; Pourchet et al., 2018). Indeed, only the perfusion bioreactor is able to mitigate both external and internal diffusional limitations; however, only external diffusional limitations (i.e., at the surface of a scaffold) are overcome in other dynamic bioreactors where the inability of medium and other nutrients to penetrate within the porous network of the scaffold remains. For this reason, metabolically active cells, such as osteoblasts, resulted in cell growth and matrix production being confined to the external aspects of each scaffold when using spinner flasks or rotating wall vessels. On the other hand, perfusion bioreactors provide several advantages for culturing scaffolds since the delivery of fresh medium also throughout their internal structures produces a more uniform mixing. This feature allows for better environmental control, a more homogeneous microenvironment, and physical stimulation of the cells in large constructs rather than only improving convection at the construct surface (Abdal-hay et al., 2017).

Continuous perfusion systems have also been investigated as seeding tools, proving advantageous for cell seeding over static cell seeding methods (Spencer et al., 2013; Mitra et al., 2017; Beşkardeş et al., 2018; Schmid et al., 2018).

3.1.1 Bioreactor design and hydrodynamic parameters

The design of bioreactors affects their mechanical environment, thus influencing experimental outcomes. Especially in perfusion bioreactors, design limitations have resulted in undesirable fluid-induced shear forces or stagnation of fluid medium, triggering mortality of cells and tissues (Israelowitz et al., 2012). Moreover, perfusion may cause deformation in the scaffold according to its porous architecture, mechanical properties, flow configuration (i.e., continuous, oscillatory, pulsatile), and medium flow rate. Therefore, to develop large engineered constructs, it is necessary to understand how medium perfusion rates influence the range of cellular responses, including the dynamics of gene expression, cellular morphology, cell-cell interactions, matrix formation, and organization (Beşkardeş et al., 2018).

Bioreactor designs are different between industrial and laboratory small-scale applications. Specifically, this review focuses on laboratory bioreactors typically designed for research applications. Nevertheless, their design cannot be transferred to an industrial scale for growing clinical-aimed tissues since an increase in the sizes of these large-scale bioreactors results in detrimentally high shear forces (Pisanti et al., 2012).

The main parameters during bioreactor design for TE applications include features allowing dynamic-culture requirements, such as variable flow, control of the flow through regions of

least resistance, and maintaining the flow through the scaffold (Bonassar et al., 2001; Stephens et al., 2007). The design of the perfusion chamber also has a fundamental role since its material and dimensions influence cell culturing conditions. Hence, it may need optimization to improve the development of biological constructs.

Bioreactor material

Bioreactor materials must be certified as biocompatible because they interact with cells or living tissues. Besides, these materials must be able to withstand sterilization techniques and should be transparent (to allow optical monitoring during cells culture) and commercially feasible. For these reasons, the most common materials are synthetic polymers, for example, polymethylmethacrylate (PMMA), polyoxymethylene, or polysulfone (Rauh et al., 2011).

Flow Rate and Shear Stress

The bioreactor design affects the flow rate, so it needs to be optimized to enhance cellular activity. For instance, when flow velocities are very low, enhanced cell viability has been reported than under higher values of flow rates (Merrill et al., 1965; Saltzman, 2004; Eberli, 2011). This feature is due to lower shear stress at a lower flow rate, which may facilitate cell attachment and spread, thus leading to higher cell viability. However, ultra-low flow rates appeared inadequate for bone tissue engineering applications because they might not accomplish an optimal distribution of nutrients, oxygen, and removal of waste products (Grayson et al., 2011; Murphy et al., 2013). On the other hand, very high flow rates can have a negative effect on cell attachment and ECM deposition, thus limiting the benefits associated with perfusion systems (Fig. 3.4) (Cartmell et al., 2003).

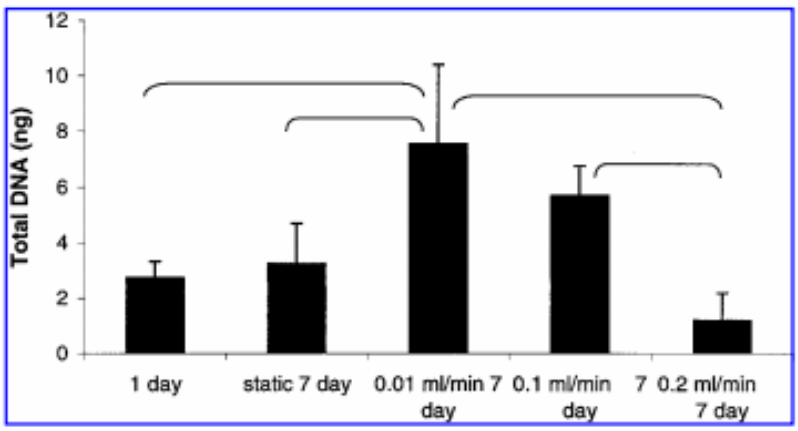

Figure 3.4 DNA assay for osteoblast-like cells after 1 week of perfusion. 1 day: 1 day seeded scaffold before perfusion. Static 7 day: static sample (not perfused). 0.01, 0.1, and 0.2 ml/min 7 day: flow rates, perfused for 1 week. Brackets: $p<0.05$. (Cartmell et al., 2003)

The Effect of Dynamic Flow

During constant perfusion, there is a continuous flow through the scaffolds. Therefore, several systems incorporating oscillatory or pulsatile flow have been tested similarly for TE purposes. The noncontinuous flow was found advantageous so that detached cells could attach back to the scaffold (Gaspar et al., 2012). Moreover, these different flow configurations have shown promising results in supporting cell seeding, leading to a uniform distribution and proliferation of cells throughout the scaffolds (Du et al., 2008). Since the arterial pressure follows a physiological pulse rate, pulsatile perfusion bioreactors have been studied to enhance the development and differentiation of small tissue-engineered blood vessels made by elastic polymeric scaffolds (Hahn et al., 2007; Song et al., 2012; Mun et al., 2013).

Electrical Stimulation

In addition to mechanical cues, electrical stimulation can be combined with mechanical signals during *in vitro* perfused cultures to achieve the targeted functionality of engineered scaffolds.

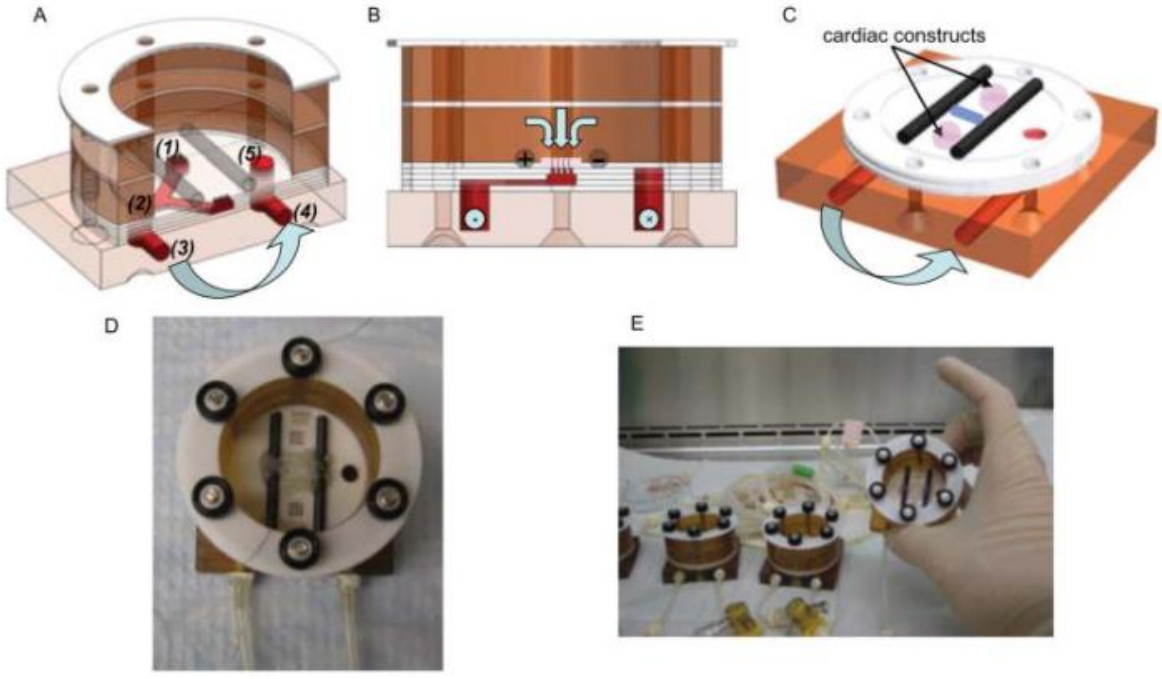

Figure 3.5 Perfusion-stimulation bioreactor setup: (A) Alternating layers of custom machined Teflon, silicone, and plastic are stacked to a "perfused dish" culture chamber where medium flows from the medium bath (1), into the "Y" shaped channel (2), out of the bioreactor (3) and through a peristaltic pump, where it is pumped back to the bioreactor inlet (4), and back into the medium bath (5). Light blue arrows denote medium flow direction. (B) Cross-sectional view of the bioreactor showing flow path through the construct and carbon rod

electrodes that provide electrical stimulation. (C) Isometric view showing placement of scaffolds over perfusion holes, between carbon rods. (D) Final assembly of the bioreactor with spacers to keep construct loosely in place and platinum wires to connect electrodes to a cardiac stimulator. (E) After autoclaving, bioreactors and tubing are assembled under sterile conditions in a tissue culture hood. (Maidhof et al., 2012)

Specifically, electrical stimuli are primarily applied in cardiac tissue engineering to regenerate the infarcted area after heart failure or accelerate the generation of fully functional, clinically sized cardiac tissue constructs (Maidhof et al., 2012; Tandon et al., 2013; Visone et al., 2018).

Mass Transfer

The mass transfer at the interior of 3D cell-seeded constructs is one of the major obstacles that hinder the practical application of TE constructs (Israelowitz et al., 2012). After cells distribute throughout porous scaffolds, the maintenance of cell viability during prolonged culture is still a challenge. Indeed, nutrients, oxygen, and regulatory molecules should be efficiently transferred from the bulk culture medium to the tissue surfaces and then to the cells within the tissue construct (Courtenay et al., 2018). On the other hand, metabolites and CO_2 should be removed by transferring them from the inner cells to the bulk medium (Karande et al., 2004). The hydrodynamic conditions in a bioreactor influence external mass transfer rates, whereas internal mass transfer rates may depend on at least a combination of diffusion and convection mechanisms, such as medium perfusion or scaffold deformation.

3.2 Airlift bioreactors (Merchuk and Gluz, 2013)

An airlift reactor (ALR) is a gas-liquid or gas-liquid-solid contacting device in which fluid circulates in a defined cyclic pattern through specifically designed channels. In ALRs, a stream of air pneumatically agitates the reactor content and facilitates the exchange of material between the gas phase and the medium: oxygen is usually transferred to the liquid phase, and products of the reaction are removed through the gas-phase exchange as they occur.

Unlike bubble columns (BCs), where the injected gas leads to ascending bubbles and random mixing, in the ALR, fluid flow pattern/circulation depends not only on the gas input but also on the system geometry. In detail, the basic design of the ALR reactor consists of a channel for the upward gas-liquid flow (the riser) and a separate duct for the downward flow (the downcomer), connected at the bottom and top to form a closed loop. As for BCs, the gas is usually injected at the bottom of the riser.

Based on their design, ALRs can be divided into two main types (Fig. 3.6):

- external loop vessels, in which circulation takes place through distinct conduits
- internal loop vessels, in which the circulation path is created by baffles placed strategically in a single vessel.

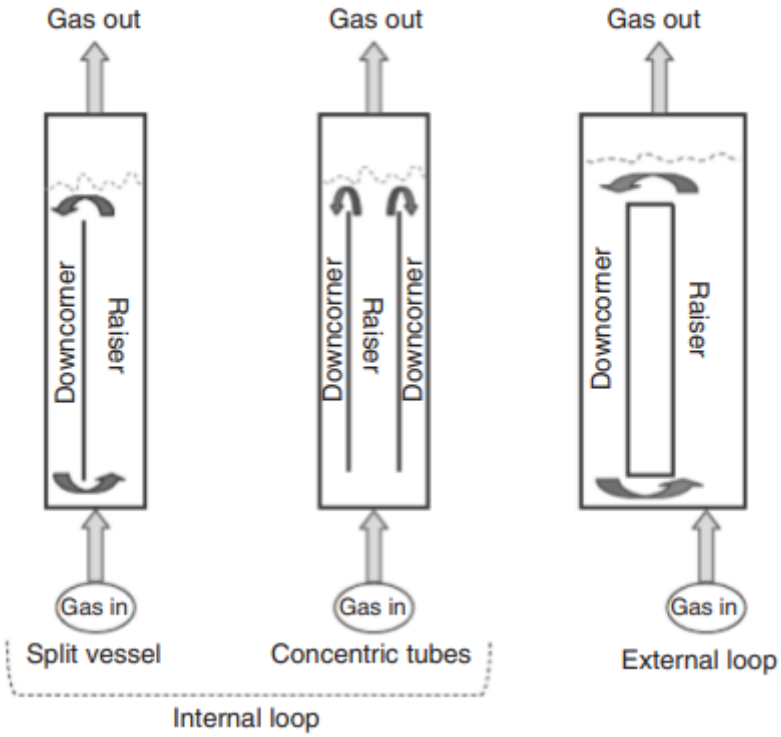

Figure 3.6 Different configurations of Air Lift Reactors (ALRs)

The top section of the reactor, which is the gas separator, allows the gas to disengage at the top. The design of this section and the operating conditions determine the fraction of gas that will disengage. The fraction of the remaining gas is trapped by the descending liquid and dragged into the downcomer, affecting the fluid dynamics and performance of the reactor.

3.2.1 ALRs geometry

Each section of ALRs presents different flow characteristics along with momentum, mass transfer, and heat transfer. Mainly, four distinct sections can be distinguished:

- Riser: the gas is injected at the bottom of this region, where the gas and liquid flows are predominantly upward.

- Downcomer: in this section, the flow of gas and liquid is predominantly downward; the liquid recirculates from the riser towards the downcomer thanks to the pressure gradient between the two columns where there is a difference in mean fluid density.
- Gas separator: this zone connects the riser to the downcomer at the top of the reactor. It serves to facilitate liquid recirculation and gas disengagement. Therefore, its design allows more time for the gas to reside in the separator than is required for bubble disengagement.
- Base: it is the bottom connection zone between the riser and downcomer. Particular attention is paid to its design which may influence the hydrodynamic parameters.

Since the four sections are interconnected, their design may influence the performance and characteristics of each of the other regions.

3.2.2 Advantages

ALRs have been extensively used as fermentation vessels for many processes based on biomass growth to provide the major requirements for culturing microorganisms, such as large gas–medium interface for the supply of oxygen and the removal of waste gases, proper nutrient distribution, temperature control, and a contamination-free environment.

Nevertheless, ALRs seem to offer superior advantages, i.e., more successful growth of microorganisms, than traditional stirred-tank fermenters (STRs). This feature is due to the difference in the fluid dynamics of ALRs and STRs. In conventional STRs, the energy required for the movement of the fluids is introduced via a stirrer at a single point in the reactor, producing high energy dissipation and shear stress in the immediate surroundings of the stirrer. However, these parameters decrease toward the vessel walls, where the fluid moves slower. This condition results in a wide variation of shear forces. Hence, in STRs, cells in culture may be exposed to very different hydrodynamic environments, with highly turbulent zones, where very high shear gradients may endanger cell integrity or influence cell morphology and metabolism.

On the other hand, in ALRs, gas injection contributes little directly to system dynamics, despite being concentrated in a single point. Indeed, liquid and gas circulation is facilitated by the difference in the average gas holdup (integrated along the reactor height) between the riser and the downcomer, generating a pressure difference at the bottom of the equipment. Hence, no focal points of energy input exist, and shear distribution is homogeneous throughout the ALR. This phenomenon creates a relatively stable environment, where

changes in the mechanical forces and shear-related damages acting on suspended cells are minimized. Similarly, velocity fluctuations related to turbulent shear are relatively homogeneously distributed in both the riser and the downcomer of an ALR. At most, the bottom of the vessel may be critical owing to a sharp 180° turn.

In summary, the main advantages offered by ALRs are:

- homogeneity of the stress forces
- mechanical simplicity and easier sterilization over agitated tanks
- enhanced mass transfer rates for a given energy input (i.e., the mass of oxygen absorbed per unit of energy invested and unit time)

Hence, the ALRs are particularly suited to processes involving slow-growing cultures, such as animal and plant cells, which have a high risk of contamination. Additionally, they are adopted with changing oxygen requirements because aeration is relatively insensitive to changes in operating conditions.

The main disadvantage of ALRs is the requirement for a minimum liquid volume to allow liquid recirculation in the reactor.

3.2.3 Fluid Dynamics

The hydrodynamic variables in an ALR are highly dependent on the design and operating variables, as presented schematically in Fig. 3.7.

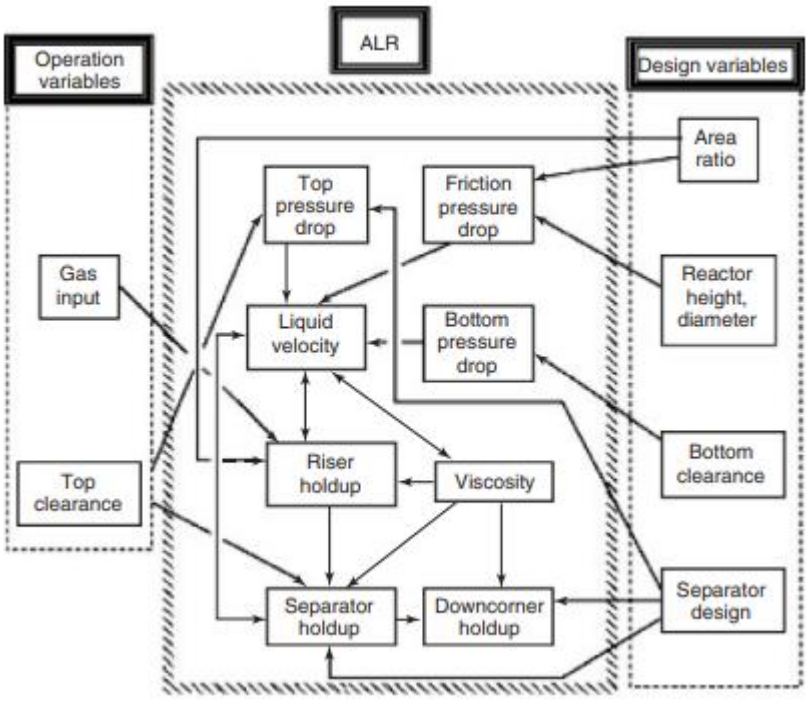

Figure 3.7 Interaction between design and operation variables in an ALRs

Among the design variables, the area ratio concerns the riser-to-downcomer area ratio; the bottom clearance is the free area for flow in the bottom which accounts for the resistance to flow in this part of the reactor. The main operating variables are the gas input rate and the top clearance, i.e., the liquid level inside the ALR.

Flow Configuration

The main gas-liquid flow configurations in ALRs are:

- homogeneous bubble flow regime, in which turbulence is low due to the presence of relatively small, uniform diameter bubbles;
- the slug-flow regime, in which large bubbles offer limited mass transfer capability;
- the churn-turbulent regime, in which a wide range of bubble sizes coexist within a very turbulent liquid.

The churn-turbulence regime can be achieved either from a homogeneous flow of bubbles by increasing the gas flow rate or from a slug flow by increasing the turbulence of the liquid through an increase in flow rate or reactor diameter (Fig. 3.8).

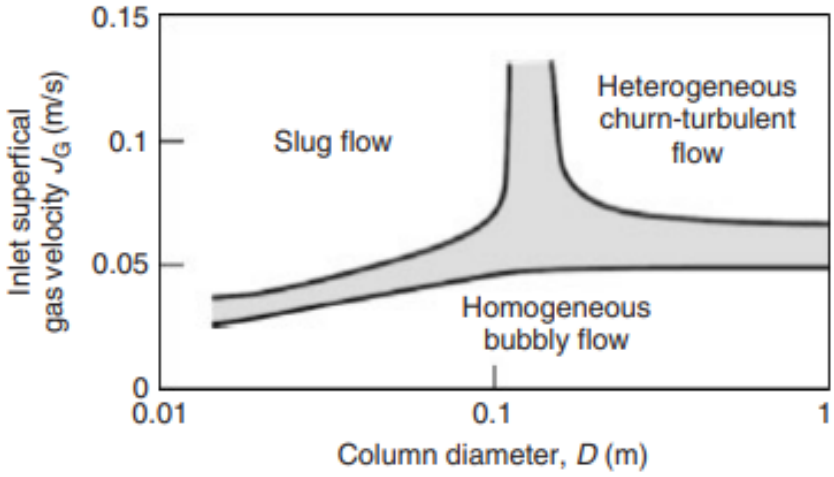

Figure 3.8 Map of flow configurations for gas-liquid concurrent flow in a vertical tube, as a function of the superficial gas velocity, and the diameter of the tube

Appropriate selection of the cross-sectional ratio of the riser to the downcomer area will establish the flow type.

In the riser, with the gas and liquid flowing upward, the velocity of the gas is usually higher than the velocity of the liquid. The only exception is homogeneous flow with microbubbles, where the free rise velocity of the bubbles is negligible compared to the rate of the liquid so that both phases rise at the same rate.

When liquid flows down into the downcomer, it can eventually bring bubbles around. The liquid velocity needs to be greater than the free rise velocity of the bubbles to trap the bubbles. This phenomenon occurs at high gas holdup in the riser, leading to liquid superficial velocity that becomes sufficiently high to entrap either the smaller or larger bubbles when further increasing in liquid velocity. On the contrary, in the case of complete disengagement, the clear liquid will be the only phase entering the downcomer. The degree of disengagement of bubbles entering the riser is also determined by the geometric design of the gas separator. For instance, a widening of this section reduces the velocity of the liquid and facilitates the disengagement of bubbles.

Gas Holdup

The gas holdup is the volumetric fraction of the gas in the total volume of a gas-liquid-solid dispersion. It is a crucial parameter in ALRs that indicates mass transfer performance (greater gas holdup means greater gas-liquid interfacial area) and the driving force for liquid circulation (the difference in gas holdup between the riser and downcomer generates this driving force).

Changes in the geometric design of the ALR affecting the liquid and gas residence time in each part of the reactor make changes to the overall holdup. For instance, the gas holdup is strongly influenced by the liquid level and the geometric design of the gas separator since they determine the extent of disengagement of the bubbles. In IL-ALRs, the higher the bubble disengagement rate, the lower the gas holdup in the downcomer. As a result, the liquid velocity increases, allowing for the large bubbles to be trapped because their free-rising velocity $U_{b\infty}$ (a function of size and viscosity) is smaller than the liquid velocity in the downcomer U_{Ld} (function of the difference in gas accumulation between the riser and downcomer and frictional losses). On the contrary, in EL-ALRs, the holdup in the riser decreases as the liquid level increases. This condition is due to turbulence in the headspace area, where most of the gas that enters the downcomer becomes trapped. Hence, when increasing the liquid height, the amount of trapped gas is reduced, then the liquid velocity increases, whereas the gas holdup decreases, both in the riser and the downcomer.

Liquid velocity

The liquid velocity is primarily a function of the gas flow rate and the holdup variation between the riser and downcomer. At the same time, it affects gas holdup in the riser and

downcomer, mixing time, average gas phase residence time, interfacial area, and mass and heat transfer coefficients. Experiments have shown that an increase in liquid velocity typically induces a decrease in mean residence time and accumulation of gas bubbles in the riser. Although the geometric design of the reactor influences the liquid velocity, it usually remains constant during operation. Indeed, at higher liquid velocities, the hydrostatic driving force is reduced owing to more bubble transfer from the gas separator to the downcomer. As a result, the overall change in liquid velocity is mitigated.

Cell Damages due to bubbles in ALRs

In ALRs, the gas bubbles themselves are associated with to shear rate that can damage cells in suspension. This phenomenon is highly dependent on cell type and bubble size, so it must be considered in reactors designed for cell culture.

Peculiarly, the source of damage seems not to be the mere presence of bubbles or their passage through the reactor but the fluid dynamic events happening during their disengagement. When a bubble emerges through a free surface, eventual ruptures liberate a relatively large amount of energy and liquid jets at very high velocities. This phenomenon is highly detrimental to the cells captured by the liquid jets and those in the immediate surrounding.

During cells culture, a design strategy is suggested to maximize the mass transferred by each bubble before bursting and minimize the number of cells in the surroundings of the bursting zones. These conditions may be achieved by increasing the residence time (i.e., increasing the column height) and maintaining a stable foam layer at the top of the reactor.

Overall, ALRs are suitable for the characteristics of biological processes where a high mass transfer rate is required. However, excessive power input can lead to cell damage due to shear effects.

3.2.4 Mass transfer

The main parameter determining the transfer rate across the gas-liquid interface is the volumetric mass transfer coefficient k_La. The latter is typically determined by unit driving force (i.e., the concentration gradient between the liquid and gas phases). The mass transfer coefficient k_La can be seen as the product of two terms: the mass transfer coefficient k_L and the specific interfacial area a, which both depend on:

- static properties of the liquid, such as density, diffusivity, and surface tension;

- dynamic (related to liquid flow) properties of the liquid, such as its rheological parameters;
- parameters that depend on liquid dynamics.

There are two methods for k_La measurement in a reactor: the steady- and unsteady-state methods. In the steady-state one, the rates of oxygen uptake in steady-state operation are evaluated by measuring the inlet and outlet gas amounts of oxygen. During this determination, the errors of measurement are significant. Unsteady-state methods use a step-change in oxygen concentration in the gas inlet stream and then follow the response of the dissolved oxygen concentration in the system. In this method, especially when viscous liquids are used, the presence of microbubbles that are depleted from oxygen very rapidly but do not disengage in the gas separator can become an inert volume of gas in the reactor, thus altering the measurements.

In ALRs, since the different sections (riser, downcomer, and gas separator) have diverse flow characteristics, the mass transfer coefficient may differ from one region to another. Commonly, the downcomer contribution to the overall mass transfer is assumed negligible compared to that in the riser.

Bubble Size and Interfacial Area

The interfacial area per unit volume a is the part of k_La that is more susceptible to changes than the mass transfer coefficient k_L. Indeed, the interfacial area depends on variations in turbulence, initial bubble size, and liquid properties. In this context, bubble size is determined by a balance between bubble rupture and coalescence.

3.2.5 Design Improvements

Several modifications to the classic ALR equipment have been proposed to improve its performance concerning oxygen transfer per unit of energy and hydrodynamic characteristics. In Figure 3.9, some of these designs are presented.

Multistage ALRs have shown a substantially higher mass transfer coefficient and a better performance in terms of oxygen transfer. They are constructed with vertical stages operating in a series that dynamically induces continuous bubble generation, breakup through rupture, and coalescence. Indeed, at the end of each stage, bubbles lost their identity. Then, new

bubbles are generated at the beginning of each stage, thus producing gas holdup higher than that in the single-stage system for the same superficial gas and liquid velocities.

ALRs using internals mechanically moved generally are used for viscous liquids. It comprises a stirrer located near the bottom of the draft tube, which operates to increase the circulation rate. This configuration showed enhanced oxygen transfer and more uniform distribution of the dissolved oxygen concentration throughout the reactor related to the unmodified ALR. However, one limitation relies on the additional cost due to a focus introduced on energy input.

ALRs with static mixers, usually located in the riser, have also been used for enhancing the performance of ALRs. An improvement in the interfacial area, higher fluidization capacity, and enhancement of k_La, especially in viscous liquids, have been reported ALRs with static mixers. The device can also comprise baffles that modify the flow paths by inducing them to move along a helix instead of going in straight lines.

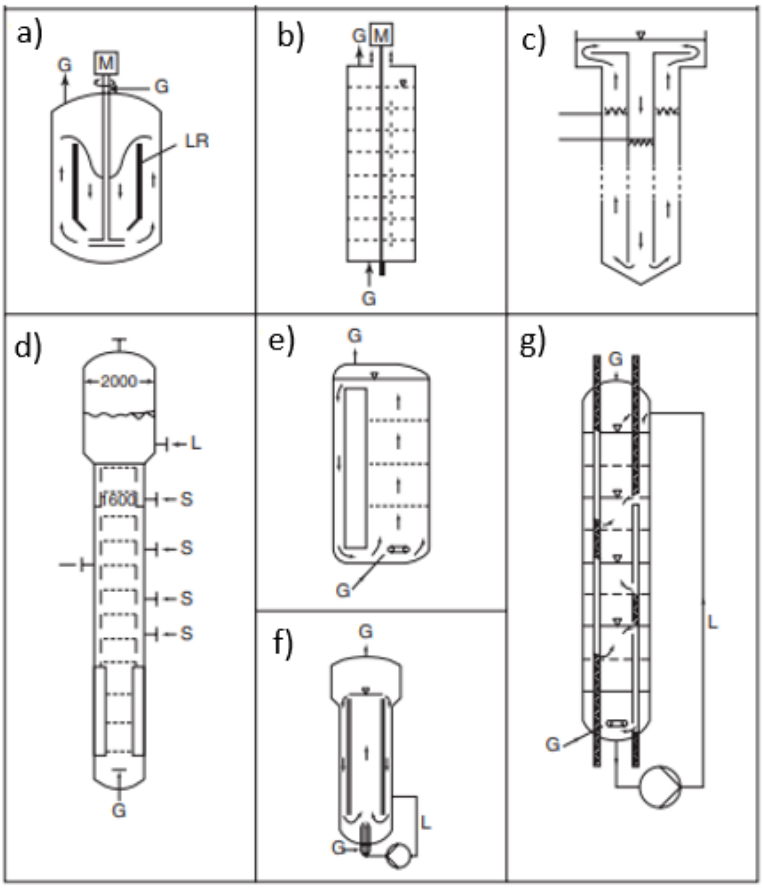

Figure 3.9 Some modifications from classic ALR morphologies. (a,b) configurations using mechanically moved internals for energy input, (c) downstream air ALR, (d) ALR with a static mixer, (e) multistage EL-ALR, (f) nozzle loop ALR, and (g) multistage ALR.

3.2.1 TE application of airlift bioreactors

From a literature overview, a limited number of researchers have used and developed an airlift for culturing tissue engineering constructs. Patil et al. (Patil et al., 2013) designed a novel airlift reactor for *in vitro* chondrocyte culture and evaluated its performance with enhanced mixing at controlled shear stress. They also studied the effects of the hydrodynamic environment on the development of tissue-engineered cartilage. Specifically, they designed a wavy-walled, internal-loop ALR with baffles on the wall of the downcomer and a wavy riser providing more surfaces for the collision of fluid flow to create turbulence. Free chondrocyte cells were grown in the novel ALR for 28 days, and the nutrition media was replaced every week. They observed that the rate of chondrocyte growth increased with respect to that of shake flasks (SF) because of extra shear and good nutrient mass transfer offered by the baffles and the wavy nature of the riser of the ALR.

In addition, this study demonstrated that, compared with shake flasks, the engineered ALR provided a culture environment that favored higher GAG (Fig. 3.10) and collagen content for chondrocyte growth, likely due to the homogeneous hydrodynamics and type of mass transfer in the bioreactor.

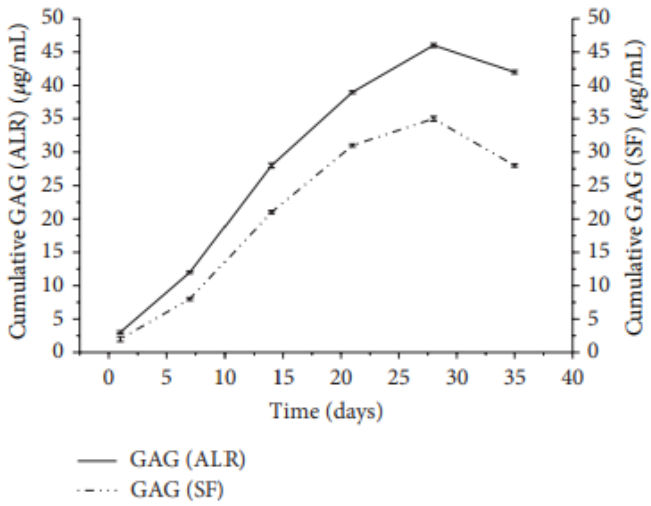

Figure 3.10 Cumulative GAG content in chondrocytes versus time (days) for ALR and SF systems. (Patil et al., 2013)

Similarly, Mallick et al. (Mallick et al., 2017) studied the strategies for cartilage tissue regeneration using a porous scaffold in a wavy walled airlift bioreactor (ALBR). By using a chitosan/poly (L-lactide)/hyaluronic acid (PLLA/chitosan/HA) composite scaffold, they evaluated the uniform chondrocyte distribution into the scaffold located in the shake flask and ALBR and performed glycosaminoglycans (GAG) quantification and proliferation

assay. From their cell culture studies, chondrocytes proliferate better in the porous scaffold when using an airlift bioreactor as a dynamic system instead of a culture plate or shake flask (Fig. 3.11).

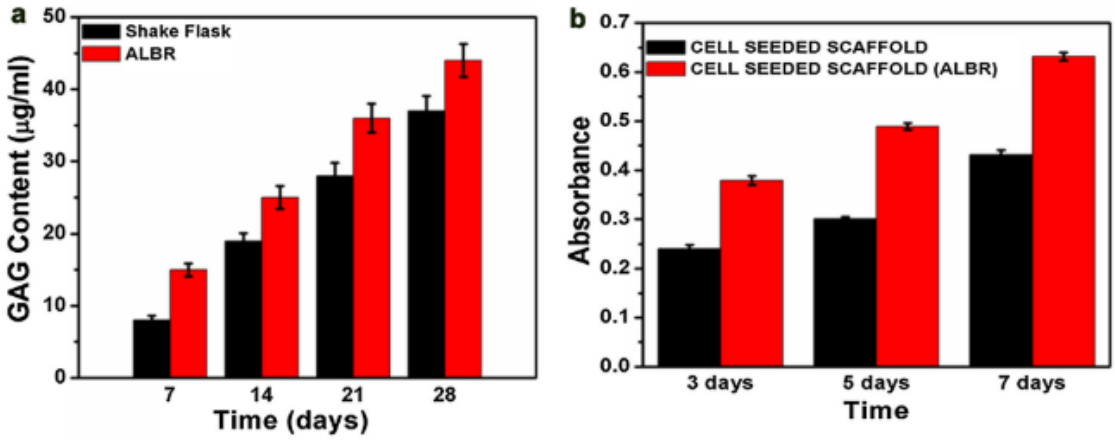

Figure 3.11 a) GAG content for shake flask and ALBR and b) proliferation assay for cell-seeded scaffold (with and without ALBR) (Mallick et al., 2017)

Li et al. (Li et al., 2008) cultured and expanded MSCs in hypoxic, three-dimensional, and dynamic conditions in vitro using an airlift loop hollow fiber membrane bioreactor (ALHFMB). Their results showed that O_2 concentration was kept constant in the ALHFMB where MSCs metabolized robustly and expanded about 50-fold within 7 days in hypoxic conditions (more than in normoxic conditions). Moreover, after being induced, the expanded cells preserved the strong muti-differentiation potential for becoming bone, cartilage, and adipose tissue.

3.3 Dual flow perfusion bioreactors

In the TE field, dual-flow bioreactors can be interpreted as bi-directional flow or biparallel flow bioreactors. In the first case, the flow runs in two different directions; in the second case, fluids move in identical directions and are separated by a wall flow.

Bi-directional continuous perfusion bioreactors have been developed for supporting the 3D growth of cells in scaffold materials. Unlike the conventional perfusion systems, bi-directional bioreactors, in addition to providing directional control of the culture medium, supply an additional direction that enhances the exchange of nutrients and the removal of metabolic products. Hence, these bioreactors can overcome the limitations of conventional systems concerning the possibility of growing only small 3D supports.

In this context, Gardel et al. (Gardel et al., 2013, 2014) designed an innovative, bi-directional flow perfusion bioreactor (BCPB) to enable the culture of large constructs, envisioning the regeneration of critical-sized defects. The bioreactor consists of a rigid tube, where the

scaffold is inserted, with perforations in the central part equivalent to the length of the 3D scaffold used. This tube is connected to a circular system, promoting medium flow from inside to outside or inwards the 3D medium. It is coaxially placed inside a single-cell culture chamber with hermetically sealed inlets/outlets. This chamber is connected to the same circular system, resulting, therefore, responsible for controlling the flow and the pressure gradient within the chamber and the perforated tube. Fig. 3.12 describes the circuit of the flow system of the designed bidirectional bioreactor. The functionality of BCPB was preliminarily evaluated in bone tissue engineering by culturing goat bone marrow stromal cells in starch–polycaprolactone scaffolds for 14 and 21 days (Gardel et al., 2013). Their results showed higher ALP levels in the bioreactor cultures than those obtained under static conditions. On the other hand, the number of cells emerged lower in constructs cultured in the bioreactor compared to static cultures, suggesting that dynamic conditions tend to privilege osteogenic differentiation over cellular proliferation.

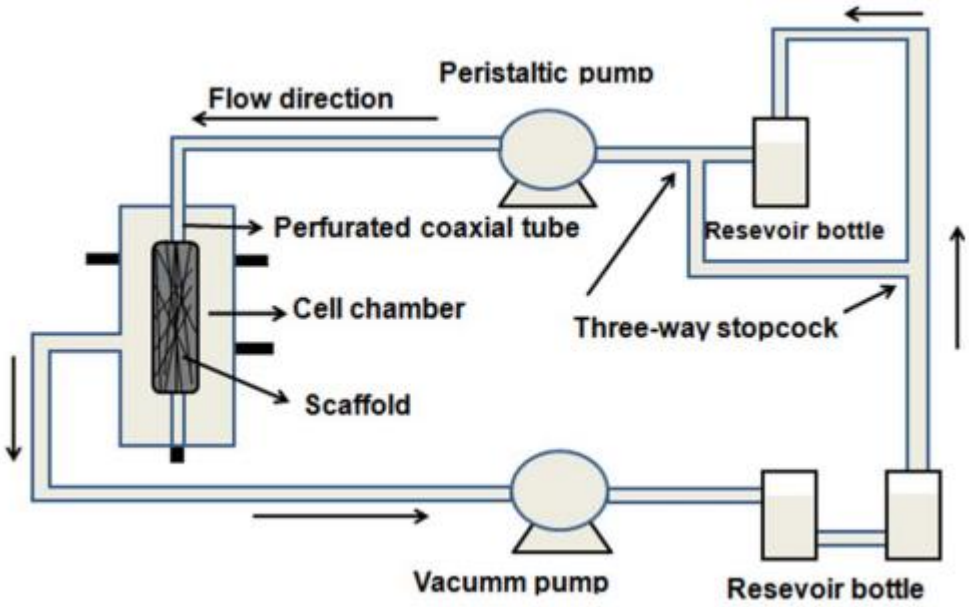

Figure 3.12 Schematic representation of the flow system "circuit" that is associated with the continuous bidirectional flow bioreactor (Gardel et al., 2013)

For another *in vitro* experiment (Gardel et al., 2014), this research group used the same blend of starch with polycaprolactone (SPCL) as scaffolds and seeded them with goat bone marrow stromal cells (GBMSCs). The seeded constructs were cultured using the designed bioreactor for 14 days and then implanted into 42-mm-sized defects in a tibial goat model for 12 weeks. Bioreactor culture with an osteogenic medium allowed early osteogenic differentiation of cells into SPCL scaffolds. The histology analysis and morphometric measurements demonstrated increased new bone formation in the perfusion-cultured scaffolds. These

results suggest that GBMSCs–SPCL constructs cultured under this flow perfusion bioreactor exhibit a higher osteogenic potential *in vitro* and *in vivo.*

In a recent work by Talò et al. (Talo`, et al.), a custom-made oscillating stretch-perfusion bioreactor (OSBP) was developed for lodging tendon constructs. It consists of multiple independent culture chambers able to combine bidirectional oscillatory perfusion with an intermittent, uniaxial strain. Although this system exploits perfusion principles, it lacks complex circuitry and a perfusion pumping system to create the bidirectional flow. In this study, decellularized tendon matrices were seeded with MSCs, exposed to bidirectional perfusion, and stretched at a programmed cycle throughout a 7-day culture. During the experiment, the control system was set to alternate a cyclic strain and perfusion phase with a rest phase during which only the perfusion was active. From their findings, the developed OSPB allowed increasing nutrient supply for cell metabolism and the elongated distribution of cells onto the construct surface.

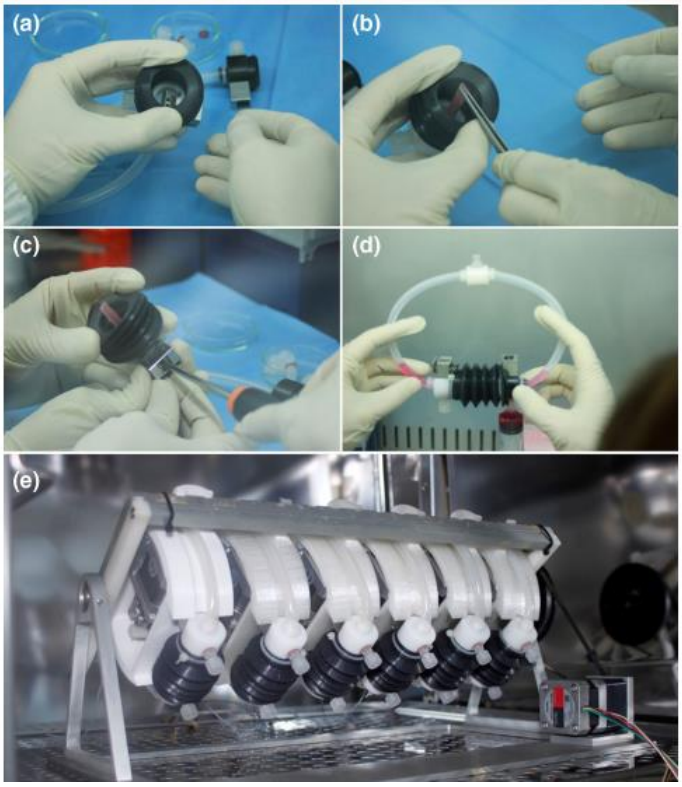

Figure 3.13 Assembly of the OSPB chamber and final system. (a); (b) the construct was firmly fixed in the clamp using tweezers; (c) the two clamps located on both sides of the chamber were activated thanks to an external screw with a screwdriver; (d) the chamber was closed and filled with culture medium; (e) complete OSPB system consisting in six separate chambers mounted on the OPB oscillating platform and placed in a standard cell culture incubator. (Talo`, et al.)

Similarly, Mayer et al. (Mayer et al., 2014) designed an oscillating bidirectional perfusion bioreactor (OPB) for engineering articular cartilage *in vitro* by using collagen sponges and human articular chondrocytes (HACs). In this system (Fig. 3.14), a scaffold holder is inserted

in a chamber attached to a loop of gas-permeable silicone rubber. Eighteen closed-loop chambers are mounted on discs and then on an incubator-compatible motorized frame oscillating the chambers around their central axis. Compared to static culture, this bidirectional system was found preferable for cell distribution and homogeneity of the neo-synthesized matrix. Moreover, the results demonstrate that perfusion stimulates the construction of a neo-matrix that matures over time with type II collagen at the expense of type I collagen, consistent with other studies on cartilage TE.

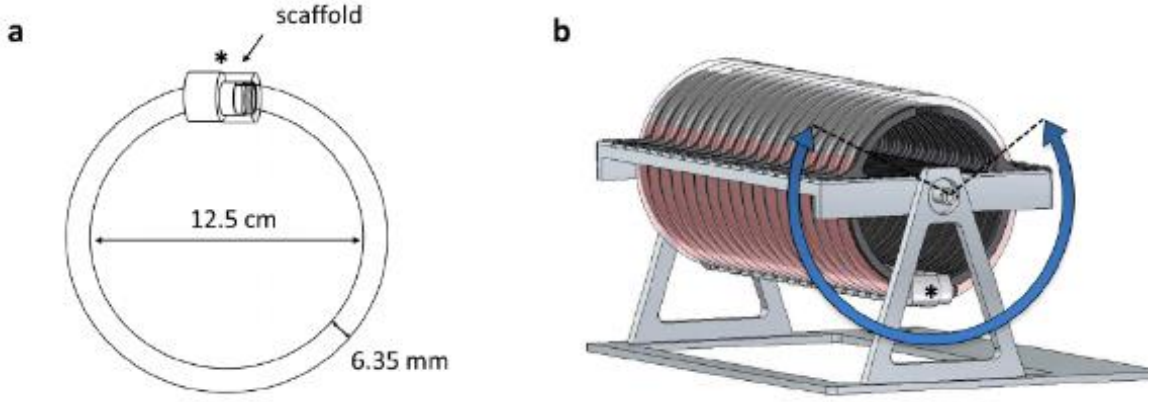

Figure 3.14 The Oscillating Perfusion Bioreactor (OPB). (a) The tissue culture unit is a closed loop of gas-permeable silicone tubing connected to a chamber (asterisk). A single collagen sponge is fixed within a scaffold holder inserted in the chamber to avoid fluid flow around the construct. (b) Eighteen independent closed-loop chambers are mounted on a motorized frame oscillating the chambers around their central axis in a pendulum-like motion (Mayer et al., 2014).

In the bone TE field, Beşkardeş et al. (Beşkardeş et al., 2017) dynamically co-cultured human osteoblasts and osteoclasts in a chitosan-HA scaffold. In their bioreactor set-up (Fig. 3.15), bidirectional perfusion was applied with recycling of the medium through 6 chambers designed to contain porous cylindrical scaffolds by means of a programmable multichannel syringe pump with eight channels. Overall, the system perfusion provided a two-way flow with recycling and ensured both sides of the tissue scaffold were cultured under similar conditions in terms of mechanical force. From their results, when compared with static culture, perfusion enhanced transport properties and flow-based mechanical stimulation, promoting higher cellularity, ECM production, and extension of differentiation.

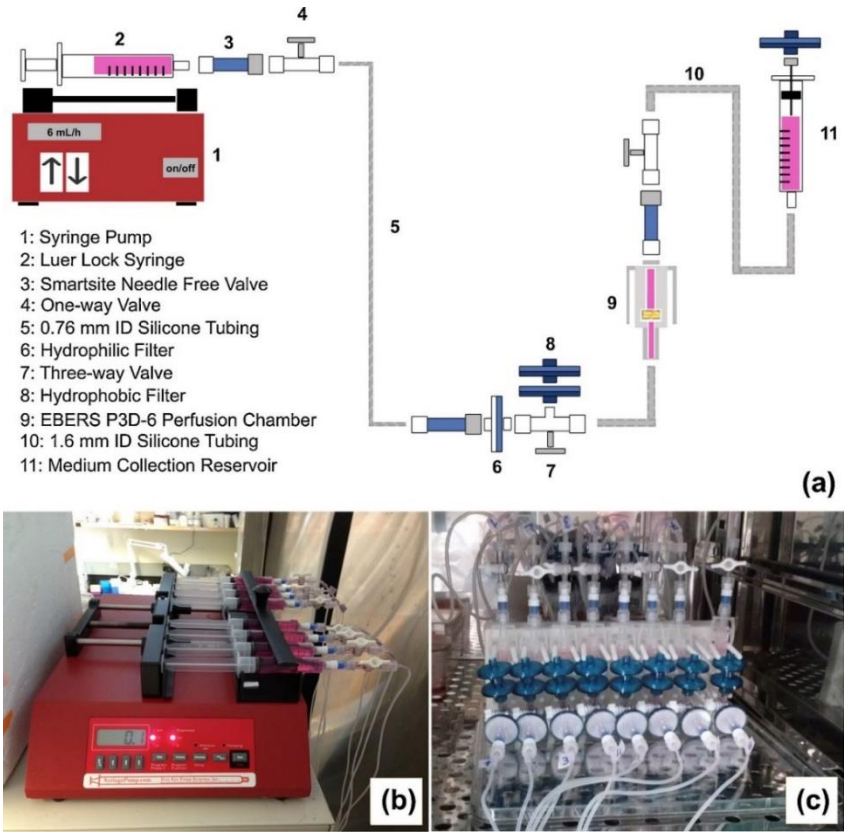

Figure 3.15 (a) Perfusion bioreactor set-up scheme for bidirectional recycled flow system. Pictures of bioreactor set-up: (b) syringe pump set to deliver 6 mL/h (bidirectional flow), (c) bioreactor system in CO_2 incubator (Beşkardeş et al., 2017).

Navarro et al. (Navarro et al., 2019) also used a perfusion approach for the simultaneous culture of cell lines. In their study, a dual-chamber bioreactor (DCB) integrating a membrane was designed to study 3D stratified cell populations for skin tissue engineering. In the DCB, two parallel flow inlets connect to a common chamber, followed by two flow outlets (Figure 3.16).

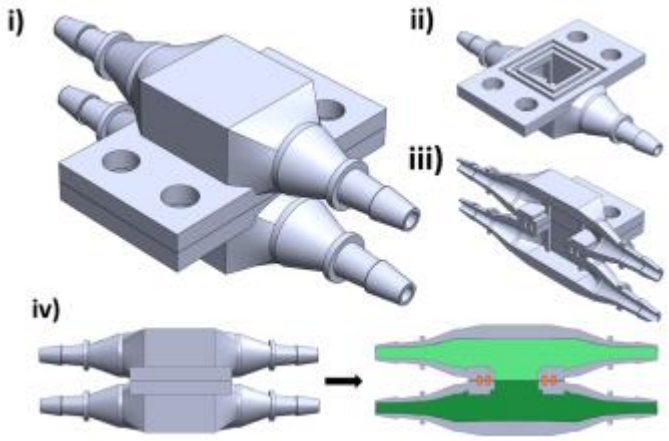

Figure 3.16 (i) The DCB is composed of two equal master parts that can be sealed together; (ii) the master parts is composed of an inlet, an outlet, and an open centerpiece, as well as including guide channels for

sealing gaskets; (iii, iv) when combined, the cross-section reveals a common chamber that provides an interface for communication between the two flow lines (Navarro et al., 2019).

They hypothesized that including a degradable membrane in the DCB's common chamber could regulate flow profiles and separation of cell populations without impeding cell populations separated to communicating with each other. Their experiments were performed using two different media on the same type of cells, hMCSs, to confirm that the bioreactor system allows biomolecular diffusion between its chambers. They used adipogenic media and regular growth media, evaluating the diffusion of adipogenic factors by quantifying intracellular lipids deposited by hMSCs in both directions of perfusion compared with an undifferentiated 2D population. The resulted data demonstrated that the DCB can perfuse two adjacent layers with different media, allowing communication between the layers via diffusion through the membrane.

A similar apparatus was developed by Lin et al. (Lin et al., 2014) for osteochondral TE applications. This system is a multi-chamber device that comprises two separate systems for medium flow and compartments for biphasic (osteochondral) constructs (Fig. 3.17).

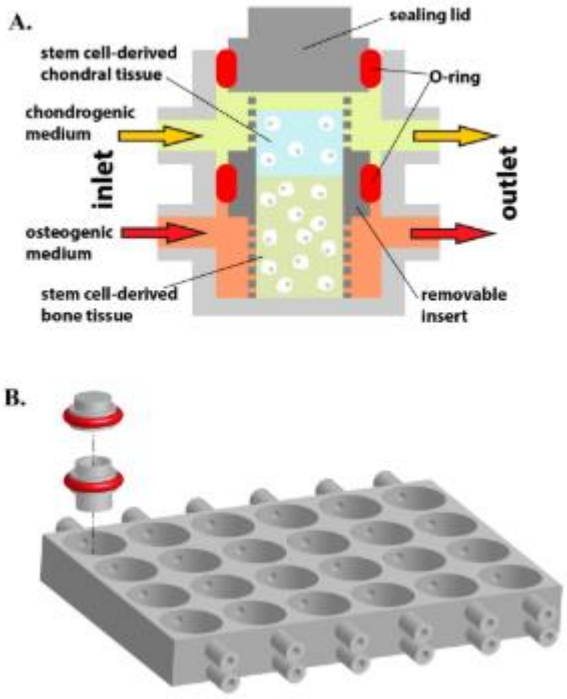

Figure 3.17 Schematic of the bioreactor for in vitro osteochondral engineering. (A) An individual bioreactor is composed of the removable insert (dark gray) within a chamber (light gray) of the microfluidic plate (B) and fixed in place with two O-rings. The osteochondral construct within the insert creates the final separation between the upper and lower medium conduits. Opposing gradients of chondrogenic and osteogenic factors and stimulants will aid in forming an interface. (B) A single bioreactor formed by the inset and lid in the context of a 24-well plate. Red circles indicate the O-rings that seal the joint space between lid/insert and chamber (Lin et al., 2014).

In the context of a 24-well plate, a single bioreactor/compartment is formed by the inset and the lid. O-rings seal the joint space between lid/insert and chamber. When the osteochondral

construct is inserted, either side of the construct is supplied by different medium streams. In this study, the dual-chamber bioreactor has specifically been developed to generate and maintain osteochondral constructs derived from human bone marrow stem cells (hBMSCs). Their results have shown that hBMSCs underwent tissue-specific differentiation in response to the tissue-specific growth media inside the two chambers. The authors also used this bioreactor to observe the effects of perfusion culture on the differentiation of undifferentiated MSCs or predifferentiated chondrocytes and osteocytes (Alexander et al., 2014). Their works showed enhanced integration of the osseous and chondral components of the construct.

Similarly, Xue et al. (Xue et al., 2019) aimed to describe an *in vitro* osteochondral perfusion co-culture system using an additive manufactured, bilayered scaffold inside a dual-chamber bioreactor (Fig. 3.18).). The co-cultured system was studied by co-culturing ATDC5 and MC3T3-E1 cells on the chondral and bone layer of the scaffold, respectively.

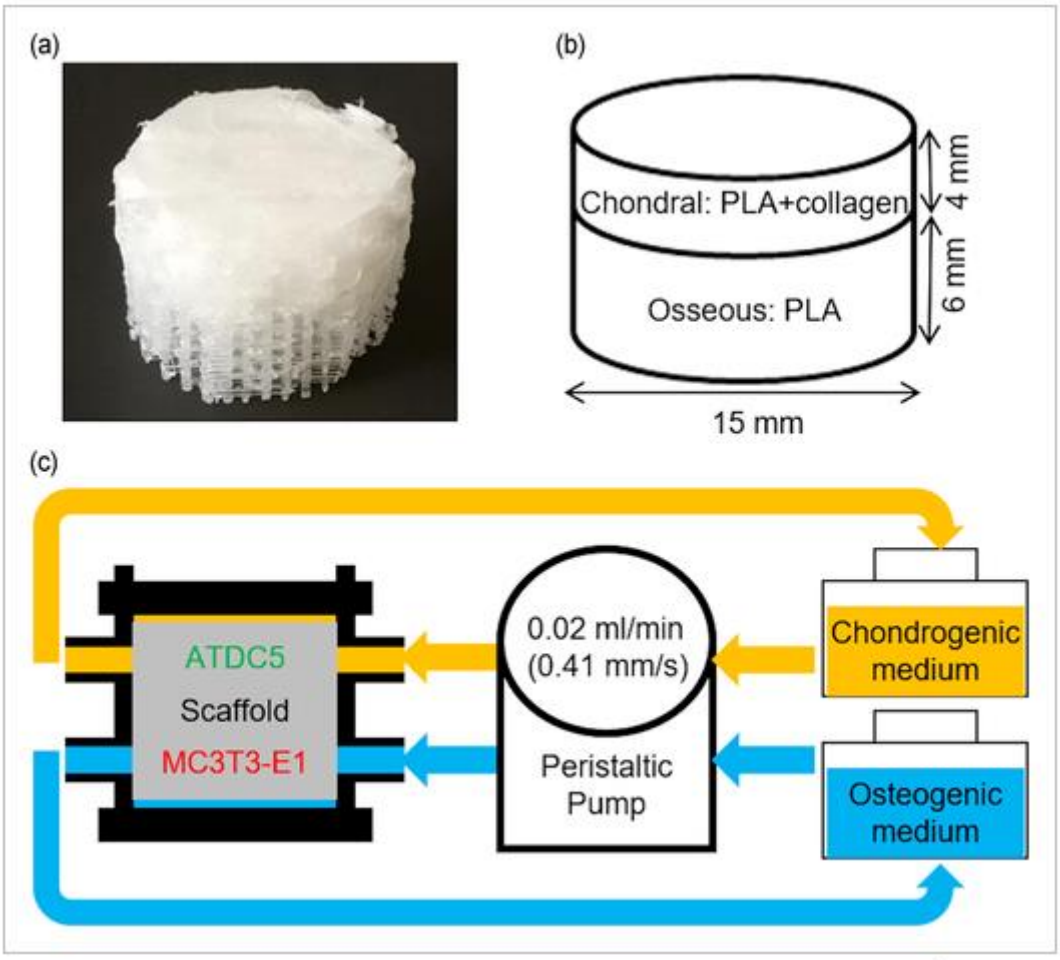

Figure 3.18 (a) Photograph of the bi-layered scaffold. (b) Schematic of scaffold composition and geometry. (c) Schematic of perfusion coculture (Xue et al., 2019)

Chondrogenic and osteogenic media were added to reservoirs connected to the top and bottom of the bioreactor, respectively. For cell viability, proliferation, distribution, and attachment, the microenvironment within the bioreactor during perfusion culture is desirable for the in vitro osteochondral model.

For cartilage TE purposes, a dual flow bioreactor was developed by Spitters et al. (Spitters et al., 2013) to couple mechanical stimulation and nutrients diffusion. This novel system is unique because it incorporates confined cyclic mechanical loading and nutrient supply via diffusion from the top and bottom separately. They successfully cultured cartilage explants and osteochondral plugs in this bioreactor for 2 weeks without significant cell death in the cartilage layers (Fig. 3.19). Moreover, this two-compartment system was proven to create gradients of nutrients and growth factors that can be modulated by applying different concentrations of molecules of interest in each compartment or by changing the orientation of the medium inlets.

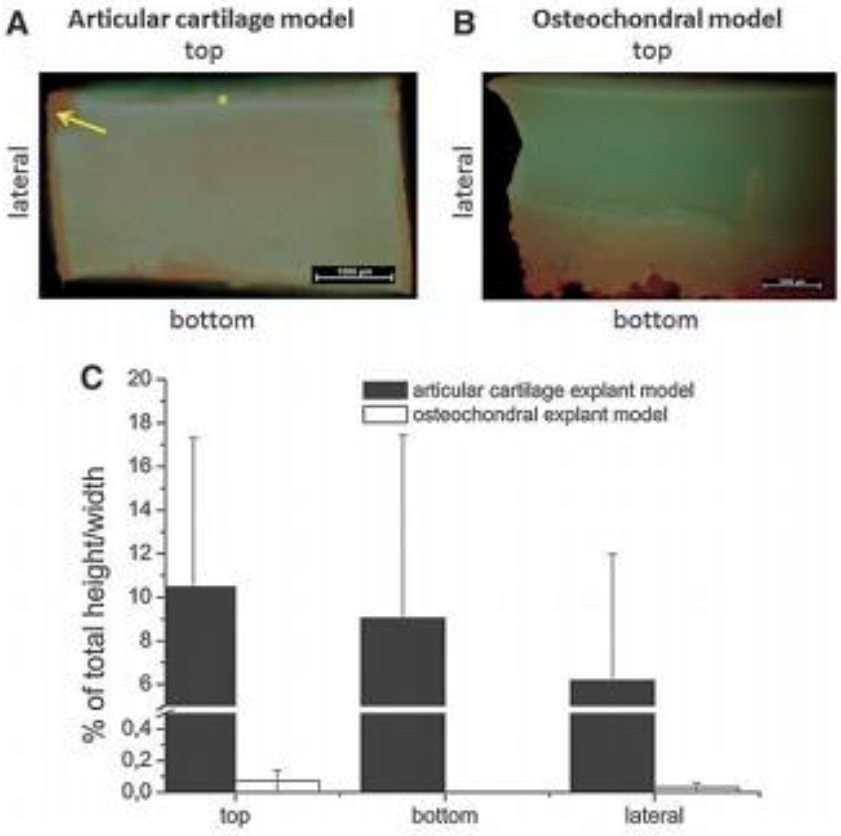

Figure 3.19 Design validation. Live/dead assays were performed on cartilage explants and the cartilage in osteochondral explants after compression (24 h (1-h compression, 7-h rest) with 0.25 MPa compressive load (*2.5% strain) at 0.33 Hz). In both constructs, cell death was only noted in layers at the periphery of the cartilage explants, but not in the center. (A) Live/dead staining of a compressed cartilage explant. The arrow indicates the area where most cell death is observed. The asterisk indicates the top center of the explant. (B) Live/dead staining of a compressed osteochondral explant. The red staining in the lower part of the explant is due to the nonspecific binding of the ethidium homodimer to the mineralized bone matrix. A representative example out of 3 specimens is shown. (C) Quantification of (A) and (B). The thickness of the layers was

measured and expressed as % – standard deviation of the total height at the top or bottom or width of the cartilage explant at the lateral sites. (n = 5 [articular cartilage model], n = 3 [osteochondral model]). (Spitters et al., 2013)

This thesis work developed and evaluated an advanced dual perfusion flow bioreactor with a simple and compact design. This system aims at providing a tunable radial flow throughout the microporous matrix of the inserted scaffold.

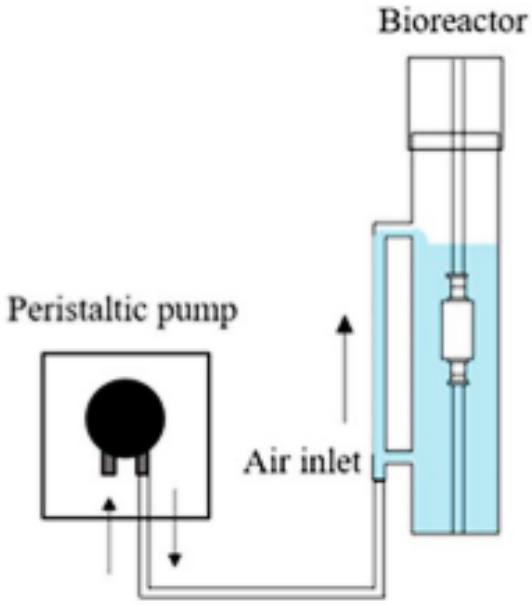

Figure 3.20 Schematic of the developed dual-flow bioreactor with the inserted scaffold (Lombardo et al., 2021)

A deep insight into the characteristics of this apparatus will be provided in further chapters. Notably, the radial perfusion was quantified using both permeability tests and a mathematical model, applying a combination of Darcy's Theory, Bernoulli's Equation, and Poiseuille's Law. The application of this apparatus in the nasal mucosa TE field is also described and discussed.

References

Abdal-hay, A., Khalil, K. A., Hamdy, A. S., and Al-Jassir, F. F. (2017). Fabrication of highly porous biodegradable biomimetic nanocomposite as advanced bone tissue scaffold. *Arab. J. Chem.* 10, 240–252. doi:10.1016/j.arabjc.2016.09.021.

Alexander, P. G., Gottardi, R., Lin, H., Lozito, T. P., and Tuan, R. S. (2014). Three-dimensional osteogenic and chondrogenic systems to model osteochondral physiology and degenerative joint diseases. *Exp. Biol. Med.* 239, 1080–1095. doi:10.1177/1535370214539232.

Beşkardeş, I. G., Aydın, G., Bektaş, Ş., Cengiz, A., and Gümüşderelioğlu, M. (2018). A systematic study for optimal cell seeding and culture conditions in a perfusion mode bone-tissue bioreactor. *Biochem. Eng. J.* 132, 100–111. doi:10.1016/j.bej.2018.01.006.

Beşkardeş, I. G., Hayden, R. S., Glettig, D. L., Kaplan, D. L., and Gümüşderelioğlu, M. (2017). Bone tissue engineering with scaffold-supported perfusion co-cultures of human stem cell-derived osteoblasts and cell line-derived osteoclasts. *Process Biochem.* 59, 303–311. doi:10.1016/J.PROCBIO.2016.05.008.

Bilodeau, K., Couet, F., Boccafoschi, F., and Mantovani, D. (2005a). Design of a perfusion bioreactor specific to the regeneration of vascular tissues under mechanical stresses. *Artif. Organs* 29, 906–912. doi:10.1111/j.1525-1594.2005.00154.x.

Bilodeau, K., Couet, F., Boccafoschi, F., and Mantovani, D. (2005b). Thoughts and Progress: Design of a Perfusion Bioreactor Specific to the Regeneration of Vascular Tissue Under Mechanical tresses. *Artif. Organs* 29, 906–922.

Bonassar, L. J., Grodzinsky, A. J., Frank, E. H., Davila, S. G., Bhaktav, N. R., and Trippel, S. B. (2001). The effect of dynamic compression on the response of articular cartilage to insulin-like growth factor-I. *J. Orthop. Res.* 19, 11–17. doi:10.1016/S0736-0266(00)00004-8.

Cartmell, S., Porter, B., García, A., and Guldberg, R. (2003). Effects of medium perfusion rate on cell-seeded three-dimensional bone constructs in vitro. *Tissue Eng.* 9, 1197–1203. doi:10.1089/10763270360728107.

Chen, H.-C., and Hu, Y.-C. (2014). Bioreactors for tissue engineering. *Springer Biotechnol. Lett.*, 1415–1423. doi:10.1007/s10529-006-9111-x.

Correia, C., Pereira, A. L., Duarte, A. R., Frias, A. M., Pedro, A. J., Oliveira, J. T., et al. (2012). Dynamic Culturing of Cartilage Tissue: The Significance of Hydrostatic Pressure. doi:10.1089/ten.tea.2012.0083.

Courtenay, J., Sharma, R., and Scott, J. (2018). Recent Advances in Modified Cellulose for Tissue Culture Applications. *Molecules* 23, 654. doi:10.3390/molecules23030654.

Du, D., Furukawa, K., and Ushida, T. (2008). Oscillatory perfusion seeding and culturing of osteoblast-like cells on porous beta-tricalcium phosphate scaffolds. *J. Biomed. Mater. Res. A* 86, 796–803. doi:10.1002/JBM.A.31641.

Dvir, T., Benishti, N., Shachar, M., and Cohen, S. (2006). A novel perfusion bioreactor providing a homogenous milieu for tissue regeneration. *Tissue Eng.* 12, 2843–2852. doi:10.1089/ten.2006.12.2843.

Eberli, D. (2011). *Tissue Engineering for tissue and organ regeneration*. Rijeka, Croatia: InTech.

Gardel, L., Afonso, M., Frias, C., Gomes, M., and Reis, R. (2014). Assessing the repair of critical size bone defects performed in a goat tibia model using tissue-engineered constructs cultured in a bidirectional flow perfusion bioreactor: *http://dx.doi.org/10.1177/0885328213519351* 29, 172–185. doi:10.1177/0885328213519351.

Gardel, L. S., Correia-Gomes, C., Serra, L. A., Gomes, M. E., and Reis, R. L. (2013). A novel bidirectional continuous perfusion bioreactor for the culture of large-sized bone tissue-engineered constructs. *J. Biomed. Mater. Res. - Part B Appl. Biomater.* 101, 1377–1386. doi:10.1002/JBM.B.32955.

Gaspar, D. A., Gomide, V., and Monteiro, F. J. (2012). The role of perfusion bioreactors in bone tissue engineering. *Biomatter* 2, 167–175. doi:10.4161/biom.22170.

Gharravi, A. M., Orazizadeh, M., Hashemitabar, M., Ansari-Asl, K., Banoni, S., Alifard, A., et al. (2013). Design and validation of perfusion bioreactor with low shear stress for tissue engineering. *J. Med. Biol. Eng.* 33, 185–192. doi:10.5405/jmbe.1075.

Gomes, M. E., Holtorf, H. L., Reis, R. L., and Mikos, A. G. (2006). Influence of the porosity of starch-based fiber mesh scaffolds on the proliferation and osteogenic differentiation of bone marrow stromal cells cultured in a flow perfusion bioreactor. *Tissue Eng.* 12, 801–809. doi:10.1089/ten.2006.12.801.

Grayson, W. L., Bhumiratana, S., Cannizzaro, C., Chao, P. H. G., Lennon, D. P., Caplan, A. I., et al. (2008). Effects of initial seeding density and fluid perfusion rate on formation of tissue-engineered bone. *Tissue Eng. - Part A.* 14, 1809–1820. doi:10.1089/ten.tea.2007.0255.

Grayson, W. L., Marolt, D., Bhumiratana, S., Fröhlich, M., Guo, X. E., and Vunjak-Novakovic, G. (2011). Optimizing the medium perfusion rate in bone tissue engineering bioreactors. *Biotechnol. Bioeng.* 108, 1159–1170. doi:10.1002/bit.23024.

Hahn, M., McHale, M., Wang, E., Schmedlen, R., and West, J. (2007). Physiologic pulsatile flow bioreactor conditioning of poly(ethylene glycol)-based tissue engineered vascular grafts. *Ann. Biomed. Eng.* 35, 190–200. doi:10.1007/S10439-006-9099-3.

Israelowitz, M., Weyand, B., Rizvi, S., Vogt, P. M., and Von Schroeder, H. P. (2012). Development of a laminar flow bioreactor by computational fluid dynamics. *J. Healthc. Eng.* 3, 455–476. doi:10.1260/2040-2295.3.3.455.

Jaasma, M. J., Plunkett, N. A., and O'Brien, F. J. (2008). Design and validation of a dynamic flow perfusion bioreactor for use with compliant tissue engineering scaffolds. *J. Biotechnol.* 133, 490–496. doi:10.1016/j.jbiotec.2007.11.010.

Karande, T. S., Ong, J. L., and Agrawal, C. M. (2004). Diffusion in musculoskeletal tissue engineering scaffolds: Design issues related to porosity, permeability, architecture, and nutrient mixing. *Ann. Biomed. Eng.* 32, 1728–1743. doi:10.1007/s10439-004-7825-2.

Li, X. Q., Liu, T. Q., Zhu, L., Song, K. D., Ma, X. H., and Cui, Z. F. (2008). Culture and expansion of mesenchymal stem cells in air-lift loop hollow fiber membrane bioreactor. *Gao Xiao Hua Xue Gong Cheng Xue Bao/Journal Chem. Eng. Chinese Univ.* 22, 985–991. doi:10.1038/cr.2008.259.

Lin, H., Lozito, T. P., Alexander, P. G., Gottardi, R., and Tuan, R. S. (2014). Stem Cell-Based Microphysiological Osteochondral System to Model Tissue Response to Interleukin-1β. doi:10.1021/mp500136b.

Lombardo, M., Carfì Pavia, F., Craparo, E., Capuana, E., Cavallaro, G., Brucato, V., et al. (2021). Novel dual-flow perfusion bioreactor for in vitro pre-screening of nanoparticles delivery: design, characterization and testing. *Bioprocess Biosyst. Eng.* 44, 2361–2374. doi:10.1007/S00449-021-02609-4.

Maidhof, R., Tandon, N., Lee, E., Luo, J., Duan, Y., Yeager, K., et al. (2012). Biomimetic perfusion and electrical stimulation applied in concert improved the assembly of engineered cardiac tissue. *J. Tissue Eng. Regen. Med.* 6. doi:10.1002/TERM.525.

Mallick, S. P., Rastogi, A., Tripathi, S., and Srivastava, P. (2017). Strategies on process

engineering of chondrocyte culture for cartilage tissue regeneration. *Bioprocess Biosyst. Eng.* 40, 601–610. doi:10.1007/s00449-016-1724-4.

Martin, I., Wendt, D., and Heberer, M. (2004). The role of bioreactors in tissue engineering. *Trends Biotechnol.* 22, 80–86. doi:10.1016/j.tibtech.2003.12.001.

Mayer, N., Silvia, L., Talò, G., Lovati, A. B., Riboldi, S. A., Moretti, M., et al. (2014). The use of a bi-directional perfusion bioreactor for cartilage engineering promotes the reconstruction of hyaline cartilage. *Osteoarthr. Cartil.* 22, S487. doi:10.1016/J.JOCA.2014.02.925.

McCoy, R. J., and O'Brien, F. J. (2010). Influence of shear stress in perfusion bioreactor cultures for the development of three-dimensional bone tissue constructs: A review. *Tissue Eng. - Part B Rev.* 16, 587–601. doi:10.1089/ten.teb.2010.0370.

Merchuk, J. C., and Gluz, M. (2013). BIOREACTORS, AIR-LIFT REACTORS. *Encycl. Ind. Biotechnol. Bioprocess, Biosep. Cell Technol.*

Merrill, E. W., Benis, A. M., Gilliland, E. R., Sherwood, T. K., and Salzman, E. W. (1965). Pressure-flow relations of human blood in hollow fibers at low flow rates. *J. Appl. Physiol.* 20, 954–967. doi:10.1152/jappl.1965.20.5.954.

Mitra, D., Whitehead, J., Yasui, O. W., and Leach, J. K. (2017). Bioreactor Culture Duration of Engineered Constructs Influences Bone Formation by Mesenchymal Stem Cells. *Biomaterials* 146, 29. doi:10.1016/J.BIOMATERIALS.2017.08.044.

Mun, C. H., Jung, Y., Kim, S.-H., Kim, H. C., and Kim, S. H. (2013). Effects of Pulsatile Bioreactor Culture on Vascular Smooth Muscle Cells Seeded on Electrospun Poly (lactide-co-ε-caprolactone) Scaffold. *Artif. Organs* 37, E168–E178. doi:10.1111/AOR.12108.

Murphy, C. M., O'Brien, F. J., Little, D. G., and Schindeler, A. (2013). Cell-scaffold interactions in the bone tissue engineering triad. *Eur. Cells Mater.* 26, 120–132. doi:10.22203/ECM.V026A09.

Navarro, J., Swayambunathan, J., Janes, M. E., Santoro, M., Mikos, A. G., and Fisher, J. P. (2019). Dual-chambered membrane bioreactor for coculture of stratified cell populations. *Biotechnol. Bioeng.* 116, 3253–3268. doi:10.1002/bit.27164.

Patil, H., Chandel, I. S., Rastogi, A. K., and Srivastava, P. (2013). Studies on a Novel Bioreactor Design for Chondrocyte Culture. *Int. J. Tissue Eng.* 2013, 1–7. doi:10.1155/2013/976894.

Pham, N. H., Voronov, R. S., Vangordon, S. B., Sikavitsas, V. I., and Papavassiliou, D. V. (2012). Predicting the stress distribution within scaffolds with ordered architecture. *Biorheology* 49, 235–247. doi:10.3233/BIR-2012-0613.

Pisanti, P., Yeatts, A. B., Cardea, S., Fisher, J. P., and Reverchon, E. (2012). Tubular perfusion system culture of human mesenchymal stem cells on poly- L- Lactic acid scaffolds produced using a supercritical carbon dioxide-assisted process. *J. Biomed. Mater. Res. - Part A* 100 A, 2563–2572. doi:10.1002/jbm.a.34191.

Porter, B., Zauel, R., Stockman, H., Guldberg, R., and Fyhrie, D. (2005). 3-D computational modeling of media flow through scaffolds in a perfusion bioreactor. *J. Biomech.* 38, 543–549. doi:10.1016/j.jbiomech.2004.04.011.

Pourchet, L., Petiot, E., Loubière, C., Olmos, E., Dos Santos, M., Thépot, A., et al. (2018). Large 3D Bioprinted Tissue: Heterogeneous Perfusion and Vascularization. *Bioprinting* 13, 1–7. doi:10.1016/j.bprint.2018.e00039.

Pu, F., Rhodes, N. P., Bayon, Y., Chen, R., Brans, G., Benne, R., et al. (2010). The use of flow perfusion culture and subcutaneous implantation with fibroblast-seeded PLLA-collagen 3D scaffolds for abdominal wall repair. *Biomaterials* 31, 4330–4340. doi:10.1016/j.biomaterials.2010.02.010.

Rauh, J., Milan, F., Günther, K. P., and Stiehler, M. (2011). Bioreactor systems for bone tissue engineering. *Tissue Eng. - Part B Rev.* 17, 263–280. doi:10.1089/TEN.TEB.2010.0612.

Ru Choi, J., Wey Yong, K., Yu Choi, J., and Jane Ru Choi, C. (2017). Effects of mechanical loading on human mesenchymal stem cells for cartilage tissue engineering. *J. Cell. Physiol.* 233, 1913–1928. doi:10.1002/jcp.26018.

Saltzman, W. M. (2004). *Tissue engineering: engineering principles for the design of replacement organs and tissues*. Oxford, UK: Oxford University Press Available at: http://books.google.com/books?id=KorDMxtkZ_wC&pgis=1.

Sandino, C., and Lacroix, D. (2011). A dynamical study of the mechanical stimuli and tissue differentiation within a CaP scaffold based on micro-CT finite element models. *Biomech. Model. Mechanobiol.* 10, 565–576. doi:10.1007/s10237-010-0256-0.

Schmid, J., Schwarz, S., Meier-Staude, R., Sudhop, S., Clausen-Schaumann, H., Schieker, M., et al. (2018). A perfusion bioreactor-system for cell seeding and oxygen-controlled cultivation of 3D-cell cultures. *Tissue Eng. Part C Methods*, ten.TEC.2018.0204. doi:10.1089/ten.TEC.2018.0204.

Seddiqi, H., Saatchi, A., Amoabediny, G., Helder, M. N., Abbasi Ravasjani, S., Safari Hajat Aghaei, M., et al. (2020). Inlet flow rate of perfusion bioreactors affects fluid flow dynamics, but not oxygen concentration in 3D-printed scaffolds for bone tissue engineering: Computational analysis and experimental validation. *Comput. Biol. Med.* 124, 103826. doi:10.1016/J.COMPBIOMED.2020.103826.

Song, L., Zhou, Q., Duan, P., Guo, P., Li, D., Xu, Y., et al. (2012). Successful Development of Small Diameter Tissue-Engineering Vascular Vessels by Our Novel Integrally Designed Pulsatile Perfusion-Based Bioreactor. *PLoS One* 7, e42569. doi:10.1371/JOURNAL.PONE.0042569.

Spencer, T. J., Hidalgo-Bastida, L. A., Cartmell, S. H., Halliday, I., and Care, C. M. (2013). In silico multi-scale model of transport and dynamic seeding in a bone tissue engineering perfusion bioreactor. *Biotechnol. Bioeng.* 110, 1221–1230. doi:10.1002/bit.24777.

Spitters, T. W. G. M., Leijten, J. C. H., Deus, F. D., Costa, I. B. F., Van Apeldoorn, A. A., Van Blitterswijk, C. A., et al. (2013). A dual flow bioreactor with controlled mechanical stimulation for cartilage tissue engineering. *Tissue Eng. - Part C Methods* 19, 774–783. doi:10.1089/TEN.TEC.2012.0435.

Stephens, J. S., Cooper, J. A., Jr., F. R. P., and Dunkers, J. P. (2007). Perfusion Flow Bioreactor for 3D In Situ Imaging: Investigating Cell/Biomaterials. *Biotechnol. Bioeng.* 97, 952–961. doi:10.1002/bit.

Talo`, G., Talo`, T., D'arrigo, D., Lorenzi, S., Moretti, M., and Lovati, A. B. Bioengineering and Enabling Technologies Independent, Controllable Stretch-Perfusion Bioreactor Chambers to Functionalize Cell-Seeded Decellularized Tendons. doi:10.1007/s10439-019-02257-6.

Tandon, N., Taubman, A., Cimetta, E., Saccenti, L., and Vunjak-Novakovic, G. (2013). Portable bioreactor for perfusion and electrical stimulation of engineered cardiac tissue. *Annu. Int. Conf. IEEE Eng. Med. Biol. Soc. IEEE Eng. Med. Biol. Soc. Annu. Int. Conf.* 2013, 6219–6223. doi:10.1109/EMBC.2013.6610974.

Vetsch, J. R., Betts, D. C., Müller, R., and Hofmann, S. (2017). Flow velocity-driven differentiation of human mesenchymal stromal cells in silk fibroin scaffolds: A combined experimental and computational approach. *PLoS One* 12, e0180781. doi:10.1371/journal.pone.0180781.

Visone, R., Talò, G., Lopa, S., Rasponi, M., and Moretti, M. (2018). Enhancing all-in-one bioreactors by combining interstitial perfusion, electrical stimulation, on-line monitoring and

testing within a single chamber for cardiac constructs. *Sci. Reports 2018 81* 8, 1–13. doi:10.1038/s41598-018-35019-w.

Xue, R., Chung, B., Tamaddon, M., Carr, J., Liu, C., and Cartmell, S. H. (2019). Osteochondral tissue coculture: An in vitro and in silico approach. *Biotechnol. Bioeng.* 116, 3112–3123. doi:10.1002/bit.27127.

Chapter 4

Modeling perfusion bioreactors: from mathematical equations to computational methods

Cell fate is strongly influenced by phenomena occurring in bioreactors systems. Hence, improving their fundamental conditions is a prerequisite to translating bioreactor technology to clinical application. However, the design of bioreactors has been generally based on an experimental trial-and-error approach, thus lacking a quantitative assessment and efficient prediction of relevant parameters.

In this context, modeling methods are promising tools to study and predict biochemical and biophysical phenomena at the macro- or micro-scale. Modeling can serve either as a method to test hypotheses or as a tool for obtaining quantitative predictions about the state of a system. Models and simulations can support expensive and time-consuming trial-and-error procedures, highlighting different aspects of the same instance. Of course, the choice of a model depends on the problem, the purpose, and the investigator's intention.

In this chapter, the current strategies for modeling perfusion bioreactor systems (i.e., mathematical and computational approaches) are discussed and investigated. In particular, the focus is on the two major model components: (1) flow and pressure profiles and resulting mechanical forces; (2) nutrient distribution, time-dependent mass transport, and consumption by the cells/tissue.

4.1 Mathematical modeling

Mathematical modeling is commonly used to study and optimize specific aspects of tissue engineering systems and components, such as the chemical, physical and biological parameters (Dvir et al., 2006). The primary consideration is choosing the appropriate equations to model these components in a correct geometry under imposed initial and boundary conditions. Then, the model can provide quantitative information about inside the analyzed system (Jeong et al., 2012). Usually, while using mathematical models, robust calibration of simulation parameters by means of experimental data is required. Indeed, it is essential to underline that those models are only approximations of reality. This aspect implies that their results should be validated experimentally, i.e., by comparing relevant

quantitative parameters that are accessible by both mathematical and experimental approaches (Maidhof et al., 2012).

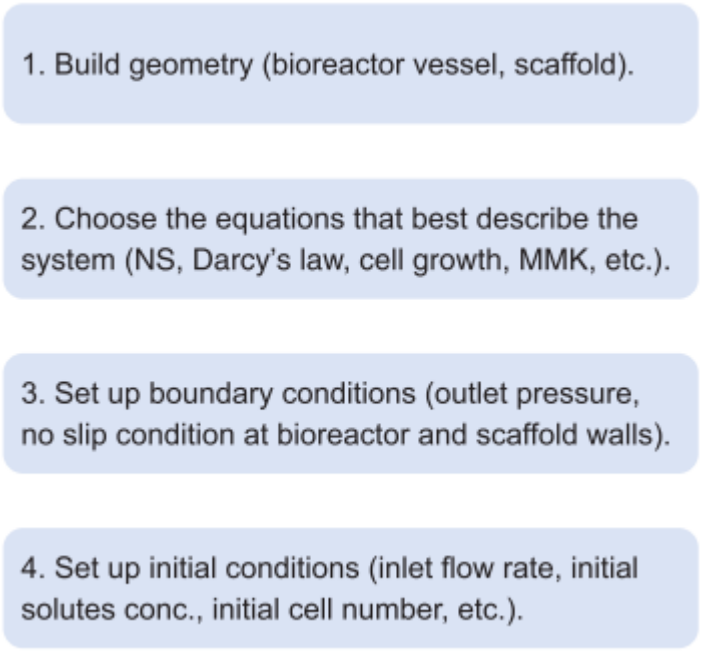

Figure 4.1 Essential stages required to set up a basic functional mathematical model of a dynamic culture: (1) building the geometry of the investigated system; (2) choosing the system of equations to describe the culture; (3) and (4) imposing the appropriate initial and boundary conditions (Burova et al., 2019).

The mathematical representation mainly relies on continuum models that provide the average behavior of the system, studying the fluid dynamics theory with the Navier–Stokes equations (Burova et al., 2019). Hence, while considering the system as a continuum, the position and velocity are assumed to be average quantities over some local regions. Continuum models usually find the solution of governing equations by means of partial differential systems, which sometimes can be solved by classical applied mathematics techniques such as asymptotic approximations. When using these models, experimental and modeling approaches can adopt some simplifying assumptions. However, continuous models lack local data, which is noteworthy when spatial inhomogeneity has a crucial effect on cell response (Vetsch et al., 2015).

Overall, modeling provides a methodical manner to test hypotheses that explain empirical observations and determine the main drivers of a specific phenomenon.

In the context of bioreactors, convection flow is the most challenging to characterize (Grayson et al., 2011). It regulates both nutrient delivery and the shear force exerted by the fluid and experienced by the cells, affecting tissue development. Mathematical solutions can model the convection regime within the bioreactor to optimize nutrient supply and mechanical stimulation in the culture. For instance, increasing the flow rate to enhance mass

transport should be balanced against potential cellular damage resulting from excessive flow shear stresses (Martin and Vermette, 2005). Shear stress, the mechanical force that causes deformation along the plane parallel to the stress direction, is considered a crucial cause of cell damage/death (Nair et al., 2009; Blaeser et al., 2016).

4.1.1 Modelling flow and pressure profiles

To quantify the fluid dynamics of a perfusion bioreactor, continuum models use the Navier-Stokes equations for mass conservation (Eq. 4.1) and moment conservation (Eq. 4.2):

$$\frac{\partial \rho}{\partial t} + \nabla \cdot (\rho u) = 0 \qquad (4.1)$$

$$\rho \left(\frac{\partial u}{\partial t} + u \cdot \nabla u\right) = \rho g - \nabla p + \mu \nabla^2 u \qquad (4.2)$$

These equations allow describing the flow of free culture media, where u (m/s) is the velocity vector, ρ (kg/m^3) is the density, ρg is the body force due to gravity, p (Pa) is the pressure, and μ (Pa·s) is the viscosity (Chung et al., 2007). Specifically, the left-hand side of Eq. 4.2 defines the inertial forces: its first term describes the time-dependent change of momentum, and the second one that due to convection. On the other hand, the right-hand side of that equation includes external forces, such as the body force due to gravity, the pressure force, and the viscous force, respectively.

On considering culture media being incompressible and Newtonian, the fluid velocity u in the bulk fluid can be described by the continuity equation (Eq. 4.3):

$$\nabla \cdot u = 0 \qquad (4.3)$$

The initial and boundary conditions need to be prescribed to solve equations and obtain the velocity field (u) and the pressure. When modeling a bioreactor, the fluid velocity is initially zero (u = 0) in the chamber. At the inlet, the velocity profile is assumed at a magnitude derived from the volumetric flow rate (Q), which can be controlled in experimental testing. Finally, conditions of zero pressure (p = 0) at the outlet and no-slip (u = 0) are usually imposed on all interior walls (Hyndman et al., 2020).

Modeling the mechanical environment due to fluid flow and its effect on cellular behavior

Once the flow profile has been estimated, it can be used to determine the fluid shear stress exerted on the cells or the scaffold walls.

In a simplified model, to determine shear stress imparted to cells at the beginning of a perfused culture, the geometry of the scaffolds can be modeled as a bundle of identical hollow cylinders arranged in parallel to form channels oriented along the flow (Grayson et al., 2008). Hence, the correlation of the mean wall shear stress τ_w with pore size for a linear flow velocity is given by:

$$\tau_w = \frac{8\,\mu\,u}{\varepsilon\,d_c} \qquad (4.4)$$

Where ε is the scaffold porosity, u is the mean superficial velocity, and d_c is the diameter of the modeled channels. The velocity u can be calculated by knowing the entrance flow rate and the geometry of the bioreactor chamber. However, this model is highly simplified, so that is generally used in experimental studies to evaluate the order of magnitude of the imposed shear stress in a specific set-up (Goldstein et al., 2001; Lujan et al., 2011; Zermatten et al., 2014). In addition, the idealization of the scaffold geometry leads to an overestimated average shear stress. A more detailed description of shear stress calculation in an accurate scaffold morphology will be provided in Chapter 7, describing the modeling of perfusion in porous media.

In a more detailed mathematical modeling, the total wall shear stress (WSS) at any position of the bioreactor can be calculated by:

$$WSS = \sqrt{\tau_{xy}^2 + \tau_{xz}^2 + \tau_{yz}^2} \qquad (4.5)$$

Each term of this equation can be determined by applying Newton's equation (Eq. 4.6) for the three components of velocity in the appropriate x, y, and z directions:

$$\tau = \mu\,\dot{\gamma} \qquad (4.6)$$

Where $\dot{\gamma}$ is the shear rate (i.e., $\dot{\gamma}_{xz}$ is the velocity gradient $\frac{\partial v_x}{\partial y}$, with the velocity in the x-direction varying along the y-direction) representing the rate of shear deformation (Cerrada, 2005).

It is necessary to declare that several studies have shown that shear stress plays a fundamental role in controlling cellular proliferation and functions. Blaeser et al. (Blaeser et al., 2016) showed that moderate levels of shear stress could even stimulate cell proliferation, while this effect is reversed when a certain stress threshold is exceeded. Moreover, it was found that shear stress drives stem cell differentiation towards lineages that experience high mechanical forces *in vivo*, such as endothelial and bone-producing cell types (Zhao et al.,

2007; Dong et al., 2009). Concerning mathematical modeling, most cell damage laws are based on a power-law function that relates the percentage of cell damage (CD%) to shear stress τ:

$$CD\% = k\tau^a \qquad (4.7)$$

This equation was proposed in 1965 by Blackshear et al. (Blackshear et al., 1965) and later improved by Grigioni et al., taking into consideration the effect of exposure time of cells to shear forces and the non-damage stress the cells can survive (τ_0) (Grigioni et al., 2005):

$$CD\% = k(\tau - \tau_0)^a t^b \qquad (4.8)$$

Parameters a, b, and k are determined experimentally for each cell type.

4.1.2 Modelling mass transport

During *in vitro* culture, mass transport can occur from convection and diffusion. Perfusion flow of the culture medium induces convective effects that trigger relatively faster mass transfer resulting from the movement of the bulk fluid. Due to limitations related to the diffusion regime (where component molecules undergo a slow motion in the direction of the concentration gradient), some regions in the scaffold may present depletion in oxygen and nutrients. Dynamic culture conditions reduce this issue, and mathematical models are suitable to quantify the effect of culture medium flow on mass transport. When considering the domain bioreactor, the model equation for calculating the mass transfer of the i-specie is described by the convection-diffusion equation (Coletti et al., 2006):

$$\frac{\partial c_i}{\partial t} = -(\nabla \cdot c_i u) + \nabla \cdot (D_i \nabla c_i) \qquad (4.9)$$

Where c_i is the concentration of the i-specie, D_i its diffusion coefficient and u is the convective velocity. In this case D_i is constant (Magrofuoco et al., 2019). Whether nutrient transport is dominated by diffusion or convection depends on the relation between the diffusion coefficient of the nutrient *D* and the medium flow velocity u. This relation is described in the dimensionless Péclet number, involving the characteristic length L, the diffusion coefficient *D*, and the convective velocity u:

$$Pe = \frac{L\,u}{D} \qquad (4.10)$$

From this definition, when Pe >> 1, convection prevails over diffusion (Rouwkema et al., 2009). Of course, the contribution of perfusion to nutrient transport is directly related to the velocity of the medium u.

It must be mentioned that during the *in vitro* culture, the formation of the extracellular matrix of tissues can result in the densification of the tissue, inducing the perfusion of the medium through the tissue becomes problematic over time. This phenomenon again can result in nutrient limitations despite the dynamic culture (Hossain et al., 2015).

Modeling consumption by the cells/tissue

When considering the scaffold domain inside a perfusion bioreactor, the presence of cells consuming nutrients and oxygen (or producing metabolites) changes Eq. 4.9 in a way where a consumption term is also included (Coletti et al., 2006; Sibilio et al., 2019). Hence, the distribution of the i-solute is modeled using mass conservation, including a reaction term, according to Eq. 4.11:

$$\frac{\partial c_i}{\partial t} = -(\nabla \cdot c_i u) + \nabla \cdot (D_i \nabla c_i) + R_i \qquad (4.11)$$

Where R_i represents the metabolic reaction.

The consumption kinetic can be evaluated through various kinetic models (Cioffi et al., 2008; Zhao et al., 2016; Burova et al., 2019). For instance, reaction kinetic equations can be used to model consumption/production from cells. These equations are usually considered to approximate a zero-order (Eq. 4.12), where the reaction rate is independent of the concentration C_i, or a first-order (Eq. 4.13), where the dependency is linear.

$$R_i = \frac{\partial c_i}{\partial t} = k = const \qquad (4.12)$$

$$R_i = \frac{\partial c_i}{\partial t} = k\, c_i \qquad (4.13)$$

Reaction kinetic equations are adopted to obtain information on chemical concentrations in the culture of solutes, such as waste products and growth factors.

Concerning nutrients consumption (such as oxygen and glucose), it strongly affects cells viability: an inappropriate supply of oxygen, for instance, may lead to the toxic conditions of hyperoxia (excessive oxygen supply) or hypoxia (partial oxygen lack) (Place et al., 2017), whereas glucose is the main source of energy for cells cultured *in vitro* (Hossain et al., 2015). Hence, a sophisticated model would help make more realistic predictions regarding nutrient diffusion in the cell culture. This model relies on the Michaelis-Menten kinetic relation:

$$R_i = \frac{\partial c_i}{\partial t} = \frac{V_{max} c_i}{c_i + K_m} \qquad (4.14)$$

where V_{max} is the maximum rate of the reaction (depending on the species and cell type), while K_m is the Michaelis–Menten constant. This latter, also called a half-saturation constant, is equal to the concentration at which the reaction rate is half V_{max}. In some cases,

V_{max} is reported per cell and multiplied by the cell density (cell/m^3). Both variables of Eq. 4.14 are determined by empirically measuring the reaction rate at various species concentrations and constructing a plot considering the variation of consumption rate as a response to the metabolite concentration (Sharifi et al., 2019). In this plot, the relationship between nutrient consumption and nutrient concentration is not linear.

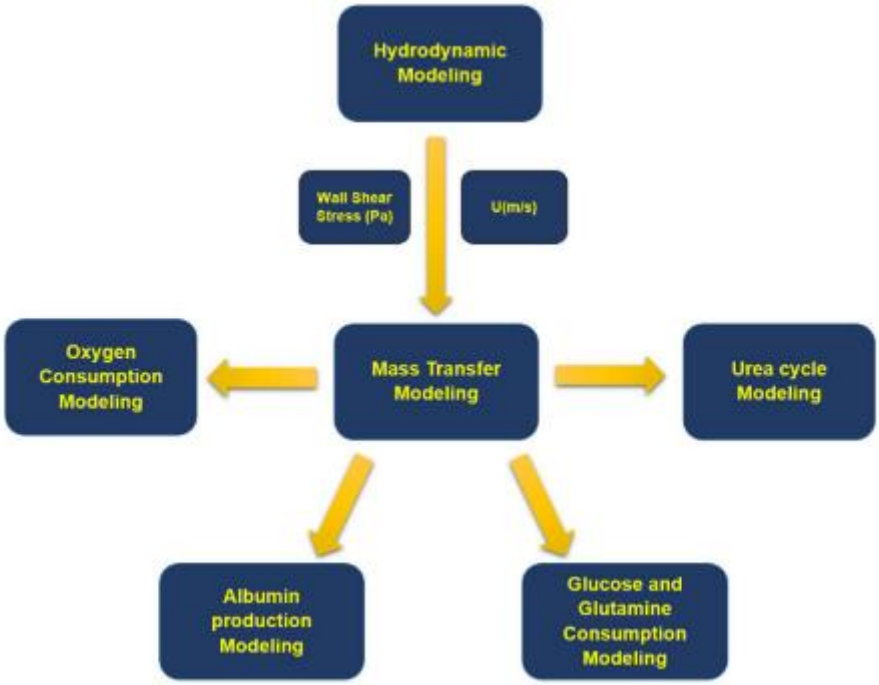

Figure 4.2 Block diagram of the modeling process: first, fluid flow equations were solved, and velocity distribution and wall shear stress inside the bioreactor were obtained; next, mass transfer equations were solved for oxygen, glucose, and metabolites, such as glutamine, ammonia, urea, and albumin. (Sharifi et al., 2019)

The local oxygen concentration is generally assumed to be the limiting nutrient, thus affecting cell growth. Mathematical models of cell proliferation consider this effect with a linear dependency between the oxygen concentration and the cell growth function:

$$\frac{\partial \varphi_c}{\partial t} = \beta \varphi_c C_O \left(1 - \frac{\varphi_c}{{\varphi_c}^{max}}\right) - d_O \qquad (4.15)$$

Where φ_c is the cell density, which is saturated at a maximum cell density ${\varphi_c}^{max}$, C_O is the local oxygen concentration, d_0 is the death (apoptosis) term, and β is the proliferation constant (Burova et al., 2019). Similarly, Similarly, cell growth of equations can account for the effect of both nutrient availability and mechanical stimulation in order to introduce a dependency of the growth rate on the shear stress. In this case, the shear stress dependency is non-linear (Zermatten et al., 2014).

Overall, when growing large amounts of cells, the media is rapidly nutrient exhausted, requiring multiple changes or frequent splitting of cells. On the other hand, bioreactors circumvent the depletion of nutrients by the constant perfusion of fresh media.

4.1.3 Literature review

The first simulations of tissue engineering in bioreactors were performed in the early 1990s in rotating wall vessel bioreactors. Since then, mathematical simulations have been widely used (even in conjunction with parametric studies) to validate the results obtained during in vitro testing, thus suggesting those factors have a significant effect on a bioreactor system (Vetsch et al., 2015). However, over the last 20 years, simple analytical models have been progressively evolved into complex and detailed computational models.

For mathematical simulations, in 2001, Goldstein et al. introduced a simple model for the estimation of shear stresses in perfused porous structures for bone TE (Fig. 4.3) (Goldstein et al., 2001).

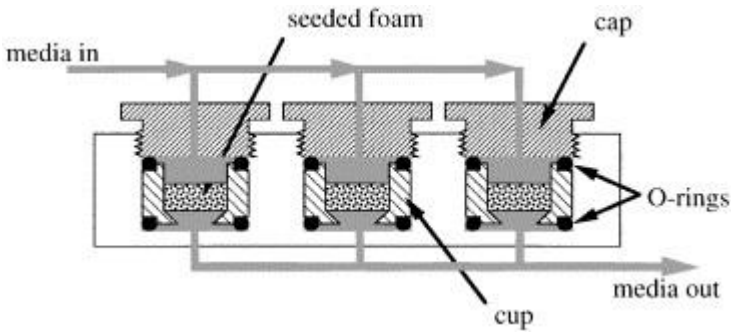

Figure 4.3 Diagram of a flow system for axial perfusion of media through cylindrical foams (Goldstein et al., 2001)

They made the assumptions of uniformly distributed flow across the structure surface and parabolic flow of the culture medium. According to this model, they calculated wall shear stresses and the mean velocity of the fluid through the pores. From their findings, the shear stress experienced by the seeded cells in the constant-flow system was more than an order of magnitude lower than that estimated for osteocytes in bone tissue under interstitial flow. Experimental results indicated that by applying this fluid flow to cultured cells, the distribution of cells in the scaffold was improved, leading to increased osteogenic differentiation.

Similarly, Grayson et al. determined shear stress imparted to cells at the beginning of culture by assuming a fully developed laminar flow (Grayson et al., 2008, 2011). The values for

wall shear stresses were calculated as a function of the mean linear flow rate using the Hagen-Poiseuille relation for laminar flow through a conduit. Reynolds numbers were calculated at different medium flow rates to validate the assumption of laminar flow. The internal geometries of the scaffolds were simplified by representing the porous network as bundles of cylindrical tubes of a given diameter arranged in parallel. The modeling results showed the estimated shear stress as a function of the channel diameter and medium flow rate (Fig. 4.4). The range of beneficial shear stresses for bone cell cultures appeared to be very wide, with the highest value 2000 times higher than the lowest value (0.0006-1.2 Pa). This outcome shows the low specificity of the cylindrical pore model due to numerous assumptions. However, the authors exploited this model to optimize the system. Specifically, because shear stress levels were low over the range of flow rates studied, they realized that future studies would be needed to investigate higher perfusion rates to support cell growth without inducing detrimental effects on construct development.

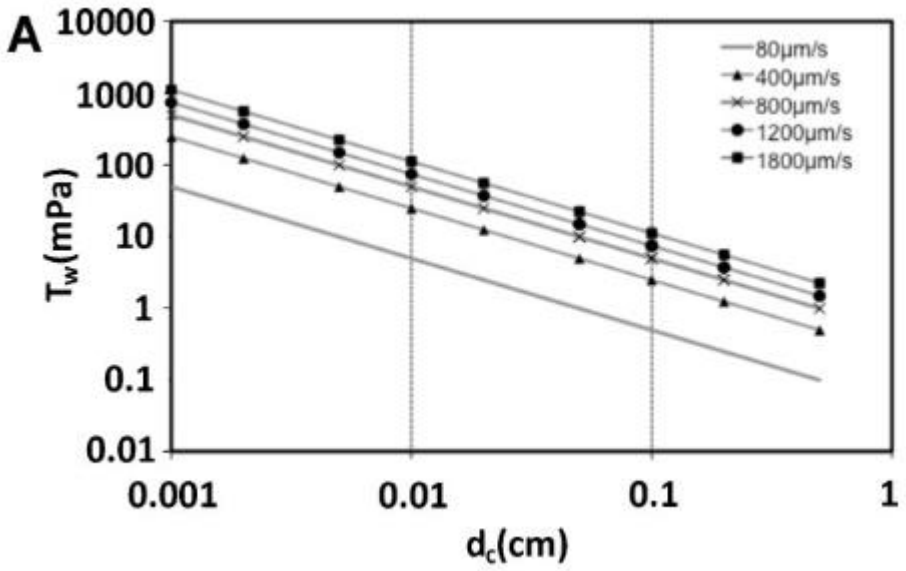

Figure 4.4 The relationship between shear stress and channel diameter for the various flow rates. The shaded region corresponds to the range of pore sizes present within the constructs used in the study (Grayson et al., 2011).

The suggestion that the analytical model of Goldstein et al. overestimates the wall shear stresses, especially at higher fluid flow velocities, was also the result of the work of Jungreuthmayer et al. (Jungreuthmayer et al., 2009). They compared the results of the cylindrical pore model to a μCT-based CFD model, finding that the difference between the two models was > 20%.

In another study, Goldstein's model was utilized to calculate shear stress during flow perfusion while also interposing mechanical stimulation (Vance et al., 2005). The authors

studied the oscillating flow-induced shear stress as a physiological mechanical stimulus interposed on perfusion flow during osteoblastic cells culture on calcium phosphate scaffolds. From the estimation of the shear stress at different perfusion rates, the authors were able to modulate the mechanical stimulation. Specifically, having estimated shear stress of 0.0007 Pa at 0.025 mL/min, they interposed an oscillatory flow on the perfusion flow as a sinusoidal profile with a 40 mL/min peak to expose the cells to an estimated maximum shear stress of 1.2 Pa once daily for 30 min at 1 Hz. At both shear-stress levels, the release of prostaglandin E2, which is thought to have an anabolic effect on the bone but is also an inflammatory marker, was significantly increased. Despite the high fluid flow velocity, DNA content was not influenced. Overall, this study supports the idea that mathematical models can be used to control the mechanical environment, thus improving the development and properties of tissue-engineered constructs.

Mathematical models were also assessed for determining oxygen transport and reaction during perfusion culture to evidence the importance of perfusion flow on cell proliferation and metabolism. Zhao et al. (Zhao et al., 2005) estimated and compared human mesenchymal stem cells (hMSC) growth kinetics and spatial growth patterns, metabolism, and oxygen consumption in static and perfusion cultures (Fig. 4.5).

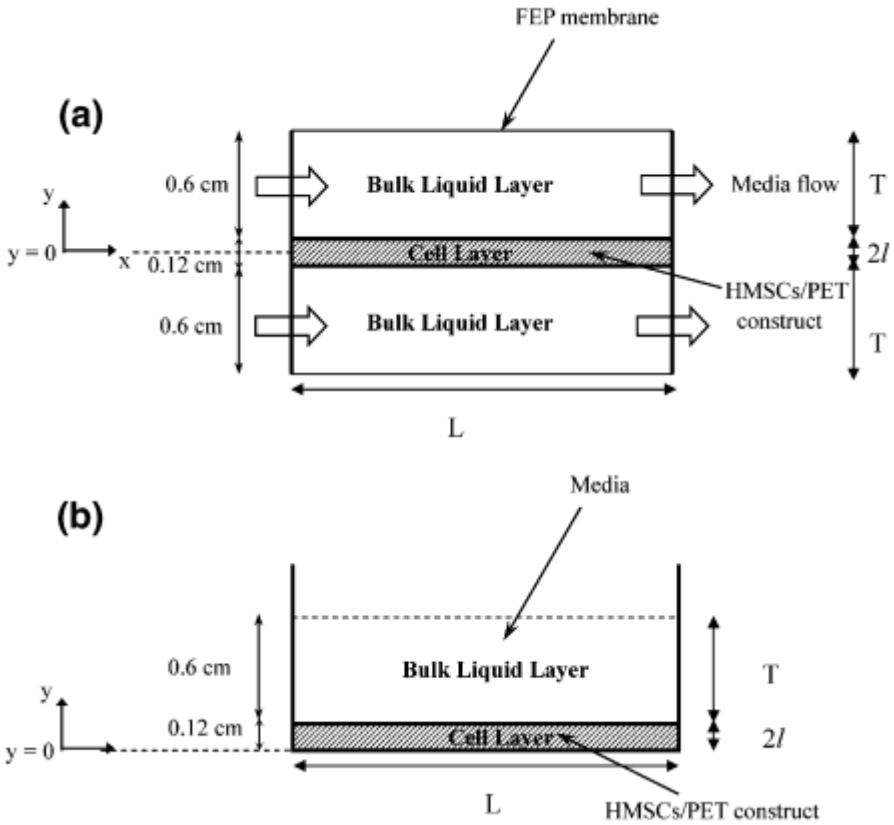

Figure 4.5 Schematic of systems used by Zhao et al. to develop a mathematical model for oxygen variation in static and perfusion systems: (a) perfusion culture, (b) static culture (Zhao et al., 2005).

They modeled oxygen transport based on experimental parameters while considering different transport conditions:

- transport of oxygen by convection and diffusion through the bulk layer of liquid;
- diffusion of oxygen from the incubator through an FEP membrane into the perfusion chambers;
- diffusive oxygen transport only in the cell layer (convective oxygen supply inside the construct was neglected because of the relatively large restrictions to flow in the matrix).

The authors reported the spatial and temporal variation of oxygen concentration in the liquid layer as the molar species continuity equation. Instead, they adopted the volume-averaged method to obtain a single continuity equation by which to calculate both mass transport by diffusion and oxygen consumption by cells in the cell layer (which is composed of two phases, i.e., cells and solution media). For these calculations, they obtained a velocity profile (assumed in laminar flow) along the length of the reactor as the function of: the average flow velocity of the medium in the perfusion chamber (i.e., the bulk liquid layer); the direction perpendicular to that of the flow (i.e., the y-direction); half the height (l) of the matrix (i.e., the cell layer); and the level (T) of the liquid layer in the bioreactor. They used the following equation:

$$v_x = \frac{6v_{ave}}{T^2}[(T + 2l)y - y^2 - l^2 + Tl] \qquad (4.16)$$

In the cell layer, the function of reaction rate kinetic describing the overall oxygen consumption (for metabolic and growth processes) was assumed to follow Michaelis-Menten kinetics. In this model, Q_m was directly determined from experimental data as a quadratic function of time, and the K_m values of hMSCs were derived from literature. Moreover, the cell mass balance in the cell layer was written assuming exponential homogeneous growth and neglecting the effects of oxygen on cell growth and cell death. Concerning boundary conditions, the oxygen concentration of the inlet flowing liquid was set to values in equilibrium with 21% gas-phase oxygen. Finally, equations describing cell growth and the variations of oxygen concentration in both the fluid and cell layers were solved simultaneously in space and time, coupled with the appropriate boundary conditions and growth parameters. This study evidenced the importance of mathematical modeling to demonstrate the limitations of static 3D culture systems compared to perfusion bioreactors.

It also suggests that oxygen transport significantly affects cell proliferation and metabolic activities.

In the work of O'Dea et al. (O'Dea et al., 2008), a continuum mathematical model was presented as a relevant tool for tissue growth processes in a perfusion bioreactor. The authors highlighted that their continuum macroscale model allows explicit considerations about the complex interactions involved in tissue growth even if it does not consider precise microscopic details. Indeed, they engaged in the averaging process while respecting appropriate microscopic considerations. The involvement of a simple mechanotransduction mechanism was also a novel aspect of this study. Specifically, they neglected the solid characteristics of the tissue construct when using a two-fluid model to represent tissue culture within a dynamic flow environment, i.e., a perfusion-type bioreactor system with an imposed flow of culture medium (Fig. 4.6). They constructed a two-phase model in which a single-phase (the cell phase) was described as the cells and ECM, and the second phase was the culture medium.

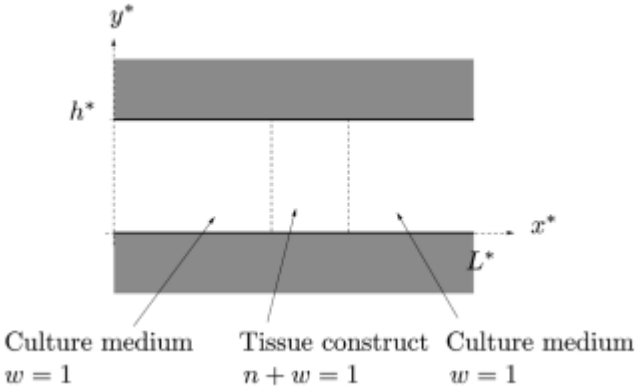

Figure 4.6 An idealized model of a perfusion bioreactor as a two-dimensional channel of length L* and width h* containing a tissue construct (O'Dea et al., 2008).

Assuming that each phase was incompressible with the same density and neglecting inertial effects, they presented the equations governing their two-phase model. Moreover, during mass transfer modeling, the authors excluded the diffusive terms for numerical convenience so that they eliminated the moving boundaries between the tissue construct and the culture medium. Also, to estimate the cell growth, they assumed that the tissue undergoes one-dimensional growth parallel to the x-axis and that associated pressure and velocity fields are functions of x and t only. Finally, they investigated the impact of an ambient flow on the growth of one-dimensional tissue. Indeed, the authors also considered the effect of coupling the growth of the cell population to the local environment, determining the characteristic

growth pattern associated with specific mechanical stimuli. To complete this model, they modify the growth and death rates with appropriate functional forms in response to local environmental factors due to mechanical stimuli. Accordingly, analytical solutions for tissue growth and stability were presented in the limit where only two sharp interfaces defined the tissue. Therefore, the authors underlined that the model they employed is suitable for tissue growth processes in which the solid characteristics of the system are unimportant.

4.2 Computational modeling

The analytical solution of mathematical equations is almost always impossible to find in real cases due to their nonlinear terms. In fluid dynamics, exceptions are represented by simple flows (such as laminar flow) and simple constitutive models (Vetsch et al., 2017). In general, numerical/discrete methods are used to find an approximate solution to the problem. A computational fluid dynamics (CFD) simulation addresses the solution of differential equations discretely, preserving a high level of detail about processes. However, in discrete models, where equations are applicable at distinct locations or governed by computational algorithms, several free parameters are employed, which may hinder the ability to perform meaningful model parameterization. All discrete models have a spatial domain divided into a grid where intersection points are called nodes, and the intervals between nodes are called elements (Krause et al.). Numerical methods commonly assign nodes to the values of the unknown primary variables of the problem (such as velocity and pressure in Eq. 4.2) and then resolve the linear- and discretized form of differential equations for each node. By concatenating the unknowns of each node to its neighbors by means of a spatial discretization technique, the final linear system is built, so that the unknown values of an approximated solution can be found (Sharifi et al., 2019).

The main CFD numerical methods are finite difference method (FDM), finite element method (FEM), and finite volume method (FVM).

4.2.1 Finite difference method

The finite difference method (FDM) solves the conservation laws in differential form by expressing the partial derivatives in the Taylor series expansion of unknown variables (Périé et al., 2005). For more accurate FDM, the order of the Taylor series can be expanded, or the division of the grid increased. FDM generally uses a structured, regular grid wherein the

position of each node is regularly determined from that of its neighbors, such as a Cartesian, cylindrical, or spherical coordinate system (Jeong et al., 2012).

Although FDM is the oldest discretization method, it is simple and effective. Its main drawbacks are that it has good accuracy and convergence only when applied to simple regular structured geometries. Moreover, since it solves the differential form of balance equations, these might not be locally satisfied, causing numerical instabilities, such as oscillations in the solution or error propagation (Burova et al., 2019).

The lattice-Boltzmann technique may be considered a finite difference approximation to solve the mathematical model describing the time-evolution of the one-particle velocity distribution function *f*(x,v,t). Zhao et al. used this technique as a computationally efficient and flexible numerical technique for modeling fluid flow in complex geometries encountered in tissue engineering constructs (Zhao et al., 2007). Specifically, they obtained the mass density, momentum density, and momentum flux from appropriate moments of *f*. Moreover, they replaced the continuous distribution of particle velocities with a few discrete values, meaning that the particles are forced to move on a regular lattice. Hence, the Boltzmann equation was derived for the discrete distribution function f_i (x, c_i, t), which represents the probability of finding a particle at node x with velocity c_i at time t, as follows:

$$\frac{\partial f_i}{\partial t} + c_i \cdot \nabla f_i = -\Omega_i(x,t) \qquad (4.17)$$

Where $\Omega_i(x,t)$ is the collision operator:

$$\Omega_i(x,t) = -\frac{1}{\zeta}(f_i - f_i^{eq}) \qquad (4.18)$$

with f_i relaxing to the equilibrium distribution f_i^{eq} with a single relaxation time ζ. The equilibrium distributions f_i^{eq} are chosen to reproduce the correct dynamic equations for the macroscopic mass density ρ (Eq. 4.19) and the momentum density ρv (where v is the macroscopic velocity) (Eq. 4.20).

$$\rho = \sum f_i \qquad (4.19)$$

$$\rho v = \sum f_i \, c_i \qquad (4.20)$$

Finally, Zhao et al. implemented the lattice-Boltzmann algorithm in two stages: in the first stage, the distributions f_i were propagated to neighboring nodes corresponding to their velocities; in the second stage, the distributions at each node were allowed to relax to equilibrium.

In the TE field, Jeong et al. proposed a numerical algorithm which is a hybrid method using both finite-difference approximations and analytic closed-form solutions (Jeong et al., 2012). For both spatial and temporal solutions, the authors first discretized the given

computational domain as a uniform grid with a space step h and a time step Δt. In their approach, the basic idea was to split the original problem into a sequence of easier problems for calculating the nutrient concentration distribution. Firstly, they implicitly solved the first part of each governing equation by a multigrid method (an FDM method); then, the remaining term of the equation was solved analytically by the method of separation of variables. As a result, the authors could interpret experimental results and identify dominating mechanisms.

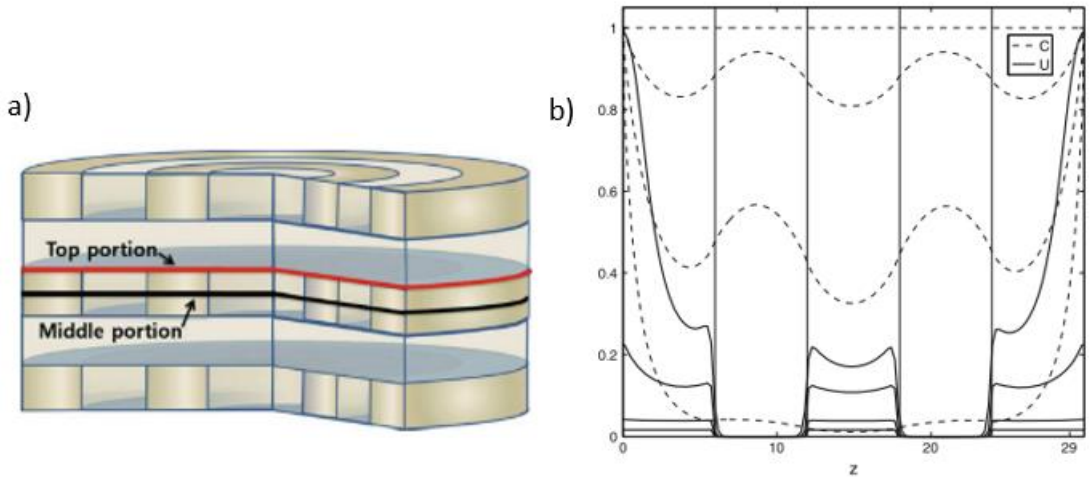

Figure 4.7 (a) Construct modeled by Jeong et al., which has an alternating concentric annulus seeding (b) Slice plot of nutrient concentration and cell density, C and U, at the axis of symmetry of the computational domain (Jeong et al., 2012).

Concerning perfusion flow, several studies have developed FDM-based models for quantifying changes in scaffolds during perfused cultures (Galbusera et al., 2007; Hossain et al., 2014; Lovecchio et al., 2014). For instance, Porter et al. (Porter et al., 2005) estimated shear stress while deriving the velocity field from a finite differences formula. The model was based on the definitions of one lattice unit and the length of one side of an element, and the production of a symmetric strain matrix. The values of the symmetric matrix were found using the Jacobi method and validated by estimating shear stresses as the analytical solution stresses for flow between two infinite plates. From their results, the difference method would always underestimate the shear rate. This study was the first 3D simulation of cell culture media flow through a perfused 3D construct that estimated local shear stresses.

Similarly, Yan et al. (Yan et al., 2012) discretized the governing equations by means of the implicit finite difference method and then solved them in MATLAB based on the Gauss-Seidel method. Their model was developed to represent the nutrient transport and cell growth in a 3D scaffold cultivated in a perfusion bioreactor. In this case, to validate the model, the

simulations results were not compared to results extracted from the literature instead of experimental results. Moreover, the authors focused on identifying the effect of factors such as culturing time (Fig. 4.8a), porosity (Fig. 4.8b), and flow rate (Fig. 4.8c) on cell cultures.

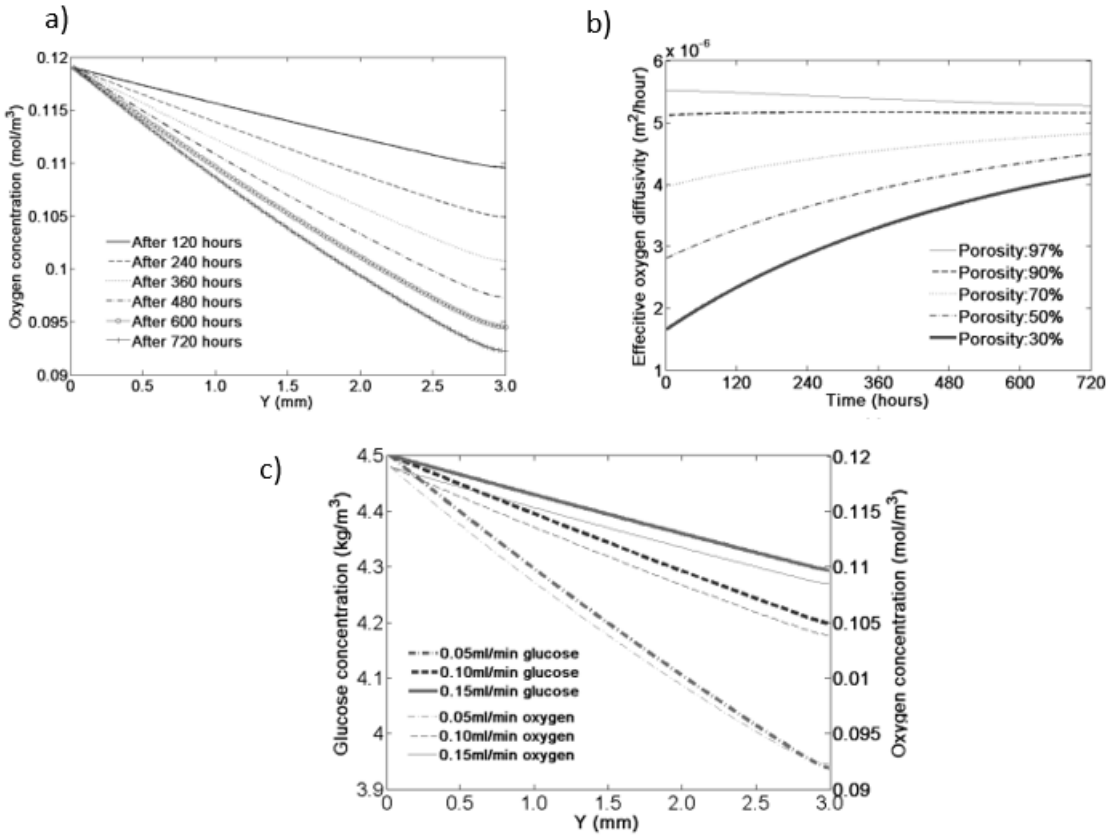

Figure 4.8 (a) Temporal Variation of Oxygen Concentration; (b) Variation of Effective Oxygen Diffusivity Different Initial Porosities; (c) Effect of Flow Rate on Glucose Concentration (Bold Line) and Oxygen Concentration (Fine Line) for a Scaffold in a Perfusion Bioreactor After 720 h. (Yan et al., 2012)

4.2.2 Finite element method

The finite element method (FEM) solves the volume integral of conservation laws expressed in a weak formulation (Zienkiewicz et al., 2013). The spatial discretization is based on interpolating the values at nodes via a polynomial basis function (i.e., linear, parabolic) with limited support, thus subdividing the entire domain into finite elements. The order of the basis function and the shape of the finite elements determine the solution accuracy. In this case, the mesh (the set of nodes and elements) is not limited to being a regular grid. The level of the mesh refinement also determines the accuracy and convergence rate.

FEM is a more robust method than FDM since it applies the conservation law in the integral form to each basis function. Moreover, it presents a natural symmetry since the solution derivatives are directly related to the basis function derivatives, and the boundary conditions

can be imposed straightforwardly. However, it is complex to implement, and even though global conservation is guaranteed, the local conservation of single elements might not be satisfied. This feature may occur if the function order is not high enough since the basis function is shared between more elements.

The most frequently used software for simulation (i.e., COMSOL, ANSYS, OpenFoam) processes their FEM-based results after implementing a numerical simulation. Hence, the finite element method is the most commonly used in TE studies of perfusion bioreactors.

In Shakeel's work (Shakeel, 2013), the author describes a simple mathematical paired model of nutrient transport and cell growth in a perfusion bioreactor. The key features of a TE process, including the fluid flow, nutrient transport, cell growth, and permeability variation of the material due to cell growth, were considered in the model. The latter was numerically solved by using the finite element solver COMSOL. Specifically, the model consisted of three differential equations (governing equations): the first representing the fluid flow through the porous material, the second indicating convection and diffusion of nutrients, and the third denoting cell proliferation. The equations were solved together with the appropriate boundary and initial conditions, introducing the variables and parameters in the model equations. In numerical calculations, it is crucial to solving the model in a determined order while substituting the obtained values in the following equations until the system approaches a steady state. In Shakeel's study, the author followed the order described in Fig. 4.9.

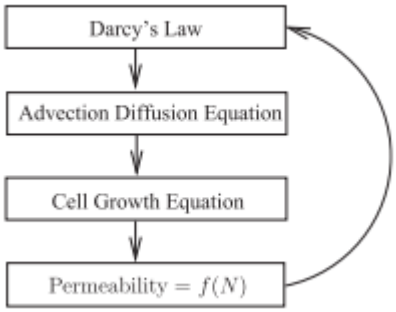

Figure 4.9 Schematic diagram of solution during the numerical analysis performed by Shakeel (Shakeel, 2013).

The results showed that the velocity of fluid and nutrient concentration were high in the regions where the permeability of the scaffold was high and vice versa. Moreover, the total cell number in the final construct did not depend on the initial seeding but on the scaffold permeability. The model was successfully verified with the analytical technique by applying certain simplifying assumptions at initial and longer times since the system could not be solved analytically at intermediate times. Overall, this work demonstrates the utility and

potential of computational models in choosing the various parameters for optimal cell growth in a perfusion bioreactor.

In another study, Israelowitz et al. (Israelowitz et al., 2012) used computational fluid dynamics (CFD) software based on FEM to simulate flow through a porous scaffold and recommend design changes based on the results. By setting laminar flow conditions, the authors analyzed different perfusion bioreactor designs regarding flow patterns and pressure distribution around a porous scaffold with changing permeability. By performing simulations, the regions of stagnant and irregular flow, and the pressure buildup upstream of the scaffold, might be detected, as shown in Figure 4.10.

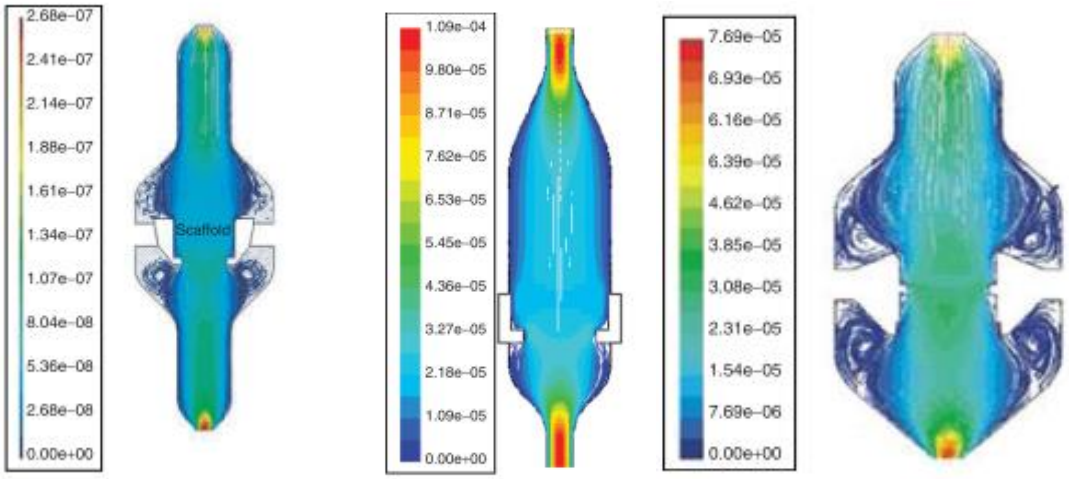

Figure 4.10 Flow path lines of different bioreactor designs investigated by Israelowitz et al.: design 1 shows significant stagnation above and below scaffold level; design 2 shows less stagnation compared to design 1; design 3 shows some stagnation at scaffold level (Israelowitz et al., 2012).

From their results, the bioreactor geometry significantly influenced the internal flow patterns and pressure distributions.

Recently, Seddiqi et al. (Seddiqi et al., 2020) modulated fluid flow dynamics and oxygen concentration in a 3D scaffold inside a perfusion bioreactor at three different inlet flow rates employing the FEM as a computational fluid dynamics approach. Unlike Shakeel, who validated its model by using an analytical approach, this was the first study to combine finite element modeling with experimental validation inside homogenous, cell-seeded 3D scaffolds within perfusion bioreactors over time. The model solved the Navier-Stokes equation numerically, yielding the fluid velocity field and fluid pressure. Then, from the fluid velocity information, the fluid shear stress was attained by using the constitutive relation for a Newtonian fluid:

$$\tau_{ij} = \mu\left(\frac{\partial u_i}{\partial x_j} + \frac{\partial u_j}{\partial x_i}\right) \qquad (4.21)$$

The governing equation for single-phase oxygen transfer through a scaffold was the convection-diffusion equation (Eq. 4.11), whereas cell density ρ_{cell} variations were modeled as follows:

$$\frac{\partial \rho_{cell}}{\partial t} = D_{cell}\nabla^2\rho_{cell} + \rho_{cell}\mu_{cell} \qquad (4.22)$$

Where D_{cell} is the cell diffusivity and μ_{cell} the cell growth rate. As for the boundary conditions, they were set as follows:

- the initial fluid velocity was zero in the simulation volume;
- the oxygen concentration throughout the scaffold was initially a constant value (0.2×10^{-6} mol cm^{-3}), equal to the standard oxygen concentration in the fresh medium;
- the initial cell density was based on the initial cell number seeded in the experimental part of the study;
- the fluid pressure at the outlet surface of the scaffold was zero;
- a boundary condition of no slip was applied to the inner surface of the scaffold.

Fig. 4.11 shows their results in terms of the effect of changes in the inlet flow rate of a perfusion bioreactor on wall shear stress distribution inside a 3D printed scaffold for 5 days.

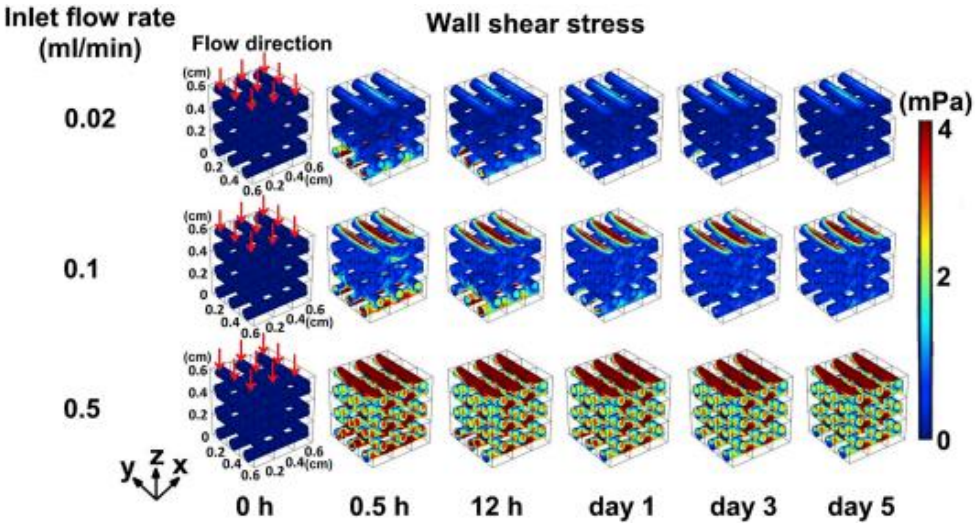

Figure 4.11 Effect of changes in inlet flow rate of a perfusion bioreactor on wall shear stress distribution and magnitude exerted on cells inside a 3D printed scaffold during 5 days (Seddiqi et al., 2020).

As can be seen, increasing the inlet flow velocity improved the shear stress in the wall and its distribution within the scaffold at all measured time points. On the other hand, oxygen concentration and cells distribution inside the scaffold appeared less affected by the inlet flow rate variation. Hence, this study reveals information about the inlet flow rate selection for optimal cell culture in perfusion bioreactors.

Similarly, Xue et al. (Xue et al., 2019) fabricated a 3D-printed scaffold and further developed a finite element model to study the effect of perfusion flow on the image from the micro-computed tomography of the fabricated scaffold and on its computer-aided design (CAD). Specifically, the authors analyzed the microenvironment inside a co-culture perfusion bioreactor during the perfusion culture, including flow velocity, fluid-induced shear stress, and mixing of two differentiation media during the co-culture. From their results, when comparing the model created with CAD with the one extracted from the μCT image, the latter showed an increase in the average magnitude of the shear stress but a decrease in the maximum values (Fig. 4.12).

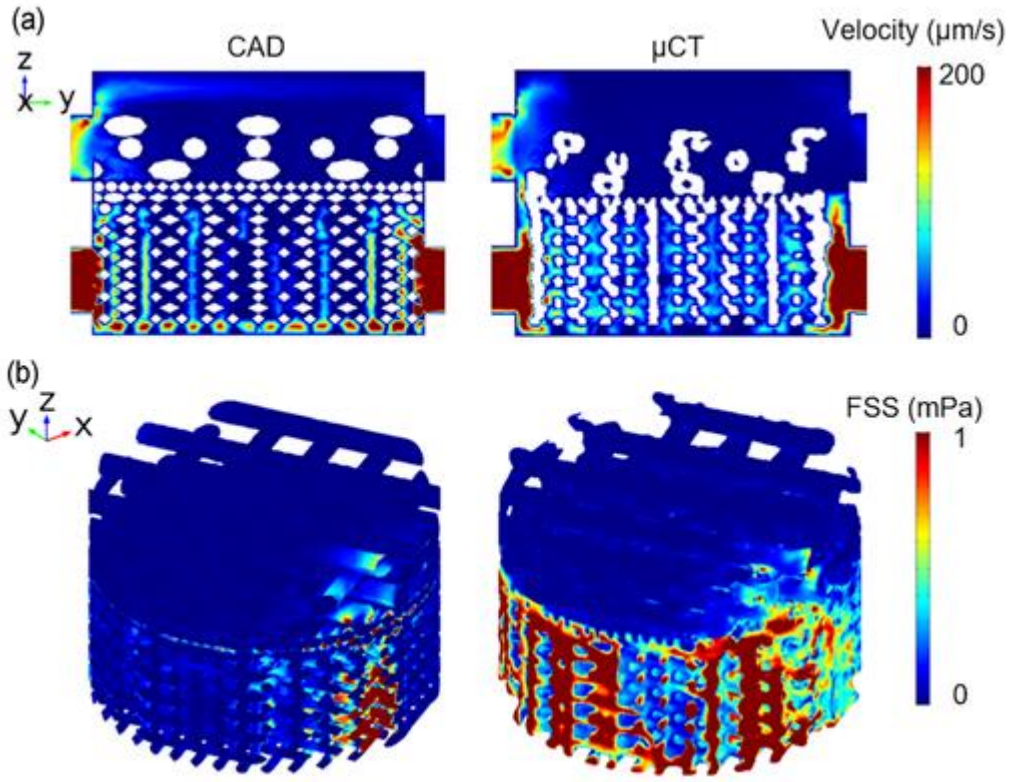

Figure 4.12 (a) Flow velocity distribution on the cross-sectional slice for CAD and μCT model. (b) Fluid-induced shear stress on the scaffold for the CAD and μCT model (Xue et al., 2019).

The authors attributed this difference in results to the less homogeneous structure caused by common additive manufacturing methods, including part accuracy, shrinkage, surface finish, and sharp corners. Concerning the media mixing, results showed that, in general, the different media were well contained in their respective sections for both structures. The importance of this study relies on the relevant investigation that can be performed by using a FEM approach in TE strategies.

The FEM approach has been largely used to investigate the dynamics of the mechanical stimuli transmitted to the cells during perfused culture with additional mechanical loadings applied (Bilodeau et al., 2005b; Sandino and Lacroix, 2011; Mccoy et al., 2012; Di Federico et al., 2014; Visone et al., 2018). In this context, the study performed by Di Federico et al. is worthy of mention (Di Federico et al., 2014). The authors studied the effect of cyclic compressive and shear strain on 3D cell-seeded constructs in a bi-axial bioreactor for cartilage TE. Using FEM analysis, the prototype specimens were optimized to ensure a well-characterized and uniform distribution of strain across the construct. Specifically, the authors configured the simulations to apply a compressive strain along the y-direction, followed by a shear strain in the x-direction. The obtained results were used to modify the design of the constructs to minimize the risk of sample failure during the dynamic culture under mechanical loading.

Other studies have incorporated information about the fluid velocity u and the shear strain γ in a bioreactor to find a parameter S, which depends on mechanical stimulation and is used in an algorithm to direct differentiation (Byrne et al., 2007; Milan et al., 2010):

$$S = \frac{\gamma}{a} + \frac{u}{b} \qquad (4.23)$$

where coefficients a and b are found experimentally. In Eq. 4.23, the velocity and strain can be found using the poroelastic finite element modeling for multiphase materials. Depending on the value of the coefficient S, the cells differentiate into fibroblasts, chondrocytes, or osteoblasts (Fig. 4.13).

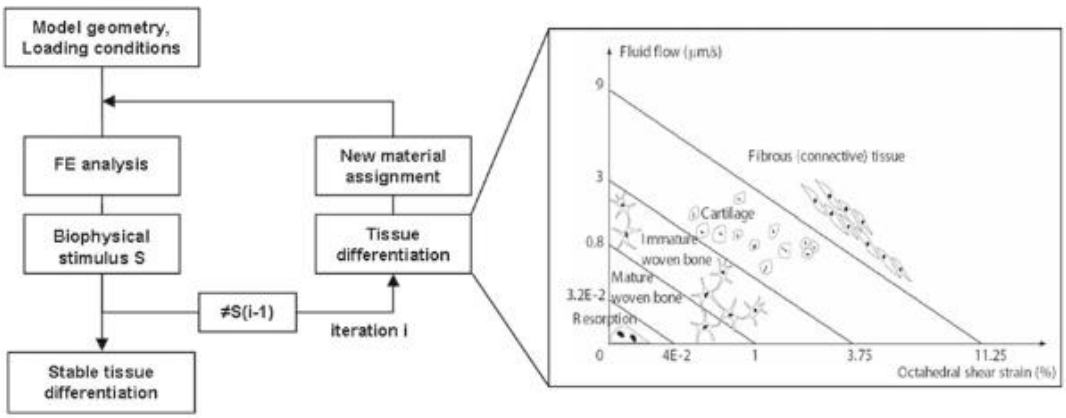

Figure 4.13 Algorithm of mechanoregulation. Iterative procedure and diagram of tissue differentiation following thresholds of mechanical stimuli (Milan et al., 2010).

For instance, very low values of S (which means very low levels of mechanical stimulation) lead to tissue resorption, low values for osteoblasts, intermediate levels for chondrocytes, and high levels for fibroblasts.

Overall, the FEM can provide valuable information about the impact of shear stress on the tissue, the response of a single cell, and the difference between the effect of different bioreactor systems and flow regimes on tissue maturation.

4.2.3 Finite volume method

The finite volume method (FVM) divides the domain into control volumes (CV) that form the mesh, regular or not. Then, it collocates the unknown values at the nodes, not at the intersection points of the grid, but at each CV centroid. Hence, this method approximates the solution with a constant value in each sub-volume. In this way, each CV centroid represents the local mean volume value of an unknown function. Further, the FDM solves the integral form of conservation law by transforming the terms of the volume integral with the unknown function in surface integrals through the divergence theorem. Then, a spatial discretization technique is introduced to express the values of the solution and its derivatives at the CV boundaries in the function of the neighbor CV centroids.

The FVM can be seen as a particular case of FEM with a stepwise constant basis function. In the case of regular structured mesh, the FVM solution can coincide with the FDM one. Overall, FVM has the advantage that the integral form of conservation law is satisfied globally and locally. This feature occurs since the surface flux terms between sharing boundaries of CVs are equal and opposite to each other and thus self-balanced. However, its main disadvantage is that, within the CV, there is a constant approximation of the solution. Moreover, the accuracy and discretization of derivatives depend on the adopted spatial discretization technique (i.e., upwind differencing scheme (UDS), central difference scheme (CDS), quadratic upwind interpolation for convective kinematics (QUICK) scheme) (Simčík et al., 2011).

The first work that aimed to model via FDM the local fluid dynamics within a direct perfusion bioreactor was completed by Cioffi et al. (Cioffi et al., 2006). By reconstructing the micro-geometry of the scaffold by μCT scanning techniques, the authors calculated shear stress using the commercial finite-volume code FLUENT. Specifically, the fluid volume was visualized by a triangulation of the surface that divided the solid structure from the void, and the fluid domain was created by meshing the void volume in rough tetrahedrons. Finally, to reduce the influence of the boundaries, only a sub-cube of each reconstructed scaffold (approximately 100 μm x 100 μm x 100 μm) was used to evaluate the shear stresses exerted on the interior surfaces of the matrix. After imposing the appropriate boundary conditions,

the steady-state Navier–Stokes equation (Eq. 4.2) was solved by the CFD software neglecting gravitational body forces. Figure 14 shows a description of the direct flow of the culture medium through the porous scaffold used by Cioffi et al. and the boundary conditions adopted for CFD simulations.

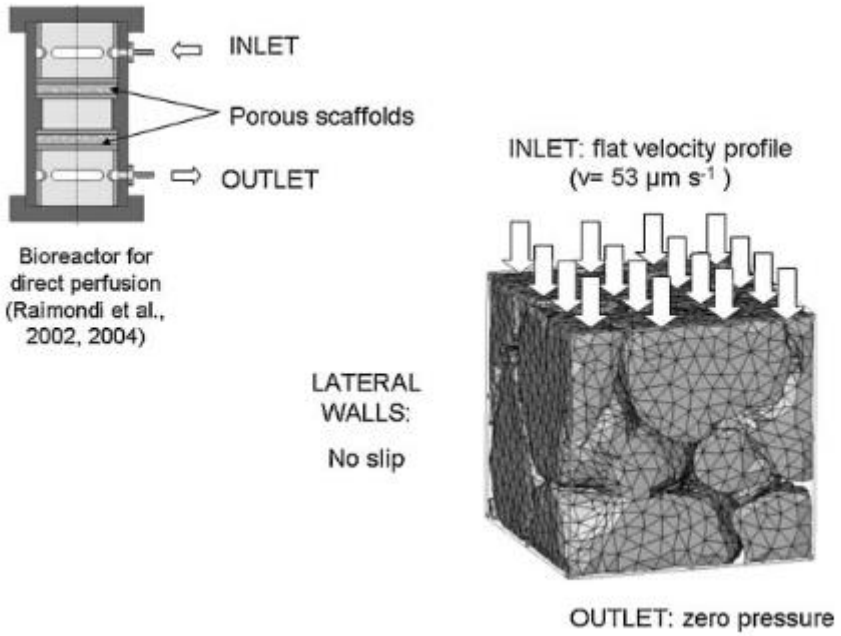

Figure 4.14 Boundary conditions adopted for CFD simulations. These conditions are representative of a direct flow of culture medium through a porous scaffold. The flow enters the domain from the top and exits from the bottom, at a flow rate of 0.5 cm3/min, through a circular scaffold, 15 mm in diameter (Cioffi et al., 2006)

The average shear stress from the FVM-based model was compared to the one calculated using an analytical model for flow through porous media. From their results, macroscopic porous models, like analytical models, cannot be applied to estimate the shear stresses within the scaffold.

Similarly, Zermatten et al. (Zermatten et al., 2014) used the commercial CFD code ANSYS, based on the finite volume technique, to solve the 3D Navier-Stokes equations (Eq. 4.1 and Eq. 4.2) for fluid flow through porous media inside a perfusion bioreactor (Fig. 4.15).

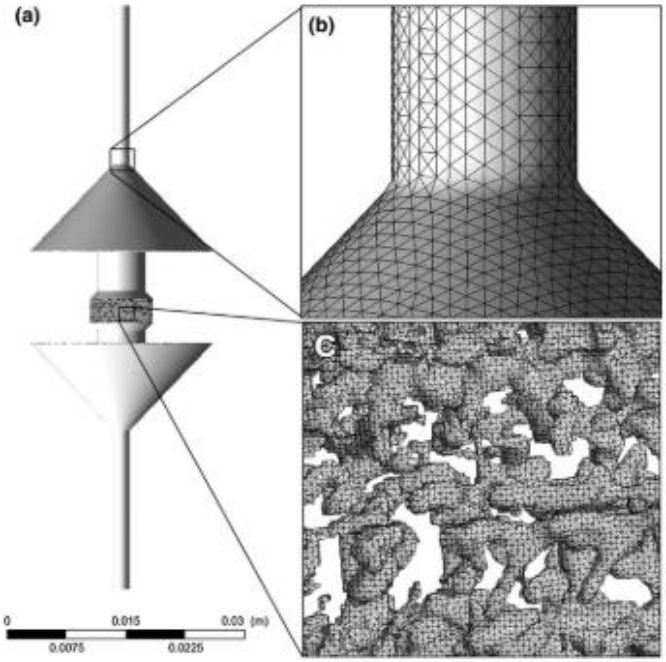

Figure 4.15 Computational domain: (a) bioreactor containing the scaffold. (b) The bioreactor meshed with a coarse grid; smallest element size 5 93.8 lm (before rounding, cutting, and smoothing). (c) The scaffold meshed with a finer grid (Zermatten et al., 2014)

Even in this case, the complex 3D geometry of the scaffold (with a cylindrical shape of 8 mm in diameter and 3 mm in length) was imaged by micro-computed tomography and used in direct pore-level simulations of the computed domain. In computational simulations, the frequency distributions of wall shear stress were evaluated at different flow rates, resulting in a monotonically increasing linear correlation between the two variables (Fig. 4.16).

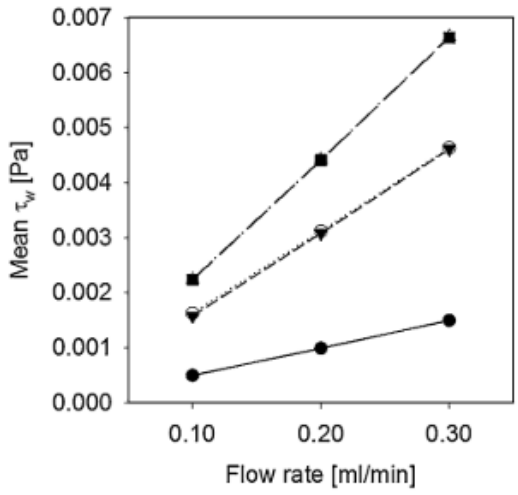

Figure 4.16 Mean wall shear stress as a function of the inlet flow rate. Each value represents the average of all shear stress values obtained in a slice in the five regions of interest (Zermatten et al., 2014)

Moreover, the authors compared the mean surface shear stress calculated by the Lattice-Boltzmann method (FDM) with that calculated by FVM. According to their results, the FDM

lacked precision around small geometrical features and used excess elements around large ones. In contrast, FVM could be adapted efficiently to small and large geometrical features often encountered in complex configurations.

Recently, FVM has been used to facilitate the determination of the effect flow rates on scaffolds fabricated for bone tissue engineering experiments *in vitro*, thus avoiding performing a series of trial and error experiments (Rietbergen; Iannetti et al., 2016; Zhao et al., 2018a, 2019; Wang et al., 2019a). Remarkable results were found by Iannetti et al. (Iannetti et al., 2016), that used the commercial code ANSYS to carry out the fluid dynamic and mass transport simulations within a perfusion bioreactor comprising two adjacent units. In their computational study, the spatial discretization was done by a cells-based finite volume method. An essential part of this study was modeling the transport of biomolecules dissolved in the culture media, such as oxygen, glucose, and proteins. The author assumed passive transport by the culture media since all solutes were considered diluted. Therefore, the equation describing the biomolecules transport in the fluid phase was:

$$\nabla \cdot \left(-D_f \nabla C_f + U C_f\right) = 0 \qquad (4.24)$$

Where C_f is the volumetric concentration in the fluid medium, and $D_{f\ is}$ the diffusion coefficient of the specific biomolecule. Then, following the theory of mixtures, the governing equations for biomolecules concentration in the porous medium were read as follows:

$$\nabla \cdot \left(-D_{s,s} \nabla (1-\gamma) C_{s,s} + (1-\gamma) U C_{s,s}\right) + (1-\gamma) S + \tau IAD\left(C_{s,s} - C_{s,f}\right) = 0 \qquad (4.25)$$

$$\nabla \cdot \left(-D_{s,f} \nabla (\gamma) C_{s,f} + (\gamma) U C_{s,f}\right) + (\gamma) S + \tau IAD\left(C_{s,f} - C_{s,s}\right) = 0 \qquad (4.26)$$

Where $C_{s,s}$ and $C_{s,f}$ are the volumetric concentration of biomolecules in the solid and in the fluid phase of the scaffold, respectively, and γ is the scaffold porosity. Hence, the volumetric concentration of biomolecules in the porous medium w was determined as the weighted average $C_s = \gamma C_{s,f} + (1-\gamma) C_s$. In addition, the mass transfer coefficient from the fluid to the solid phase of the porous medium was indicated as τ, and IAD was the interfacial density of the surface area separating the two phases. As a result, the term $\tau IAD(C_{s,s} - C_{s,f})$ represents the flux exchanged between the two phases of the porous medium. For estimating the mass transfer coefficient τ, the authors assumed that mass transfer was dominated by diffusion at the pore scale. Finally, the symbol S denotes the source term representing the consumption of nutrients by living cells disseminated into the scaffold. For the computational solution of the problem, all equations were solved simultaneously through a monolithic linear system

spanning all degrees of freedom. Specifically, the Laplace operator in the fluid momentum and oxygen transport equations was approximated by a centered scheme, while the convective terms were discretized by means of an upwind method.

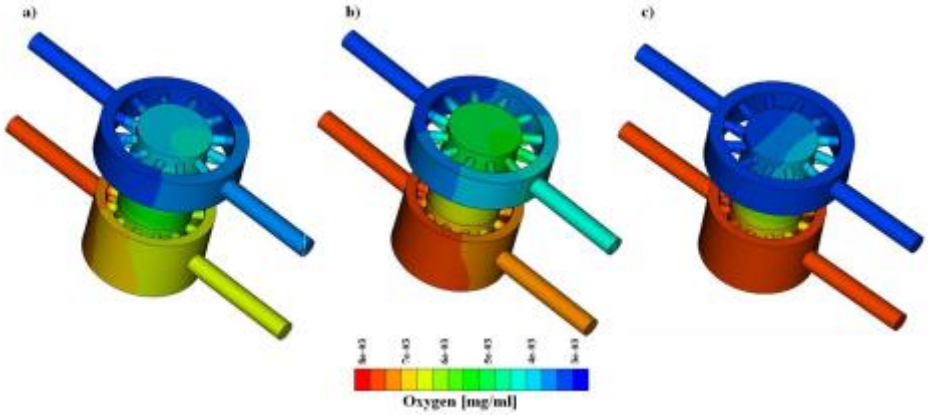

Figure 4.17 Oxygen concentration with PLLA scaffold. From left to right, flow pair of 1–1 [ml/day], 1–2 [ml/day], 10–10 [ml/day] (Iannetti et al., 2016)

Figure 4.17 shows the obtained oxygen concentration profile within a PLLA scaffold inserted into the bioreactor at different flow rates of the two circuits. From their results, the oxygen concentration in the top region of the scaffold was higher in the case of low flow rate than in the case of high flow rate. Hence, the computational model served as a valuable tool to estimate whether each scaffold region receives enough nutrients. Overall, the main contribution of this study was the success in implementing the model of the complex multi-physics of a perfusion bioreactor into a commercial computational platform, showing the significant potential of computational tools in biomedical research.

4.3 Conclusions

The development of analytical and/or computational models allows describing the cell and ECM production inside 3D scaffolds during perfusion bioreactor culture. Hence, it facilitates researchers in optimizing the system performance while minimizing the associated costs of experiments. In some cases, the analytical and numerical solutions can be validated against each other or used to obtain various information about the system with a different degree of approximation.

Analytical calculations play a valuable role in predicting the overall dynamic response in different parts of bioreactors. On the other hand, numerical evaluation provides insight into local hydrodynamics in tissue constructs in order to generate quantitative anticipation of

tissue development within a bioreactor system. Thanks to the development of computational tools, CFD is used to discretize mathematical equations and accurately predict bioreactor operational conditions. The major advantage of such a mathematical model is that it provides a robust tool to solve complicated mathematical equations.

Depending on the degree of data accuracy, additional mathematical complexity provided by CFD simulations is avoidable, so simplified models may be employed to describe biological tissue growth. For instance, homogenized/analytical models can be employed to describe macroscopic mass transport, saving considerable computational costs. However, the challenge of analytical methods lies in managing the information lost due to the simplification process.

References

Bilodeau, K., Couet, F., Boccafoschi, F., and Mantovani, D. (2005). Thoughts and Progress: Design of a Perfusion Bioreactor Specific to the Regeneration of Vascular Tissue Under Mechanical tresses. *Artif. Organs* 29, 906–922.

Blackshear, P., Dorman, F., and Steinbach, J. (1965). Some mechanical effects that influence hemolysis. *Trans. Am. Soc. Artif. Intern. Organs* 11, 112–117. doi:10.1097/00002480-196504000-00022.

Blaeser, A., Duarte Campos, D., Puster, U., Richtering, W., Stevens, M., and Fischer, H. (2016). Controlling Shear Stress in 3D Bioprinting is a Key Factor to Balance Printing Resolution and Stem Cell Integrity. *Adv. Healthc. Mater.* 5, 326–333. doi:10.1002/ADHM.201500677.

Burova, I., Wall, I., and Shipley, R. J. (2019). Mathematical and computational models for bone tissue engineering in bioreactor systems. *J. Tissue Eng.* 10. doi:10.1177/2041731419827922.

Byrne, D. P., Lacroix, D., Planell, J. A., Kelly, D. J., and Prendergast, P. J. (2007). Simulation of tissue differentiation in a scaffold as a function of porosity, Young's modulus and dissolution rate: Application of mechanobiological models in tissue engineering. *Biomaterials* 36, 5544–5554. doi:10.1016/J.BIOMATERIALS.2007.09.003.

Cerrada, M. L. (2005). Introduction to the Viscoelastic Response in Polymers.

Chung, C., Chen, C., Chen, C., and Tseng, C. (2007). Enhancement of cell growth in tissue-engineering constructs under direct perfusion: Modeling and simulation. *Biotechnol. Bioeng.* 97, 1603–1616. doi:10.1002/BIT.21378.

Cioffi, M., Boschetti, F., Raimondi, M. T., and Dubini, G. (2006). Modeling evaluation of the fluid-dynamic microenvironment in tissue-engineered constructs: A micro-CT based model. *Biotechnol. Bioeng.* 93, 500–510. doi:10.1002/bit.20740.

Cioffi, M., Küffer, J., Ströbel, S., Dubini, G., Martin, I., and Wendt, D. (2008). Computational evaluation of oxygen and shear stress distributions in 3D perfusion culture systems: Macro-scale and micro-structured models. *J. Biomech.* 41, 2918–2925. doi:10.1016/j.jbiomech.2008.07.023.

Coletti, F., Macchietto, S., and Nlvassore, N. (2006). Mathematical modelling of three-dimensional cell cultures in perfusion bioreactors. Part II. *Comput. Aided Chem. Eng.* 21, 1699–1704. doi:10.1016/S1570-7946(06)80292-0.

Di Federico, E., Bader, D. L., and Shelton, J. C. (2014). Design and validation of an in vitro loading system for the combined application of cyclic compression and shear to 3D chondrocytes-seeded agarose constructs. *Med. Eng. Phys.* 36, 534–540. doi:10.1016/j.medengphy.2013.11.007.

Dong, J., Gu, Y., Li, C., Wang, C., Feng, Z., Qiu, R., et al. (2009). Response of mesenchymal stem cells to shear stress in tissue-engineered vascular grafts. *Acta Pharmacol. Sin. 2009 305* 30, 530–536. doi:10.1038/aps.2009.40.

Dvir, T., Benishti, N., Shachar, M., and Cohen, S. (2006). A novel perfusion bioreactor providing a homogenous milieu for tissue regeneration. *Tissue Eng.* 12, 2843–2852. doi:10.1089/ten.2006.12.2843.

Galbusera, F., Cioffi, M., Raimondi, M. T., and Pietrabissa, R. (2007). Computational modeling of combined cell population dynamics and oxygen transport in engineered tissue subject to interstitial perfusion. *https://doi.org/10.1080/10255840701318404* 10, 279–287. doi:10.1080/10255840701318404.

Goldstein, A. S., Juarez, T. M., Helmke, C. D., Gustin, M. C., and Mikos, A. G. (2001). Effect of convection on osteoblastic cell growth and function in biodegradable polymer foam scaffolds. *Biomaterials* 22, 1279–1288. doi:10.1016/S0142-9612(00)00280-5.

Grayson, W. L., Bhumiratana, S., Cannizzaro, C., Chao, P. H. G., Lennon, D. P., Caplan, A. I., et al. (2008). Effects of initial seeding density and fluid perfusion rate on formation of tissue-engineered bone. *Tissue Eng. - Part A.* 14, 1809–1820. doi:10.1089/ten.tea.2007.0255.

Grayson, W. L., Marolt, D., Bhumiratana, S., Fröhlich, M., Guo, X. E., and Vunjak-Novakovic, G. (2011). Optimizing the medium perfusion rate in bone tissue engineering bioreactors. *Biotechnol. Bioeng.* 108, 1159–1170. doi:10.1002/bit.23024.

Grigioni, M., Morbiducci, U., D'Avenio, G., Benedetto, G. Di, and Gaudio, C. Del (2005). A novel formulation for blood trauma prediction by a modified power-law mathematical model. *Biomech. Model. Mechanobiol. 2005 44* 4, 249–260. doi:10.1007/S10237-005-0005-Y.

Hossain, M. S., Bergstrom, D. J., and Chen, X. B. (2014). Prediction of cell growth rate over scaffold strands inside a perfusion bioreactor. *Biomech. Model. Mechanobiol. 2014 142* 14, 333–344. doi:10.1007/S10237-014-0606-4.

Hossain, M. S., Bergstrom, D. J., and Chen, X. B. (2015). Modelling and simulation of the chondrocyte cell growth, glucose consumption and lactate production within a porous tissue scaffold inside a perfusion bioreactor. *Biotechnol. Reports* 5, 55–62. doi:10.1016/j.btre.2014.12.002.

Hyndman, L., McKee, S., Mottram, N. J., Singh, B., Webb, S. D., and McGinty, S. (2020). Mathematical modelling of fluid flow and solute transport to define operating parameters for in vitro perfusion cell culture systems. *Interface Focus* 10. doi:10.1098/RSFS.2019.0045.

Iannetti, L., D'Urso, G., Conoscenti, G., Cutrì, E., Tuan, R. S., Raimondi, M. T., et al. (2016). Distributed and lumped parameter models for the characterization of high throughput bioreactors. *PLoS One* 11. doi:10.1371/JOURNAL.PONE.0162774.

Israelowitz, M., Weyand, B., Rizvi, S., Vogt, P. M., and Von Schroeder, H. P. (2012). Development of a laminar flow bioreactor by computational fluid dynamics. *J. Healthc. Eng.* 3, 455–476. doi:10.1260/2040-2295.3.3.455.

Jeong, D., Yun, A., and Kim, J. (2012). Mathematical model and numerical simulation of the cell growth in scaffolds. *Biomech. Model. Mechanobiol.* 11, 677–688. doi:10.1007/S10237-011-0342-Y.

Jungreuthmayer, C., Donahue, S., Jaasma, M., Al-Munajjed, A., Zanghellini, J., Kelly, D., et al. (2009). A comparative study of shear stresses in collagen-glycosaminoglycan and calcium phosphate scaffolds in bone tissue-engineering bioreactors. *Tissue Eng. Part A* 15, 1141–1149. doi:10.1089/TEN.TEA.2008.0204.

Krause, A. L., Beliaev, D., Van Gorder, R. A., and Waters, S. L. Lattice and Continuum Modelling of a Bioactive Porous Tissue Scaffold. doi:10.1093/imammb/dqnxxx.

Lovecchio, J., Mjoll Jonsdottir-Buch, S., Einarsdottir, G. K., Zurich, E., and Orlygsson, G. (2014). Assessment of perfusion bioreactors system using X-ray lCT technology and 3D modeling methods. Available at: https://www.researchgate.net/publication/263089498 [Accessed September 27, 2021].

Lujan, T. J., Wirtz, K. M., Bahney, C. S., Madey, S. M., Johnstone, B., and Bottlang, M. (2011). A novel bioreactor for the dynamic stimulation and mechanical evaluation of multiple tissue-engineered constructs. *Tissue Eng. Part C. Methods* 17, 367–74. doi:10.1089/ten.TEC.2010.0381.

Magrofuoco, E., Flaibani, M., Giomo, M., and Elvassore, N. (2019). Cell culture distribution in a

three-dimensional porous scaffold in perfusion bioreactor. *Biochem. Eng. J.* 146, 10–19. doi:10.1016/j.bej.2019.02.023.

Maidhof, R., Tandon, N., Lee, E., Luo, J., Duan, Y., Yeager, K., et al. (2012). Biomimetic perfusion and electrical stimulation applied in concert improved the assembly of engineered cardiac tissue. *J. Tissue Eng. Regen. Med.* 6. doi:10.1002/TERM.525.

Martin, Y., and Vermette, P. (2005). Bioreactors for tissue mass culture: Design, characterization, and recent advances. *Biomaterials* 26, 7481–7503. doi:10.1016/j.biomaterials.2005.05.057.

Mccoy, R. J., Jungreuthmayer, C., and O'Brien, F. J. (2012). Influence of flow rate and scaffold pore size on cell behavior during mechanical stimulation in a flow perfusion bioreactor. *Biotechnol. Bioeng.* 109, 1583–1594. doi:10.1002/bit.24424.

Milan, J., Planell, J., and Lacroix, D. (2010). Simulation of bone tissue formation within a porous scaffold under dynamic compression. *Biomech. Model. Mechanobiol.* 9, 583–596. doi:10.1007/S10237-010-0199-5.

Nair, K., Gandhi, M., Khalil, S., Yan, K., Marcolongo, M., Barbee, K., et al. (2009). Characterization of cell viability during bioprinting processes. *Biotechnol. J.* 4, 1168–1177. doi:10.1002/BIOT.200900004.

O'Dea, R. D., Waters, S. L., and Byrne, H. M. (2008). A two-fluid model for tissue growth within a dynamic flow environment. *Eur. J. Appl. Math.* 19, 607–634. doi:10.1017/S0956792508007687.

Périé, D., Korda, D., and Iatridis, J. C. (2005). Confined compression experiments on bovine nucleus pulposus and annulus fibrosus: Sensitivity of the experiment in the determination of compressive modulus and hydraulic permeability. *J. Biomech.* 38, 2164–2171. doi:10.1016/j.jbiomech.2004.10.002.

Place, T. L., Domann, F. E., and Case, A. J. (2017). Limitations of oxygen delivery to cells in culture: An underappreciated problem in basic and translational research. *Free Radic. Biol. Med.* 113, 311–322. doi:10.1016/j.freeradbiomed.2017.10.003.

Porter, B., Zauel, R., Stockman, H., Guldberg, R., and Fyhrie, D. (2005). 3-D computational modeling of media flow through scaffolds in a perfusion bioreactor. *J. Biomech.* 38, 543–549. doi:10.1016/j.jbiomech.2004.04.011.

Rietbergen, van Changes in scaffold porosity during bone tissue engineering in perfusion bioreactors considerably affect cellular mechanical stimulation for mineralization. doi:10.1016/j.bonr.2020.100265.

Rouwkema, J., FJM Koopman, B., Van Blitterswijk, C. A., Dhert, W. J., and Malda, J. (2009). Supply of Nutrients to Cells in Engineered Tissues. *Biotechnol. Genet. Eng. Rev.* 26, 163–178. doi:10.5661/bger-26-163.

Sandino, C., and Lacroix, D. (2011). A dynamical study of the mechanical stimuli and tissue differentiation within a CaP scaffold based on micro-CT finite element models. *Biomech. Model. Mechanobiol.* 10, 565–576. doi:10.1007/s10237-010-0256-0.

Seddiqi, H., Saatchi, A., Amoabediny, G., Helder, M. N., Abbasi Ravasjani, S., Safari Hajat Aghaei, M., et al. (2020). Inlet flow rate of perfusion bioreactors affects fluid flow dynamics, but not oxygen concentration in 3D-printed scaffolds for bone tissue engineering: Computational analysis and experimental validation. *Comput. Biol. Med.* 124, 103826. doi:10.1016/J.COMPBIOMED.2020.103826.

Shakeel, M. (2013). 2-D coupled computational model of biological cell proliferation and nutrient delivery in a perfusion bioreactor. *Math. Biosci.* 242, 86–94. doi:10.1016/j.mbs.2012.12.004.

Sharifi, F., Firoozabadi, B., and Firoozbakhsh, K. (2019). Numerical Investigations of Hepatic

Spheroids Metabolic Reactions in a Perfusion Bioreactor. *Front. Bioeng. Biotechnol.* 7, 221. doi:10.3389/fbioe.2019.00221.

Sibilio, S., De Gregorio, V., Urciuolo, F., Netti, P. A., and Imparato, G. (2019). Effect of peristaltic-like movement on bioengineered intestinal tube. *Mater. Today Bio* 4, 100027. doi:10.1016/j.mtbio.2019.100027.

Simčík, M. ˇ, Mota, A., Ruzicka, M. C., Vicente, A., and Teixeira, J. (2011). CFD simulation and experimental measurement of gas holdup and liquid interstitial velocity in internal loop airlift reactor. doi:10.1016/j.ces.2011.01.059.

Vance, J., Galley, S., Liu, D. F., and Donahue, S. W. (2005). Mechanical stimulation of MC3T3 osteoblastic cells in a bone tissue-engineering bioreactor enhances prostaglandin E2 release. *Tissue Eng.* 11, 1832–1839. doi:10.1089/TEN.2005.11.1832.

Vetsch, J. R., Betts, D. C., Müller, R., and Hofmann, S. (2017). Flow velocity-driven differentiation of human mesenchymal stromal cells in silk fibroin scaffolds: A combined experimental and computational approach. *PLoS One* 12, e0180781. doi:10.1371/journal.pone.0180781.

Vetsch, J. R., Müller, R., and Hofmann, S. (2015). The evolution of simulation techniques for dynamic bone tissue engineering in bioreactors. *J. Tissue Eng. Regen. Med.* 9, 903–917. doi:10.1002/term.1733.

Visone, R., Talò, G., Lopa, S., Rasponi, M., and Moretti, M. (2018). Enhancing all-in-one bioreactors by combining interstitial perfusion, electrical stimulation, on-line monitoring and testing within a single chamber for cardiac constructs. *Sci. Reports 2018 81* 8, 1–13. doi:10.1038/s41598-018-35019-w.

Wang, Z., Huang, C., Wang, J., Wang, P., Bi, S., and Abbas, C. A. (2019). Design and Simulation of Flow Field for Bone Tissue Engineering Scaffold Based on Triply Periodic Minimal Surface. *J. Mech. Eng* 32, 19. doi:10.1186/s10033-019-0329-7.

Xue, R., Chung, B., Tamaddon, M., Carr, J., Liu, C., and Cartmell, S. H. (2019). Osteochondral tissue coculture: An in vitro and in silico approach. *Biotechnol. Bioeng.* 116, 3112–3123. doi:10.1002/bit.27127.

Yan, X., Bergstrom, D. J., and Chen, X. B. (2012). Modeling of cell cultures in perfusion bioreactors. *IEEE Trans. Biomed. Eng.* 59, 2568–2575. doi:10.1109/TBME.2012.2206077.

Zermatten, E., Vetsch, J. R., Ruffoni, D., Hofmann, S., Müller, R., and Steinfeld, A. (2014). Micro-Computed Tomography Based Computational Fluid Dynamics for the Determination of Shear Stresses in Scaffolds Within a Perfusion Bioreactor. *Ann. Biomed. Eng.* 42, 1085–1094. doi:10.1007/s10439-014-0981-0.

Zhao, F., Chella, R., and Ma, T. (2007). Effects of shear stress on 3-D human mesenchymal stem cell construct development in a perfusion bioreactor system: Experiments and hydrodynamic modeling. *Biotechnol. Bioeng.* 96, 584–595. doi:10.1002/BIT.21184.

Zhao, F., Melke, J., Ito, K., van Rietbergen, B., and Hofmann, S. (2019). A multiscale computational fluid dynamics approach to simulate the micro-fluidic environment within a tissue engineering scaffold with highly irregular pore geometry. *Biomech. Model. Mechanobiol. 2019 186* 18, 1965–1977. doi:10.1007/S10237-019-01188-4.

Zhao, F., Pathi, P., Grayson, W., Xing, Q., Locke, B. R., and Ma, T. (2005). Effects of oxygen transport on 3-D human mesenchymal stem cell metabolic activity in perfusion and static cultures: Experiments and mathematical model. *Biotechnol. Prog.* 21, 1269–1280. doi:10.1021/BP0500664.

Zhao, F., van Rietbergen, B., Ito, K., and Hofmann, S. (2018). Flow rates in perfusion bioreactors

to maximise mineralisation in bone tissue engineering in vitro. *J. Biomech.* 79, 232–237. doi:10.1016/J.JBIOMECH.2018.08.004.

Zhao, F., Vaughan, T. J., and McNamara, L. M. (2016). Quantification of fluid shear stress in bone tissue engineering scaffolds with spherical and cubical pore architectures. *Biomech. Model. Mechanobiol.* 15, 561–577. doi:10.1007/s10237-015-0710-0.

Zienkiewicz, O. C., Taylor, R. L., and Nithiarasu, P. (2013). The Finite Element Method for Fluid Dynamics: Seventh Edition. *Finite Elem. Method Fluid Dyn. Seventh Ed.*, 1–544. doi:10.1016/C2009-0-26328-8.

Chapter 5

A novel dual-flow perfusion bioreactor

In Chapter 3, dual-flow bioreactors were described as systems that supply an additional direction of flow enhancing transport properties and flow-based mechanical stimulation. This chapter illustrates an innovative dual perfusion flow bioreactor and a 3D porous channeled PLLA scaffold used to model the diffusion of drug carriers from blood to tissue or to develop a potentially dynamic *in vitro* approach to replicate a functional nasal cavity. The contribution of this thesis work in the applications just mentioned consisted in analyzing, validating, and optimizing the fluid dynamics of the scaffold-bioreactor system.

Tissue Engineering application of the novel scaffold-bioreactor system

5.1 Pre-clinical drug model

Traditionally, drug screening methods have included *in vivo* animal experiments and *in vitro* 2D-cultured cell line-based screening assays (Brajša et al., 2016). However, when using these models, many drugs pre-clinically evaluated as "active" were further proved to be clinically useless in the human system. For instance, 2D static cultures do not accurately represent the native in vivo environment due to many limitations, particularly nutrient and oxygen distribution and removal of waste products (Saltzman, 2004; Azuaje, 2011; Fu et al., 2017).

On the other hand, *in vivo* and *in vitro* animal models in the Tissue Engineering field have been fundamental for achieving remarkable progress in the knowledge of disease mechanisms and for novel therapies testing (Mak et al., 2014). However, the animals' use shows significant disadvantages and limits (Caddeo et al., 2017):

- it is a central ethical debate;
- it is not always reliable as human-like models (even though some human pathologies can be induced in animal models, the molecular mechanisms driving their onset and progression are often significantly different);
- it can be extremely costly;

- it is influenced by in vivo systemic effects and high inter-subject variability that do not allow either controlling or obtaining precise real-time information on individual bioprocess parameters;
- it cannot effectively summarize human physiology (existing animal models have shown human ineffectiveness of certain drugs successfully tested on animals).

In this context, the 3Rs principle (Replacement, Reduction, and Refinement) was introduced by Russell et al. (Russell and Burch, 1960) to propose advanced alternatives to animal testing for scientific purposes, pre-clinical testing, and more ethical research. Among the advanced bioengineering tools and technologies for developing better and more predictive alternative methods, the novel bioreactor described in this thesis can be a potential tool to provide monitored and controlled 3D *in vitro* culture conditions. Once validated, such apparatus may find application in the testing of drugs, or the evaluation of new substitute biomaterials, reducing the use of laboratory animals, according to the 3Rs principle.

Similarly, in the research field of drug delivery and pre-screening tests, a tubular perfusion bioreactor mimicking a blood vessel was developed by Al-Attar et al. (Al-Attar and Madihally, 2020). This study aimed to investigate the role of fluid flow on the release profile of a drug encapsulated in electrospun microfibers. This model showed how several operating parameters, such as inlet fluid velocity, bioreactor geometry, and cellular uptake rate, can affect the drug release from a porous tissue-like microenvironment. It is a faith of this work that more reliable results can be achieved when modeling the drug response by using bioreactors and 3D dynamic culture compared to the traditional 2D in vitro cell culture and the animal in vivo testing.

5.2 *In vitro* model for nasal mucosa

Long-term functional solutions for extensive airway disease and damage are prominent types of research in regenerative medicine and tissue engineering. Traditional techniques for airway reconstruction and regeneration by means of prosthetic materials, autologous and allogeneic tissues have proven to be unsuccessful in providing a physiologically balanced environment within the damaged tissue (Fishman et al., 2014). Among the airway tissue of the human body, the nose is the first site to be exposed to inhaled agents, such as pollutants, particles, allergen, or gases, since it is the entry point to the respiratory system (Müller et al., 2013). In vitro study of nasal cavity might provide manifest advancements in laboratory models of the respiratory lining, therapeutic tests for drug delivery, and characterization of tissue response to nasal airflows (Even-Tzur et al., 2010; Kreft et al., 2015; Papazian et al.,

2016). To create a nasal mucosa equivalent, an air-liquid-interface (ALI) culture is needed so that epithelial cells can form motile cilia, allowing the movement of mucus and foreign particles toward the throat (Soleas et al., 2012). Porous membranes have been extensively utilized for respiratory epithelium culture to investigate the mechanisms involved in the airway microenvironment (de Jong et al., 1994; Even-Tzur et al., 2010; Morris et al., 2014; Charles et al., 2019). However, this type of culture system is not suitable for large-scale culture, a structural characteristic widely ignored by conventional in vitro culture methods but crucial for therapeutic applications (Raredon et al., 2015).

In a dynamic 3D system that recreates the native environment of the nasal mucosa, several tests of airflow need to be performed to pump a correct airflow rate, which varies from 80 to 200 ml/s during normal breathing (Issakhov et al., 2021). In short, there are different approaches to the functional regeneration of airway mucosa, such as ALI mono-layered culture (Lee et al., 2005), in vitro studies of epithelial cells from isolated mucosa tissue or biopsies (Martens et al., 2019), and bioreactor systems using a culture medium in combination with pumped air (Ghaedi et al., 2014). These bioreactor systems create an ideal cell culture model that offers more controllable, versatile, and reproducible setups than other approaches: detailed airflow comparisons over restricted ranges of airflow rate and their cellular response could be experimentally studied. This feature offers a significant advantage over the numerical inspiratory airflow simulations that can only provide a fluid-dynamic analysis to reproduce the complex nasal tissue (Croce et al., 2006; Doorly et al., 2008; Li et al., 2017). Moreover, large-scale dynamic culture on 3D scaffolds inside a bioreactor could provide an innovative nasal model over most airway tissue models that merely mimic the epithelial layer (Steinke et al., 2014). Nasal cartilage and mucosa should be presented as co-culture systems, including epithelial and chondrocyte cells seeded on composite scaffolds, for producing clinically viable tissues around reconstructing the human nose (Oseni et al., 2013). Xu et al. successfully created engineered cartilage with a 3D-printing technique as human nasal alar cartilage, resulting in cell and tissue morphologic features similar to native lateral cartilage (Xu et al., 2015). Although perfectly adequate for nasal cartilage reconstruction, such 3D scaffolds cannot recreate an integrated architecture representing the ALI interface for the mucosa environment. On the other hand, developing 3D scaffolds as more intricate matrices for the *in vitro* testing of the entire nasal cavity could provide a more representative model to support cell culture and study nasal airways.

In this thesis, the designed novel bioreactor system and the channeled scaffold described in 4.1.1 were also used to provide an *in vitro* model to test large-scale cell culture for nasal

reconstruction. The scaffold-bioreactor assembly was assessed for dynamic perfusion of culture media and continuous airflow. To investigate whether such apparatus was suitable for mimicking nasal airway and allowing cell culture, the fluid dynamics of the system were evaluated in terms of airflow regimen and radial diffusion of culture media from the external surface towards the lumen of the scaffold. The peculiar geometry of the scaffold gives the advance of culturing different cells type both in the lumen and in the porous wall of the 3D construct, as the nasal cavity requires for cartilage and mucosa tissues generation. Subsequently, a dynamic system combining both 3D matrix and bioreactor system was provided to create a potential tool with particular architecture properties for nasal tissue engineering applications. Finally, the growth of lung epithelial cells (16HBE and H292 cell lines) was preliminarily investigated in static conditions on the tubular scaffold at an air-liquid interface.

5.3 Experimental apparatus

The design of a novel dual-flow perfusion bioreactor

An advanced dual-flow perfusion bioreactor was designed to induce a tunable radial flow throughout the microporous matrix of a hollow cylindrical scaffold.

The system consists of two cylindrical glass tubes connected by means of two horizontal ducts (Fig. 5.1a). The bigger column (ID= 3.6 cm and H= cm) locates a thin glass tube (ID = 0.5 cm and H = 3.5 cm) where the scaffold is fixed. The smaller column is a glass tube with ID = 1.2 cm and H = 15 cm. A glass lid with a central hole through which the thin glass tube (ID = 0.5 cm) is inserted closes the bioreactor system in order to maintain sterility. The two columns and the thin glass tube allow the individual control of two perfusion flows: the External Perfusion Circuit (EPC) and the Internal Perfusion Circuit (IPC). The EPC (Figure 5.1b) contains the bubble column, the main column, and a peristaltic pump (Model M025; VerderFlex). The latter ensures the recirculation and oxygenation of the medium, thus forcing the air bubbles to rise in the small column and to drag part of the liquid towards the bigger one. The IPC consists of a thin glass tube and a peristaltic pump feeding the scaffold lumen with air or liquid phase. In brief, the two perfusion circuits allow both radial perfusion through a porous polymeric matrix (IPC circuit) and a continuous circulation of culture medium, at a fixed flow rate, inside the device (EPC circuit).

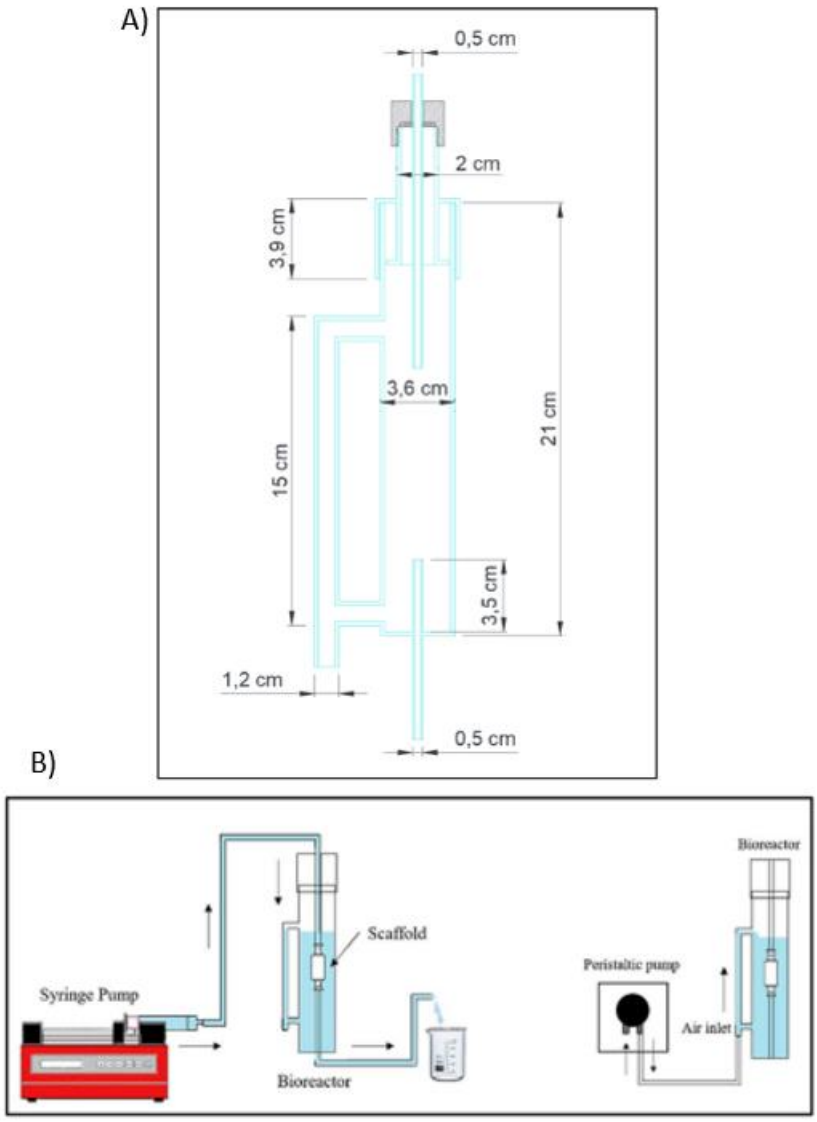

Figure 5.1 A) Scheme of the dual-flow bioreactor design. B) Scheme of the Inner Perfusion Circuit (IPC) (left) and the Externa Perfusion Circuit (right). (Lombardo et al., 2021)

Biocompatible polypropylene Luer-Lock connectors (Kiyatec) were used for connecting the scaffold to the thin tube. The scaffold can be attached to the center of the main column of the IPC while maintaining sterile conditions and avoiding leakage during liquid circulation.

Cylindrical PLLA hollow scaffold fabrication and characterization

Cylindrical PLLA hollow scaffolds were fabricated using the thermally induced phase separation (TIPS) technique. A 4% (wt/wt) PLLA solution was prepared by dissolving the PLLA (RESOMER L 209 S) in 1-4 dioxane (Merck KGaA, Darmstadt, Germany) as the solvent and adding deionized water as non-solvent. The dioxane/water ratio was fixed at 87/13 (La Carrubba et al., 2010; Carfì Pavia et al., 2019). The solution was initially kept at 60°C to induce its homogenization and then poured into the sample holder consisting of an

empty aluminum cylinder with an external diameter of 3.5 cm and a height of 4 cm. Additionally, a stainless-steel rod was used to create the lumen of the hollow scaffold (Fig. 5.2).

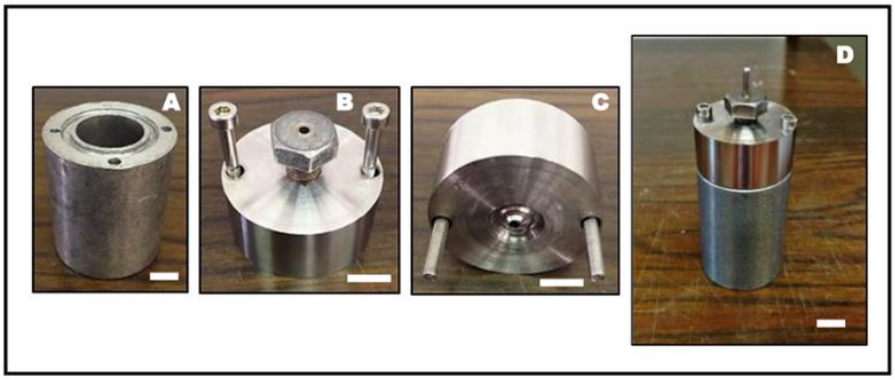

Figure 5.2 Aluminum sample holder for hollow cylindrical scaffold synthesis via TIPS: body (A), cover top view (B), cover bottom view (C); sample holder assembled (D). Scale bar 1 cm.

In the TIPS protocol, the thermal-time path included a sudden lowering of the temperature up to 0°C to induce the phase separation, a pool immersion of the sample holder into a thermostatic water bath for 10 minutes, and a quench step in an ethyl alcohol bath at -20°C for 15 min. Then, the PLLA matrix was pulled out from the sample holder, rinsed with deionized water to remove any solvent trace, and dried overnight under vacuum at 35°C. Morphological analysis of the as-prepared scaffolds was carried out with a Scanning Electron Microscope (Phenom Pro-X, Phenom-World, Netherlands) operating at an accelerating voltage of 10 kV. The samples were fractured in liquid nitrogen to obtain a thickness of around 0.5 cm. Then, they were mounted on a metal stub using a sticky carbon disc and finally coated with gold (thickness ~ 4 nm) in a sputter coater under an argon atmosphere to increase the conductivity. The average pore size was determined by performing image analysis on the SEM micrographs using Image-J software.

Perfusion system characterization for pre-clinical drug model

Permeability tests were performed to evaluate the efficiency of radial perfusion through the scaffold. A quantitative diffusion test was carried out to explore the possibility of controlling the radial perfusion flow in terms of flow direction and flow rate. Deionized water at a constant flow rate (0.5 ml/min and 1 ml/min) was dispensed by a syringe pump (New Era Single Syringe Pump NE-1000) via the IPC inside the lumen of the scaffold located into the water-filled main column. After a well-defined time, the water coming out from the circuit was weighted. The radial flow across the scaffold was obtained by subtracting the mean

weight of the water outflowing from the syringe pump (measured independently previously) from the mean reading of three measurements. Several tests were conducted by varying the height level between the bottom of the scaffold and the outlet of the IPC tube (H), as depicted in Fig. 5.3. Five different levels were investigated, with ΔH of 5 cm among them.

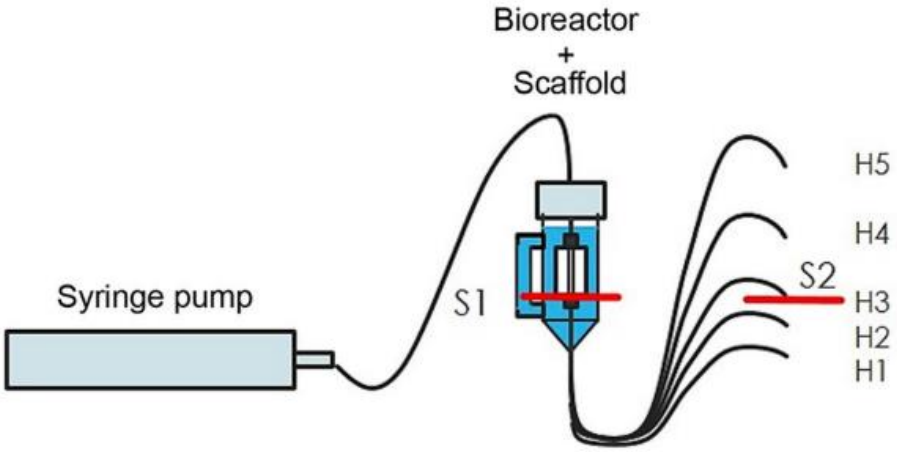

Figure 5.3 Experimental apparatus for scaffold permeability evaluation. For the calculation of the pressure in the lumen of the scaffold, Bernoulli's law was applied between level S1 and level S2 (solid red lines).

These data were also used to estimate the permeability of the scaffold. Darcy's Law was applied in cylindrical geometry for the permeability evaluation (Eq. 5.1).

$$Q = \frac{K\ 2\ \pi\ h_s(P_{ext}-P_{int})}{\mu\ ln\frac{r_{ext}}{r_{int}}} \qquad (5.1)$$

where Q is the radial flow, K is the permeability (m^2), h_s is the scaffold height (m), P_{ext} and P_{int} (Pa) are the pressure values at the scaffold external surface and in the lumen, respectively, μ is the fluid viscosity (Pa s), and r_{ext} and r_{int} are the external and internal radii of the scaffold (m), respectively. To calculate the permeability K, Darcy's Equation ought to be solved for a range of pressure drops across the perfused scaffold, as specified in Eq. 5.2:

$$K = \frac{Q}{(P_{ext}-P_{int})}\frac{\mu\ ln\frac{r_{ext}}{r_{int}}}{2\ \pi\ h_s} \qquad (5.2)$$

where $Q/(P_{ext} - P_{int})$ is the slope of the curve representing permeate flow as a function of pressure drop across the scaffold. To derive this curve, permeated flux, previously measured at different H, was used. The corresponding pressure drops across the scaffold were obtained from the hydrostatic wall pressure of the surrounding water at the scaffold base (Pe_{xt}) and by applying Bernoulli's Law (Eq. 5.3) to determine the average pressure at the inner channel of the scaffold (P_{int}).

$$\frac{P_1}{\rho g} + \frac{v_1^2}{2g} + z_1 = \frac{P_2}{\rho g} + \frac{v_2^2}{2g} + z_2 + y_{distr} \quad (5.3)$$

where P_i is the pressure at the considered i-section (Pa), v_i the fluid velocity (m/s), z_i is the static height (m), g the gravitational acceleration (m^2/s), ρ is the fluid density (kg/m^3), and y_{distr} the pressure drops (m). Specifically, Bernoulli's law was applied between the outlet of the IPC tube (S2) and the bottom of the scaffold (S1), as defined in Fig. 5.3.

If using a tube with the same diameter as the inner channel of the scaffold (2 mm), Bernoulli's equation was reduced to:

$$P_1 = P_2 + (z_2 - z_1 - y_{distr})\rho g \quad (5.4)$$

where P_1 corresponds to P_{int}, P_2 is the atmospheric pressure (Pa), and $z_2 - z_1$ is the above-defined H. According to the evaluated Reynold's number for the applied fluid flows, y_{distr} was estimated by the Poiseuille's Law (Eq. 5.5), valid for Newtonian and incompressible fluid flowing in a laminar regime.

$$y_{distr} = \frac{2fLv^2}{Dg} \quad (5.5)$$

where f is the friction factor (calculated as 16/Re for laminar flow regimes), L is the length of the tube, v is the fluid velocity along the tube, and D is the tube diameter. The obtained curve of the perfused flow rate as a function of the pressure drop across the scaffold was derived for two flow rates (0.5 ml/min and 1 ml/min), and the resulting permeability values were calculated. All the obtained data were plotted using Origin Lab Software.

Internal perfusion circuit (IPC) flow analysis for *in vitro* model of nasal mucosa

In this case, the IPC consists of the thin glass tube and a peristaltic pump feeding the scaffold lumen with air, as occurs to the *in vitro* airway model for nasal mucosa.

To simulate the native physiology of the nasal mucosa, cells should grow on the internal lumen of the scaffold while facing a specific gas flow rate. In the described system, the air flow rate is a function of the rpm, i.e., the voltage provided by the peristaltic pump connected to the interior lumen. For measuring the air flow rate, the bioreactor was connected to a graduated glass tube to which a water-soap solution was injected into the base. Specifically, the time taken by a soap bubble to reach a specific height of the graduated column was evaluated while varying the applied voltage. A range of 4-9 V, corresponding to 40-100 rpm, has been studied. In addition, to expand the range of available flow rates, measurements

were made using two silicon tubes of different diameters (2 and 4 mm) connected to the peristaltic pump.

Perfusion system characterization for *in vitro* model of nasal mucosa

For assessing the efficiency of radial perfusion through the scaffold, permeability tests were performed. First, a qualitative analysis was carried out to evaluate whether the liquid diffuses from the bulk towards the lumen of the scaffold. Thus, the fluid can reach the inner lumen and supply nourishment to the seeded mucosal cells. The qualitative diffusion analysis was carried out by adding toluidine blue as a dye for the deionized water (0.1% v/v) to observe the staining of the scaffold. Eight tests have been carried out at different timespan by combining the on- and off-mode of the two pumps connected to the internal and external flow of the bioreactor, respectively: (i) both pumps off for 30 minutes; (ii) only EPC on for 30 minutes; (iii) both pumps off for 60 minutes; (iv) only EPC on for 60 minutes; (v) only IPC on for 30 minutes; (vi) both pumps on for 30 minutes; (vii) only IPC on for 60 minutes; (iix) both pumps on for 60 minutes. Then, scaffolds were extracted and cut into slices.

A second test aimed to measure the radial perfusion flow through the scaffold pores from the bulk to the lumen of the scaffold in the bioreactor filled with water. Two external conditions were evaluated: atmospheric pressure and hydrostatic pressure. In the atmospheric pressure system, the outlet pipe (connected to the bioreactor and expelling the diffused water) was exposed to air, and different air flow rates of IPC were applied. As for the system under hydrostatic pressure, the outlet tube (connected to the bioreactor and ejecting the diffused water) was submerged at different levels inside a beaker containing water. Six different submerging levels were investigated, which are 1, 2, 3, 4, 5, and 5.5 cm below the free surface, at the air flow rate of 1.5 ml/s. The goal of the hydrostatic pressure set-up was to calculate, at a fixed air flow rate, the level of liquid inside the beaker that could arrest the lowering of the liquid in the bioreactor and, thus, diffusion through the scaffold. For both conditions, a lowering of the liquid height in the bioreactor was calculated by measuring the volume of liquid that missed reaching the initial liquid level after a well-defined time. Indeed, this volume corresponds to the water diffused through the scaffold.

Cell culture for *in vitro* model of nasal mucosa

The cell line 16HBE (human bronchial epithelial cell line) was isolated from the bronchus of a heart-lung patient and immortalized with pSVori, an origin-of-replication-defective SV40 plasmid. The 16HBE were kept in culture with a mixture (1:1 ratio) of high glucose

Dulbecco's Modified Eagle's Medium (DMEM) supplemented with 10% heat-inactivated fetal bovine serum (FBS), 100 u/mL penicillin, and 100 μg/mL streptomycin and induced to grow in a T-75 flask. The flask was placed in an incubator at a temperature of 37°C. H292 cell line (human pulmonary mucoepidermoid carcinoma cell line) was maintained in Roswell Park Memorial Institute (RPMI) 1640 Medium supplemented with 10% heat-inactivated fetal bovine serum (FBS), 100 u/mL penicillin, and 100 μg/mL streptomycin and let it grow in a T-75 flask.

Cell seeding on polymeric tubular scaffolds for *in vitro* model of nasal mucosa

Before performing the cell seeding, scaffolds were incubated in 1X DPBS for 24 hours at 4°C to soften their texture. Subsequently, the tubular scaffolds were incubated for 24 hours at 4°C in high glucose Dulbecco's Modified Eagle's Medium (DMEM) supplemented with 100 u/mL penicillin and 100 ug/mL streptomycin and 10% heat-inactivated fetal bovine serum (FBS) to allow the following adhesion of cells to the scaffold. 16HBE and H292 cell lines were detached using 0.25X trypsin, and 30.000 cells were seeded onto 3 polymeric scaffolds (0.2 cm2 diameter; 2 cm length) for each cell line. Both groups were cultured for three weeks. Cultures were monitored for three weeks. At the end of every week, one sample for every group has been fixed for subsequent analysis.

Formalin-fixed paraffin-embedded scaffolds for *in vitro* model of nasal mucosa

Formalin-fixed, paraffin-embedded tubular scaffolds were prepared for each experimental condition. Each scaffold was treated with 10% formalin, dehydrated with alcohols of increasing grade and embedded in kerosene wax. Specifically, 4-5 μm-thick sections were obtained from the kerosene blocks of the included scaffolds with a cutting microtome. These sections were dewaxed in xylene for 30 min at 60°C and, after immersion in decreasing graded alcohols, rehydrated in distillation water at 23°C. After deparaffination, sections were stained with hematoxylin and eosin (H&E), rinsed in water, and dehydrated in graded alcohols. Finally, the sections were observed with an optical microscope.

5.4 Results

Morphology and porosity of PLLA scaffold

The TIPS technique was employed for synthesizing a hollow cylindric PLLA scaffold using a specific aluminum sample holder. Thin slices (thickness 0.5 cm) from different areas of

the as-obtained scaffold (OD = 2.5 cm, ID = 0.2 cm, H = 3.5 cm) were analyzed to verify the homogeneity of the sample structure. The cross-section morphologies are shown in Fig. 5.4. SEM micrograph of the external polymeric matrix revealed an average pore size of about 30–40 μm (Fig. 5.4A). The surface of the lumen was also microporous, with a pore size of 20–30 μm, as observed in Fig. 5.4B.

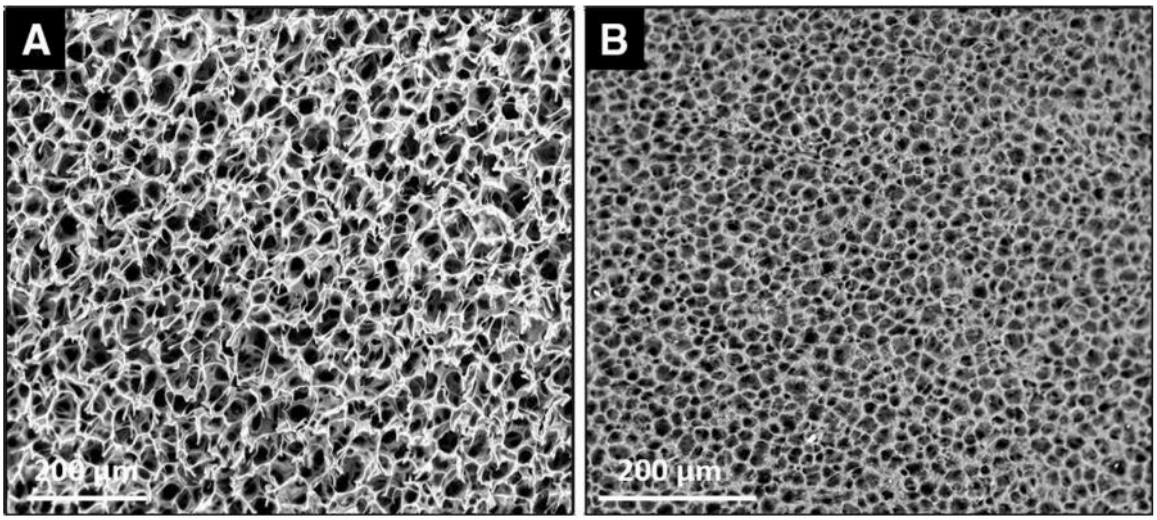

Figure 5.4 SEM micrographs of PLLA scaffold produced by TIPS at 0 °C for 10 min. A) External polymeric matrix. B) Lumen surface in contact with the metallic support. Scale bar 200 μm

The efficiency of the perfusion system and evaluation of the scaffold permeability

Radial flow rates were measured through the hollow cylindrical scaffold at two different IPC flow rates (0.5 ml/min and 1 ml/min) and for different heights (H) (Fig. 5.5).

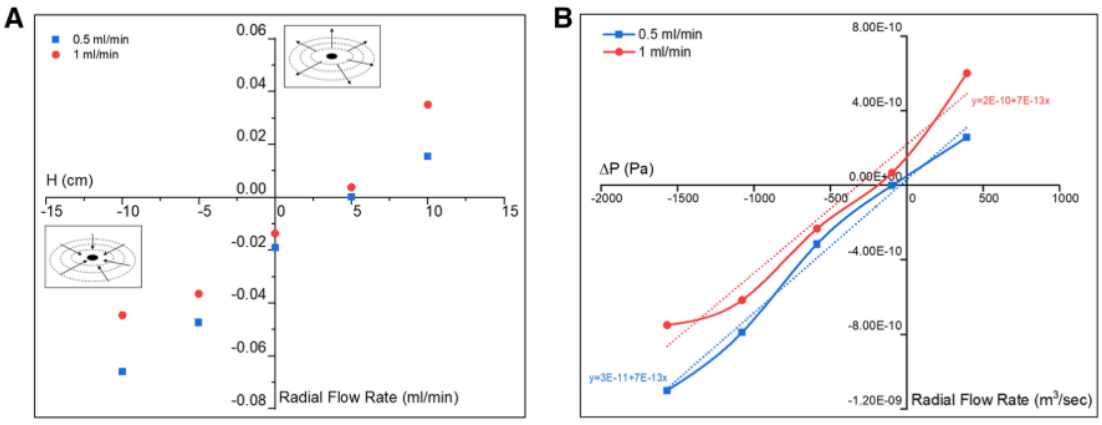

Figure 5.5 A) Radial flow rate (ml/min) through the scaffold as a function of different height levels H (cm) between the bottom of the scaffold and the outlet of the IPC tube. B) Radial Flow Rate (m^3/sec) throughout the scaffold as a function of the estimated pressure drop ($\Delta P = P_{ext} - P_{int}$) (Pa).

Figure 5.5A shows the calculated radial flow rates. By convention, the flow was assumed as negative flow from the edge to the internal channel of the scaffold (inflow), and a positive sign was adopted for the opposite flow direction (outflow). For both tested flow rates, when H is negative (i.e., the tube outlet is further down to the scaffold), a radial flux from the outside towards the inner surface of the scaffold was observed (inflow). When the tube outlet was raised, flow rate decreased to zero at the 5-cm level. Further lifting the tube, a change in the flow direction was observed as the fluid flowed radially from the inner channel to the mass (outflow). For both tested IPC flow rates, the flow increased by increasing H.

Building on the previous results, the absolute permeability of the as-produced scaffold was evaluated, according to Eq. 5.2, by combining the permeated flow rate measurements with Darcy's Theory, Bernoulli's Equation, and Poiseuille's Law. Figure 5.5B describes the permeate flow across the scaffold plotted against the estimated total pressure drop for the two pumped flow rates. Although the linear fitting of the 1 ml/min curve revealed a minor accuracy, still exhibiting an $R^2 > 0.95$, an identical slope resulted for the two fitting lines, thus leading to a constant permeability value. By solving Eq. 5.2, the calculated permeability K was $1.12 \times 10^{-14}\,m^2$.

Air flow fluid characterization for *in vitro* model of nasal mucosa

An experimental setup was carried out to evaluate the amplitude order of the air flow rate in the IPC caused by a pumping speed of 40-100 RPM. For this assessment, the PLLA scaffold was located at the center of the main column and fixed via standard Luer-Lock connectors that allowed an easy assembly while avoiding leakage during the fluid circulation. Using two different silicon tubes as connectors between the pump and the IPC, air flow rates varying from 0.5 to 2.5 ml/s were measured, as seen in Fig. 5.6, where data are plotted as a function of the voltage of the peristaltic pump.

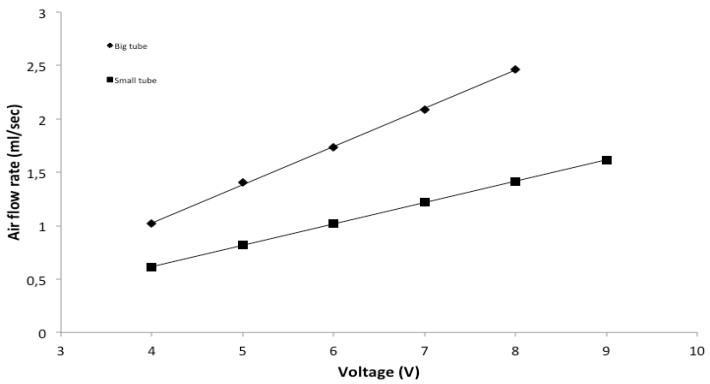

Figure 5.6 Measured air flow rates vs pump voltage. Due silicon tubes with different diameters were used to widen the air flow rates range.

As can be noted, the increase in air flow rate is linear as the voltage applied to the pump varies. Moreover, the Reynolds number values within the lumen resulted in the laminar range for all the tested air flows (Re = 22-112).

The efficiency of the perfusion system for *in vitro* model of nasal mucosa

After the eight tests were carried out at different timespan and modes of the two pumps connected to IPC and EPC, scaffolds were extracted and cut into slices. In Fig. 5.7, the radial staining of the matrix cross-section can be observed.

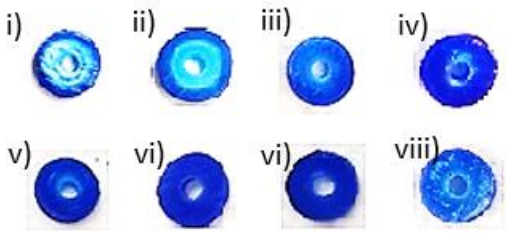

Figure 5.7 Cross-section of the scaffold slices after the test with the dye at different timespan and by combining the on- and off-mode of the two pumps connected to the internal and external flow of the bioreactor, respectively: (i) both pumps off for 30 minutes; (ii) only EPC on for 30 minutes; (iii) both pumps off for 60 minutes; (iv) only EPC on for 60 minutes; (v) only IPC on for 30 minutes; (vi) both pumps on for 30 minutes; (vii) only IPC on for 60 minutes; (iix) both pumps on for 60 minutes.

As a practical matter, after tests with just EPC on, we did not detect appreciable staining inside the scaffold channel (Fig. 5.7i, ii, iii, and iv). Better penetration of the blue dye through the porous structure (from the external surface to the lumen of the scaffold) was observed only as the IPC was activated. This behavior is suggestive that fluid could permeate through scaffolds more efficiently with air pumped into the lumen, leading to an efficient distribution of nutrients and a potential cell culture inside that channel.

The ability of the system to remain functional to support fluid flow towards the lumen was also evaluated by quantifying the radial flow rate of the fluid at different air flow rates and external pressure (atmospheric pressure and hydrostatic pressure). The change in airflow rate at the atmospheric pressure did not result in a wide range of radial flow (8 – 10 µl/min) but rather in a controllable liquid diffusion that increased with increasing inlet air flow rate. When considering higher external pressure, obtained data revealed a global range of 0 – 10 µl/min, as shown in Fig. 5.8.

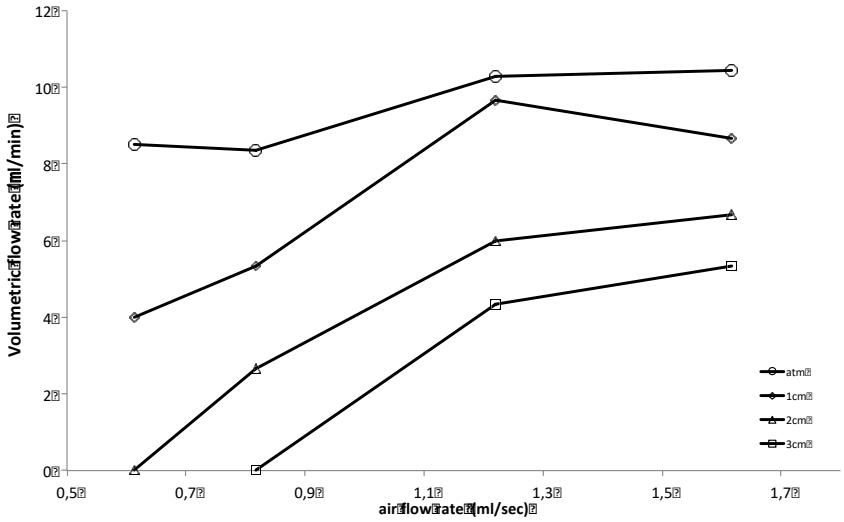

Figure 5.8 Diffusive radial flow rate as a function of air flow rate at atmospheric (outlet tube open to external atmosphere) and hydrostatic pressures (outlet tube submerged in a water-filled beaker at 1, 2, and 3 cm below the free surface) as external pressure of the outlet tube.

When the outlet tube was submerged at 2 and 3 cm, the absence of radial flow was observed at the lowest air flow rate, suggesting a balance between external and internal pressures. This condition could be desired during a post-seeding phase (during which the culture medium reaches the cellular layer of the lumen) for nasal mucosa since its physiology involves airflow over liquid flow. Overall, at a defined air flow rate, the system can precisely control the diffusive flow rate of the liquid, in terms of value and direction, until an equilibrium state is reached and diffusion between the outer walls and the scaffold lumen no longer occurs.

Preliminary seeding on tubular scaffolds for *in vitro* model of nasal mucosa

The ability of PLLA tubular scaffolds to support H292 and 16HBE culture in vitro was verified. Simultaneously, the same cell lines were seeded on classical cell culture flasks and used as a control. At the end of each time point during the three-week experiment, microscopic analysis was performed to study cell growth.

The adhesion and the growth of H292 and 16HBE microscopically evaluated appeared to evolve from monolayer to multi-layer (Fig. 5.9). However, the poor adhesion of the cells to the inner polymeric face of the three-dimensional PLLA scaffold and the evidence that cells were not tightly joined were the biggest criticalities. Moreover, it was also possible to notice that the growth was discontinuous around the circumference of the scaffold, creating small clots of cells in a few spots (Fig. 5.10a, b, c).

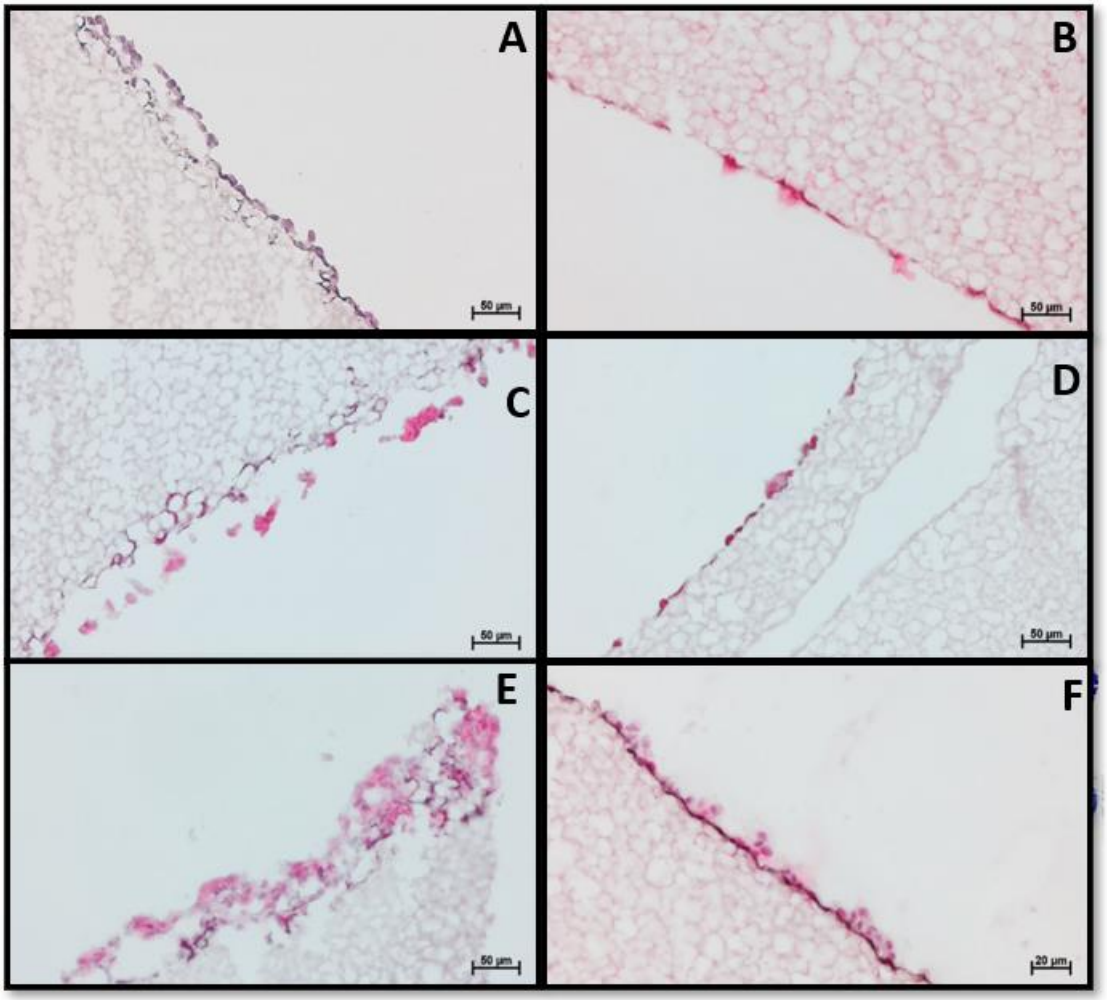

Figure 5.9 Cell adhesion after one (a-b) two (c-d) and three (e-f) weeks/ growth of 16HBE (a-c-e) and H292 (b-d-f) cell lines on the inner side of the 3D PLLA scaffolds. The growth, from a monolayer to a multi-layer, is not completely adhered to the inner face of the scaffold. Each cell does not appear to be tightly joined to each other.

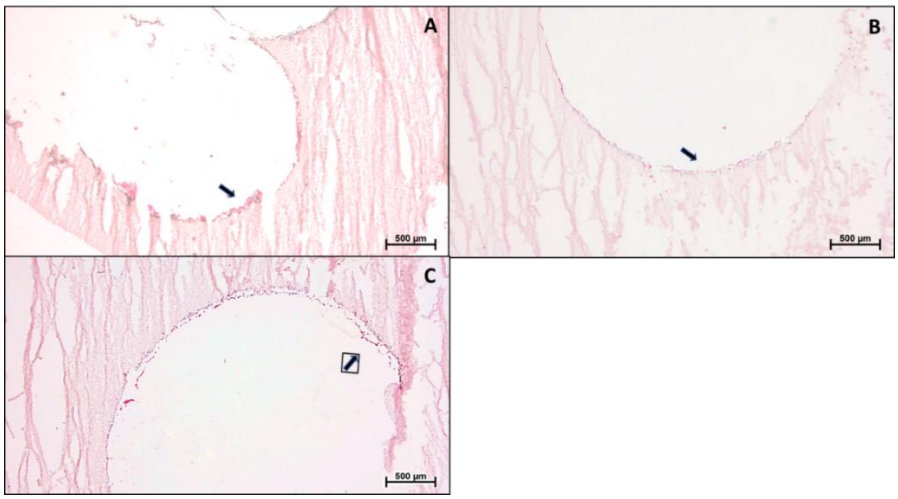

Figure 5.10 Cell growth all around the circumference of the scaffold after three weeks of culture. Small clots of cells in few spots (black arrows) can be observed.

5.5 Discussion

In this thesis work, a custom-made device was presented as an improvement of a common perfusion bioreactor. The goal was to design a perfusion bioreactor with two flow circuits, thus enlarging the traditional use of the bioreactor for TE applications to pharmaceutical purposes, such as the in vitro pre-screening of new drugs, and to a 3D model for the in vitro growth and testing of nasal mucosa cells, thus improving therapy and the total or partial regression of pathological states affecting patients with chronic airway conditions. The performed tests showed that a PLLA scaffold could be fixed to the center of the main column of the IPC while maintaining the sterility conditions of the system and avoiding leakage during the liquid circulation.

An interesting result emerged from the permeability tests, which revealed that the direction of radial flow could be managed simply by changing the height of the IPC tube outlet. Consequently, according to the desired application, one can precisely set the direction of the radial flow rate without specific devices (Egger et al., 2017) or the more approximating results of a computational simulation (Nguyen et al., 2016; Navarro et al., 2019). Recently, Tan et al. presented a new calibration method for the permeability measuring set-ups by testing the outwards radial flow through two concentric annular slits (Tan and Pillai, 2009). Compared with our outflowing results, this research also revealed an increase in the total pressure drop across the mold at higher flow rates. Although scaffold morphology differs from Tan's tested apparatus, both systems are within Darcy's flow regime, with an absolute permeability independent of the flow rate. Specifically, for our bioreactor, the validity of this assumption was assessed through a semi-empirical method. Our result was perfectly in line with the typical water permeability values for TE scaffolds, ranging from 10^{-16} to 10–9 m^2 (Pennella et al., 2013). Similarly, Wang et al. investigated the Darcy permeability of microporous (5–15 μm) PCL scaffold by monitoring fluid flow in response to a range of pressure differentials generated by a Bose Enduratec BioDynamic chamber (Wang et al., 2010). From their results, 6×10^{-14} m^2 was measured as permeability to water, matching with our PLLA microporous construct (20–40 μm). Owing to the similar morphological and mechanical properties of PCL and PLLA polymers (Díaz et al., 2014; Báez and Marcos-Fernández, 2015), the agreement between the results of our semi-empirical method and the more accurate measurements of a BioDynamic chamber consolidates the reliability of our protocol. Moreover, we used a low-cost procedure that does not require costly devices, such

as pressure transducers (Bilodeau et al., 2005a; Tan and Pillai, 2009; Israelowitz et al., 2012) and/or dynamic chambers (Wang et al., 2010).

To simulate the drug release process, it is necessary to achieve a homogeneous distribution of particles within the porous medium. For the designed bioreactor, the efficiency of the radial flow was evaluated using Polymeric Fluorescent Nanoparticles (FNPs) as a potential drug carrier model. α,β-Poly(N-2-hydroxyethyl)-d,l-aspartamide (PHEA) is the biocompatible protein-like copolymer chosen as precursors for the FNPs, showing good water solubility, absence of toxicity, antigenicity, and teratogenicity (Lombardo et al., 2021). A satisfactory level of penetration and uniform distribution of the particles was achieved throughout the entire polymeric matrix (Fig. 5.11), thus demonstrating the potential of our system as an in vitro model for drug pre-screening. This study was carefully analyzed by my research group, but more in-depth details are beyond the scope of my thesis work. More details are described by Lombardo et al. in the related article (Lombardo et al., 2021).

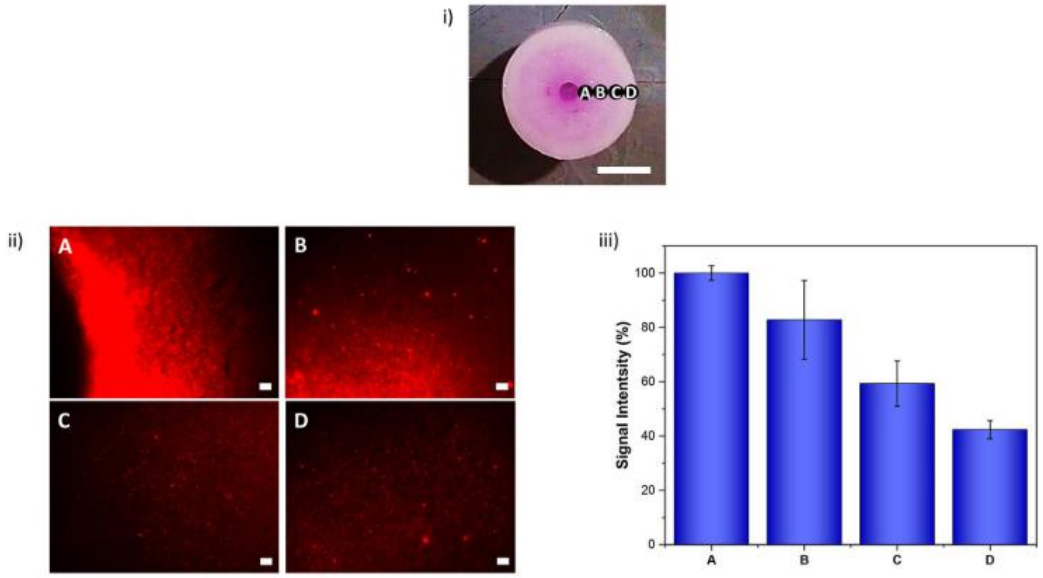

Figure 5.11 (i) Real picture of the PLLA scaffold cross-section with the 4 areas analyzed: A) lumen, B) close to the lumen, C) far from the lumen, and D) external surface. Scale bar 1 cm (ii) Fluorescence microscopy images of PLLA scaffold cross-section after the perfusion of FNPs diffused inside the bioreactor. Scale bar: 50 μm (iii) Fluorescence signal intensity (%) of the 4 different areas of the scaffold post perfusion. Data represent mean ± SD. There is no statistically significant difference between the samples ($p > 0.05$).

For the nasal mucosa model, while using the TIPS technique and a hollowed sample holder, PLLA scaffolds were fabricated with an internal lumen (ID = 2mm) where seeded cells might be simultaneously in contact with the culture medium ad air. To obtain this condition, a specific bioreactor has been used in which two independent flows (one external and one internal) can be applied. Specifically, the external flow recirculates the liquid along the entire bioreactor, while the internal flow sends air inside the lumen of the scaffold. The results

showed that, although increasing the timespan for dye diffusion improved the staining along the radial direction, there were noticeable differences in response to the active flow. For each tested timespan, the internal flow allowed a better dye penetration than the external flow, thus enhancing the nutrients supply to the cells in the scaffold thanks to the fluid diffusion through the porous wall. When a quantitative analysis was assessed to measure the resulting radial liquid flow rate at different air flows, it was evident that the radial diffusion also differed with altered external exit pressure. Overall, the results show the ability of the developed apparatus to elicit distinct liquid flow in terms of value and direction, thus demonstrating the significance of this system in the development of in vitro studies for mucosa defects. As expected, higher exit pressure affected the radial flow through the scaffold, resulting in a lower diffusion towards the internal lumen. This behavior is likely due to a generated back-pressure altering the ratio of permeate to retentate flowrates (Shipley et al., 2010), corroborating that differences in radial diffusion could be accurately controlled when a defined air flow rate is applied.

The change in airflow rate at the atmospheric pressure did not result in a wide range of radial flow (8 – 10 µl/min) but rather in a controllable liquid diffusion that increased with increasing the inlet air flow rate. To achieve zero radial flow condition, which occurs when the balance between external and internal pressures prevents radial diffusion, higher exit pressure than the atmospheric pressure needed to be adopted. Indeed, the nasal mucosa is an airway tissue, intimately in contact with the inspired air, thus, exposed to a mere air flow without liquid traces during its metabolic activity (Christiane Schmidt et al., 1998).

The system capability to mimic *in vitro* the *in vivo* environment of the nasal mucosa was assessed, and it was evident that there was the potential for a dynamic 3D culture. This evidence could provide a more realistic representation of the cellular behavior due to a more accurate morphological and physiological in vivo–like cell response (Salah, 2018). A recent study using human tracheobronchial epithelial cells and fibroblasts seeded on a biological scaffold found that monocultures do not resemble the situation *in vivo* (Steinke et al., 2014). Another study demonstrated that a rotating bioreactor provides a successful epithelial expansion while alternately rolling a porous, absorbent construct through media and air, inducing human epithelial cells to express their native markers (Raredon et al., 2015). Overall, these findings suggest that scaffolds with seeded cells in a dynamic 3D environment support better tissue growth *in vitro*, which may have considerable implications for clinical use, such as experiments that rely on the growth and differentiation of nasal mucosa.

The most notable advantage of our system is that changes in airflow velocity inside the internal walls of the scaffold were seen to be controllable. High airflow velocity creates high shear stress that would mimic a normal cough, during which the native tissue shears secretions and foreign matter off its wall (Ren et al., 2020). On the other hand, expiratory flow rates generally decrease during airways diseases, such as emphysema (i.e., destruction of alveolar walls) and fibrosis (Ren et al., 2020). In addition, it was evident that our system can appropriately account for the range of Reynold's Number for airflow velocity since the typical rate of respiration in the nasal cavity is seen as a laminar flow (Ren et al., 2020).

To further investigate the effectiveness of our system for studying the nasal mucosa, it is also necessary to analyze the morphology and structural characteristics of the fabricated scaffold. Grafts must replicate the size, shape, and mechanical properties of the native defect to achieve the functional requirements for tissue repair (Niermeyer et al., 2020). The results of previous works (La Carrubba et al., 2008; Carfì Pavia et al., 2016; Conoscenti et al., 2017) demonstrated that the TIPS technique is one of the most versatile for scaffolds fabrication since engineered constructs with controlled structure and morphology can be prepared. Specifically, in this technique, a temperature variation induces the separation of a homogeneous polymer solution. Moreover, the combination of the operating conditions adopted in the process (i.e., polymer concentration, solvent/non-solvent ration, demixing temperature, and time) affects the structure and morphology of the obtained scaffolds in terms of average pore size and distribution, interconnectivity, and mechanical properties.

The aim of nasal tissue engineering is regenerating and/or healing mucosal tissue and cartilage in large-sized defects (Sharma et al., 2015). The designed system could achieve this outcome by using a cell source for the respiratory mucosal tissue, mechanical support mimicking the nasal cartilage (i.e., the PLLA scaffold), and a bioreactor able to reproduce a microenvironment similar to the desired tissue type. The ALI condition was also simulated in a previous study in which olfactory and respiratory primary cells were mono-layer cultured in specific inserts under air-liquid interface conditions for 21 days, achieving a successful mucus production (Ladel et al.). Other studies have also described reproducible methods to generate mono-layer ALI models in order to produce functional ciliated cells as in the nasal epithelial physiology (Lee et al., 2005; Ong et al., 2016; Martens et al., 2019).

In this thesis, the growth of lung epithelial cells (16HBE and H292 cell lines) was preliminarily investigated in static conditions on the fabricated tubular scaffold at an air-liquid interface. Both cell lines represent an ideal standardized model to reproduce respiratory epithelial cells. These specific cell lines were selected for their suitability to

reproduce respiratory mucosa ex-vivo within a tubular scaffold in an automated system (Martens et al., 2018; Upadhyay and Palmberg, 2018). After 3 weeks in culture, the cells were located at the edge of the scaffold or arranged in clusters. This observation is consistent with other studies on the bronchial epithelium, in which the scaffolds had clusters of cells in adjacent pores (Saksena et al., 2016; Dye et al., 2020).

Both nasal mucosa and cartilage tissue play a fundamental role in a full-thickness nasal reconstruction. No studies have been already completed demonstrating the creation of a functional composite graft that includes nasal mucosa and cartilage tissue (Niermeyer et al., 2020). In this thesis, a bioreactor and a 3D scaffold were utilized, and it was evident that a biological nasal-like reproduction might be feasible. Fluid dynamic analysis revealed that accurate control of the flow of the culture medium could be applied, reaching the inner channel of the scaffolding, where the mucosal cells would be seeded. For this future evaluation, PLLA scaffolds with a larger mean pore size (100 μm) than that used in this work (10 μm) should be designed in the scaffold thickness from the external surface to the internal channel, accomplishing cartilage tissue engineering properties, as indicated by Conoscenti et al. (Conoscenti et al., 2017). This scaffold morphology, with different pore sizes between the inner lumen and the remaining porous structure, is not easily fabricated via the TIPS technique. Interestingly, a previous work successfully produced and colonized a PLLA scaffold by combining thermally induced and diffusion induced phase separation techniques (TIPS and DIPS, respectively) for regenerating complex tissue (Carfì Pavia et al., 2010). Overall, this research has the potential to optimize the architecture of scaffolds for nasal reconstruction and thus direct dynamic cell culture into a suitable bioreactor that improves biological activities. Given the promising biological results of the preliminary analyses, the system is ready for further cell culture tests in dynamic for the *in vitro* study of complex biological systems, such as that of the nasal mucosa. Several variables will need to be taken into account during such tests in dynamic, including the maintenance of long-term performance (longer than 24 hours) in an environment with different physical conditions (incubator) and the removal of the waste products from the cells seeded on the inner channel. Future studies should also be voted to fabricate composite scaffolds suitable for nasal applications and biologically validate the presented apparatus, further to make such approach a reliable tool for large scale research.

5.6 Conclusions

A dual-flow perfusion bioreactor was developed and evaluated as a potential system for pre-screening in vitro assays and in vitro fabrication of the air-liquid interface of the nasal

mucosa. The size of the apparatus was designed to allow it to be housed in a standard cell culture incubator, thus reducing the volume of the medium, which should be sufficient for long-term cell culture. The fluid-dynamic properties of the bioreactor were tested and demonstrated that its original design offers several significant advantages over existing bioreactors.

First, the device offers the independent control of two flows across a hollow cylindrical porous scaffold: the external perfusion flow ensures good recirculation and oxygenation of the medium; the internal one provides radial diffusion through the entire volume of the scaffold. The direction of this radial flow and the perfusion rate can be precisely adjusted, depending on the desired application. Therefore, the dual-flow design enhances the effectiveness of dynamic cell culture perfusion within the 3D device. We have also shown that the apparatus allows easy measurement of scaffold permeability of the scaffold without the use of any pressure sensor, which is the most common tool for this type of evaluation. Finally, the tunable radial flow from the inner to the outer surface of the scaffold and vice versa demonstrates that our system can control the migration/diffusion of fluids through a hollow scaffold while mimicking flow conditions suitable for the release of drugs from nano-carriers and the delivery of nutrients to cells seeded in the scaffold channel. Although the device has the disadvantage of holding only one sample per time, it has a great potential to be used as a versatile device for multiple purposes, including pharmaceutical applications for new therapeutic breakthroughs, that in vitro reproduction of tissues with an air-liquid interface.

References

Al-Attar, T., and Madihally, S. V. (2020). Modeling the impact of fluid flow on resveratrol release from electrospun fibers. *Comput. Biol. Med.* 117. doi:10.1016/j.compbiomed.2020.103622.

Azuaje, F. (2011). Computational discrete models of tissue growth and regeneration. *Brief. Bioinform.* 12, 64–77. doi:10.1093/bib/bbq017.

Báez, J. E., and Marcos-Fernández, Á. (2015). A Comparison of Three Different Biodegradable Aliphatic Oligoesters (PGA, PLLA, and PCL) with Similar Linear Alkyl End Groups by DSC and SAXS. *Int. J. Polym. Anal. Charact.* 20, 637–644. doi:10.1080/1023666X.2015.1054138.

Bilodeau, K., Couet, F., Boccafoschi, F., and Mantovani, D. (2005). Design of a perfusion bioreactor specific to the regeneration of vascular tissues under mechanical stresses. *Artif. Organs* 29, 906–912. doi:10.1111/j.1525-1594.2005.00154.x.

Brajša, K., Trzun, M., Zlatar, I., and Jelić, D. (2016). Three-dimensional cell cultures as a new tool in drug discovery. *Period. Biol.* 118, 59–65. doi:10.18054/pb.2016.118.1.3940.

Caddeo, S., Boffito, M., and Sartori, S. (2017). Tissue Engineering Approaches in the Design of Healthy and Pathological In Vitro Tissue Models. *Front. Bioeng. Biotechnol.* 0, 40. doi:10.3389/FBIOE.2017.00040.

Carfì Pavia, F., Di Bella, M. A., Brucato, V., Blanda, V., Zummo, F., Vitrano, I., et al. (2019). A 3D-scaffold of PLLA induces the morphological differentiation and migration of primary astrocytes and promotes the production of extracellular vesicles. *Mol. Med. Rep.* 20, 1288–1296. doi:10.3892/MMR.2019.10351.

Carfì Pavia, F., La Carrubba, V., Ghersi, G., and Brucato, V. (2010). A composite PLLA scaffold for regeneration of complex tissues. *Int. J. Mater. Form.* 3, 571–574. doi:10.1007/s12289-010-0834-9.

Carfì Pavia, F., Palumbo, F. S., La Carrubba, V., Bongiovì, F., Brucato, V., Pitarresi, G., et al. (2016). Modulation of physical and biological properties of a composite PLLA and polyaspartamide derivative obtained via thermally induced phase separation (TIPS) technique. *Mater. Sci. Eng. C* 67, 561–569. doi:10.1016/j.msec.2016.05.040.

Charles, D. D., Fisher, J. R., Hoskinson, S. M., Medina-Colorado, A. A., Shen, Y. C., Chaaban, M. R., et al. (2019). Development of a Novel ex vivo Nasal Epithelial Cell Model Supporting Colonization With Human Nasal Microbiota. *Front. Cell. Infect. Microbiol.* 9, 165. doi:10.3389/fcimb.2019.00165.

Christiane Schmidt, M., Peter, H., Lang, S. R., Ditzinger, G., and Merkle, H. P. (1998). In vitro cell models to study nasal mucosal permeability and metabolism. *Adv. Drug Deliv. Rev.* 29, 51–79. doi:10.1016/S0169-409X(97)00061-6.

Conoscenti, G., Schneider, T., Stoelzel, K., Carfì Pavia, F., Brucato, V., Goegele, C., et al. (2017). PLLA scaffolds produced by thermally induced phase separation (TIPS) allow human chondrocyte growth and extracellular matrix formation dependent on pore size. *Mater. Sci. Eng. C* 80, 449–459. doi:10.1016/j.msec.2017.06.011.

Croce, C., Fodil, R., Durand, M., Sbirlea-Apiou, G., Caillibotte, G., Papon, J. F., et al. (2006). In Vitro Experiments and Numerical Simulations of Airflow in Realistic Nasal Airway Geometry. *Ann. Biomed. Eng.* 34, 997–1007. doi:10.1007/s10439-006-9094-8.

de Jong, P. M., van Sterkenburg, M. A., Hesseling, S. C., Kempenaar, J. A., Mulder, A. A., Mommaas, A. M., et al. (1994). Ciliogenesis in human bronchial epithelial cells cultured at

the air-liquid interface. *Am. J. Respir. Cell Mol. Biol.* 10, 271–277. doi:10.1165/ajrcmb.10.3.8117445.

Díaz, E., Puerto, I., Sandonis, I., and Ibañez, I. (2014). Morphology and Mechanical Properties of PLLA and PCL Scaffolds. *Polym. - Plast. Technol. Eng.* 53, 150–155. doi:10.1080/03602559.2013.843699.

Doorly, D. J., Taylor, D. J., and Schroter, R. C. (2008). Mechanics of airflow in the human nasal airways. *Respir. Physiol. Neurobiol.* 163, 100–110. doi:10.1016/j.resp.2008.07.027.

Dye, B. R., Youngblood, R. L., Oakes, R. S., Kasputis, T., Clough, D. W., Nagy, M. S., et al. (2020). Human lung organoids develop into adult airway-like structures directed by physico-chemical biomaterial properties. *Biomaterials* 234, 119757. doi:10.1101/564252.

Egger, D., Fischer, M., Clementi, A., Ribitsch, V., Hansmann, J., and Kasper, C. (2017). Development and characterization of a parallelizable perfusion bioreactor for 3D cell culture. *Bioengineering* 4. doi:10.3390/bioengineering4020051.

Even-Tzur, N., Jaffa, A., Gordon, Z., Gottlieb, R., Kloog, Y., Einav, S., et al. (2010). Air-liquid interface culture of nasal epithelial cells on denuded amniotic membranes. *Cell. Mol. Bioeng.* 3, 307–318. doi:10.1007/s12195-010-0118-y.

Fishman, J. M., Wiles, K., Lowdell, M. W., De Coppi, P., Elliott, M. J., Atala, A., et al. (2014). Airway tissue engineering: An update. *Expert Opin. Biol. Ther.* 14, 1477–1491. doi:10.1517/14712598.2014.938631.

Fu, N., Zhang, X., Sui, L., Liu, M., and Lin, Y. (2017). "Application of Scaffold Materials in Cartilage Tissue Engineering," in *Cartilage Regeneration, Stem Cell Biology and Regenerative Medicine*, ed. Y. Lin (Humana Press, Cham), 21–39. doi:10.1007/978-3-319-51617-2_2.

Ghaedi, M., Mendez, J. J., Bove, P. F., Sivarapatna, A., Raredon, M. S. B., and Niklason, L. E. (2014). Alveolar epithelial differentiation of human induced pluripotent stem cells in a rotating bioreactor. *Biomaterials* 35, 699–710. doi:10.1016/j.biomaterials.2013.10.018.

Israelowitz, M., Weyand, B., Rizvi, S., Vogt, P. M., and Von Schroeder, H. P. (2012). Development of a laminar flow bioreactor by computational fluid dynamics. *J. Healthc. Eng.* 3, 455–476. doi:10.1260/2040-2295.3.3.455.

Issakhov, A., Zhandaulet, Y., Abylkassymova, A., and Issakhov, A. (2021). A numerical simulation of air flow in the human respiratory system for various environmental conditions. *Theor. Biol. Med. Model.* 18, 2. doi:10.1186/s12976-020-00133-8.

Kreft, M. E., Jerman, U. D., Lasič, E., Rižner, T. L., Hevir-Kene, N., Peternel, L., et al. (2015). The characterization of the human nasal epithelial cell line RPMI 2650 under different culture conditions and their optimization for an appropriate in vitro nasal model. *Pharm. Res.* 32, 665–679. doi:10.1007/s11095-014-1494-0.

La Carrubba, V., Pavia, F. C., and Brucato, V. (2010). Tubular scaffold for vascular tissue engineering application. *Int. J. Mater. Form.* 3, 567–570. doi:10.1007/s12289-010-0833-x.

La Carrubba, V., Pavia, F. C., Brucato, V., and Piccarolo, S. (2008). PLLA/PLA scaffolds prepared via thermally induced phase separation (TIPS): Tuning of properties and biodegradability. *Int. J. Mater. Form.* 1, 619–622. doi:10.1007/s12289-008-0332-5.

Ladel, S., Schlossbauer, P., Flamm, J., Luksch, H., Mizaikoff, B., and Schindowski, K. Improved In Vitro Model for Intranasal Mucosal Drug Delivery: Primary Olfactory and Respiratory Epithelial Cells Compared with the Permanent Nasal Cell Line RPMI 2650. doi:10.3390/pharmaceutics11080367.

Lee, M. K., Yoo, J. W., Lin, H., Kim, Y. S., Kim, D. D., Choi, Y. M., et al. (2005). Air-liquid

interface culture of serially passaged human nasal epithelial cell monolayer for in vitro drug transport studies. *Drug Deliv. J. Deliv. Target. Ther. Agents* 12, 305–311. doi:10.1080/10717540500177009.

Li, C., Jiang, J., Dong, H., and Zhao, K. (2017). Computational modeling and validation of human nasal airflow under various breathing conditions. *J. Biomech.* 64, 59–68. doi:10.1016/j.jbiomech.2017.08.031.

Lombardo, M., Carfì Pavia, F., Craparo, E., Capuana, E., Cavallaro, G., Brucato, V., et al. (2021). Novel dual-flow perfusion bioreactor for in vitro pre-screening of nanoparticles delivery: design, characterization and testing. *Bioprocess Biosyst. Eng.* 44, 2361–2374. doi:10.1007/S00449-021-02609-4.

Mak, I. W. Y., Evaniew, N., and Ghert, M. (2014). Lost in translation: Animal models and clinical trials in cancer treatment. *Am. J. Transl. Res.* 6, 114–118. doi:1943-8141/AJTR1312010.

Martens, A., Amann, G., Schmidt, K., Gaupmann, R., Böhm, B., Dehlink, E., et al. (2019). An optimized, robust and reproducible protocol to generate well-differentiated primary nasal epithelial models from extremely premature infants. *Sci. Rep.* 9, 1–10. doi:10.1038/s41598-019-56737-9.

Martens, K., Hellings, P. W., and Steelant, B. (2018). Calu-3 epithelial cells exhibit different immune and epithelial barrier responses from freshly isolated primary nasal epithelial cells in vitro. *Clin. Transl. Allergy* 8, 40. doi:10.1186/S13601-018-0225-8/FIGURES/2.

Morris, G. E., Bridge, J. C., Brace, L. A., Knox, A. J., Aylott, J. W., Brightling, C. E., et al. (2014). A novel electrospun biphasic scaffold provides optimal three-dimensional topography for in vitro co-culture of airway epithelial and fibroblast cells. *Biofabrication* 6, 035014. doi:10.1088/1758-5082/6/3/035014.

Müller, L., Brighton, L. E., Carson, J. L., Fischer, W. A., and Jaspers, I. (2013). Culturing of human nasal epithelial cells at the air liquid interface. *J. Vis. Exp.* 80, e50646. doi:10.3791/50646.

Navarro, J., Swayambunathan, J., Janes, M. E., Santoro, M., Mikos, A. G., and Fisher, J. P. (2019). Dual-chambered membrane bioreactor for coculture of stratified cell populations. *Biotechnol. Bioeng.* 116, 3253–3268. doi:10.1002/bit.27164.

Nguyen, B., Ko, H., and Fisher, J. (2016). Tunable osteogenic differentiation of hMPCs in tubular perfusion system bioreactor. *Biotechnol. Bioeng.* 113, 1805–1813. doi:10.1002/BIT.25929.

Niermeyer, W. L., Rodman, C., Li, M. M., and Chiang, T. (2020). Tissue engineering applications in otolaryngology—The state of translation. *Laryngoscope Investig. Otolaryngol.* 5, 630–648. doi:10.1002/lio2.416.

Ong, H. X., Jackson, C. L., Cole, J. L., Lackie, P. M., Traini, D., Young, P. M., et al. (2016). Primary air-liquid interface culture of nasal epithelium for nasal drug delivery. *Mol. Pharm.* 13, 2242–2252. doi:10.1021/acs.molpharmaceut.5b00852.

Oseni, A. O., Butler, P. E., and Seifalian, A. M. (2013). Nasal reconstruction using tissue engineered constructs: An update. *Ann. Plast. Surg.* 71, 238–244. doi:10.1097/SAP.0b013e31824f20a3.

Papazian, D., Würtzen, P. A., and Hansen, S. W. K. (2016). Polarized Airway Epithelial Models for Immunological Co-Culture Studies. *Int. Arch. Allergy Immunol.* 170, 1–21. doi:10.1159/000445833.

Pennella, F., Cerino, G., Massai, D., Gallo, D., Falvo D'Urso Labate, G., Schiavi, A., et al. (2013). A survey of methods for the evaluation of tissue engineering scaffold permeability. *Ann. Biomed. Eng.* 41, 2027–2041. doi:10.1007/s10439-013-0815-5.

Raredon, M. S. B., Ghaedi, M., Calle, E. A., and Niklason, L. E. (2015). A Rotating Bioreactor for Scalable Culture and Differentiation of Respiratory Epithelium. *Cell Med.* 7, 109–121. doi:10.3727/215517914x681794.

Ren, S., Li, W., Wang, L., Shi, Y., Cai, M., Hao, L., et al. (2020). Numerical Analysis of Airway Mucus Clearance Effectiveness Using Assisted Coughing Techniques. *Sci. Rep.* 10, 2030. doi:10.1038/s41598-020-58922-7.

Russell, W. M. S., and Burch, R. L. (1960). The Principles of Humane Experimental Technique. *Med. J. Aust.* 1, 500–500. doi:10.5694/J.1326-5377.1960.TB73127.X.

Saksena, R., Gao, C., Wicox, M., and Mel, A. de (2016). Tubular organ epithelialisation. *J. Tissue Eng.* 7, 2041731416683950. doi:10.1177/2041731416683950.

Salah, N. A. (2018). In Vitro Bronchial Mucosa Model using Air-Liquid Interface culture on PLLA Electrospun Membrane.

Saltzman, W. M. (2004). *Tissue engineering: engineering principles for the design of replacement organs and tissues*. Oxford, UK: Oxford University Press Available at: http://books.google.com/books?id=KorDMxtkZ_wC&pgis=1.

Sharma, A., Janus, J. R., and Hamilton, G. S. (2015). Regenerative medicine and nasal surgery. *Mayo Clin. Proc.* 90, 148–158. doi:10.1016/j.mayocp.2014.10.002.

Shipley, R. J., Waters, S. L., and Ellis, M. J. (2010). Definition and validation of operating equations for poly(vinyl alcohol)-poly(lactide-co-glycolide) microfiltration membrane-scaffold bioreactors. *Biotechnol. Bioeng.* 107, 382–392. doi:10.1002/BIT.22815.

Soleas, J. P., Paz, A., Marcus, P., McGuigan, A., and Waddell, T. K. (2012). Engineering airway epithelium. *J. Biomed. Biotechnol.* 2012, 982971. doi:10.1155/2012/982971.

Steinke, M., Gross, R., Walles, H., Gangnus, R., Schütze, K., and Walles, T. (2014). An engineered 3D human airway mucosa model based on an SIS scaffold. *Biomaterials* 35, 7355–7362. doi:10.1016/j.biomaterials.2014.05.031.

Tan, H., and Pillai, K. M. (2009). A method to estimate the accuracy of radial Flowg-based permeability measuring devices. *J. Compos. Mater.* 43, 2307–2332. doi:10.1177/0021998308102464.

Upadhyay, S., and Palmberg, L. (2018). Air-Liquid Interface: Relevant In Vitro Models for Investigating Air Pollutant-Induced Pulmonary Toxicity. *Toxicol. Sci.* 164, 21–30. doi:10.1093/TOXSCI/KFY053.

Wang, Y., Tomlins, P. E., Coombes, A. G. A., and Rides, M. (2010). On the determination of darcy permeability coefficients for a microporous tissue scaffold. *Tissue Eng. - Part C Methods* 16, 281–289. doi:10.1089/ten.tec.2009.0116.

Xu, Y., Fan, F., Kang, N., Wang, S., You, J., Wang, H., et al. (2015). Tissue engineering of human nasal alar cartilage precisely by using three-dimensional printing. *Plast. Reconstr. Surg.* 135, 451–458. doi:10.1097/PRS.0000000000000856.

Chapter 6

Mathematical and numerical modeling of an airlift perfusion bioreactor for tissue engineering applications

This chapter analyzes the engineering parameters of a bioreactor system to identify an advantageous range of operational variables. Specifically, the hydrodynamic parameters and oxygen transport were investigated using mathematical equations and Computational Fluid Dynamics (CFD) analysis modeling on a novel perfusion bioreactor working as an airlift external loop. The essential hydrodynamic parameters (gas holdup and liquid flow rate) (Becker et al., 1994) were determined by modeling a two-phase flow in a bubbly flow regime. Mathematical models and numerical simulation were associated with experimental results at different configurations to evaluate the effect of the reactor parameters on its hydrodynamics. Hence, the CFD simulation was used to confirm mathematical solutions and estimate the liquid flow profile inside the bioreactor at different gas inlet flow rates. The results obtained from the numerical analysis were used to optimize the design and performance of the bioreactor during dynamic cell culture in 3D constructs. Then, to assure the *in vitro* viability and growth of cellularized engineered tissues, the mass transfer of oxygen was predicted for the fibroblasts cell line (NIH-3T3) by adopting mathematical equations or numerical computation.

6.1. Introduction

The optimization of *in vitro* culture conditions is a fundamental step for developing distributed uniformly, high cell density, and functional three-dimensional (3D) engineered constructs. The use of conventional static tissue-culture parameters may result in heterogeneous cellular distribution, and low penetration depth of cells, caused by the inadequate mass transfer of nutrients, gases, and metabolites, along with insufficient waste removal (Vacanti and Langer, 1999; Beşkardeş et al., 2018; Magrofuoco et al., 2019). Yet, to become functional, the size of engineered tissue should be larger than that obtained under conditions of low mass transfer rate (as occurs in the static culture environment), which allows nourishing cells only by diffusion (Salehi-Nik et al., 2013). Hence, one of the most challenging targets that tissue engineering (TE) applications face is to overcome the mass transport limitation.

The use of perfusion bioreactors, where the medium flows through the internal pores of cellularized 3D scaffolds, enables improving nutrient mass transfer and waste removal due to both diffusion and convection (Bancroft et al., 2003; Saltzman, 2004; Gaspar et al., 2012). Furthermore, some researchers have found that perfusion leads to an increased mixing flow which provides a hydrodynamic stimulation of cells and may improve the production of higher amounts of desired biochemical components (Pisanti et al., 2012; Lin et al., 2014; Grossemy et al., 2020). Actually, by changing the design parameters of bioreactors, different hydrodynamic forces may develop and further affect cells structure and properties (Patil et al., 2013).

Among perfusion bioreactors, an airlift reactor has been recently used for TE applications owing to its homogeneous distribution of nutrients along with good hydrodynamics (Li et al., 2008; Mallick et al., 2017). In the external-loop airlift bioreactors, sterile filtered air is fed at the bottom of a tube (riser), inducing the flow of both liquid and bubbles; then, gas escapes from the top of the bioreactor, and the liquid phase circulates down to the downcomer section (Wang and Zhong, 2007; Zhu, 2007). In these reactors, the bubble-free downcomer area accommodates tissue and/or cells supports, thus, avoiding direct contact between the tissues and air bubbles, which may cause damaging stress for the engineered constructs (Martin and Vermette, 2005). Since cells receive their oxygen needs from the fed air, an efficient oxygen mass transfer is essential for their viability and metabolic activity, mainly due to the poor solubility of oxygen in the culture medium (Salehi-Nik et al., 2013). Hence, determining ideal flow conditions is essential to offer uniform nutrient transport and proper mechanical stimuli.

In TE applications, it is necessary to investigate the effect of fluid profile and hydrodynamic conditions for bioreactors design and troubleshooting. Therefore, researchers have presented various mathematical models and/or numerical methods to solve governing equations, compare experimental data, and predict system parameters (Salehi-Nik et al., 2013; Place et al., 2017; Magrofuoco et al., 2019; Grossemy et al., 2020). Recently, numerical procedures have gained remarkable popularity to solve flow problems (Groen, 2004; Shi, 2008; Pereira et al., 2014; Wang et al., 2019b) even if the development of mathematical models remains a robust tool to improve experimental protocols and outcomes and simulate the optimal operating conditions (Salehi-Nik et al., 2013; Burova et al., 2019; Magrofuoco et al., 2019). In mathematical modeling, the use of simple mathematical equations offers a crucial benefit for helping to predict the complex mechanisms involved in a system (Shakeel, 2013).

However, these models are dependent on simplifications, and the solved equations usually give only an average value of the studied parameter. This issue has motivated researchers to use numerical tools to evaluate local properties and how specific variables, such as the fluid velocity profile, are distributed within a bioreactor system (Chabanon, 2015).

Hossain et al. (Hossain et al., 2015) investigated the fluid flow and glucose mass transfer through a generic scaffold inside a perfusion bioreactor. The authors found that the supply of glucose increased by increasing the inlet glucose concentration or inlet velocity. To improve the cell growth rate, Zhou et al. (Zhou et al., 2008) developed a mathematical model to study the correlation between glucose transport, cell growth, fluid flow, and pH value for its scaffold system. Moreover, to obtain the optimal parameters, their study performed a computational simulation. These results indicated that increasing the distance between the scaffold strands and reducing the diameter of the strands can also increase the transport of glucose inside the construct.

6.2 Materials and methods

6.2.1 Bioreactor design

In this thesis, a mathematical model was proposed to characterize a novel perfusion bioreactor. It is a bubble column working as an airlift external loop reactor, with two glass cylindrical tubes (downcomer and riser) connected to through two horizontal ducts with an internal diameter (ID) of 0.8 cm and height (H) of 1 cm (Fig. 6.1A). As shown in Figure 1, the downcomer is the larger column that would accommodate the seeded scaffolds, with an ID of 3.5 cm H of 22.1 cm. The riser is the smaller glass tube (ID = 1 cm and H = 16.1 cm) that is attached to a peristaltic pump (Model M025; VerderFlex) with a silicone tube and a sterile syringe filter (pore size 0.2 μm) (Fig. 6.1B). The air bubbles rise through the riser and drag part of the culture medium towards the wider column, thus inducing the liquid phase to circulate and promoting gas-liquid mass transfer and oxygenation of the medium (Shaikh and Al-Dahhan, 2013). A glass lid ensures the sterility of the system. It includes a holed ring acting as a bubble-breaker that avoids the leakage of foam derived by the recirculation of bubbles and culture medium. During operation, the whole system can be placed in a standard cell-culture incubator at 37°C in a humidified atmosphere of 95% air and 5% CO_2 to maintain steady operating conditions.

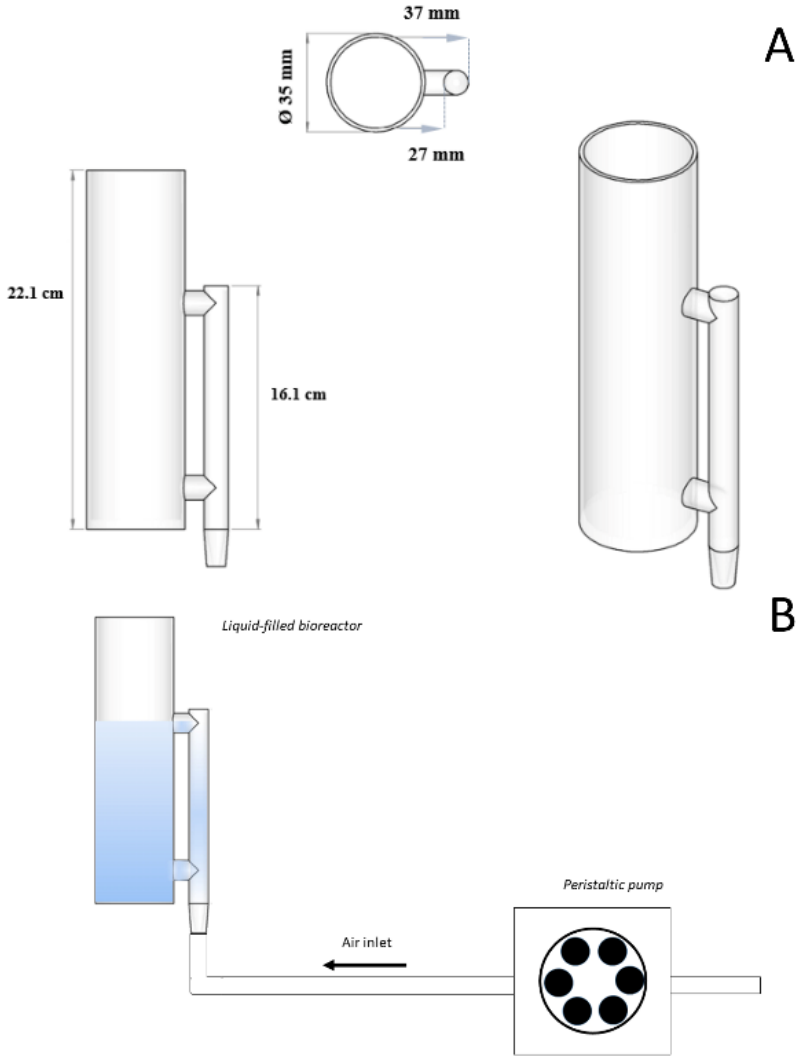

Figure 6.1 Schematic of the airlift external-loop bioreactor and the perfusion circuit: (A) The downcomer (big column) and the riser (small tube) are connected by means of two horizontal tubes, giving a total working volume of 150ml. (B) A peristaltic pump feeds sterile air toward the riser creating air bubbles that promote the recirculation of the culture medium.

6.2.2 Experimental Methods

Measurement of hydrodynamic characteristics: Bubble size and rise velocity

The photographic technique was used for the experimental measurement of the bubble size inside the gas-liquid system. Air was dispersed into the culture medium (DMEM) at three different flow rates (22.5, 40, and 73 ml/min), and a high-resolution camera was placed outside the bubble column to capture the image of the single bubble generated by the nozzle of the riser. Following the completion of the experiment, the captured images were analyzed

and processed to obtain the sphere-equivalent diameter of the single bubble by using the equation (Sam et al., 1996) $d_{eq} = (a\ b^2)^{1/3}$, where *a* and *b* are the vertical and horizontal axis of the ellipsoidal-shaped bubble. These results were compared to the values estimated from Miller's correlation (Eq. 6.2), as described in the following section of mathematical models. The rise velocity of bubbles was measured by making a video recording of the flow while using a high-speed camera. Then, the video was divided into different pictures to extract a sequence of bubble motion images. The latter were analyzed by image processing software (ImageJ) to measure the average terminal velocity. Finally, a mathematical equation was used for results comparison.

Measurement of hydrodynamic characteristics: Pressure drop and liquid flow rate

It was necessary to use a U manometer and a flow meter to quantify the pressure drop and the liquid flow rate inside the bioreactor. According to the specific measurement, two different configurations were adopted: with the bioreactor empty or already filled with liquid. To measure the pressure drop generated by the sterile filter, the bioreactor was left liquid-free, and the filter was appropriately inserted or not between the pump and the column. On the other hand, using the bioreactor filled with liquid, different liquid hydrostatic heights (0, 1, and 2cm below the weir level) and different air flow rates (1-700 ml/min) were tested to analyze the pressure drop profile in the effective system. For each value of hydrostatic height, measurements of pressure drop and liquid flow rates were performed at increasing air velocity. A linear regression of the liquid-gas flow rates curve was also implemented to calculate the minimum gas flow rate that ensures the liquid overflow at the weir.

Finally, the wall shear stress τ_w was obtained as concerns the proper liquid flow rate for cell viability. When the top of a Newtonian fluid is open to the atmosphere, the shear stress τ_w [Pa] for unidirectional laminar flow is given by the equation (Grossemy et al., 2020):

$$\tau_w = \frac{3\mu_l Q_l}{r^2 h} \qquad (6.1)$$

where Q_l is the liquid flow rate [m^3/s], r the downcomer radius [m], and h the liquid hydrostatic level [m].

6.2.3 Mathematical Model

Bubble characterization: size and terminal velocity (bubbly flow regime)

The experimental evidence allowed us to assume a bubbly flow regime in the riser for the whole range of tested gas flow rates in the present model. In this homogeneous regime, the size and rise velocity of the bubble are uniformly distributed and affected by the same parameters (Kantarci et al., 2005). For a single bubble generated at an orifice, the average bubble size [m] could be calculated from Miller's correlation:

$$d_b = \left[\frac{6\sigma d_o}{g(\rho_l - \rho_g)}\right]^{1/3} \qquad (6.2)$$

Where σ is the surface tension of liquid [N/m], d_o the orifice diameter [m], g the gravitational acceleration [m^2/s], and ρ_l and ρ_g the liquid and gas density [kg/m^3], respectively.

According to the wall effect model, when a bubble is rising through a stagnant liquid filled in a vertical column, the terminal velocity V_T is affected by the ratio (λ) of the sphere-equivalent bubble diameter d_{eq} to the column diameter D_c, and the Reynolds number $Re_{t\infty}$ in the absence of wall (Arsenijević et al., 2010). Specifically, in the viscous and turbulent bubbly flow regimes (Re_p<1 and Re_p>100, respectively), the terminal velocity V_T is independent of $Re_{t\infty}$ and described by the following equation:

$$V_T = f(\lambda)V_{T,\infty} \qquad (6.3)$$

where $V_{T,\infty}$ the terminal velocity of a single bubble in an infinite stagnant liquid, and *f* is the wall factor (Tomiyama et al., 2003). In the present system, the $V_{T,\infty}$ evaluation was assessed via a theoretical model. Specifically, Clift *et al*. (Clift et al., 1978) conducted various experimental studies for the $V_{T,\infty}$ measurement in an infinite water medium, while varying the equivalent diameter of single bubbles.

The results of Clift's study are summarized in Fig. 6.2, which distinguishes the terminal velocities in clean and contaminated liquids due to the changes in bubble shape with the contamination level (Clift et al., 1978). Among the best-known empirical correlations proposed for the wall factor *f* and accurately reported by Arsenijević (Arsenijević et al., 2010), the Munroe's was chosen as the most appropriate for the system:

$$f(\lambda) = 1 - \lambda^{1.5} \qquad (6.4)$$

which is valid for $0.1 \leq \lambda \leq 0.8$ and $943 \leq Re_{t\infty} \leq 11{,}000$.

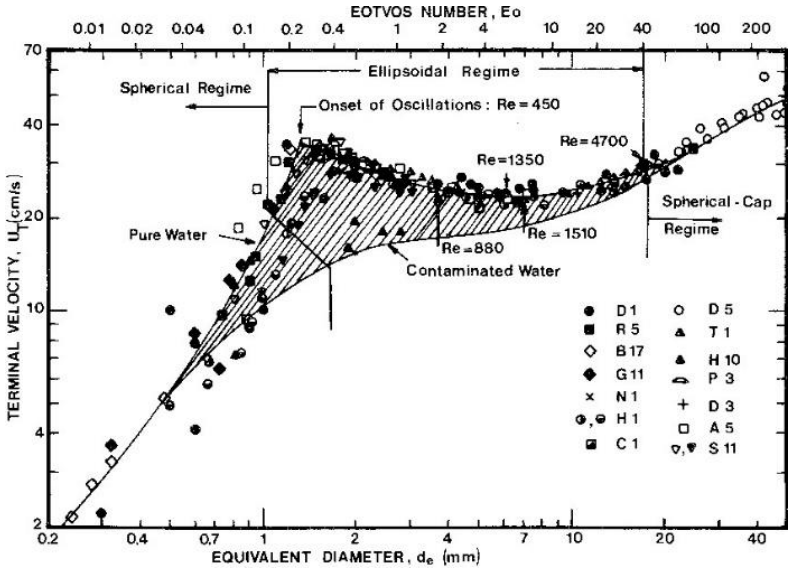

Figure 6.2 Variation of the terminal velocity of a single bubble in water with the bubble spherical equivalent diameter (Clift et al., 1978)

Gas holdup

The gas holdup is a crucial parameter that directs the flow dynamic in two-phase bioreactors (AL-Mashhadani et al., 2015). The gas holdup φ_g is a measure of the interfacial area available for the phase mass transfer and the mean pressure drop in a column with the concurrent gas-liquid flow (Tojo et al., 1974; Kojić et al., 2017).

In this thesis, the average gas holdup φ_g in the riser was calculated as the superficial gas velocity V_S (varying with the gas flow rate) divided by the bubble rise velocity V_T (Hughmark, 1967; Nedeltchev and Schumpe, 2008). This estimation was conducted at different liquid hydrostatic heights (0, 1, and 2 cm below the weir level). To verify the reliability of the calculated φ_g at the same heights conditions, the mean pressure drop of the system was measured into a specific range of gas flow rates (0-150 ml/min). The following equation was used (Tojo et al., 1974):

$$\Delta P = \Delta P_0 - \rho_l \, \varphi_g \, l \, g \quad (6.5)$$

Where l is the difference between the pressure taps of the manometer [m] and ΔP_0 the pressure drop at zero-air flow rate [Pa]. Specifically, l and ΔP_0 change at each tested hydrostatic liquid height.

6.2.4 Numerical Methods

Validation of Numerical Simulation of hydrodynamic characteristics

Although high-resolution and high-speed cameras allow determining fundamental hydrodynamic parameters (i.e., bubble size and bubble rise velocity), it is not sufficient to estimate the efficiency of the mixing process. On the contrary, Computational Fluid Dynamics (CFD) enables to accurately map the internal flow patterns of complex dynamic systems by discretizing mathematical equations.

In the current study, Comsol Multiphysics software (version 5.3a) was utilized as a hydrodynamic simulation tool to validate the mathematical results and to assess the detailed profile of the velocity field inside the bioreactor. Specifically, the gas holdup and liquid velocity were investigated as main flow dynamic parameters.

The simulation was carried out using a 3D model with xz-plane symmetry and varying the gas inlet flow rate (1 ml/min, 3.4 ml/min, 5.8 ml/min, 8.1 ml/min, 10 ml/min). Air and water were considered as the gas and liquid phase, respectively. The liquid phase was assumed as the continuous phase in the two-phase flow model with a hydrostatic height at the weir level. The turbulent bubbly flow model with a bubble diameter of 6mm was used to investigate the flow regime inside the bioreactor as the Reynolds number for the fully developed flow was higher than $1x10^4$. Assuming that bubbles travel with their terminal velocity, only one set of Navier-Stokes equations could be solved for the continuous phase. Within the COMSOL interface, the turbulence of the liquid phase is modeled through the *k*-ε theory, giving the moment transfer equation (Manual; COMSOL®, 2016):

$$\varphi_l \rho_l \frac{\partial u_l}{\partial t} + \varphi_l \rho_l u_l \cdot \nabla u_l = -\nabla P + \nabla \cdot [\varphi_l(\mu_l + \mu_T)\left(\nabla u_l + \nabla u_l^T - \frac{2}{3}(\nabla u_l) I\right)] + \varphi_l \rho_l g + F \quad (6.6)$$

Where φ_l is the liquid volume fraction [m^3/m^3], ρ_l is the liquid density [kg/m^3], u_l is the vector of the velocity of the liquid phase [m/s], P is the pressure [Pa], μ_l is the liquid viscosity [Pa s], μ_T is the turbulent viscosity [Pa s], g is the gravity acceleration [m^2/s], and F is the sum of the acting volume forces [N/m^3]. According to the *k*-ε theory, the turbulent viscosity $\mu_T$is defined by Eq. 6.7:

$$\mu_T = \rho_l C_\mu \frac{k^2}{\varepsilon} \quad (6.7)$$

Where C_μ is a standard constant whose value is 0.09, k is the turbulent kinetic energy, ε is the dissipation rate of turbulent energy. Additionally, the turbulence induced by bubbles is expressed by the source term S_k defined by the following equation:

$$S_k = -C_k \varphi_g \nabla p \cdot u_{slip} \quad (6.8)$$

where C_k is a constant within the range of $0.01 < Ck < 1$ (Nalband and Jalilnejad, 2019).

The slip model used for the study is the pressure-drag balance with the drag coefficient C_d for large bubbles (above 2 mm). In this model, the balance between drag and pressure forces on a bubble is assumed, leading to the following equation for u_{slip} calculation:

$$-\nabla p = C_d \frac{3}{4} \frac{\rho_l}{d_b} |u_{slip}| u_{slip} \quad (6.9)$$

As regards boundary conditions, the outlet face was assumed as a free surface at atmospheric pressure, allowing the gas efflux and the slip condition for the liquid phase. On the bioreactor walls, no-slip and no flux conditions were used for the liquid and gas phase, respectively, so that the velocities were assumed to be zero.

For this study, a mesh resolution study was conducted starting from 8443 tetrahedral elements, showing that the calculation of the reported parameter was not affected by doubling the elements, so mesh resolution did not influence the analysis of the results. Hence, a tetrahedral meshing with 8443 elements was used as a generalized mesh resolution.

6.2.5 Oxygen Mass Transport

Mathematical model

One central aspect that needs to be addressed during bioreactors design is the mass transfer from the gas to liquid phase, which is crucial for ensuring cells metabolism. In bioreactors providing perfusion of culture medium, the dynamic fluid flow should improve the supply of nutrients and oxygen to cells, thus promoting cell growth and/or differentiation (Grossemy et al., 2020).

During cell growth, cells require a specific oxygen consumption for maintaining their viability. Hence, the higher the cells concentration, the higher the oxygen consumption to support cells survival and metabolic activity (Grayson et al., 2011; Yan et al., 2012). In this study, a mathematical approach was used to determine the oxygen transport from the gas to liquid phase, which is also a measure of the adequate cells density for this novel system. Mass balance equations and numerical correlation were adopted from the literature to

determine the oxygen concentration in the bioreactor (Hughmark, 1967; Talvy et al., 2007; Green and Perry, 2008).

The designed bioreactor has the characteristics of an airlift reactor which creates circular mixing patterns in which liquid is assumed to be perfectly mixed (Talvy et al., 2007). Hence, the global oxygen mass balance equation in the liquid phase is given by (Talvy et al., 2007; Magrofuoco et al., 2019):

$$\frac{dC_l}{dt} = k_l a_l (C_l^* - C_l) - R_{O_2} \qquad (6.10)$$

In this expression, $k_l a_l$ is the global mass transfer coefficient (s^{-1}), C_l the concentration in the liquid bulk (mg/L), C_l^* the concentration at the interface (mg/L), and R_{O_2} is the biological oxygen consumption rate [mg / L s]. The first term of the right side of the equation describes the oxygen transferred from bubbles to the liquid phase in the riser, whereas the second one is the reaction term, that is a function of the cells number (χ), of the *specific oxygen consumption rate* (q_0) and the liquid volume V inside bioreactor (Eq. 6.11). For this evaluation, the oxygen transfer in the downcomer was neglected because the previous hydrodynamic results showed the absence of bubbles in this zone.

$$R_{O_2} = \frac{\chi q_0}{V} \qquad (6.11)$$

To solve Eq. 6.6, the mass transfer coefficient k_l was estimated referring to the two-resistance theory, thus, it was derived by combining Eq. 12 and Eq. 15 (Hughmark, 1967).

$$Sh = 2 + c[(Re_p)^{0.484}(Sc)^{0.339}\left(\frac{d_b g^{\frac{1}{3}}}{D^{\frac{2}{3}}}\right)^{0.072}]^e \qquad (6.12)$$

For single gas bubbles, c=0.061, e=1.61.

Parameters of Eq. 6.12 were calculated by Eq. 6.9-6.11:

$$Re_p = \frac{\rho_l V_{T,r} d_b}{\mu_l} \qquad (6.13)$$

$$Sc = \frac{\mu_l}{\rho_l D} \qquad (6.14)$$

$$Sh = \frac{k_l d_b}{D} \qquad (6.15)$$

In Eq. 6.13, $V_{T,r}$ is the relative rising velocity of the single bubble, that can be calculated as:

$$V_{T,r} = V_T - \frac{Q_l}{S} \qquad (6.16)$$

Where S is the cross-sectional area of the riser and Q_l is the liquid flow rate.

To estimate the specific gas-liquid interfacial area a_l (1/m), Eq. 17 is commonly used (Talvy et al., 2007):

$$a_l = \frac{\varphi_g S_b}{V_b} \quad (6.17)$$

Where S_b is the bubble surface and V_b is its volume. When the sphere-equivalent diameter of the bubble is known, Eq. 6.17 can be written as:

$$a_l = \frac{6\varphi_g}{d_b} \quad (6.18)$$

Where d_b is the sphere-equivalent diameter of the generated bubble. In this work, Eq. 6.18 was used to calculate a_l.

In Eq. 10, the concentration at the interface C_l* is generally calculated by using Henry's law:

$$C_l^* = He\ P_{O_2} \quad (6.19)$$

In this expression, *He* is the Henry's Law constant [mg/(L atm)] and P_{O_2} the oxygen partial pressure [atm] (Magrofuoco et al., 2019).

The steady-state solution of the oxygen concentration in the liquid phase was calculated at different cells number while using equations 6.6-6.15. Moreover, from the steady-state solution, a calculation of the maximum cells number that might be cultured inside the bioreactor was implemented by imposing a bulk concentration of 1.7 mg/L as the physiological oxygen concentration for survival and proliferation of cells (Place et al., 2017).

The non-steady solution of Eq. 6.10 was also mathematically determined, describing the evolution of the average oxygen concentration in the liquid phase for a fixed cells number. For this evaluation, the initial oxygen concentration in the liquid bulk was considered zero; hence, the bulk concentration over time was calculated as:

$$C_l = \left(C_l^* - \frac{\chi\, q_0}{V\, k_l\, a_l}\right)\left(1 - e^{-k_l a_l\, t}\right) \quad (6.20)$$

Overall, the global mass transfer $k_l\, a_l$ can be interpreted as the inverse of the timescale τ, corresponding to a relaxation time of mass transfer, i.e. when the concentration of oxygen in the liquid is equal to 63% of its steady-state value (Talvy et al., 2007).

Validation of Numerical Simulation of Mass Transfer (prediction of mass transfer from gas bubble to liquid)

The commercial CFD software COMSOL was utilized to simulate the local oxygen mass transfer inside the bioreactor, assuming 0 mg/L as the initial oxygen concentration in the water and setting an inlet gas flow rate of 10 ml/min. Specifically, the continuity equation for two phases system (Eq. 6.21) and the momentum transport equation for the gas phase (Eq. 6.22) were used as follows:

$$\frac{\partial}{\partial t}\left(\rho_l \varphi_l + \rho_g \varphi_g\right) + \nabla \cdot \left(\rho_l \varphi_l u_l + \rho_g \varphi_g u_g\right) = 0 \qquad (6.21)$$

$$\frac{\partial \rho_g \varphi_g}{\partial t} + \nabla \cdot \left(\rho_g \varphi_g u_g\right) = -m_{gl} \qquad (6.22)$$

Where m_{gl} is the mass transfer from the gas to the liquid phase [kg/(m^3 s)] (Nalband and Jalilnejad, 2019).

The transport of diluted species interface was used to determine the concentration of oxygen dissolved in the liquid, and the two-theory film model was assumed to solve the mass transfer from gas bubble to the liquid phase:

$$C_l^* = (P + P_{ref})\, He \qquad (6.23)$$

$$N = k_l (C_l^* - C_l) \qquad (6.24)$$

$$m_{gl} = N M a_l \qquad (6.25)$$

$$\frac{\partial C_l}{\partial t} + \nabla \cdot (C_l u_l) = \nabla \cdot (D \nabla C_l) + \frac{m_{gl}}{M} \qquad (6.26)$$

Within Henry's Law (Eq. 6.19), P_{ref} is a user input to set the pressure mode (relative/absolute). By combining Eq. 24 (describing the molar flux per interfacial area N [mol/s m^2]) and Eq. 6.25 (involving the interfacial area a_l per volume [m^2/m^3]), the concentration of the dissolved gas C_l was calculated from Eq. 6.26, where M is the molecular weight of the species [kg/kmol].

Since no gas fraction inside the downcomer, the mass transfer was simulated only in the riser domain. The resulting data were compared to mathematical predictions.

6.2.6 Scaffold Preparation

Poly-L-lactic-acid (PLLA, Resomer® L 209 S), 1,4 dioxane (Sigma-Aldrich, Munich, Germany), and double-distilled water were utilized as polymer, and solvents to prepare the

ternary solution. A suspension made of a homogeneous ternary solution (composed of PLLA, dioxane, water) was prepared, with constant dioxane to water weight ratio of 87/13 wt/wt and a concentration of PLLA of 4% wt. The thermal protocol was designed and set up as follows. The solution was initially kept at 60°C. Then, the temperature was suddenly lowered to 30°C for 45 minutes (Mannella et al., 2014). Later, a quench was made by direct pool immersion in an ethyl alcohol bath at a temperature of -25 °C. The foams obtained were subjected to washing in deionized water and drying at 35 °C under vacuum to remove any remaining solvent trace.

6.2.7 Cell Culture

NIH-3T3, fibroblastic cells line from Mouse Swiss NIH embryo (ECACC, European Collection of Cells Cultures) was used for the experiments. Cells were cultured at 37°C in a 5% CO2 atmosphere using Dulbecco's modified Eagle's medium (DMEM, Sigma) supplemented with 1% glutamine, 1% antibiotics (Sigma), and 10% of Fetal Bovine Serum (FBS) (Euro Clone). Cells were cultivated in conventional T-flasks inside a cell culture incubator until reaching a sufficient cell number for experiments.

6.2.8 Cell Seeding

PLLA scaffolds, produced as described above, were sterilized by soaking in 70% v/v ethanol solution overnight. After triple rinsing with sterile complete Phosphate Buffer Saline 1X (PBS) (Sigma), the polymeric supports were coated with collagen Type I solution (1mg/ml) (Rat Tail Collagen, Corning) as described in Lombardo et al. (Lombardo et al., 2019). Meanwhile, cells were trypsinized, detached from the culture flask, and counted using The Burker's counting chamber (Thermo Fisher Scientific). After centrifugation at 1000 rpm for 5 min, cells were re-suspended in fresh DMEM until reaching a concentration of $5 \cdot 10^6$ cells/ml. 500 µl of this suspension was seeded on each PLLA scaffold placed into a well of a 6-multiwell plate. Cells were allowed to attach to the scaffold surface for 2 hours inside a CO_2 incubator at 37°C. Subsequently, 5 ml of fresh DMEM was added to each well, and the cells/scaffolds were incubated again. After 24 hours in static culture, the cell-seeded scaffolds were randomly assigned to static and dynamic culture. For the dynamic culture, three scaffolds were located inside the bioreactor within specific support fixed in the central part of the downcomer. The bioreactor was previously filled with about 150 mL of fresh medium. After a defined time, the samples were extracted from the bioreactor for analysis.

Three scaffolds were left in static during the same period and used as control. The same experiment was repeated at different culture times (1, 3, 4, 5, 6, 7, 8, 11, and 15 days).

6.2.9 Acridine Orange Stain Assay

DNA-binding dye Acridine orange (AO, Sigma) was used for the morphological detection of viable and apoptotic/necrotic cells on the scaffolds both in a static and dynamic culture. After 7 days of culture, the samples were placed in a 24-well plate and rinsed in sterile PBS (Sigma). The cells were stained with 500 μl of dye mixture (100 μg/ml acridine orange in complete PBS) and incubated at 37°C for 10 s. Therefore, the scaffolds were thoroughly washed with PBS. A fluorescence microscope (Leica DM 2500, Leica MicroSystems), equipped with a charge-coupled device camera, was used to visualize the cells.

6.2.10 Biochemical Analysis: DNA Content Assay

All samples, both in static and dynamic culture, were fixed in 70% v/v ethanol and incubated at -20°C overnight for the subsequent biochemical analysis. Double-stranded nucleic acid (DNA) content in NIH3T3 cells grown inside the polymeric matrix was determined using a conventional DNA extraction in phenol/chloroform. After one night at -20°C, the PLLA scaffolds were roughly shredded and centrifuged at 1000 rpm for 10 min. 500μl of lysis buffer (4M Guanidinium thiocyanate and 10% Sodium Laurosyl Sarcosinate, (1:1/v:v); 0.3 M Sodium Citrate; pH8) was added, and the samples were incubated for 15 min at 65°C and 900 rpm. At this point, a step of heat shock was carried out. First, each scaffold was maintained at 60°C for 10 min, and then at 4°C at 500 rpm for 5 min. This cycle was repeated three times. To enhance cell detachment from the polymeric supports, the samples were placed inside a filter and centrifuged at 10000 rpm for 3 min. The as-obtained supernatant was recovered and centrifuged again for 5 min at 10000 rpm. Then, a step of deproteinization was performed by using organic solvents. First, we added the same volume of saturated Phenol: Chloroform: isoamyl alcohol (50:49:1) solution and, then, gently mixed by inversion to obtain a homogeneous solution. After centrifuging at 10000 rpm for 20 min, the upper phase was recovered and loaded in a 1ml sample tube (Eppendorf). This operation was repeated several times for the dirty or contaminated samples. The samples were incubated with a solution of RNase (40 g / ml) at 37°C for 1 hr. The final volume of the supernatant containing the extracted DNA was collected and measured. Then, we added defined volumes of 3 M Sodium Acetate and cold isopropanol, according to protocol. The obtained solution

was gently mixed and incubated at -20°C for 30 min. For the precipitation of DNA, samples were centrifuged at 14000 rpm for 30 min. The DNA obtained was washed with 1 ml of 96% cold ethanol and then centrifuged for 5 min at 14000 rpm to remove any trace of ethanol. The as-obtained DNA was suspended in milli-Q water and incubated at room temperature to allow it to swell. The DNA content in each sample was determined using a spectrophotometer (NanoDrop 1000, Thermo Scientific).

6.2.11 Confocal Microscopy

After 7 days under static culture condition and perfusion-flow culture inside the bioreactor, the scaffolds were washed in PBS. Cells were fixed in 3.7% formaldehyde solution for 10 min at room temperature. The samples were rinsed 3 times in PBS and one time with distilled water. Nuclei of NIH-3T3 cells were stained by Propidium Iodate (PI; 1:3000, Sigma) for 30 min at 37°C. Then, scaffolds were incubated for 2 hrs at 37°C with Phalloidin^{FITC} (1:3000, Sigma) for staining F-actin. The Phalloidin staining reveals the alignment of the cytoskeleton of cells grown in the 3D support, while PI highlights cell nuclei disposition. The scaffold surface and cross-section were observed under Olympus Floview FV300 laser confocal microscope (2-mm laser sections).

6.3 Results and discussion

6.3.1 Hydrodynamic characteristics

The present thesis aims to develop a mathematical model for studying the fluid dynamics of the proposed bioreactor and its effects on oxygen mass transport and cellular activity. Several experiments were also performed to validate the mathematical solutions about bubble characteristics, i.e. bubble size, gas holdup, and terminal velocity, which influence the mass transfer rate in the gas-liquid system (Groen, 2004).

The hydrodynamic characterization of bioreactors significantly affects the experimental and mathematical results since parameter investigation strictly depends on the flow regime prevailing in the system. Hence, to design a bioreactor, the flow regime analysis is the first step to alternatively set appropriate models that may simplify its complex hydrodynamics (Kantarci et al., 2005).

Substantially, concerning the superficial gas velocity that is generated in a bubble column, three types of flow regimes can be maintained: the homogeneous (bubbly flow) regime, the heterogeneous (churn-turbulent) regime, and the slug flow regime (Groen, 2004).

Bubble size

From the picture shown in Fig. 6.3, one can notice single bubbles rising from the nozzle through the riser. This experimental observation of uniformly sized and homogeneously dispersed bubbles led us to assume a constant bubbly flow regime for the whole range of superficial gas velocities (0 – 0.31 m/s) (AL-Mashhadani et al., 2015). From the analysis of the pictures, the shape and size of the bubbles did not change when varying the air flow rate. Specifically, bubbles showed an ellipsoidal shape with a constant aspect ratio E = a/b = 0,7 (with a and b, the vertical and horizontal axis, respectively). By using this value, a sphere-equivalent diameter of 6 ± 0.07 mm was measured. Table 6.1 shows the average values and their standard deviation obtained from measurements at each tested air flow rate.

Figure 6.3 A single bubble rising through the riser tube: this picture corroborates the theoretical results of a bubbly flow as the generated hydrodynamic regime inside the riser.

Table 6.1 Values of the experimental measurements of the sphere-equivalent diameter.

Gas flow rate [ml/min]	**a [mm]**	**b [mm]**	**d_{eq} [mm]**
22.5	5.30 ± 0.02	7.7 ± 0.01	6.00 ± 0.03
40	5.40 ± 0.01	7.6 ± 0.03	6.05 ± 0.01
73	5.30 ± 0.02	7.6 ± 0.02	5.90 ± 0.04

The measured mean equivalent diameter matches the estimated average diameter obtained using Eq. 6.2, i.e., 6.05mm, thus, confirming the correspondence between the mathematical model and experimental measurements in the bubble size analysis.

Terminal velocity

Two different approaches were applied to evaluate V_T: a visual observation via high-definition video and a mathematical model.

To solve Eq. 6.3, $V_{T,\infty}$ was obtained from Figure 6.2 by utilizing the equivalent diameter calculated via Eq. 2 and assuming no water contamination. The evaluation of $V_{T,\infty}$ and consequently of $Re_{t\infty}$ allowed choosing the more appropriate correlation (Eq. 6.4) for calculating the wall factor *f* (Arsenijević et al., 2010). All the obtained data (values) are summarized in Table 6.2.

The experimental value of V_T was measured in a column filled with culture medium while using the video imaging technique. Predicted and measured rise velocities resulted in 11.88 and 12 ± 0.17 cm/s, respectively, demonstrating the reliability of the applied mathematical model for bubble motion in this novel system.

Table 6.2 Parameters characterizing the hydrodynamics of the system obtained by Eq. 6.1-6.4.

Sphere-equivalent bubble diameter (d_{eq}) [cm]	0.6
$\boldsymbol{\lambda\ (d_{eq}/D_c)}$	0.6
Wall factor *f*	0.54
$\mathbf{V_{T\infty}}$ **[cm/s]**	22
$\mathbf{Re_{t\infty}}$	1200
V_T [cm/s]	11.88

Gas holdup

The gas holdup plays an important role in the design and analysis of bubble columns (Kantarci et al., 2005). Several correlations can be found in the literature to predict this fundamental parameter in a gas-liquid system (Hughmark, 1967; Groen, 2004; Kantarci et al., 2005; Talvy et al., 2007; Nedeltchev and Schumpe, 2008; Kojić et al., 2017). Although most of the recent works focused on the implementation of numerical procedures to model gas holdup distribution (Han et al., 2007; Nedeltchev and Schumpe, 2008; Bai et al., 2012;

Law and Battaglia, 2013), the bubbly flow regime allowed to obtain gas holdup via the simple Hughmark (1967) equation ($\varphi_g = V_S/V_T$) (Hughmark, 1967).

By using this correlation, gas holdup should linearly increase when increasing the inlet air flow rate. The pressure drop in the gas-liquid system was measured and compared to the pressure drop profile calculated by using Eq. 6.5 to verify the effectiveness of this assumption (Kojić et al., 2017).

In Figure 6.4, one can see the measured pressure drop data of the gas-liquid system at different liquid hydrostatic heights and air flow rates. By varying these heights, the liquid flow rate that runs from the riser to the downcomer is expected to change since a lower driving force is established (Law and Battaglia, 2013). Overall, the principal evidence of Fig. 6.4 is the agreement between the experimental measurements and the applied mathematical model (dot line). This result demonstrates that the system accurately follows a linear increase of the gas holdup with increasing superficial gas velocity, thus, confirming the findings from Kawagoe et al. of a uniform bubble size distribution in a bubbly flow regime (Kantarci et al., 2005).

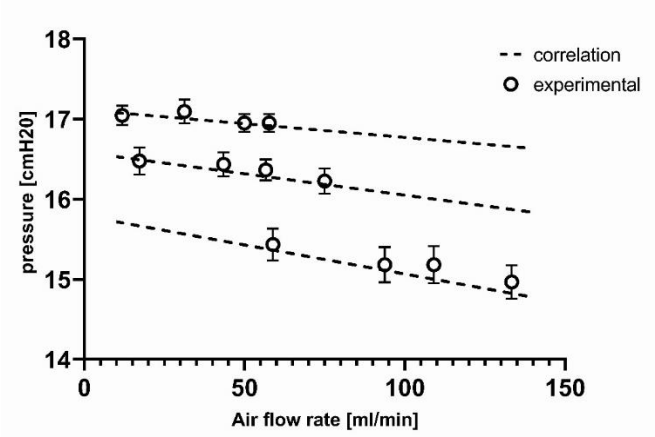

Figure 6.4 Comparison between experimental and calculated total pressure drop inside the bioreactor at different liquid hydrostatic heights (0, 1, and 2cm below the upper horizontal duct) as a function of air flow rate; the dotted line depicts the correlation outcome, the line represents the experimental data with their linear fitting. Error bars concern the standard deviations of the measured values.

Moreover, the effectiveness of Eq. 6.5, taking into account the total pressure drop within the riser and the downcomer, suggests the absence of bubbles in the downcomer. This latter is true when the liquid level is close to the weir and at low air flow rates, where the measured and predicted pressure headlines strictly match up. However, gas bubbles can be dragged towards the downcomer even though the liquid level is 2 cm under the weir.

Pressure drop and liquid flow rate

For the airlift bioreactors, pressure variation between the two columns is the driving force for the liquid circulation which depends on the density difference (i.e., the gas holdup) between the riser and downcomer (Groen, 2004; Kantarci et al., 2005; Kojić et al., 2017). By testing a range of gas flow rates of 0-500 ml/min, the filter induced higher pressure drop within the system compared to the other set-up, as Fig. 6.5 shows.

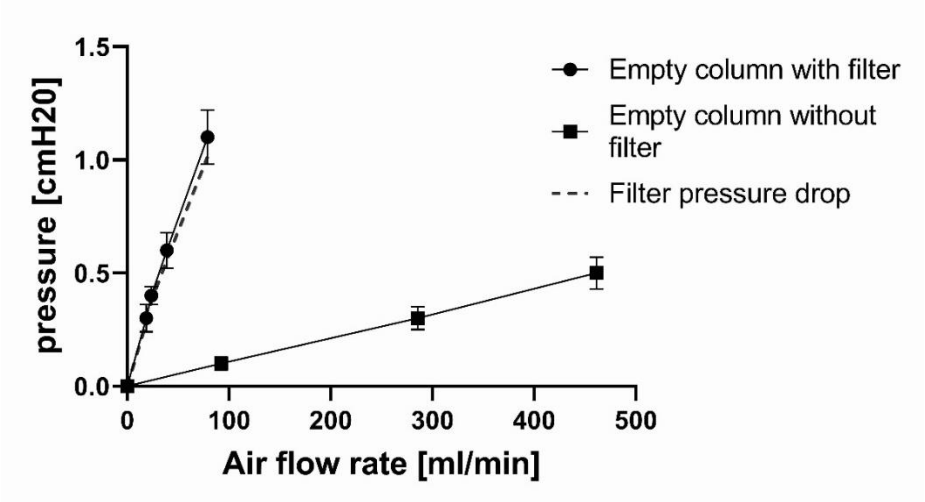

Figure 6.5 Pressure drop measurements within the bioreactor empty of liquid. The pressure drop generated by the sterile filter, calculated from the difference between the two lines, is represented by the dotted line.

On the other hand, Fig. 6.6A shows the liquid flow rate from the riser to the downcomer at the different tested liquid hydrostatic heights and air flow rates. The liquid flow rate always increases when increasing air flow rate, whereas it decreases at lower hydrostatic liquid levels. Similar findings were shown by Kojic *et al.* (Kojić et al., 2017) that obtained weaker liquid circulation and worse mixing when lowering the liquid level inside an airlift reactor. Moreover, a transition regime at 2 cm was assumed since the same linearity between liquid flow rate and air flow rate (Fig. 6.6A) was not found as for 0 cm and 1cm. This assumption was confirmed as some slugging bubbles that raised the column were experimentally observed during the flow perfusion.

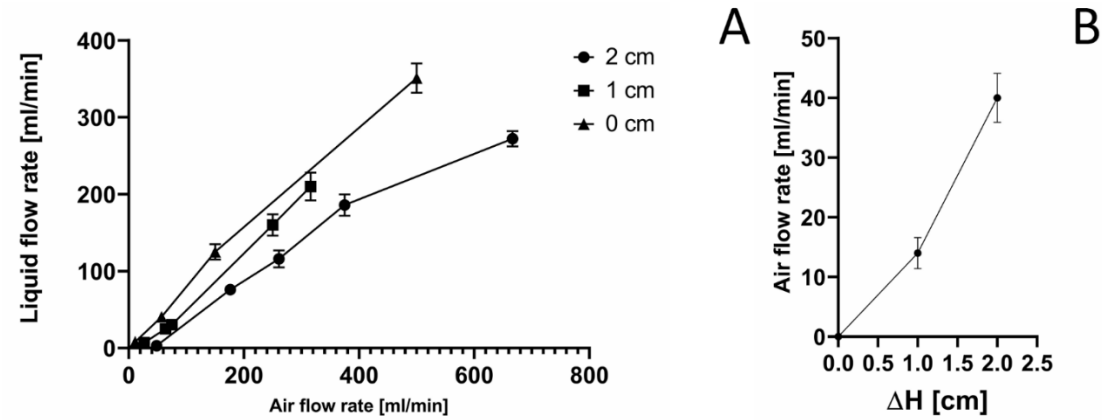

Figure 6.6 (A) Liquid flow rate measurements at different levels of culture medium (0, 1, and 2cm below the upper horizontal duct) as a function of air flow rate. (B) Minimum air flow rate ensuring liquid circulation from the riser to the downcomer as a function of the liquid level (expressed as the distance from the upper horizontal duct) inside the bioreactor. Error bars concern the standard deviations of the measured values.

By observing Fig. 6.6A, one could notice that the minimum air flow rate ensuring the liquid circulation was different for each liquid hydrostatic height. By exploiting the flow rate data, the minimum airflow rate was determined by performing a linear extrapolation at the zero of the y-axis (Fig. 6.6B).

6.3.2 Validation of Numerical Simulation of hydrodynamic characteristics

Computational Fluid Dynamics (CFD) has been recently exploited as a valuable tool to simulate the flow field based on the bioreactor geometry and the mesh convergence study (Fig 6.7A, B) (Burova et al., 2019). In this study, the volume fraction of air and the liquid velocity were investigated at different times and inlet gas velocities in the bioreactor. The stationary condition was reached after about 18 seconds when the hydrodynamic profile became stable. Fig. 6.7C shows the distribution of gas volume fraction (i.e., gas holdup) at 20s for an inlet flow rate of 10 ml/min.

A good agreement resulted between the mathematical model and the CFD simulation on gas holdup, a fundamental hydrodynamic parameter affecting mass transfer in airlift reactors (Kojić et al., 2017). As observed in Fig. 6.7C, the numerical simulation confirmed the absence of gas bubbles inside the downcomer, with a small amount of gas circulating through the upper duct before exiting the bioreactor. In line with this work, Ebrahimifakar et al. investigated the hydrodynamic parameters of an internal airlift bioreactor by using CFD simulation (Ebrahimifakhar et al., 2020). From their findings, the density difference between the liquid and gas phases caused the air to move up the riser. Moreover, they observed that

the volume of the gas fraction was zero in the downcomer region, with few bubbles of gas in the passage between the draft tube and the wall into the downcomer. Although the system geometry differs from the internal-loop configuration of the cited research, the agreement between the outcomes of the two experimental apparatus is legitimate by the use of the same mathematical model, i.e., the multiphase flow of gas bubbles rising through a liquid in a turbulent bubbly flow regime.

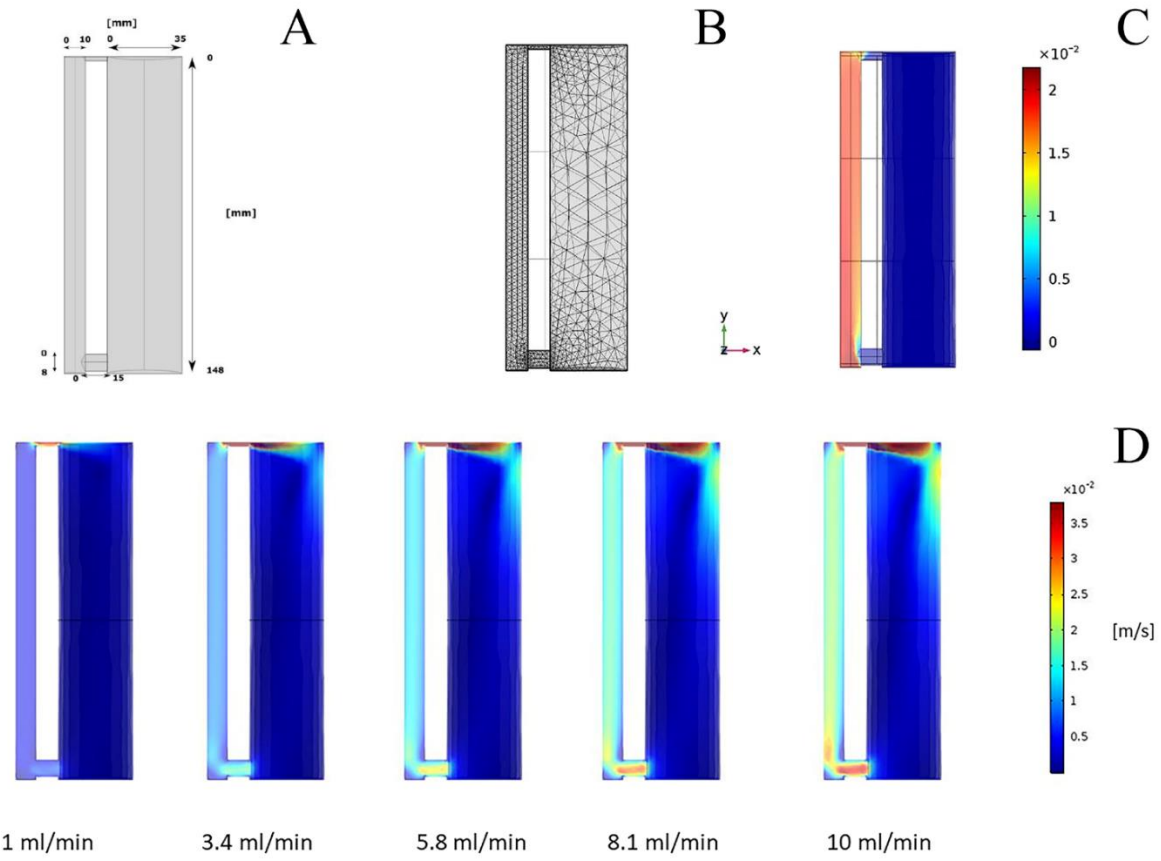

Figure 6.7 (A) Bioreactor geometry in symmetry mode designed within the COMSOLsoftware. (B) Mesh representation of the simulated bioreactor system. (C) CFD data of gas holdup distribution at the steady-state inside the bioreactor. (D) Liquid velocity profile inside the bioreactor at different inlet gas flow rates. An inhomogeneous color scale shows no uniform velocity distribution inside the downcomer zone.

Moreover, the simulated gas holdup data in the riser for various inlet gas velocities exactly overlapped the values obtained from the mathematical model, predicting a linear increase of gas hold up with an increasing inlet gas flow rate (Kantarci et al., 2005).

Fig. 7D shows the velocity profiles throughout the whole bioreactor at different inlet gas flow rates. The range of these flow rates was chosen to cover the values compatible with the cell culture dynamics. For inlet gas flow rates higher than 1 ml/min, irregular velocities distribution occurred in the downcomer. As expected, the liquid velocity increases when the

inlet gas velocity increases both in the downcomer and the riser. The volume of the water that returns from the downcomer to the riser is smaller at lower flow rates since liquid circulation is driven by the difference in the gas holdup between the two zones, which decreases when decreasing gas velocities (Nedeltchev and Schumpe, 2008). Consequently, when inlet gas flow rates decrease, the liquid velocity in the riser is diminished, along with the turbulence in the velocity profile of the liquid in the downcomer (AL-Mashhadani et al., 2015).

As one can observe, a more turbulent zone is localized in the same region (i.e., the edge opposite to the riser in the area around the upper duct) at each gas flow rate. It is reasonable to state that the turbulence in this region is due to the higher liquid flux arriving from the riser and hitting the bioreactor wall, where the friction force accelerates part of the surrounding liquid (Groen, 2004). Specifically, for each tested inlet flow rate, Fig. 6.8A describes the simulation data for the liquid velocity profiles across the downcomer diameter at three different heights.

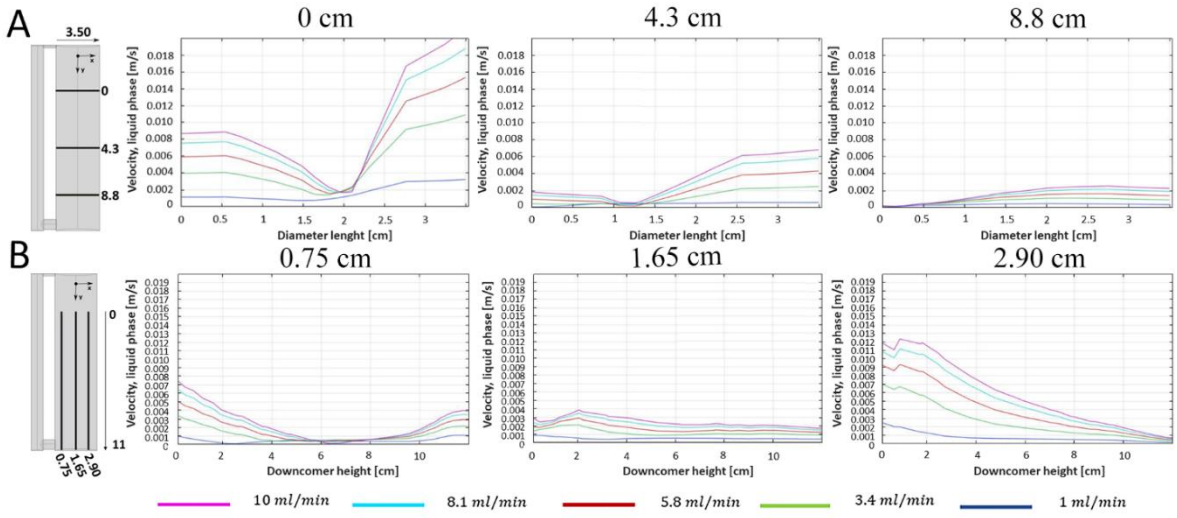

Figure 6.8 (A) Liquid velocity profiles across the downcomer as a function of the diameter length at different inlet gas flow rates, and for three heights in the bioreactor. (B) Liquid velocity profiles across the downcomer as a function of the height of the bioreactor at different inlet gas flow rates, and for three distances from the riser.

At the highest height analyzed, a very irregular velocity profile can be noticed when moving from the riser to the opposite side of the reactor. This non-uniform behavior remarkably increased when the flow rate increased. This phenomenon tends to attenuate when going down through the downcomer and seems to disappear only at the level of the lower horizontal duct.

An additional analysis, shown in Fig. 6.8B, was conducted through the Z direction (vertical) at three distances from the riser along the diameter (0.75cm, 1.65cm, and 2.9cm). In this case, from the numerical data, non-uniform velocity profiles were detected for all the analyzed vertical lengths at the totality of the inlet flow rate tested except 1 ml/min.

Overall, an adequate liquid mixing allowing a homogeneous liquid velocity profile could not occur in the so-tested system, thus, resulting even inconvenient for TE application. Therefore, to overcome this issue, a new CFD simulation was implemented by inserting a perforated grid in the upper region of the downcomer, precisely at a distance of 11.8 cm from the base of the bioreactor (Fig. 6.9).

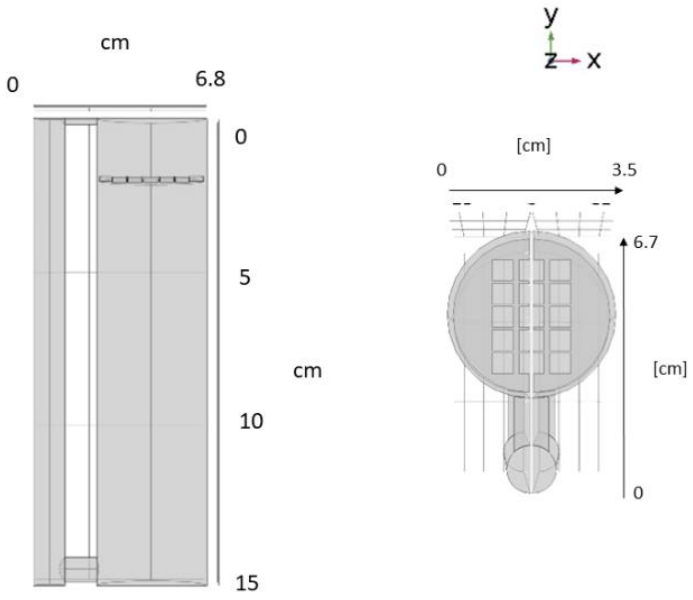

Figure 6.9 COMSOL schematic of the x-z plane section and the custom-made grid inserted within the downcomer domain of the bioreactor.

The grid, which operates as a liquid distributor, presents 15 squared holes (length=4mm), placed in an array of 5 holes per three lines (Fig. 6.9). The simulation was run at the highest inlet air flow rate investigated in the previous simulations (10 ml/min).

Remarkably, at the steady-state condition, reached after 30s, the obtained liquid velocity profile appeared uniform below the grid, thus creating a homogeneous volume available for scaffolds placement (Fig. 6.10).

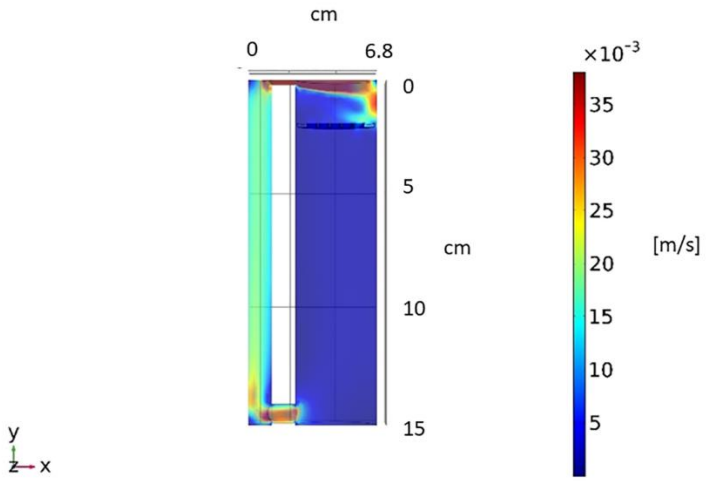

Figure 6.10 Liquid velocity profile at the steady-state resulting from the numerical simulation. A uniform velocity distribution can be observed in the region below the grid, where the scaffolds would be located.

Velocity profile analyses for this configuration were carried out at the same regions (i.e., the diameter at different reactor levels and the vertical direction at three distances from the riser) and compared the results. Data from the two simulations are shown in Fig. 6.11.

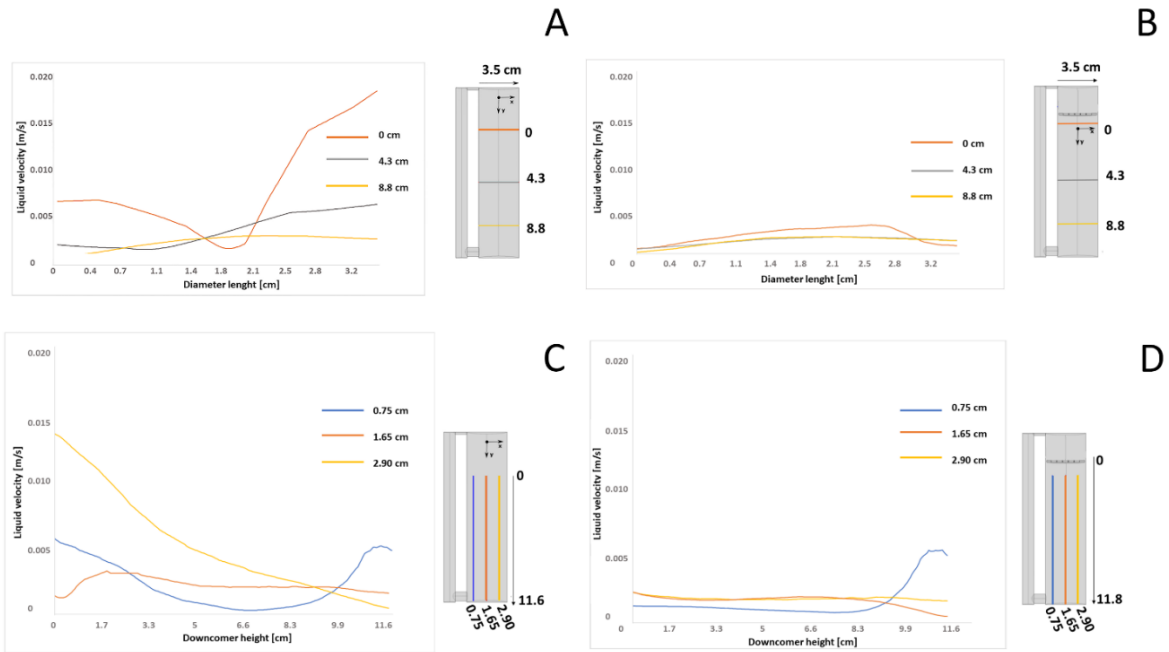

Figure 6.11 Liquid velocity profiles: (A) without the inserted grid as a function of the diameter length for three levels of the reactor; (B) with the inserted grid at the diameter length for three levels of the reactor; (C) without the inserted grid along the height of the bioreactor for three distances from the riser (0.75cm, 1.65cm, and 2.9cm); (D) with the inserted grid as a function of the height of the bioreactor for three distances from the riser (0.75cm, 1.65cm, and 2.9cm). The inlet gas flow rate was always set at 10 ml/min.

Overall, the insertion of the distributor allowed to reach the desired liquid velocity profile since this hydrodynamic parameter resulted substantially constant through all the tested

directions, assuming a value of 10ml/min as the inlet gas flow rate for both x and z-coordinates. Reasonably, the only region with a rate deviating from the constant one along the z-direction is the region where the flow enters the riser, where accelerations occur due to the constriction near the riser inlet. Hence, by obtaining a homogeneous velocity inside the bioreactor, this novel system may ensure a more uniform distribution of nutrients and cell fraction inside the scaffolds while improving the mass transfer and the environment surrounding the cells (Magrofuoco et al., 2019).

6.3.3 Oxygen Mass Transport

Mathematical model

Bioreactors offer a closer representation of *in vivo* conditions for nutrient and oxygen distribution and exert specific hydrodynamic forces that may overcome any mass transfer deficiencies, thus, improving the supply of metabolites during cell culture (Grossemy et al., 2020). Specifically, it has been established that airlift bioreactors perform efficient mass transfer from a dispersed gas phase (air bubble) to a continuous liquid phase (culture media) (Talvy et al., 2007). In this work, once assessed the effectiveness of the hydrodynamics modeling, the objective was to predict the mass transfer of oxygen during dynamic cell culture.

In this simulation, an air flow rate of 10ml/min was assumed, and 150ml was the volume of the liquid medium inside the whole bioreactor. Considering the fibroblastic line NIH-3T3 as cell type (q_0=96 x 10^{-17} g/cells x s), and the incubator conditions of 37 °C and 1atm, mass transfer results from correlations 6.19-6.23 are reported in Tab. 6.3.

Table 6.3 Parameters characterizing mass transfer from bubble to liquid phase obtained by Eq. 6.19-6.23

Sphere-equivalent bubble diameter [mm]	6
Reynolds number	847.4
Schmidt number	269.2
Sherwood number	1448.5
k_l [m/s]	7.5 x 10^{-4}
a_l [m^{-1}]	18
C_l* [mg/l]	6.76

For the steady-state distributions of phases, the oxygen concentration in the liquid bulk was predicted from:

$$C_{l\infty} = \left(C_l^* - \frac{\chi\, q_0}{V\, k_l\, a_l}\right) \qquad (6.27)$$

The solution of Eq. 6.27 was evaluated for a range of cells number of 10^6 – 10^9, corresponding to a cells density of 6.7 x 10^4 – 6.7 x 10^6 cells/ml, in line with the maximum cell densities of 1-5 x 10^6 cells/ml reported for standard animal-cell bioreactor (Dill et al., 2019). Nevertheless, for the considered type of cells (NIH-3T3), the steady-state solution resulted independent from the oxygen consumption rate term, i.e., from cell number, indicating the oxygen transfer from bubbles to the culture medium as the unique transport-limiting factor. Moreover, a number of 1 x 10^{16} cells, corresponding to a cell density of 6.7 x 10^{13} cells/ml, was calculated as the maximum admissible value, which ensures the minimum cells oxygen concentration to maintain their physiological activity inside the bioreactor (1.7 mg/l). This parameter emerged far higher than the maximum standard animal-cell densities in media suspensions (1-5 x 10^6 cells/ml) inside bioreactors, demonstrating the operability of the designed system for maintaining cells survival during dynamic cultures. Similarly, by considering 10^8 cells/ml as the maximum cell density inside a seeded scaffold (Krause et al.), the maximum cell density inside the bioreactor (150 ml of media suspension) theoretically allows the dynamic culture of 1500 cylindrical scaffolds of 5 mm-diameter and 5 mm-height.

Concerning the time evolution of oxygen in the liquid phase (Eq. 6.20), Fig. 6.12 shows the plot of the average oxygen concentration, which also resulted independent from cells number for the investigated range of 10^6 – 10^9 NIH-3T3 cells, since the consumption term $(\chi\, q_0)/(V\, k_l\, a_l)$ emerged negligible compared to the saturation concentration C_l^*.

Therefore, since the renewal of bubbles and the oxygen consumed by cells in the downcomer can be considered null, it might be assumed that the riser was the unique region of the system involved in the oxygen mass transport. This transport was merely reduced to the oxygen transfer from bubbles in the riser to the surrounding culture medium.

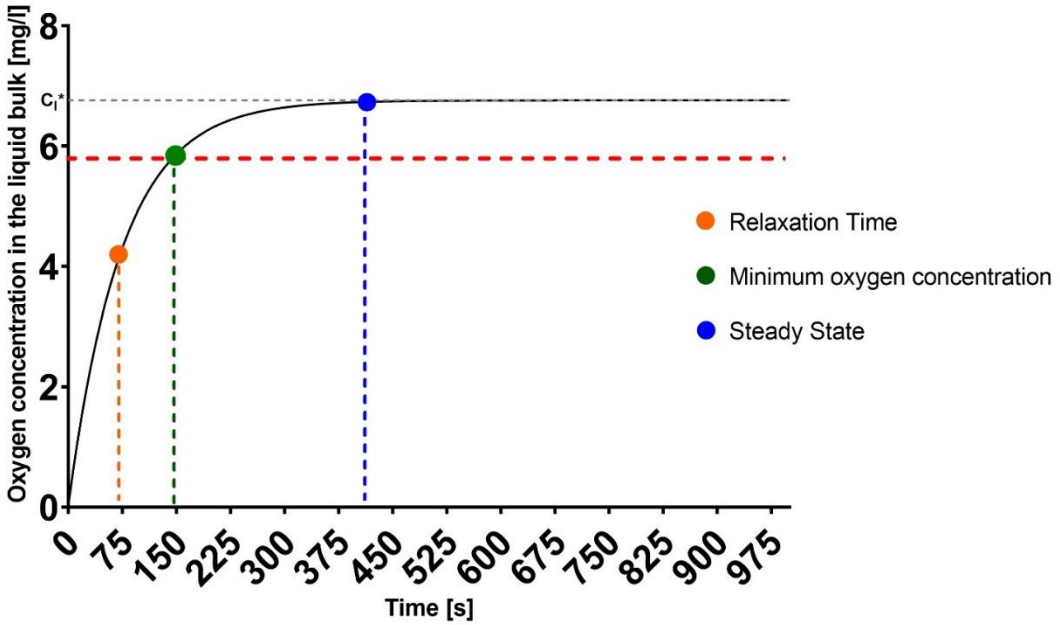

Figure 6.12 Oxygen concentration profile transferred by bubbles to the liquid phase as a function of time, obtained by solving Eq. 6.27.

From Fig. 6.12, it can be noticed that the main temporal parameters, i.e., the relaxation time (τ = 74s), the interval needed for reaching the steady-state concentration (≈ 400s), and the time to achieve the minimum oxygen concentration for cells viability (≈150s), resulted in line with the time-based dynamics of cell cultures (Flaibani et al., 2009; Dill et al., 2019).

Validation of Numerical Simulation of Mass Transfer (prediction of mass transfer from gas bubble to liquid)

The other objective of this study was to confirm the accuracy of the proposed mathematical modeling about the oxygen concentration inside the bioreactor. Hence, a numerical simulation of mass transfer was run in a two-phase bubbly flow. COMSOL software applies the two-fluid model derived from Reynolds-averaged Navier–Stokes equations in two-phase flow to compute mass transfer (Talvy et al., 2007). As a result, the evolution of oxygen concentration in the liquid was predicted as a function of time. By comparing data from the mathematical and numerical models, it could be estimated how the presence of the turbulence, included in the CFD model, affected the calculation for $k_l a_l$. Fig. 6.13 shows the comparison between the numerical simulation results (blue line) and mathematical data

(green line) plotted against the time evolution. In Fig. 6.13A, by rearranging Eq. 6.20, mathematical data are plotted as follows:

$$\ln\left(C_l^* - C_l\right) = \ln\left(C_l^*\right) - t * (k_l\, a_l) \qquad (6.28)$$

As expected, by using the calculated values of Tab. 6.2, Eq. 28 resulted in a straight line (green line) whose slope is ($-k_l a_l$). On the other hand, from the results of the CFD simulation, the oxygen concentration data were fitted as a one-exponential equation and plotted in the form of Eq. 6.28 in Fig. 6.13A. In this case, since a non-linear curve was found (blue line), it could be demonstrated that the temporal evolution of oxygen concentration predicted by the CFD simulation is not a one-exponential function. This aspect was probably due to the turbulence in the liquid phase, taken into account in the numerical model, which increases the mass transfer (Talvy et al., 2007). Overall, the oxygen concentration at the steady-state (600s) is equal in the two models, as shown in Fig. 6.13B. The latter is the plot of the oxygen concentration transferred from bubbles to the liquid phase as a function of time, according to the mathematical calculation (green line) and numerical results (blue line).

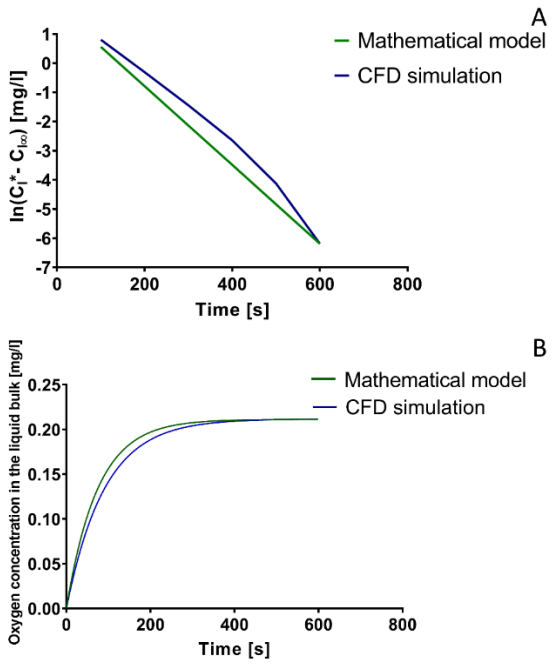

Figure 6.13 (A) Logarithmic plot of the oxygen concentration as a function of time, as obtained from the results of numerical simulation and Eq. 6.27 of the mathematical model. (B) Time evolution of the oxygen concentration transferred from bubbles to the liquid phase obtained from the mathematical model and numerical simulation.

As Fig. 6.13B shows, the simulated evolution of oxygen concentration in the liquid phase inside the riser has a good agreement with the mathematical solution of Eq. 6.16 for the full range of time (600s). For the proposed model of oxygen concentration profile, this result

confirms that the diffusive term remains limited compared to the convective transport in the effectiveness of oxygen transfer (Martin and Vermette, 2005). Overall, at the selected operating parameters, the simulated hydrodynamic environment validates the suitability of this novel bioreactor in bringing a sufficient amount of oxygen to growing cells during animal cell culture.

6.3.4 Influence of perfusion system on cell viability and proliferation in the PLLA scaffold

According to the literature (Martin et al., 2004; Flaibani et al., 2009; Sailon et al., 2009), a superficial liquid velocity lower than $1.7*10^{-3}$ m/s provides the most appropriate dynamic conditions for avoiding cell damage. In this work, a 10ml/min liquid flow rate was chosen as the operating flow rate for further experiments with cells, corresponding to $1.4 *10^{-3}$ m/s superficial liquid velocity through a 6mm-diameter, 90% porosity scaffold. From this value, the average hydrodynamic shear stress generated by the flow in the downcomer and experienced by cells was estimated using Eq. 6.1 as 3.3×10^{-6} Pa. This obtained value is well below the level of shear stress generally considered to damage cultured mammalian cells (1–10 Pa) and cultured neurons (1.0–4.5 Pa) (Grossemy et al., 2020).

In this work, we tested the effectiveness of the perfusion flow on cell growth and proliferation inside 3D polymeric scaffolds for long-term culture. First, the viability of the cells was determined using the AO test. AO is absorbed by both viable and non-viable cells and emits green fluorescence if associated with DNA or red fluorescence if bound to single-stranded nucleic acid (RNA) (Balaji and Gothandam, 2016). After 7 days of both static and dynamic cell culture, no remarkable differences in terms of cell viability were observed in the two different culture systems (Fig. 6.14A). Few red nuclei, ascribable to physiological turnover, are detectable in both cases. Then, the proliferation of NIH3T3 cells on PLLA scaffolds was evaluated by measuring DNA content. Since DNA content is proportional to the cell number (Mygind et al., 2007), cell proliferation inside the polymeric scaffold was followed over 15 days of culture, both in static and dynamic conditions. During the first 8 days, cell growth was evident in both conditions (Fig. 6.14B). However, cells in static scaffolds exhibited a slower growth rate than those cultured in the perfused system. Moreover, a decrease in the number of cells in static culture was observed after 8 days.

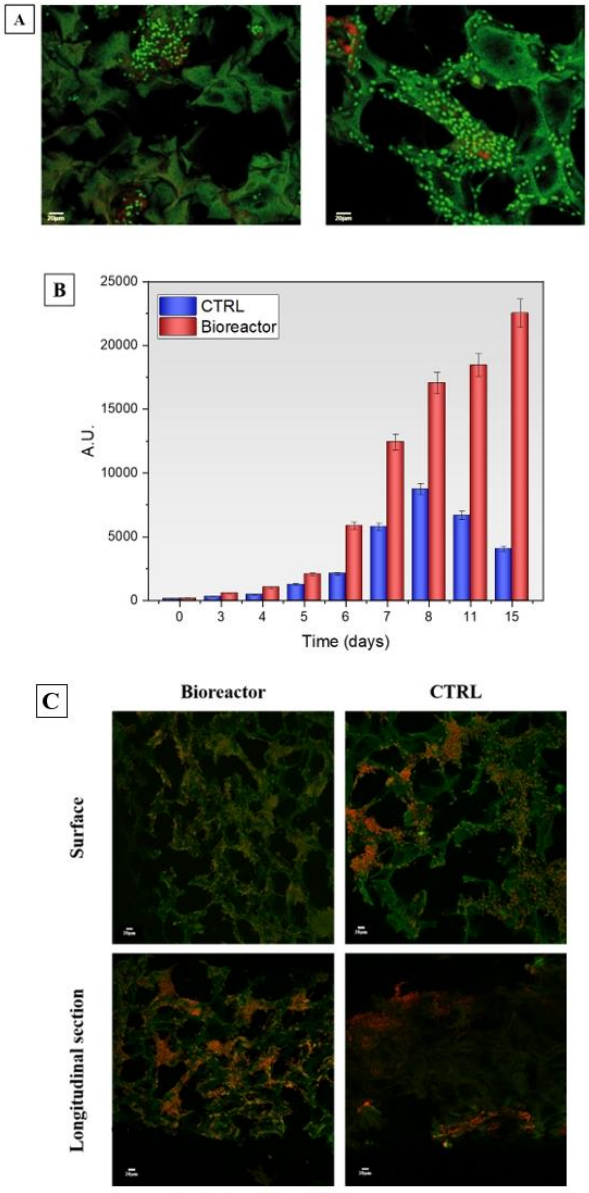

Figure 6.14 A) Fluorescence images of NIH3T3 cells stained by AO after 7 days of static (left) and dynamic culture (right). Red points indicate necrotic cells; green points indicate live cells. Scale bar: 20μm. B) Histogram reporting the cell growth in 3D scaffold under static and dynamic conditions inside the bioreactor. Blue bars indicate the control (static culture); red bars indicate the scaffold inside the bioreactor (dynamic culture). C) Confocal microscopy images of NIH3T3 cells on PLLA scaffold surface and longitudinal-section of a scaffold after 7 days of dynamic culture; (right column) surface and longitudinal-section of a scaffold after 7 days of static culture. Nuclei (red) are stained with PI and cytoskeleton (green) with Phalloidin. Scale bar: 20μm.

On the other hand, the cells grown under flow-perfusion continued to proliferate without reaching a plateau until the last time-point investigated. Finally, by using confocal microscopy, we investigated the attachment and proliferation of the cells on the scaffold after 7 days of culture. Fig. 6.14C shows the cross-section of two scaffolds kept under static and dynamic culture. In the first case, cells are detected only at the surface of the scaffold,

whereas evident bulk colonization was observed in the samples dynamically cultured. As a result, in comparison to static conditions, dynamic culture was found to optimize cell expansion in 3D scaffolds by offering a microenvironment capable of improving cell culture conditions.

These results combined with the previous outcomes demonstrated that the designed bioreactor could provide suitable perfusion for cell viability and proliferation inside a 3D polymeric scaffold, suggesting the potential for future TE applications, such as long-period dynamic cultures.

6.4 Conclusions

In this study, mathematical equations and numerical analysis were proposed to characterize and optimize a novel perfusion bioreactor that has been designed as an external loop airlift reactor. Principally, the focus was on the liquid circulation velocity, gas holdup, and oxygen mass transfer in the riser. The hydrodynamic properties of the bioreactor were investigated under different operating conditions using experimental testing, mathematical method, and CFD simulation, showing good agreement between the modeling and experiments. Interestingly, the computational simulation turned out to be an effective tool for optimizing the bioreactor design: the challenges derived from the inhomogeneous liquid velocity profile within the downcomer zone were successfully overcome by changing the bioreactor geometry. Moreover, results from modeling revealed an optimal oxygen concentration profile inside the device, which guarantees its suitability for ensuring the viability and proliferation of animal cell culture in a 3D matrix. Overall, this study offers a valid model for bioreactor studies since the combination of the validated mathematical equations, accurate computational simulation, and specific experimental techniques turned out to be a powerful tool for the characterization and optimization of the system.

Nomenclature

Subscript "b" = bubble	*h = liquid hydrostatic level [m]*	*t = time [s]*
Subscript "g" = gas	*He = Henry's Law constant [mg/(L atm)]*	*u = velocity vector [m/s]*
Subscript "l" = liquid	*ID = internal diameter of the downcomer [m]*	u_{slip} *= slip velocity [m/s]*
a = bubble major semi-axis [m]	*k = turbulent kinetic energy per unit mass* $[m^2/s^2]$	V *= volume* $[m^3]$
a_l *= specific interfacial area (referred to dispersion volume)* $[m^2/m^3]$	k_l *= mass transfer coefficient [m/s]*	V_s *= superficial velocity [m/s]*
b = bubble minor semi-axis [m]	*l = difference between the pressure taps of the manometer [m]*	V_T *= terminal velocity of single bubbles [m/s]*
C_μ *= standard constant of the k-*ε *theory (dimensionless), Eq. 6.7*	*M = molecular weight [kg/kmol]*	$V_{T,\infty}$ *= terminal velocity of single bubbles in an infinite environment [m/s]*
C_d *= drag force coefficient (dimensionless), Eq. 6.9*	m_{gl} *= mass transfer rate from gas to liquid* $[kg/(m^3\ s)]$	$V_{T,r}$ *= relative rising velocity of the single bubble [m/s], Eq. 6.13, 6.16*
C_k *= = standard constant of the k-*ε *theory (dimensionless), Eq. 6.8*	*N = molar flux per interfacial area* $[mol/(s\ m^2)]$	ΔP *= pressure difference [Pa]*
C_l *= concentration of the dissolved gas in the liquid phase* [mg/L]	*P = operating pressure [Pa]*	ΔP_0 *= pressure drop at zero-air flow rate [Pa]*
C_l** = concentration of the dissolved gas at the liquid interface* [mg/L]	Q *= flow rate* $[m^3/s]$	ε *= turbulent energy dissipation rate per unit mass* $[m^2/s^3]$
d_b *= bubble diameter [m]*	q_0 *= specific oxygen consumption rate [mg/s]*	λ *= ratio of the sphere-equivalent bubble diameter* d_{eq} *to the column diameter* D_c *(dimensionless), Eq. 6.3, 6.4*
D *= diffusivity coefficient* $[m^2/s]$	r *= radius [m]*	μ *= dynamic viscosity [Pa s]*
D_c *= column diameter* $[m^2]$	Re_p *= particle Reynolds number (dimensionless), Eq. 12,13*	μ_T *= turbulent viscosity [Pa s], Eq. 6.6, 6.7*
d_{eq} *= bubble equivalent diameter [m]*	$Re_{t\infty}$ *= Reynolds number in the absence of wall (dimensionless)*	ρ *= density* $[kg/m^3]$
d_o *= orifice diameter [m]*	R_{O2} *= oxygen consumption rate [mg/L s]*	σ *= surface tension [N/m]*

E = aspect ratio between minor and major axes of ellipsoidal bubbles (dimensionless)	*S = surface [m^2]*	*τ = relaxation time of mass transfer [s]*
f = wall factor, Eq.4	*Sc = Schmidt number (dimensionless), Eq. 6.14*	*τ_w = shear stress [Pa]*
g = gravitational acceleration [m^2/s]	*Sh= Sherwood number (dimensionless), Eq. 6.12, 6.15*	*φ = fractional phase holdup (dimensionless)*
H = column height [m]	*S_k = turbulent kinetic energy added term [kg/(m s^3)]*	*χ = number of cells (dimensionless)*

References

AL-Mashhadani, M. K. H., Wilkinson, S. J., and Zimmerman, W. B. (2015). Airlift bioreactor for biological applications with microbubble mediated transport processes. *Chem. Eng. Sci.* 137, 243–253. doi:10.1016/J.CES.2015.06.032.

Arsenijević, Z. L., Grbavčić, Ž. B., Garić-Grulović, R. V., and Bošković-Vragolović, N. M. (2010). Wall effects on the velocities of a single sphere settling in a stagnant and counter-current fluid and rising in a co-current fluid. *Powder Technol.* 203, 237–242. doi:10.1016/j.powtec.2010.05.013.

Bai, W., Deen, N. G., and Kuipers, J. A. M. (2012). Numerical investigation of gas holdup and phase mixing in bubble column reactors. *Ind. Eng. Chem. Res.* 51, 1949–1961. doi:10.1021/ie102557h.

Balaji, K., and Gothandam, K. M. (2016). Cytotoxic effect on cancerous cell lines by biologically synthesized silver nanoparticles. *Brazilian Arch. Biol. Technol.* 59. doi:10.1590/1678-4324-2016150529.

Bancroft, G. N., Sikavitsas, V. I., and Mikos, A. G. (2003). Design of a flow perfusion bioreactor system for bone tissue-engineering applications. *Tissue Eng.* 9, 549–554. doi:10.1089/107632703322066723.

Becker, S., Sokolichin, A., and Eigenberger, G. (1994). Gas-liquid flow in bubble columns and loop reactors: Part II. Comparison of detailed experiments and flow simulations. *Chem. Eng. Sci.* 49, 5747–5762. doi:10.1016/0009-2509(94)00290-8.

Beşkardeş, I. G., Aydın, G., Bektaş, Ş., Cengiz, A., and Gümüşderelioğlu, M. (2018). A systematic study for optimal cell seeding and culture conditions in a perfusion mode bone-tissue bioreactor. *Biochem. Eng. J.* 132, 100–111. doi:10.1016/j.bej.2018.01.006.

Burova, I., Wall, I., and Shipley, R. J. (2019). Mathematical and computational models for bone tissue engineering in bioreactor systems. *J. Tissue Eng.* 10. doi:10.1177/2041731419827922.

Chabanon, M. (2015). Multiscale study of a perfusion bioreactor for bone tissue engineering.

Clift, R., Grace, J., and Weber, M. (1978). *Bubbles, Drops, and Particles*.

COMSOL® (2016). CFD Module User ’s Guide. *COMSOL Multiphysics*, 1–710.

Dill, V., Ehret, J., Zimmer, A., Beer, M., and Eschbaumer, M. (2019). Cell density effects in different cell culture media and their impact on the propagation of foot-and-mouth disease virus. *Viruses* 11. doi:10.3390/v11060511.

Ebrahimifakhar, M., Mohsenzadeh, E., Moradi, S., Moraveji, M., and Salimi, M. (2020). CFD simulation of the hydrodynamics in an internal air-lift reactor with two different configurations. doi:10.1007/s11705-011-1116-x.

Flaibani, M., Luni, C., Sbalchiero, E., and Elvassore, N. (2009). Flow cytometric cell cycle analysis of muscle precursor cells cultured within 3D scaffolds in a perfusion bioreactor. *Biotechnol. Prog.* 25, 286–295. doi:10.1002/btpr.40.

Gaspar, D. A., Gomide, V., and Monteiro, F. J. (2012). The role of perfusion bioreactors in bone tissue engineering. *Biomatter* 2, 167–175. doi:10.4161/biom.22170.

Grayson, W. L., Marolt, D., Bhumiratana, S., Fröhlich, M., Guo, X. E., and Vunjak-Novakovic, G. (2011). Optimizing the medium perfusion rate in bone tissue engineering bioreactors. *Biotechnol. Bioeng.* 108, 1159–1170. doi:10.1002/bit.23024.

Green, D. W., and Perry, R. H. (2008). Perry's Chemical Engineers' Handbook, Eighth Edition. Available at: /content/book/9780071422949 [Accessed July 22, 2020].

Groen, J. S. (2004). Scales and structures in bubbly flows.

Grossemy, S., Chan, P. P. Y., and Doran, P. M. (2020). Stimulation of cell growth and neurogenesis using protein-functionalized microfibrous scaffolds and fluid flow in bioreactors. *Biochem. Eng. J.* 159, 107602. doi:10.1016/j.bej.2020.107602.

Han, L., Liu, Y., and Luo, H. (2007). Numerical Simulation of Gas Holdup Distribution in a Standard Rushton Stirred Tank Using Discrete Particle Method. *Chinese J. Chem. Eng.* 15, 808–813. doi:10.1016/S1004-9541(08)60007-5.

Hossain, M. S., Bergstrom, D. J., and Chen, X. B. (2015). Modelling and simulation of the chondrocyte cell growth, glucose consumption and lactate production within a porous tissue scaffold inside a perfusion bioreactor. *Biotechnol. Reports* 5, 55–62. doi:10.1016/j.btre.2014.12.002.

Hughmark, G. A. (1967). Holdup and mass transfer in bubble columns. *Ind. Eng. Chem. Process Des. Dev.* 6, 218–220. doi:10.1021/i260022a011.

Kantarci, N., Borak, F., and Ulgen, K. O. (2005). Bubble column reactors. *Process Biochem.* 40, 2263–2283. doi:10.1016/j.procbio.2004.10.004.

Kojić, P. S., Popović, S. S., Tokić, M. S., Šijački, I. M., Lukić, N. L. J., Jovičević, D. Z., et al. (2017). Hydrodynamics of an external-loop airlift reactor with inserted membrane. *Brazilian J. Chem. Eng.* 34, 493–505. doi:10.1590/0104-6632.20170342s20150399.

Krause, A. L., Beliaev, D., Van Gorder, R. A., and Waters, S. L. Lattice and Continuum Modelling of a Bioactive Porous Tissue Scaffold. doi:10.1093/imammb/dqnxxx.

Law, D., and Battaglia, F. (2013). Numerical simulations for hydrodynamics of air-waterexternal loop airlift reactorflows with bubble break-up and coalescence effects. *J. Fluids Eng. Trans. ASME* 135. doi:10.1115/1.4024396.

Li, X. Q., Liu, T. Q., Zhu, L., Song, K. D., Ma, X. H., and Cui, Z. F. (2008). Culture and expansion of mesenchymal stem cells in air-lift loop hollow fiber membrane bioreactor. *Gao Xiao Hua Xue Gong Cheng Xue Bao/Journal Chem. Eng. Chinese Univ.* 22, 985–991. doi:10.1038/cr.2008.259.

Lin, H., Lozito, T. P., Alexander, P. G., Gottardi, R., and Tuan, R. S. (2014). Stem Cell-Based Microphysiological Osteochondral System to Model Tissue Response to Interleukin-1β. doi:10.1021/mp500136b.

Lombardo, M. E., Carfì Pavia, F., Vitrano, I., Ghersi, G., Brucato, V., Rosei, F., et al. (2019). PLLA scaffolds with controlled architecture as potential microenvironment for in vitro tumor model. *Tissue Cell* 58, 33–41. doi:10.1016/j.tice.2019.04.004.

Magrofuoco, E., Flaibani, M., Giomo, M., and Elvassore, N. (2019). Cell culture distribution in a three-dimensional porous scaffold in perfusion bioreactor. *Biochem. Eng. J.* 146, 10–19. doi:10.1016/j.bej.2019.02.023.

Mallick, S. P., Rastogi, A., Tripathi, S., and Srivastava, P. (2017). Strategies on process engineering of chondrocyte culture for cartilage tissue regeneration. *Bioprocess Biosyst. Eng.* 40, 601–610. doi:10.1007/s00449-016-1724-4.

Mannella, G. A., Carfì Pavia, F., Conoscenti, G., La Carrubba, V., and Brucato, V. (2014). Evidence of mechanisms occurring in thermally induced phase separation of polymeric systems. *J. Polym. Sci. Part B Polym. Phys.* 52, 979–983. doi:10.1002/polb.23518.

Manual, A. L. CFD Module Application Library.pdf.

Martin, I., Wendt, D., and Heberer, M. (2004). The role of bioreactors in tissue engineering. *Trends Biotechnol.* 22, 80–86. doi:10.1016/j.tibtech.2003.12.001.

Martin, Y., and Vermette, P. (2005). Bioreactors for tissue mass culture: Design, characterization, and recent advances. *Biomaterials* 26, 7481–7503. doi:10.1016/j.biomaterials.2005.05.057.

Mygind, T., Stiehler, M., Baatrup, A., Li, H., Zou, X., Flyvbjerg, A., et al. (2007). Mesenchymal stem cell ingrowth and differentiation on coralline hydroxyapatite scaffolds. *Biomaterials* 28, 1036–1047. doi:10.1016/j.biomaterials.2006.10.003.

Nalband, M., and Jalilnejad, E. (2019). 3D cfd simulation of gas hold-up and mass transfer in a modified airlift reactor with net draft tube. *Int. J. Chem. React. Eng.* 17, 1–12. doi:10.1515/ijcre-2019-0060.

Nedeltchev, S., and Schumpe, A. (2008). A new approach for the prediction of gas holdup in bubble columns operated under various pressures in the homogeneous regime. *J. Chem. Eng. Japan* 41, 744–755. doi:10.1252/jcej.08we005.

Patil, H., Chandel, I. S., Rastogi, A. K., and Srivastava, P. (2013). Studies on a Novel Bioreactor Design for Chondrocyte Culture. *Int. J. Tissue Eng.* 2013, 1–7. doi:10.1155/2013/976894.

Pereira, R. F., Freitas, D., Tojeira, A., Almeida, H. A., Alves, N., and Bártolo, P. J. (2014). Computer modelling and simulation of a bioreactor for tissue engineering. in *International Journal of Computer Integrated Manufacturing* (Taylor and Francis Ltd.), 946–959. doi:10.1080/0951192X.2013.812244.

Pisanti, P., Yeatts, A. B., Cardea, S., Fisher, J. P., and Reverchon, E. (2012). Tubular perfusion system culture of human mesenchymal stem cells on poly- L- Lactic acid scaffolds produced using a supercritical carbon dioxide-assisted process. *J. Biomed. Mater. Res. - Part A* 100 A, 2563–2572. doi:10.1002/jbm.a.34191.

Place, T. L., Domann, F. E., and Case, A. J. (2017). Limitations of oxygen delivery to cells in culture: An underappreciated problem in basic and translational research. *Free Radic. Biol. Med.* 113, 311–322. doi:10.1016/j.freeradbiomed.2017.10.003.

Sailon, A. M., Allori, A. C., Davidson, E. H., Reformat, D. D., Allen Jr., R. J., and Warren, S. M. (2009). A Novel Flow-Perfusion Bioreactor Supports 3D Dynamic Cell Culture. *J. Biomed. Biotechnol.*

Salehi-Nik, N., Amoabediny, G., Pouran, B., Tabesh, H., Shokrgozar, M. A., Haghighipour, N., et al. (2013). Engineering parameters in bioreactor's design: A critical aspect in tissue engineering. *Biomed Res. Int.* 2013. doi:10.1155/2013/762132.

Saltzman, W. M. (2004). *Tissue engineering: engineering principles for the design of replacement organs and tissues*. Oxford, UK: Oxford University Press Available at: http://books.google.com/books?id=KorDMxtkZ_wC&pgis=1.

Sam, A., Gomez, C. O., and Finch, J. A. (1996). Axial velocity profiles of single bubbles in water/frother solutions. *Int. J. Miner. Process.* 47, 177–196. doi:10.1016/0301-7516(95)00088-7.

Shaikh, A., and Al-Dahhan, M. (2013). Scale-up of bubble column reactors: A review of current state-of-the-art. *Ind. Eng. Chem. Res.* 52, 8091–8108. doi:10.1021/ie302080m.

Shakeel, M. (2013). 2-D coupled computational model of biological cell proliferation and nutrient delivery in a perfusion bioreactor. *Math. Biosci.* 242, 86–94. doi:10.1016/j.mbs.2012.12.004.

Shi, Y. (2008). Numerical simulation of global hydro-dynamics in a pulsatile bioreactor for

cardiovascular tissue engineering. *J. Biomech.* 41, 953–959. doi:10.1016/j.jbiomech.2008.01.001.

Talvy, S., Cockx, A., and Line, A. (2007). Modeling of oxygen mass transfer in a gas-liquid airlift, reactor. *AIChE J.* 53, 316–326. doi:10.1002/aic.11075.

Tojo, K., Miyanami, K., and Yano, T. (1974). Gas holdup and pressure drop in a multistage vibrating disk column with cocurrent gas-liquid flow.

Tomiyama, A., Nakahara, Y., Adachi, Y., and Hosokawa, S. (2003). Shapes and Rising Velocities of Single Bubbles rising through an Inner Subchannel. *J. Nucl. Sci. Technol.* 40, 136–142. doi:10.1080/18811248.2003.9715343.

Vacanti, J. P., and Langer, R. (1999). Tissue engineering: the design and fabrication of living replacement devices for surgical reconstruction and transplantation. *Lancet* 354, S32–S34. doi:10.1016/S0140-6736(99)90247-7.

Wang, S. J., and Zhong, J. J. (2007). "Bioreactor Engineering," in *Bioprocessing for Value-Added Products from Renewable Resources* (Elsevier), 131–161. doi:10.1016/B978-044452114-9/50007-4.

Wang, Z., Huang, C., Wang, J., Wang, P., Bi, S., and Abbas, C. A. (2019). Design and Simulation of Flow Field for Bone Tissue Engineering Scaffold Based on Triply Periodic Minimal Surface. *Chinese J. Mech. Eng. (English Ed.* 32, 1–10. doi:10.1186/s10033-019-0329-7.

Yan, X., Bergstrom, D. J., and Chen, X. B. (2012). Modeling of cell cultures in perfusion bioreactors. *IEEE Trans. Biomed. Eng.* 59, 2568–2575. doi:10.1109/TBME.2012.2206077.

Zhou, S., Cui, Z., and Urban, J. (2008). Nutrient gradients in engineered cartilage: metabolic kinetics measurement and mass transfer modeling. *Biotechnol. Bioeng.* 101, 408–421. doi:10.1002/BIT.21887.

Zhu, Y. (2007). "Immobilized Cell Fermentation for Production of Chemicals and Fuels," in *Bioprocessing for Value-Added Products from Renewable Resources* (Elsevier), 373–396. doi:10.1016/B978-044452114-9/50015-3.

Chapter 7

Computational modeling of Micro-Computed scaffolds cultured in an airlift perfusion bioreactor: a numerical study and *in vitro* characterization

This chapter presents the models currently used to study fluid dynamics at the level of the pores of the scaffold. A complex study combining numerical analysis and *in vitro* testing is then discussed. Specifically, to evaluate the effects of the operational parameters of the airlift bioreactor described in Chapter 5, numerical simulations were performed to solve the fluid velocity profile within that bioreactor, also containing a multi-grids support which allows the allocation of multiple seeded scaffolds simultaneously. Since the effects of the porous microstructure of scaffolds on the extracellular matrix deposition play a crucial role in perfusion cultures, the numerical simulation was also implemented at the pore level of the scaffold for fluid flow through porous media during perfused culture. Micro-computed tomography was used to obtain the digital 3D image of the complex geometry of a PLLA scaffold, offering a detailed analysis from a volume-based methodology without simplifications of the results as for pore- or Darcy's Law-models. Predictions about the uniformity of the flow field through the scaffolds-bioreactor system have been assessed by quantifying the cell viability of a perfusion culture while using pre-osteoblastic cells seeded on 24 PLLA scaffolds up to 6 days.

7.1 Theoretical modeling of scaffolds in a perfusion bioreactor

Tissue engineering (TE) strategies for therapeutic purposes aim to develop functional tissue models (Salah, 2018) but are limited in their ability to provide reliable approaches for mimicking *in vitro* the *in vivo* fluid dynamic environments. Numerical simulations are currently applied to circumvent these problems without trial-and-error experiments and examine pore-scale flow across the extracellular matrix (ECM) substitutes.

Besides the culture medium flow rate, the microstructure of the scaffold, including porosity (Salerno and Domingo, 2015), pore size (Pan and Ding, 2012), and pore interconnection (Erdemir et al., 2015), influence the stimuli exerted on cells during the culture period, such as fluid shear stress and liquid velocity distribution on the surface of the scaffold where cells

are attached. It is essential to investigate the effect of the flow that cells experience within the porous scaffold to reproduce the native dynamic environment with *in vitro* models. The goal is to study the flow field through the original architecture of the scaffold under controlled fluid flow, for example, within a perfusion bioreactor.

Recently, Yamada *et al*. (Yamada et al., 2021) computationally estimated the fluid flow characteristics through a porous scaffold inside a perfusion bioreactor. By assuming the porosity and the permeability calculated from the Darcy' Law applied to data of a Micro-Computed Tomography (micro-CT) analysis, they provided the velocity and shear distribution through scaffold constructs. Similarly, Mahammod et al. (Pasha Mahammod et al., 2019) combined micro-CT images of the scaffold with Darcy's Law to quantify the permeability of the scaffold for bone tissue engineering. In particular, the authors used both the Newtonian fluid model and the non-Newtonian fluid model to analyze the fluid domain in the porous region. The latter is regarded as the blood flowing into the bone micro-vessels. From their results, non-Newtonian analyses found a lower permeability value than Newtonian analyses. In addition, no significant variations in the velocity distribution between the two models appeared, which concludes that the velocity of the fluid within the scaffold depends primarily on the geometry (i.e., porosity and pore size) and inlet velocity into the scaffold. For these two studies (Pasha Mahammod et al., 2019; Yamada et al., 2021), although the geometry was derived from micro-CT scans, thus accurately modeled without any assumptions, the local distribution of estimated parameters was not accurate due to the use of quantities obtained from theoretical models that generate approximations.

In other studies, a similar approach was used to estimate the permeability and fluid dynamics through pores in scaffold produced by additive manufacturing, thus having a regular morphology and easier to analyze numerically (Ali and Sen, 2017; Xue et al., 2019) (Fig. 7.1). In these cases, with reference to the CAD parameters and the derived pressure drop from a CFD analysis, scaffolds permeability was calculated using Darcy's law as follows:

$$k = \frac{Q\mu L}{A\Delta P} \qquad (7.1)$$

where Q, μ, L, A, and ΔP are the fluid flow rate, dynamic fluid viscosity, model length, the cross-sectional area of a unit cell, and pressure drop, respectively. Overall, with increasing pore sizes and porosity of the scaffolds, permeability also increased (Ali and Sen, 2017).

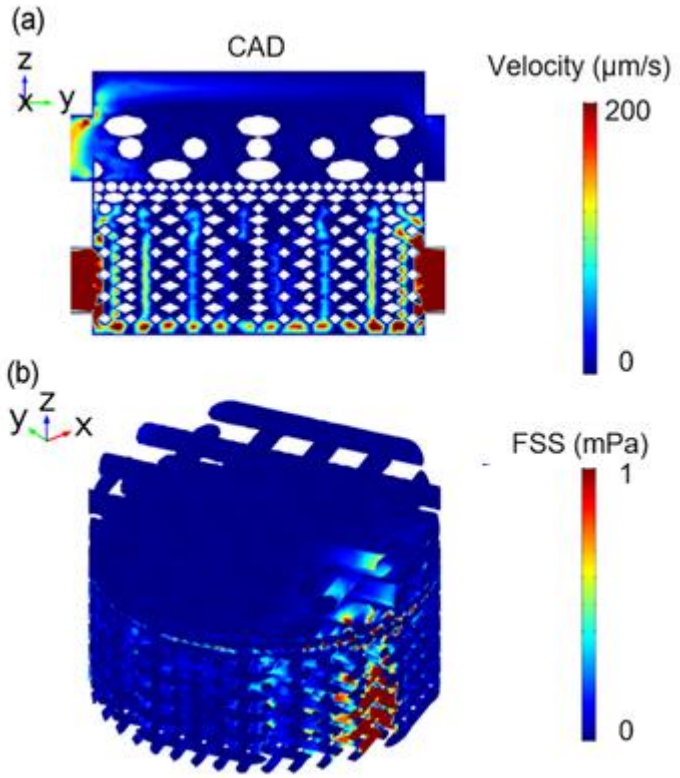

Figure 7.1 (a) Flow velocity distribution on the cross-sectional slice for CAD model. (b) Fluid-induced shear stress on the scaffold for the CAD model. CAD, computer-aided design. (Xue et al., 2019)

In addition to Darcy's law, other analytical models have been used to correlate permeability and fluid dynamics to the properties of scaffold pores. Among these, the Kozeny– Carmen equation is the most adopted (Eq. 7.2) (Pok et al., 2013; Podichetty and Madihally, 2014; Podichetty et al., 2014) for permeability calculation:

$$k = \frac{\pi}{128} n_A d^4 \qquad (7.2)$$

where d is the pore diameter and n_A is the number of pores per unit area. When this equation is used, the Brinkman equation is commonly employed to characterize flow in the scaffold (porous) region (Eq. 3):

$$\mu \nabla^2 u_s - \frac{\mu}{k} u_s = \nabla p \qquad (7.3)$$

where k is the permeability, u_s denotes the fluid superficial velocity vector in 3D, p is the fluid pressure (Pa), and μ is the effective viscosity in the porous medium. The Brinkman equation consists of an additional viscous term compared to Darcy's equation. This term accounts for the momentum transport by microscopic shear effects and pressure gradients. In a flow-through bioreactor design, Podichetty et al. (Podichetty and Madihally, 2014) assessed the differences in predicted pressure drop from the simulations performed using Darcy's equation and the Brinkman equation. From their findings, the pressure drop with the

Brinkman equation was higher than that with Darcy's equation, and the deviations increased with flow rate. The viscous term in the Brinkman equation represents the no-slip boundary condition, leading to increased pressure loss due to friction losses. It's interesting how the authors show that you could use the Brinkman equation to calculate the pressure drop at various permeability, which will give an inverse proportionality to *k* at a constant flow rate. In a continuous-flow bioreactor, the flow rate shall be increased to account for increased flow resistance if the permeability of the scaffold is reduced to ensure sufficient nutrient supply.

Another approach using the Lattice-Boltzmann method (LBM) is also used based on the Brinkman equation. The Lattice Boltzmann method is usually limited to a small portion of the scaffold to evaluate the local flow properties of media inside the pores. In particular, the LBM is a numerical technique for simulating hydrodynamics while solving the discrete Boltzmann equation. LBM is particularly suitable for modeling the flow to the scale of pores through porous media due to the simplicity with which it manages complicated boundaries. When considering the lattice nodes, the fluid nodes are those within the flow field (i.e., within the empty pore space), and the wall nodes are those making up the rigid wall. Advantages of this method include the ability to model very complex geometries with few grid constraints and run complicated models on modestly sized computers. Hence, several works have coupled this method with micro-CT to reconstruct the scaffold (Porter et al., 2005; Voronov et al., 2010b, 2010a). With this methodology, the flow field can be obtained in detail within the scaffolds, and the shear stresses are calculated locally within the pores.

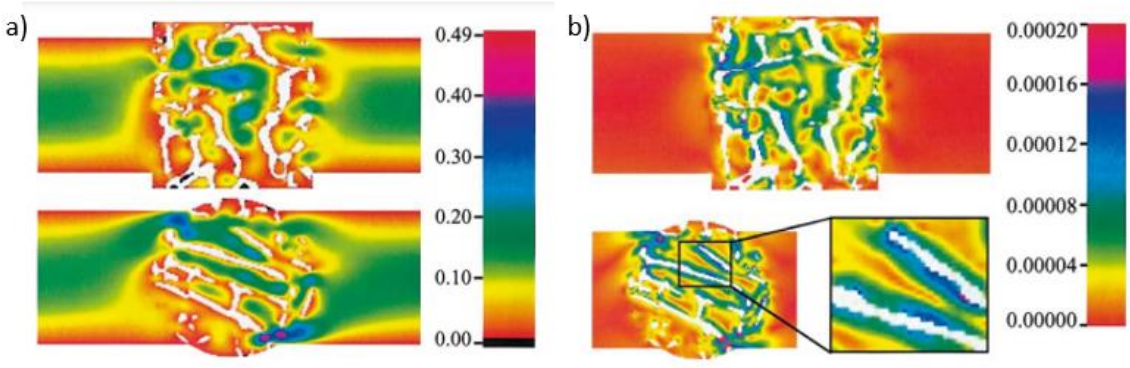

Figure 7.2 (a) Velocity flow field: speed of media flow (mm/s) through a transversely perfused cylindrical trabecular bone scaffold (shown in white) from the side and top views. (b) Local shear stress field: map of shear stresses (Pa) in media transversely perfused through a 3D trabecular bone scaffold from the side and top views (Porter et al., 2005).

7.2 Experimental modeling of scaffolds in the airlift bioreactor

In the present research, Micro-CT has been used for the realistic reproduction of the scaffold morphology further employed in the computational study. Micro-CT is a non-invasive technique that allows the build-up of a digital 3D reconstruction from cross-section scans of a defined structure (Gaspar et al., 2012; Basu, 2017; Vetsch et al., 2017; Siddiqui et al., 2018; Zeinali et al., 2021). More important is how the flow rate distributes within the pores of the scaffold (where cells are attached), influenced by the geometry of the bioreactor and the pores themselves. The combination of CFD simulations and micro-CT allows avoiding inaccuracies in the calculated values, as occurs when using pore scale and pore network models (Boschetti et al., 2006; Lawrence et al., 2009; Muljadi et al., 2016). Pore models have the limitations of reproducing simplified geometries that have differences from the complex native porous structure, specifically in terms of interconnection and distribution of pores. In literature, pore modeling is commonly coupled with either Darcy's law (Abu-Al-Saud et al., 2020) or with a numerical methodology (Golparvar et al., 2018). While the former provides an order of magnitude of the mean values within an idealized pore structure, the latter investigates locally the pore-level mechanisms of fluid-solid interactions but in an unrealistic scaffold structure. In scaffold-based approaches, all these factors have implications in cellular behaviors during *in vitro* tests (Karande et al., 2004; Gaspar et al., 2012; Mehrian et al., 2020; Geven et al., 2021; Zeinali et al., 2021).

This research aims to validate an advanced and reliable system for the dynamic culture of multiple scaffolds in the TE field. Here, we ran several computational simulations to characterize the fluid flow profile within a perfusion bioreactor with specific support for scaffolds allocation and within the porous microstructure of a micro-CT scanned scaffold made of poly-L-lactic acid (PLLA). This scaffold was produced using the thermally induced phase separation (TIPS) technique, thus having a complex morphology consisting of interconnected micropores (Capuana et al., 2021a). Because of such complexity involving high computational costs, the micro-CT scanned scaffold was manipulated into a sub-volume and used as input of the numerical simulation under flow conditions. Specifically, the flow field was obtained by the numerical solution of the Navier-Stokes equations. By combining a micro-CT 3D reconstruction and the CFD analysis, the actual and local fluid dynamic properties of scaffolds subjected to perfusion flow could be determined and characterized as a uniform distribution of flow velocities at the pore level. Finally, the numerical results of uniform fluid flow through our perfused porous media were

corroborated by determining the cell proliferation inside 24 seeded PLLA scaffolds cultured within the perfusion bioreactor for up to 6 days.

7.3 Materials and methods

7.3.1 CAD design of a multi-grids support

Custom-made support was CAD-designed using Solidworks software (Fig. 2) to allocate multiple scaffolds inside the bioreactor. Specifically, the support was considered an assembly of different components: a base, basic grids, and grids with legs for scaffolds placement, two cylindrical threaded poles, and a top-weight. The main features of this system are discussed in the results section.

7.3.2 Computational Fluid Dynamics (CFD) Simulations of the Bioreactor with the multi-grids support

COMSOL Multiphysics version 5.3a was used to perform a computational fluid dynamic (CFD) simulation to define the velocity profile inside the bioreactor in the presence of multi-grids support during the perfusion flow. As discussed in Chapter 5, the system was considered an external-loop airlift column that works in a bubbly flow turbulent regime. According to the COMSOL module, the transport equation is governed by the k-ε model, which adds a turbulent viscosity to the physical one in the momentum transport equation (Amores Vera and Rodríguez Ruiz, 2012):

$$\rho_l \frac{\partial k}{\partial t} + \rho_l(\bar{u}_l \cdot \nabla)k = \nabla \cdot \left[\left(\mu + \frac{\mu_T}{\sigma_k}\right)\nabla k\right] + P_k - \rho_l \varepsilon + S_k \qquad (7.4)$$

Where k is the turbulence kinetic energy *k*, and the term P_k is given by:

$$P_k = \mu_T[\nabla \bar{u}_l : (\nabla \bar{u}_l + (\nabla \bar{u}_l)^T)] \qquad (7.5)$$

The turbulent viscosity μ_T is described by:

$$\mu_T = \rho_l C_\mu \frac{k^2}{\varepsilon} \qquad (7.6)$$

where C_μ is a constant.

In Eq. 7.4, ε is the evolution of the turbulent's energy dissipation rate, and it is modeled by:

$$\rho_l \frac{\partial \varepsilon}{\partial t} + \rho_l (\bar{u}_l \cdot \nabla)\varepsilon = \nabla \cdot \left[\left(\mu + \frac{\mu_T}{\sigma_\varepsilon}\right)\nabla\varepsilon\right] + C_{\varepsilon 1}\frac{\varepsilon}{k}P_k - C_{\varepsilon 2}\rho_l \frac{\varepsilon^2}{k} + C_\varepsilon S_k \frac{\varepsilon}{k} \quad (7.7)$$

Within this model, the turbulence induced by bubbles is referred to as the term S_k, described by:

$$S_k = -C_k \varphi_g \nabla p \cdot \bar{u}_{slip} \quad (7.8)$$

In our model, the boundary conditions were set as follows: an inlet gas flow rate of 0.0042 m/s, constant outlet pressure of 1 atm, and no-slip of the fluid at the solid walls. The culture medium was modeled as a water-like incompressible Newtonian fluid, having a density of 1000 kg/m^3 and dynamic viscosity of 1×10^{-3} Pa·s, the inlet gas density was fixed at 0.9727 kg/m^3, and the simulation temperature was set to 37°C, representing the incubator/body temperature. The flow velocity profiles were analyzed as the principal simulation outcomes.

7.3.3 Scaffold fabrication

PLLA scaffolds were prepared via TIPS, as earlier described (Mannella et al., 2014; Conoscenti et al., 2017; Lombardo et al., 2019). Briefly, a homogeneous ternary solution was prepared by dissolving 4% wt/wt PLLA in constant dioxane to water weight ratio of 87/13. The solution at 60 ºC was poured into a cylindrical Teflon holder (d=2 cm and h=3 cm), first immersed in a 30 ºC thermostatic bath for 45 minutes and then in an ethyl alcohol bath at -20 ºC for 15 minutes to freeze the resulting structure. Scaffolds were washed overnight in deionized water and dried at 40 °C for 8 hours to remove any dioxane trace.

7.3.4 Micro-computed Tomography

Micro-CT analysis (micro-CT Skyscan 1272, Bruker) was completed to acquire the 3D microarchitecture of the produced PLLA scaffold. Measurements were made using dried scaffolds, operating at 40 kV and 250 mA and without using the filter. The images of cross-sections were provided in greyscale and saved in 8 bits with 256 grey levels to reconstruct the complete set of projections.

7.3.5 Computational Fluid Dynamics (CFD) Simulations Micro-computed scan of the PLLA scaffold

The image dataset obtained from the micro-CT scans was converted to .stl format in order to have a 3D element. Autodesk Meshmixer software was used to edit .stl files, converting

the parts into solids. The obtained mesh was edited to maintain a good level of accuracy while correcting the corners with smooth function or removing tiny elements of the solid that would increase the complex morphology of the sample. A reconstruction of the scaffold with a cylindrical shape of 0.4mm in diameter and 0.2mm in height was obtained, according to the refinement process during the mesh sensitivity study. Then, for the numerical simulation, the geometry of the scaffold was created by strictly overlapping eight 0.4mm-diameter and 0.2mm-height cylinders along the vertical direction. As a result, a D = 400 μm and H = 1.600 mm sample with a detailed pore-scale was analyzed to understand the pores contribution to larger-scale flow performance.

As the solid was imported to COMSOL Multiphysics and the mesh was generated, the properties of the materials were set by using water as perfusion media, having dynamic viscosity of $1 \times 10{-}3$ Pa·s, and density of 1000 kg/m^3. The flow velocity and shear stress profiles were calculated at the surface of the PLLA scaffold by using the single-phase laminar flow model based on the Navier–Stokes equation. In the single-phase laminar flow module, 0.02 m/s as inlet velocity and nonslip conditions were imposed at the top of the scaffold and on the wall of the construct, respectively.

Results of the computational study were obtained as a steady-state analysis of the flow field and shear stress at the surface of the 3D scaffold.

7.3.6 Support printing

The support components were manufactured via 3D printing with a Stratasys Object 30 PRO 3D printer. A preliminary test was carried out in order to assure the non-cytotoxicity of the printed pieces.

7.3.7 Cell seeding

For the cell seeding assay, cylindrical PLLA scaffolds were first transversally cut onto 5 mm disk and then misshapen into 5 mm-diameter and 5 mm-height cylinders using a biopsy punch (Fig. 7.3A). Then, scaffolds were sterilized in 70% ethanol under vacuum for 8 hours (so that the infiltration of ethanol was sufficient to penetrate the entire construct), washed in Phosphate Buffered Saline (PBS), and soaked in Dulbecco's modified Eagle's-high glucose medium (DMEM, Sigma Aldrich, Italy) to increase their hydrophilicity. Pre-osteoblastic MC3T3-E1 cells (Sigma-Aldrich, Italy) were grown in DMEM medium supplemented with

10% (v/v) fetal bovine serum (FBS) (Euroclone, Celbar, Italy), 100 units per ml penicillin G, 100 μg ml^{-1} streptomycin (Euroclone, Celbar, Italy), and 2 mM L-glutamine (Euroclone, Celbar, Italy) at 37°C and in a humidified atmosphere of 5% CO_2. Ten microliters of cell suspension containing $10x10^4$ cells were inoculated on each scaffold base ($20x10^4$ cells/scaffold) at 30-minute incubation time intervals (37°C and 5% CO_2) to facilitate initial cellular attachment. After the second incubation period, scaffolds were transferred into a medium-filled Petri dish (9 cm diameter x 1.4 cm height) for assessing cell proliferation and viability.

7.3.8 Perfusion culture

Scaffolds seeded with cells were transferred onto the multi-grids (4 grids) support in a number of 6 scaffolds per grid (Fig. 7.3B, C, D), reaching a totality of 24 scaffolds cultured under perfusion flow conditions with complete DMEM medium. Then the support was inserted into the bioreactor, and the system was placed into the CO_2 incubator. After 24 hours, the dynamic culture was established at an inlet air flow rate of 10ml/min.

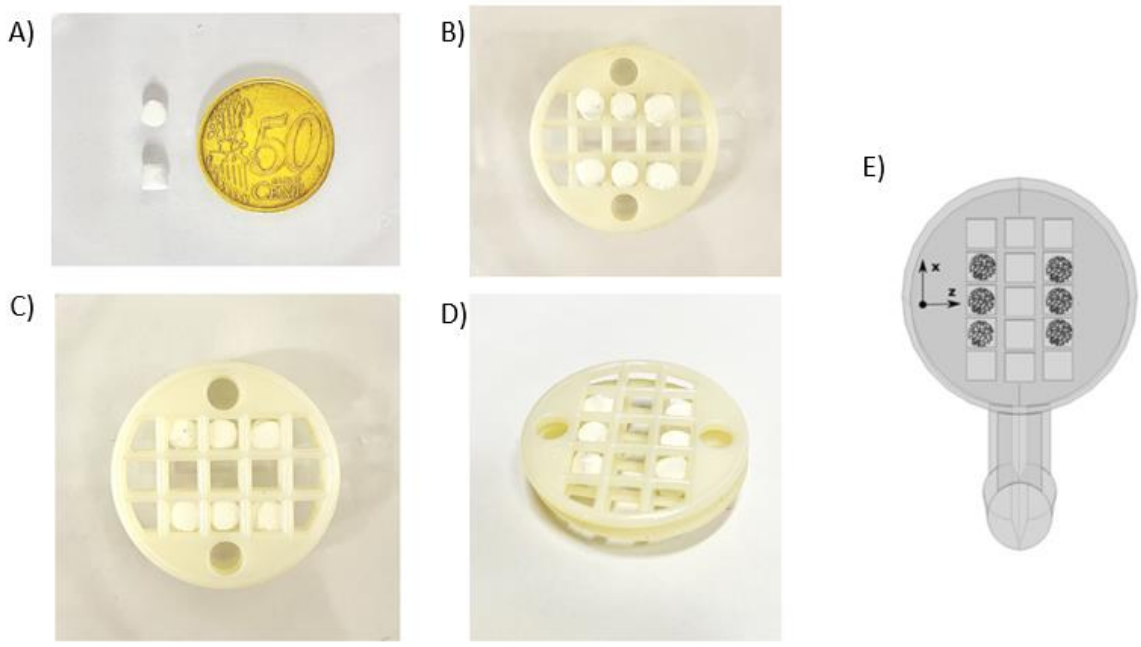

Figure 7.3 Schematic of the allocation of scaffolds on the grid: six scaffolds (5 mm diameter, 5 mm height) are located between a grid with legs and a simple grid. This operation is repeated for the four levels of the support.

Cells grew for up to 6 days without growth medium replacement. At the same time, 24 cells-seeded scaffolds were kept into the medium and used as static control. After the defined culture time, all the scaffolds were recovered and processed for further analysis.

7.3.9 AlamarBlue Assay

To evaluate cell proliferation, AlamarBlue Cell Viability Reagent was used. For each type of analysis, scaffolds were transferred into a 48-wells plate, covered with 500 µl/well of the AlamarBlue Reagent (10x) diluted (1:10) in the culture medium, and incubated for 3 hrs at 37°C, 5% CO_2. When it penetrates living cells, resazurin (non-fluorescent) is reduced to resorufin, a red in color and highly fluorescent compound. The DU-730 Life Science spectrophotometer (Beckman Coulter) was used to read fluorescence values at an excitation wavelength of 530/25 and an emission wavelength of 590/35. The analysis was carried out by using a scaffold without cells as blank.

7.3.10 Statistical analysis

Unpaired t-test and Welch's ANOVA test were performed using GraphPad Prism Software version 8 to evaluate differences between two or more groups, respectively. Statistical difference was considered at p-values < 0.05.

7.4 Results

7.4.1 Support design

The custom-made support (33 mm diameter, 114 mm height) was CAD-designed using Solidworks software (Fig. 7.4). Specifically, the support was ideated as an assembly of different components, i.e., a base (Fig. 7.4A), grids with legs (Fig. 7.4B) and simple grids (Fig. 7.4C), two threaded poles (Fig. 7.4D), and a top-weight (Fig. 7.4E), for properly culturing multiple scaffolds inside the perfusion bioreactor.

The base (Fig. 7.4A) consists of a block with two internally threaded holes to screw the two long externally-threaded poles (Fig. 7.4D) and allows the spatial stability of the assembly. It has a diameter of 35 mm, compatible with the bioreactor socket, and its location at the bottom of the support makes it the only one in contact with the bioreactor. The grids with legs (Fig. 7.4B) were designed to allocate scaffolds on a mesh divided into 15 square holes of 4.5 mm in length. The latter size is less than the supposed diameter of the scaffold (5 mm) so that its surface exposed to the flow is maximum.

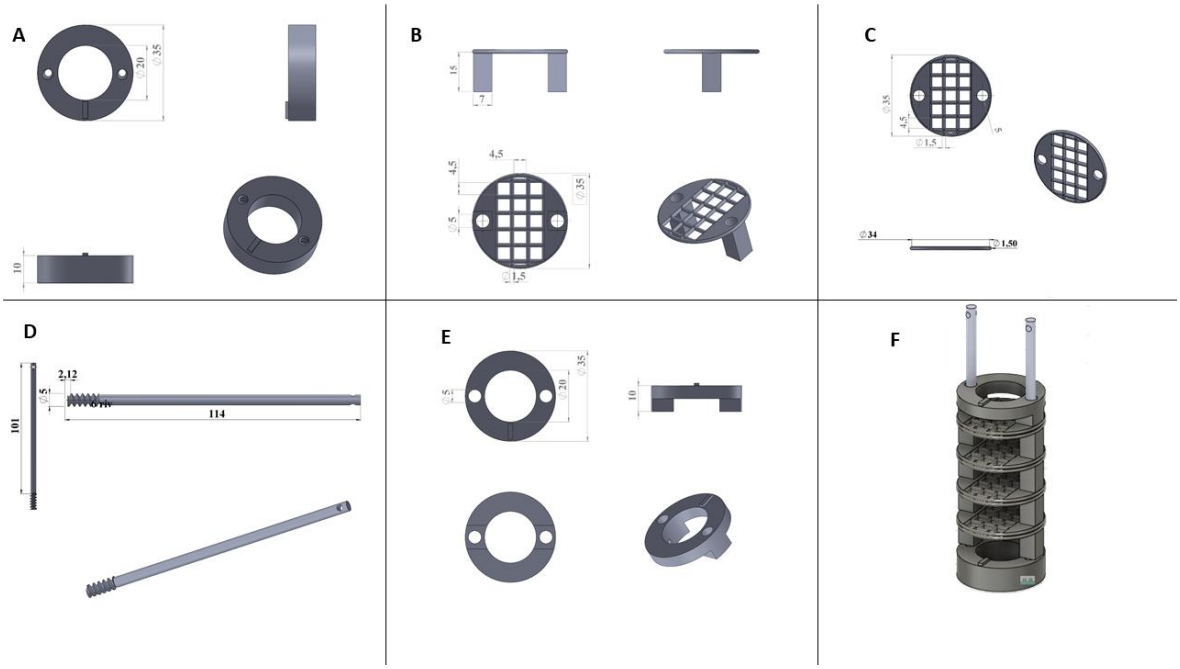

Figure 7.4 SolidWorks assembly (F) of the multi-grids support: A) a base; B) grids with legs; C) grids; D) two poles; and E) an upper weight were CAD-designed for the 3D printing.

The diameter of the grid is 33 mm, less than the diameter of the bioreactor (35 mm), thus facilitating the introduction of the assembled support into the bioreactor. The legs (h = 5mm) act as spacers between the different levels of the support, making the scaffolds well outdistanced and reducing the arrival of waste products from the cellular metabolism to the underlying scaffold. The simple grids (Fig. 7.4C) ensure confinement of the scaffolds exposed to the fluid flow and laying on grids with legs, thus holding and stabilizing the scaffolds allocation. Finally, a top-weight (Fig. 7.4E) was designed to avoid floating in the liquid medium. Indeed, when submerging the support, a volume shift of the culture medium can cause the movement of the scaffolds from their location. Hence, the weight was made as protection and surmounted the last grid.

The assembled support (Fig. 7.4F) can be extracted from the rest of the bioreactor while preserving a sterile environment to perform biological assessments for each level or/and at different periods. This system design was validated as concerns uniform flow through each level and low wall velocity (to avoid cell detachment) and applied for perfusion studies using cell-seeded PLLA scaffolds.

7.4.2 Computational Fluid Dynamics (CFD) Simulations of the Bioreactor with the multi-grids support

A CFD analysis was implemented to simulate fluid dynamic conditions inside the bioreactor with the multi-grids support. The bioreactor system and the multi-grids support (modeled as 4 couples of grids and an upper grid as a liquid distributor) were selected as the fluid (i.e., the region filled with culture medium) and the solid domains, respectively (Fig. 7.5). Grids were placed at 5 mm of distance, corresponding to a supposed thickness of scaffolds.

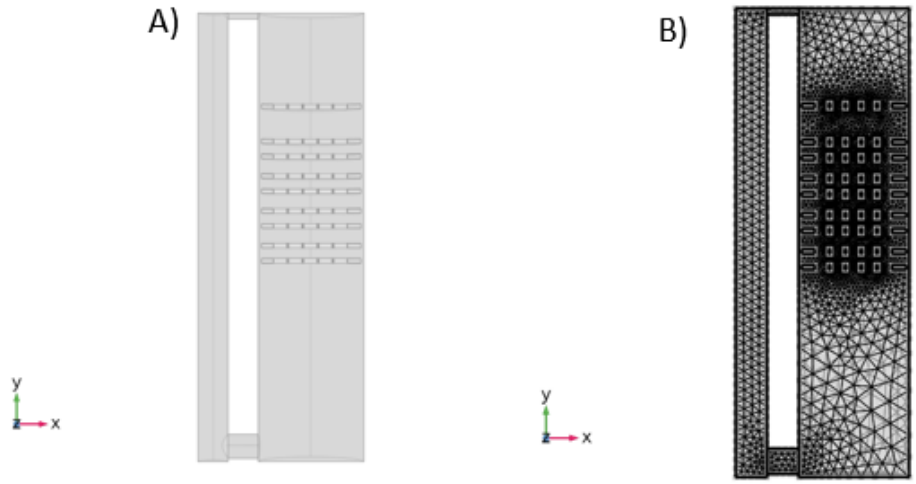

Figure 7.5 Representation of the bioreactor with the multi-grids apparatus along a vertical section: (A) bioreactor-grids system; (B) mesh of the bioreactor-grids system obtained in COMSOL.

Within the numerical simulation, an inlet gas flow rate of 10 ml/min (Re > 100, turbulent bubbly flow) was set, corresponding to an average velocity (0.0042 m/s) that avoids cells detachments and ensures an appropriate oxygen transfer in the dynamic environment (Koynov et al., 2007; Klöckner et al., 2013). Fig. 7.6 reports the magnitude of the velocity field at the steady-state condition (after 120 s) inside the bioreactor.

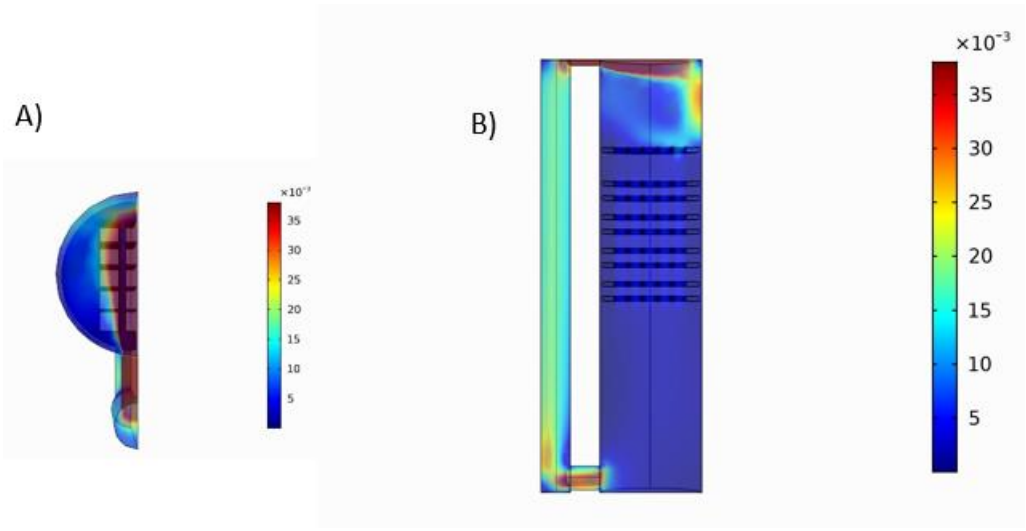

Figure 7.6 Volume graph of the liquid velocity profile obtained by COMSOL: (A) upper view of the bioreactor with the multi-grids support; (B) frontal view of the bioreactor-grids system.

Despite a turbulent flow above the upper grid, a liquid velocity was established that was uniformly distributed in the bioreactor environment. According to the system design, the scaffolds are located in the midst of two grids where a homogeneous velocity profile can be observed. Moreover, the distributions merely below the top grid of each pair of grids showed velocity peaks corresponding to the grid holes, with behavior mostly identical at each height and planar direction of the bioreactor. Overall, the variation in fluid velocity in the hole region between two grids resulted in the range 0.0043 - 0.0059 m/s, as shown in Figure 5, describing the velocity profiles in the intra-grid zone in each direction of interest considering each pair of grids. Specifically, the investigated directions were: the main diameter of the grid (Fig. 7.7A); the parallel of the grid direction through the holes (Fig. 7.7B); and the perpendicular direction of the main diameter and passing through the lines of the holes where the scaffolds should be located (Fig. 7.7C). According to Figure 7.7A, the maximum velocity of the liquid along the main diameter was found at the holes of the grid where the scaffolds are placed. This velocity was between 0.0047 and 0.006 m/s, considering the profile through the diameter length and the considered heights. In particular, it was observed that, along all the holes, the velocities of the second and fourth levels were practically coincident. Instead, those in the first and third ones emerged lightly smaller, except in the hole farther from the riser. The same trend was observed for the direction parallel to the main diameter (Fig. 7.7B) and passing through the remaining holes. In this direction, overall, the range of peak velocities was slightly lower (0.0044-0.0054 m/s). Finally, when considering the perpendicular direction of the main diameter in the inter-grid space, a range of 0.0046-0.0057 m/s was recorded (Fig. 7.7C).

In Figure 7.7B, the region bounded by the rectangle represents the one actually (and symmetrically with respect to the main diameter) occupied by the scaffolds placed on each grid. Therefore, the effective velocity range across the scaffolds is 0.046-0.054m/s. Based on these values, the scaffold micro-CT simulation was performed (consistent with computational costs) using a speed of three times to consider the condition limit in terms of shear stress on cells.

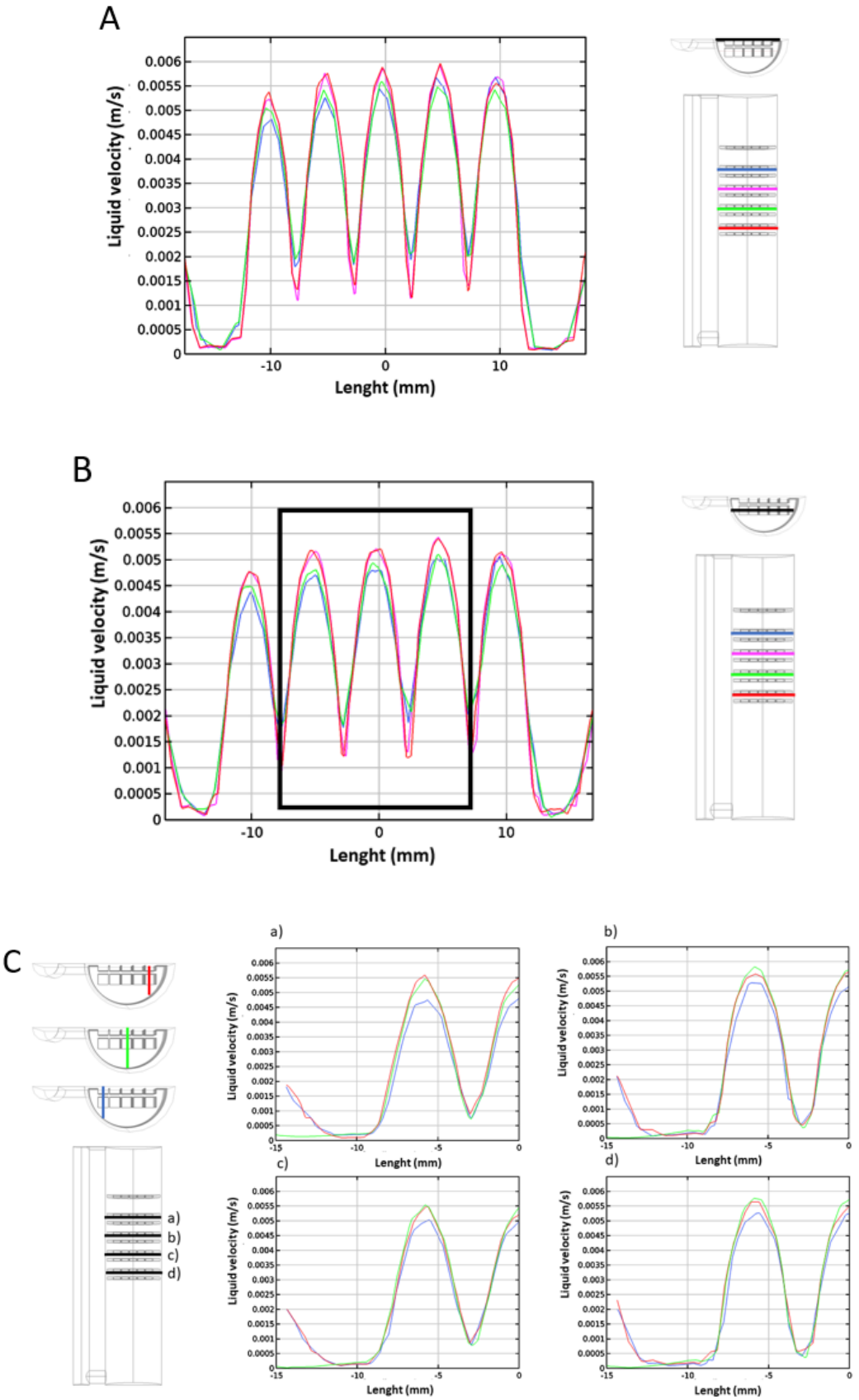

Figure 7.7 Plot of the liquid velocity versus the length of the segments along the directions of interest at the various grid level: (A) main diameter; (B) direction parallel to the main diameter; (C) direction perpendicular to the main diameter. The squared region in (B) comprises the holes where scaffolds are located.

A biological analysis with a rigorous statistical study was performed to test whether this interval had a different effect on system scaffolds.

7.4.3 Computational Fluid Dynamics (CFD) Simulations of the Micro-computed PLLA scaffold

The micro-CT scans (Fig. 7.8A) were overlapped (Fig. 7.8B) to build the 3D reconstruction for the CFD study, and then a sub-volume (Fig. 7.8C) was obtained after a mesh sensitivity analysis on the COMSOL software.

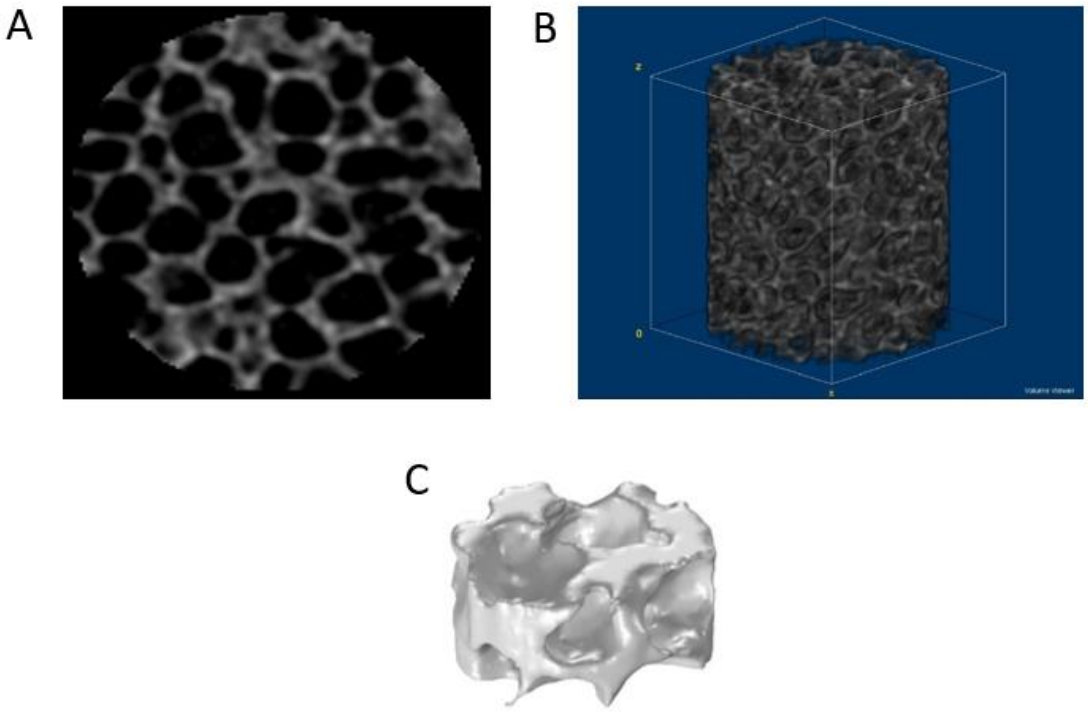

Figure 7.8 Images of the reconstruction of the 3D PLLA scaffold: (A) scan of the cross-section of the scaffold; (B) 3D reconstruction from the image stack of the micro-CT scans; (C) sub-volume of the scaffold used as initial geometry for the numerical simulation.

For computational reasons, we built a large-scale scaffold (0.4mm-diameter and 1.6mm-height) by closely overlapping 8 sub-volumes (0.4mm-diameter and 0.2mm-height). It was used for the implemented simulation. This assumption could be employed thanks to the uniform morphology distribution of the porous structure obtained via the TIPS technique. Then, a reconstructed mesh was generated by using the dedicated meshing software Meshmixer. A final volume mesh with 1502281 elements was generated (Fig. 7.9).

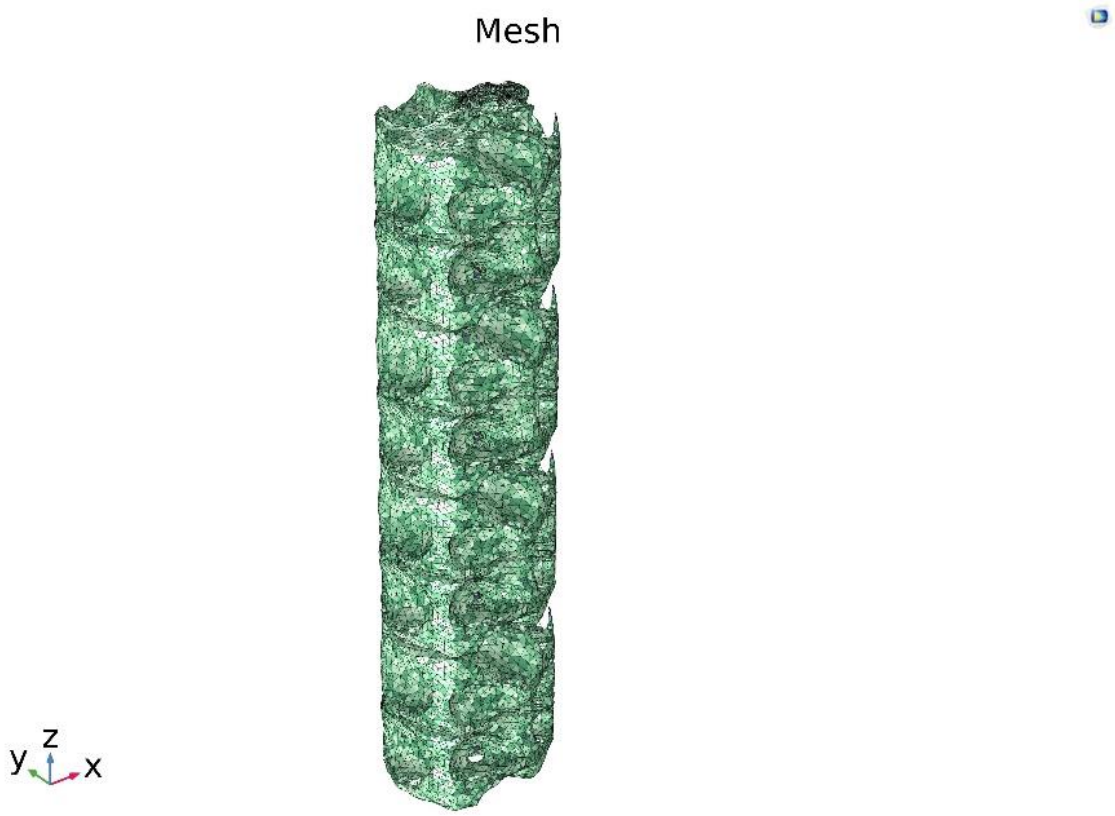

Figure 7.9 Mesh of the scaffold used for the numerical simulation: eight sub-volumes of the micro-CT reconstruction were accurately overlapped to generate a large-scale geometry.

The velocity profile through the scaffold was studied with CFD using the appropriate flow module inside the COMSOL software, without geometry simplifications as for pore channel models.

Fig. 7.10 shows the 3D fluid flow profile across the surface of the micro-CT scaffold from a stationary study. According to the bioreactor perfusion, the flow direction was assumed from the top to the bottom of the construct. The flow velocity was visualized as a color-coded field through the scaffold volume.

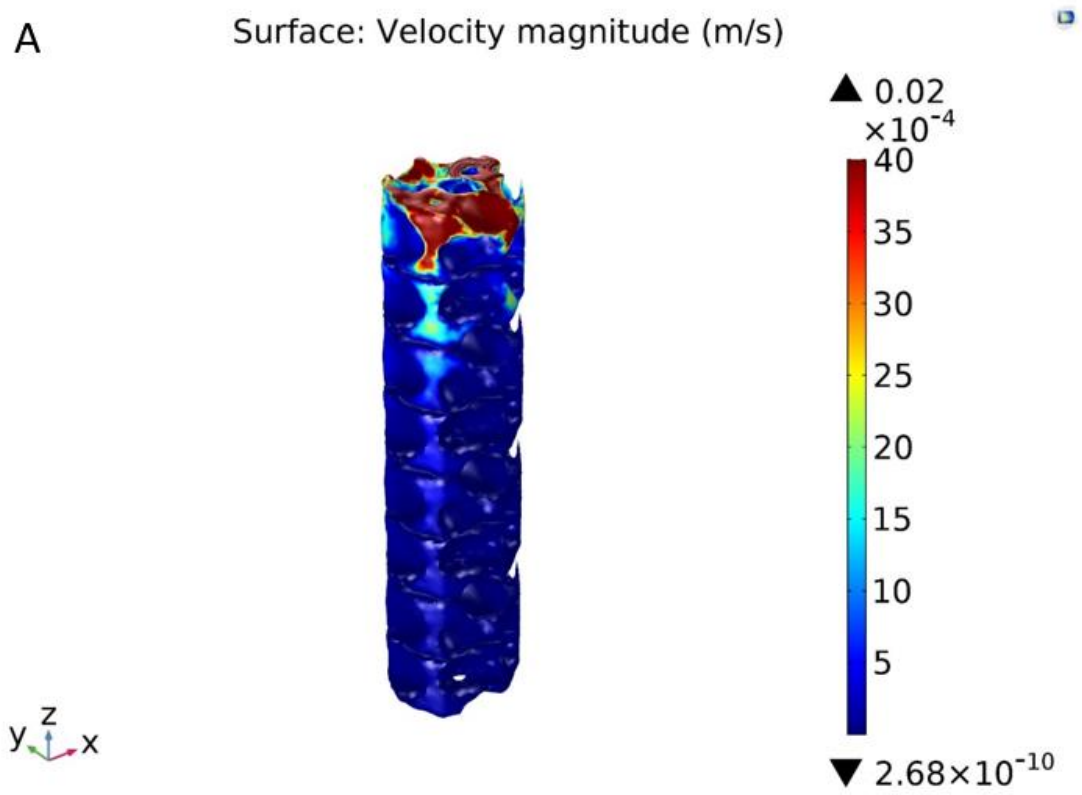
A
Surface: Velocity magnitude (m/s)
▲ 0.02
×10-4
40
35
30
25
20
15
10
5
▼ 2.68×10-10
z
y
x

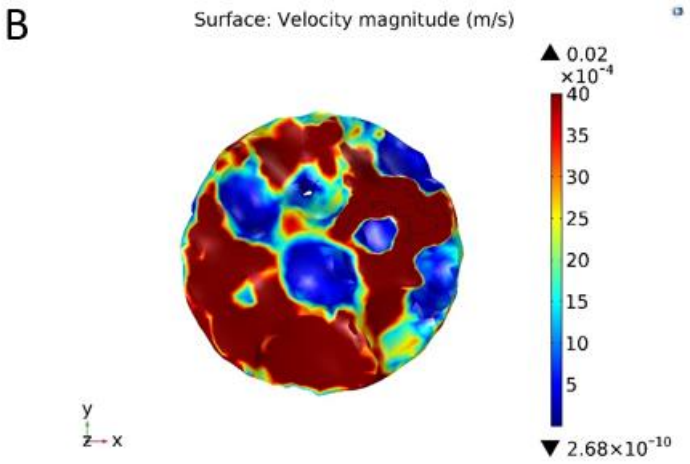
B
Surface: Velocity magnitude (m/s)
▲ 0.02
×10-4
40
35
30
25
20
15
10
5
▼ 2.68×10-10
y
z
x

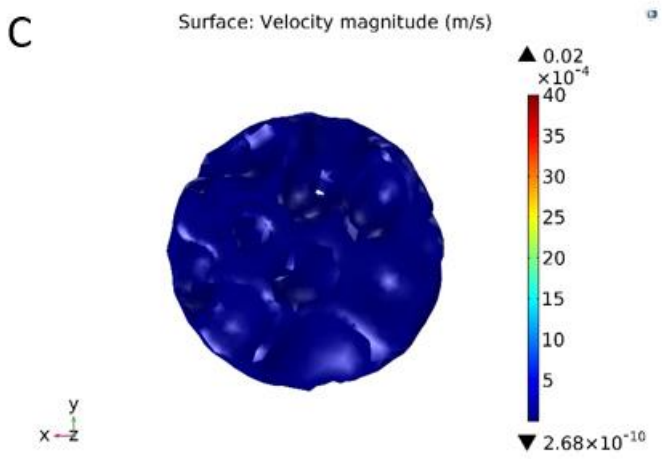

Figure 7.80 Volume plot of the liquid velocity at the scaffold surface: (A) frontal view, (B) upper horizontal view, (C) lower horizontal view. Higher velocities are faced in the upper region where the scaffold is initially fluxed.

According to the plot, velocity values were found to have a maximum of 0.004 m/s. Liquid velocity appeared to become slower into pore spaces due to the flow resistance inside the connected pores. The flow field at the surface of all the single pores resulted homogeneous ($\approx 10^{-6}$ m/s), with different velocities at the two bases of the scaffold (Fig. 7.10B, C), especially at the inlet base that is the zone invested by the flow.

Fig. 7.11 shows the shear stress distribution at the surface of the scaffold.

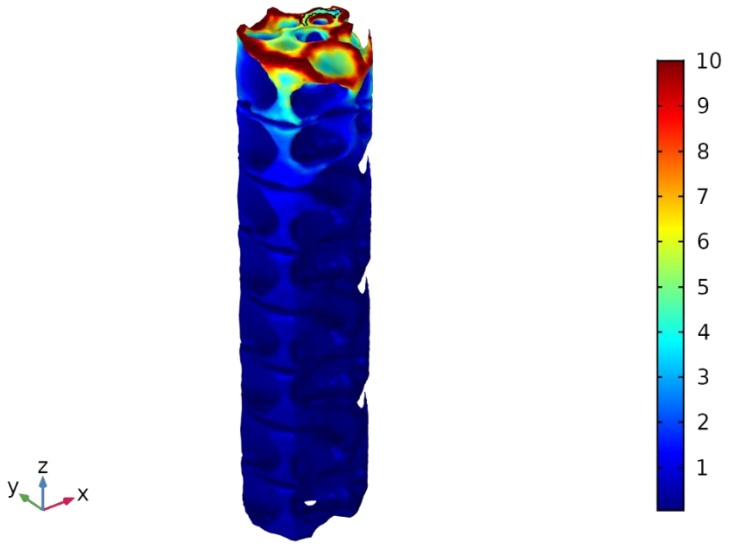

Figure 7.11 Volume plot of the shear stress at the scaffold surface: except for the entrance region, the shear stress distribution is uniform at the wall of the pores and has a mean value of 0.007Pa.

Except for the upper region of the external surface (the flow direction is from top to bottom), at the surface of the inner pores, the shear stress varied from 0.002 to 0.8 Pa with a mean value of 0.007 Pa.

7.4.4 Biological validation of the multi-grids support

The computational outcomes of uniform flow, both between the grids and within the scaffold, were verified by estimating the cell proliferation on scaffolds dynamically cultured within the bioreactor.

Pre-osteoblastic MC3T3-E1 cells were preliminarily seeded on PLLA scaffolds, and 6 scaffolds were placed on each grid. Four grids were vertically stacked into the support in order to obtain a system of 24 scaffolds widely distributed in the bioreactor that could be simultaneously analyzed (Fig. 7.12i). At the same time, 24 seeded scaffolds were maintained in static condition inside Petri dishes.

Compared to the standard 2D culture, the seeding efficiency in a 3D structure is strongly influenced by several factors (i.e., scaffold morphology, suspension drop size, and scaffold wettability) and, consequently, a very different number of cells could be present in each scaffold at the beginning of an experiment (Vissers et al., 2015). For this reason, once the average values of viability and their standard deviations were obtained, we focused on verifying if the value variability was caused by seeding variability or bioreactor factors. To this end, the percentage ratio was calculated between the standard deviation and the mean value of fluorescence of the total amount of scaffolds. Statistically, static scaffolds exhibited a percentage deviation of 19.8%, exclusively due to the seeding variability. The percentage deviation of the scaffolds cultured dynamically was 20.7%. The similarity of the two values led us to state that the difference in terms of the viability of the cells grown into the bioreactor is not attributable to an inhomogeneous flow.

Alamar blue assay was carried out on each scaffold to strictly evaluate the system efficiency in terms of flow homogeneity and estimate its cell viability and, thus, perform statistical analysis. Several groups were compared to validate the fluid dynamics of the bioreactor-support system. Figure 7.12 shows the geometry of the system and the nomenclature adopted to express the analyzed statistics.

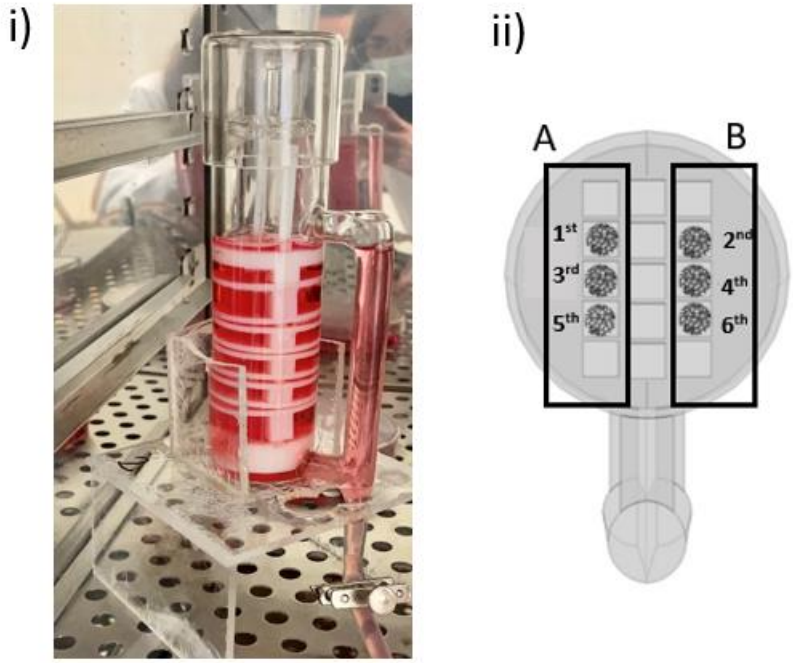

Figure 7.12 (i)Picture of the bioreactor-support-scaffolds system: 24 seeded scaffolds are dynamically cultured inside the perfusion bioreactor. (ii) Six scaffolds are located on each level of grids couple: for the statistical analysis, A and B consist of two groups.

The viability of cells grown on the scaffolds (N=6) of the four different levels of the multi-grids support was evaluated using Welch's ANOVA test. As shown in Fig. 7.13, no significant differences (p=0.16) resulted in the inter-grids viability among cells seeded in the scaffolds from all levels after 6 days.

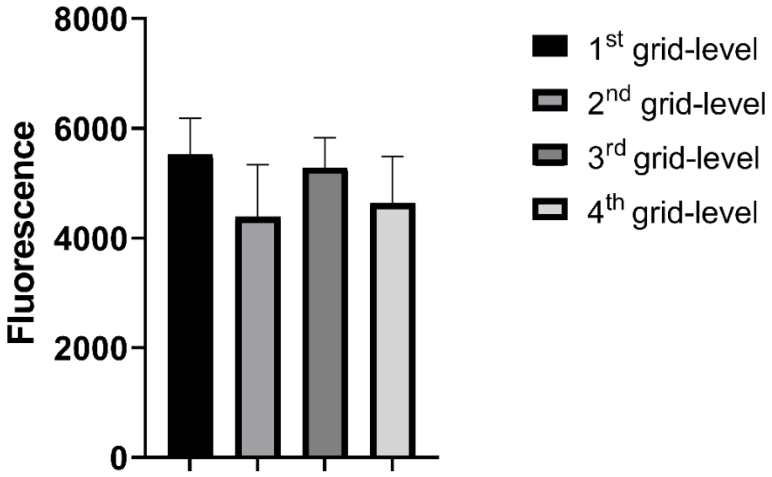

Figure 7.139 Results of Welch's ANOVA test for the inter-grids analysis of cell proliferation (Alamar Blue) after 6 days of dynamic culture: mean values of fluorescence of each grid-level were compared. Significant differences were considered for $p<0.05$.

No significant difference (p = 0.65) was found in cell viability between the six scaffolds placed in the same grid along the four levels (N = 4). This result suggests that the location in the xz planes does not affect cellular viability, probably because the average flow is the same regardless of their position (Fig. 7.14).

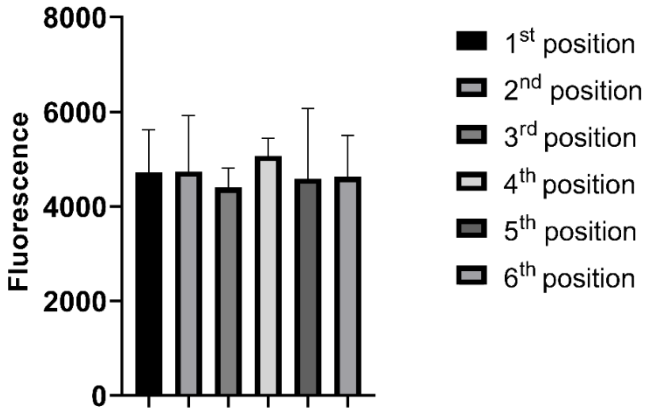

Figure 7.1410 Results of Welch's ANOVA test for the intra-grid analysis of cell proliferation (Alamar Blue) after 6 days of dynamic culture: mean values of fluorescence of each position along the four grid levels were compared. Significant differences were considered for $p<0.05$.

For a more rigorous analysis, other groups were compared statistically about Alamar blue results (Table 7.1). Specifically, t-tests were performed for each couple of grid levels of the bioreactor and between the two sides of the grids (i.e., A and B, according to Figure 7.12). The latter were analyzed as symmetrical in the CFD analysis. In addition, the Welch ANOVA test was applied to verify that was no difference among the four levels of the bioreactor while considering the scaffolds on each side (A or B).

Table 7.1. Results of the statistical analysis for the considered groups. Significant differences were considered for $p<0.05$.

Groups	**Test**	**P value**
4 Grid levels; N=6 per 4 levels	Welch ANOVA	0.1623
1st level – 2nd level	t-test	0.0583
1st level – 3rd level	t-test	0.5114
1st level – 4th level	t-test	0.0954
2nd level – 3rd level	t-test	0.1083

2nd level – 4th level	t-test	0.6708
3rd level – 4th level	t-test	0.1853
6 positions along the levels; N=4 per 6 positions	Welch ANOVA	0.6484
1st level **A** – 1st level **B**	t-test	0.5793
2nd level **A** – 2nd level **B**	t-test	0.0996
3rd level **A** – 3rd level **B**	t-test	0.9759
4th level **A** – 4th level **B**	t-test	0.2412
A group along the levels; N=3 per 4 levels	Welch ANOVA	0.0626
B group along the levels; N=3 per 4 levels	Welch ANOVA	0.3175

Overall, all the results indicated a $p>0.05$ value, showing that a dynamic culture within our system offers a uniform distribution of cell growth and, therefore, fluid-dynamic conditions.

7.5 Discussion

This Chapter is a CFD study that attempts to validate a scaffold-bioreactor system for tissue engineering applications. The bioreactor is a custom-made apparatus that can induce perfusion flow to multiple scaffolds thanks to a multi-grids support. The latter can be adapted to small and large geometrical scaffolds, including complex structural configurations.

Using numerical-based analysis, we previously modeled the designed bioreactor without support (Capuana et al., 2021b). After an optimization analysis, a uniform velocity field distribution was achieved when boundary conditions were adjusted to mimic cell experiments. Here, considering the geometry of the multi-grids support, computed data were predicted for the liquid domain as a dynamic environment under flow-induced forces. Interestingly, each region between two grids showed the same behavior on the distribution of the liquid flow rates. As predictable, the holes of the grids seemed to condition the flow and induced velocity peaks, reaching a maximum value of 0.006 m/s, consistent with previous computational studies involving scaffolds cultured inside a perfusion bioreactor (Maes et al., 2009; Vetsch et al., 2017; Sibilio et al., 2019). In addition, this maximum velocity provides a Reynolds Number within the laminar flow regime, thus allowing the flow

to be imposed as a single-phase in the CFD simulation on the porous scaffold. Computational analysis can predict relevant fluid-dynamic conditions affecting cellular activity, even without experimentally validated data. The uniformity of fluid flow acting on cells seeded onto scaffolds is a significant challenge for cell viability and proliferation on multiple scaffolds (Dvir et al., 2006). By controlling the inlet gas flow rate in the perfusion model, it is possible to generate ranges of liquid velocity that promote a definite type of metabolic activity. The effect of fluid velocity through and around tissue-engineered scaffolds also guides nutrient transport (Lee et al., 2006; Eberli, 2011; Salehi-Nik et al., 2013; Paopo, 2014). In Chabanon's study (Chabanon, 2015), the convection of the perfusion system was addressed as the transfer mechanism reducing the diffusion limitations on oxygen exchange, affecting cell distribution and proliferation profile. When using the multi-grids apparatus, its geometry could provide effects of variance in flow stimuli on each located scaffold. Therefore, the exposure of cells to a uniform mean flow was evaluated by performing a dynamic 3D culture viability test, considering the variance due to the sowing efficiency in the static controls. We evaluated this uniform distribution for the entire pool of scaffolds (n = 24) at six days or between scaffolds situated in different grids (n=6). It is noteworthy that no apparent variation was found for the 24 scaffolds perfused on different grids while considering seeding variance and among the different levels of the support. Multiple factors, such as fluid distribution, bioreactor geometry, and operating conditions commonly affect the experimental outcome, not allowing the comparison of various culture conditions (Burova et al., 2019). However, our results reflect the homogeneity of interstitial flow experienced by constructs cultured under convective conditions. This outcome demonstrates that the proposed bioreactor provides a controlled environment that poorly affects the *in vitro* performance of cell growth.

The fluid flow is a crucial stimulus whose effect, however, varies with the geometry and morphologies of the scaffolds (Yamada et al., 2021). Computational analysis is commonly utilized to estimate these effects while avoiding expensive devices that allow accurate measurements during experimental investigations (Azuaje, 2011; Burova et al., 2019). In this study, we investigated the morphology of the 3D PLLA scaffold by micro-CT analysis and, hence, exploited the obtained scans for the reconstruction of the porous geometry within the numerical simulation. Due to computational reasons, we numerically analyzed a sub-volume of the original 3D reconstruction. In this way, the obtained mesh could be studied with reasonable computational costs. Hence, we could evaluate the exact fluid characteristics

inside the interconnected pores of the scaffold without the use of pore models. Currently used pore models generally include the porosity and permeability of the scaffold and have the limitation of approximation and simplifications (Lawrence et al., 2009; Vetsch et al., 2017; Zhao et al., 2018c). Particularly, the choice of the reconstruction for the pore-equivalent structure significantly affects the outcomes about local parameters (Sandino and Lacroix, 2011; Vetsch et al., 2015). Instead, here, a computational study is proposed that carefully mapped the flow field and the distribution of shear stress on the surface of the porous scaffold, Hence, providing a tool to verify that perfusion cannot cause damage to the viability of cells. Interestingly, the architecture of the pores seemed to strongly influence the flow distribution in downstream regions, experiencing a low fluid velocity. This result is consistent with previous computational works studying porous flow in a laminar regime (Tuan and Hutmacher, 2005; Zermatten et al., 2014). More importantly, the results demonstrated the suitability of the micro-CT scans in allowing an accurate fluid dynamic characterization by coupling and performing CFD analysis on a dynamic environment. This work presents a complete study that considers both the bioreactor geometry and an exact macro-scale pore structure, thus, overcoming uncertainties derived from low resolution and inaccurate geometrical features. In addition, when the scaffold is produced using the TIPS technique, the ability to control pore size and porosity allows for selecting the range of fluid velocities generated, thus promoting specific tissue formation (Boschetti et al., 2006; Lesman et al., 2010). Our CFD study evaluated these local distributions inside a micro-computed porous construct whose geometrical parameters closely obey the requirements of an ideal TE scaffold (i.e., high porosity, micrometric pore size, and large-scale dimension (Eltom et al., 2019)). Other studies similarly provided a pore-scale simulation of fluid flow for either rocks geometries (Blunt et al., 2013; Raeini et al., 2014; Golparvar et al., 2018; Abu-Al-Saud et al., 2020; Choi et al., 2020) or scaffolds architectures (Zermatten et al., 2014) but analyzing large-scale but low porosities (< 56%) structures or low-scale constructs (up to 0.1 mm) with high porosity (≈ 70%) (Cioffi et al., 2006). On the other hand, our numerical study was implemented on a porous scaffold with a 93% porosity, large-scale dimension (0.4 mm diameter and 1.6 mm height), and interconnected pores. The large-scale dimension is generally referred to as the mean pore size. The previous study has demonstrated that when studying a flow distribution on a sub-volume, called representative elementary volume (REV), its length parallel to the flow direction should be at least 3.5 times the mean diameter of pores with the aim of not influencing the results (Zermatten et

al., 2011). Since our scaffold had an average diameter of 0.2 mm, the construct followed this condition.

According to our results, velocities at the surface of the pores had a maximum value of 0.004 m/s, which is safe for cell viability (Sibilio et al., 2019). The simulation demonstrated that the liquid velocity had a relatively uniform distribution within the scaffold pores. Moreover, the liquid velocity within the pores was the same as at their surface, thus demonstrating that no velocity gradients are generated at the porous region. Generally, this result defines a homogeneous level of fluid stimuli throughout the surface of the pores, which is the region of interest for the seeded cells. Even the shear stress distribution resulted homogeneous in the inner region of the scaffold, as also resulted by the work from Zermatten et *al*. (Zermatten et al., 2014). The average shear stress was found to be 0.007 Pa, a value comparable to that found in similar studies (McCoy and O'Brien, 2010; Zermatten et al., 2011) at equivalent inlet liquid velocities. Remarkably, the maximum shear stress exerted on the simulated scaffold was 10 Pa, i.e., the limit level of shear stress generally considered to damage cultured mammalian cells (1–10 Pa) (Grossemy et al., 2020).

Shear stress at the surface of the scaffold affects the cell viability and proliferation of the cells attached to scaffolds (Zhao et al., 2016). Hence, we performed a biological test up to six days to experimentally verify the uniform distribution of flow stimuli inside the bioreactor system, thus validating the bioreactor-support apparatus. The comparison in cell viability of pre-osteoblastic MC3T3-E1 cells grown on PLLA scaffolds maintained in static or dynamical conditions was performed to individuate the experimental condition variability range. Specifically, the cell proliferation percentage deviation was uniform among the scaffolds in both static and dynamic conditions (around 20%), confirming that the variance registered was not dependent on bioreactor factors but was caused by experimental seeding variability. Cells dynamically cultured on the 24 scaffolds showed comparable viability independently of their position inside the bioreactor. Therefore, cells grown on scaffolds of the same grid and those of other grids of the four different levels registered the same proliferation grade after six days, suggesting that all the scaffolds received medium and nutrients in the same manner inside the bioreactor, thanks to the constant and homogenous flux. In this manner, it is possible to follow and compare 24 different samples at once in just one experiment in a dynamic system, reducing the variability that could be registered between several independent experiments.

One limitation of the current work is that it did not consider the mass transport through the bioreactor volume in the presence of the support. Our bioreactor-support CFD study solved the system before placing the scaffold onto the holes of the grids. After scaffolds accommodation, the cells consume oxygen and, over time, they would alter the oxygen concentration profile during the perfusion culture. This continuous convective-diffusive oxygen transport may result in different oxygen supplies, inducing cell proliferation while satisfying their nutrient needs (Chu et al., 2009; Devarapalli et al., 2009; Azuaje, 2011; Truscello et al., 2012). Although these concerns, previous CFD simulations without the multi-grids support confirmed that the dynamic fluid flow conditions during cell culture assure the oxygen supply necessary for cell viability. More advanced 3D simulation computing is required to analyze this situation within the entire bioreactor-support apparatus.

7.6 Conclusions

The fluid flow distribution was studied in 3D scaffolds placed inside a designed custom-made bioreactor apparatus that supports the dynamic culture of multiple seeded constructs while inducing perfusion stimuli. The flow velocity field was numerically analyzed into the perfused system and the scaffold pores. The complex computed reconstruction of the 3D scaffold was appropriately manipulated to obtain a sub-volume that could accomplish the geometry/mesh requirements for CFD simulation. This method allowed evaluating the fluid dynamic effect of the porous structure of a scaffold without simplifying the pores morphology, thus obtaining reliable and predictable outcomes. The computational method was coupled with experimental analysis to demonstrate that the system can exert a uniformly distributed flow to all the cultured scaffolds, resulting in a homogeneous flow stimulus that evenly enhances cell proliferation. The results revealed that the performance of the proposed system and the effective methodology applied for scaffold analysis at the pore-scale could find future applications to study the fluid-scaffold-cells interactions. Therefore, this experimental configuration can be further developed to investigate the fundamental characteristics of long-time cell culture under perfusion conditions.

Nomenclature		
Subscript "g" = gas	*P_k = production of turbulence kinetic energy, Eq. 7.4-4.6*	*ε = turbulent energy dissipation rate per unit mass [m^2/s^3], Eq. 7.4,7.6, 7.7*
Subscript "l" = liquid	*p = mean static pressure [Pa], Eq. 7.8*	*μ = dynamic viscosity [Pa s]*
$C_{\varepsilon 1}$, $C_{\varepsilon 2}$, C_{ε} = coefficients in the dissipation equation (Eq.7.7)	*Re = Reynolds number (dimensionless)*	*μ_T = turbulent viscosity [Pa s], Eq. 7.4-7.7*
C_{μ} = standard constant of the k-ε theory (dimensionless), Eq. 7.6	*S_k = turbulent kinetic energy added term [kg/(m s^3)], Eq. 7.4,7.7, 7.8*	*ρ = density [kg/m^3]*
C_k = = standard constant of the k-ε theory (dimensionless), Eq. 7.8	*t = time [s]*	*σ_{ε} = coefficient in the dissipation-rate equation, Eq. 7.7*
ID= internal diameter of the downcomer [m]	*u = velocity vector [m/s]*	*σ_k = coefficient in the turbulent kinetic energy equation, Eq. 7.4*
k = turbulent kinetic energy per unit mass [m^2/s^2], Eq. 7.4,7.6, 7.7	*u_{slip} = slip velocity [m/s]*	*φ = fractional phase holdup (dimensionless)*

References

Abu-Al-Saud, M., Gmira, A., Al-Enezi, S., and Yousef, A. (2020). Pore-scale simulation of fluid flow in carbonates using micro-CT scan images. *Int. Pet. Technol. Conf. 2020, IPTC 2020*. doi:10.2523/iptc-19832-ms.

Ali, D., and Sen, S. (2017). Finite element analysis of mechanical behavior, permeability and fluid induced wall shear stress of high porosity scaffolds with gyroid and lattice-based architectures. *J. Mech. Behav. Biomed. Mater.* 75, 262–270. doi:10.1016/j.jmbbm.2017.07.035.

Amores Vera, E., and Rodríguez Ruiz, J. (2012). Comparison between Turbulent and Laminar Bubbly-Flow for Modeling H 2 /H 2 O Separation. *Proceeding COMSOL Conf.*

Azuaje, F. (2011). Computational discrete models of tissue growth and regeneration. *Brief. Bioinform.* 12, 64–77. doi:10.1093/bib/bbq017.

Basu, B. (2017). "Three Dimensional Porous Scaffolds: Mechanical and Biocompatibility Properties," in (Springer, Singapore), 353–384. doi:10.1007/978-981-10-3059-8_10.

Blunt, M. J., Bijeljic, B., Dong, H., Gharbi, O., Iglauer, S., Mostaghimi, P., et al. (2013). Pore-scale imaging and modelling. *Adv. Water Resour.* 51, 197–216. doi:10.1016/j.advwatres.2012.03.003.

Boschetti, F., Raimondi, M. T., Migliavacca, F., and Dubini, G. (2006). Prediction of the micro-fluid dynamic environment imposed to three-dimensional engineered cell systems in bioreactors. *J. Biomech.* 39, 418–425. doi:10.1016/j.jbiomech.2004.12.022.

Burova, I., Wall, I., and Shipley, R. J. (2019). Mathematical and computational models for bone tissue engineering in bioreactor systems. *J. Tissue Eng.* 10. doi:10.1177/2041731419827922.

Capuana, E., Lopresti, F., Pavia, F. C., Brucato, V., and Carrubba, V. La (2021a). Solution-Based Processing for Scaffold Fabrication in Tissue Engineering Applications: A Brief Review. *Polym. 2021, Vol. 13, Page 2041* 13, 2041. doi:10.3390/POLYM13132041.

Capuana, E., Pavia, F. C., Lombardo, M. E., Rigogliuso, S., Ghersi, G., La Carrubba, V., et al. (2021b). Mathematical and numerical modeling of an airlift perfusion bioreactor for tissue engineering applications. *Biochem. Eng. J.*, 108298. doi:10.1016/J.BEJ.2021.108298.

Chabanon, M. (2015). Multiscale study of a perfusion bioreactor for bone tissue engineering.

Choi, C.-S., Lee, Y.-K., and Song, J.-J. (2020). Equivalent Pore Channel Model for Fluid Flow in Rock Based on Microscale X-ray CT Imaging. *Materials (Basel).* 13, 2619. doi:10.3390/ma13112619.

Chu, X. H., Shi, X. L., Feng, Z. Q., Gu, J. Y., Xu, H. Y., Zhang, Y., et al. (2009). In vitro evaluation of a multi-layer radial-flow bioreactor based on galactosylated chitosan nanofiber scaffolds. *Biomaterials* 30, 4533–4538. doi:10.1016/j.biomaterials.2009.05.020.

Cioffi, M., Boschetti, F., Raimondi, M. T., and Dubini, G. (2006). Modeling evaluation of the fluid-dynamic microenvironment in tissue-engineered constructs: A micro-CT based model. *Biotechnol. Bioeng.* 93, 500–510. doi:10.1002/bit.20740.

Conoscenti, G., Schneider, T., Stoelzel, K., Carfì Pavia, F., Brucato, V., Goegele, C., et al. (2017). PLLA scaffolds produced by thermally induced phase separation (TIPS) allow human chondrocyte growth and extracellular matrix formation dependent on pore size. *Mater. Sci. Eng. C* 80, 449–459. doi:10.1016/j.msec.2017.06.011.

Devarapalli, M., Lawrence, B. J., and Madihally, S. V. (2009). Modeling nutrient consumptions in

large flow-through bioreactors for tissue engineering. *Biotechnol. Bioeng.* 103, 1003–1015. doi:10.1002/bit.22333.

Dvir, T., Benishti, N., Shachar, M., and Cohen, S. (2006). A novel perfusion bioreactor providing a homogenous milieu for tissue regeneration. *Tissue Eng.* 12, 2843–2852. doi:10.1089/ten.2006.12.2843.

Eberli, D. (2011). *Tissue Engineering for tissue and organ regeneration*. Rijeka, Croatia: InTech.

Eltom, A., Zhong, G., and Muhammad, A. (2019). Scaffold Techniques and Designs in Tissue Engineering Functions and Purposes: A Review. *Adv. Mater. Sci. Eng.* 2019. doi:10.1155/2019/3429527.

Erdemir, A., Bennetts, C., Davis, S., Reddy, A., and Sibole, S. (2015). Multiscale cartilage biomechanics: technical challenges in realizing a high-throughput modelling and simulation workflow. *Interface Focus* 5, 20140081. doi:10.1098/rsfs.2014.0081.

Gaspar, D. A., Gomide, V., and Monteiro, F. J. (2012). The role of perfusion bioreactors in bone tissue engineering. *Biomatter* 2, 167–175. doi:10.4161/biom.22170.

Geven, M. A., Lapomarda, A., Guillaume, O., Sprecher, C. M., Eglin, D., Vozzi, G., et al. (2021). Osteogenic differentiation of hBMSCs on porous photo-crosslinked poly(trimethylene carbonate) and nano-hydroxyapatite composites. *Eur. Polym. J.*, 110335. doi:10.1016/j.eurpolymj.2021.110335.

Golparvar, A., Zhou, Y., Wu, K., Ma, J., and Yu, Z. (2018). A comprehensive review of pore scale modeling methodologies for multiphase flow in porous media. *Adv. Geo-Energy Res.* 2, 418–440. doi:10.26804/ager.2018.04.07.

Grossemy, S., Chan, P. P. Y., and Doran, P. M. (2020). Stimulation of cell growth and neurogenesis using protein-functionalized microfibrous scaffolds and fluid flow in bioreactors. *Biochem. Eng. J.* 159, 107602. doi:10.1016/j.bej.2020.107602.

Karande, T. S., Ong, J. L., and Agrawal, C. M. (2004). Diffusion in musculoskeletal tissue engineering scaffolds: Design issues related to porosity, permeability, architecture, and nutrient mixing. *Ann. Biomed. Eng.* 32, 1728–1743. doi:10.1007/s10439-004-7825-2.

Klöckner, W., Gacem, R., Anderlei, T., Raven, N., Schillberg, S., Lattermann, C., et al. (2013). Correlation between mass transfer coefficient kLa and relevant operating parameters in cylindrical disposable shaken bioreactors on a bench-to-pilot scale. *J. Biol. Eng.* 7, 28. doi:10.1186/1754-1611-7-28.

Koynov, A., Tryggvason, G., and Khinast, J. G. (2007). Characterization of the localized hydrodynamic shear forces and dissolved oxygen distribution in sparged bioreactors. *Biotechnol. Bioeng.* 97, 317–331. doi:10.1002/BIT.21281.

Lawrence, B. J., Devarapalli, M., and Madihally, S. V. (2009). Flow dynamics in bioreactors containing tissue engineering scaffolds. *Biotechnol. Bioeng.* 102, 935–947. doi:10.1002/bit.22106.

Lee, C., Grad, S., Wimmer, M., and Alini, M. (2006). The Influence of Mechanical Stimuli on Articular Cartilage Tissue Engineering. *Top. Tissue Eng.* 2. Available at: http://www.oulu.fi/spareparts/ebook_topics_in_t_e_vol2/abstracts/alini_0102.pdf [Accessed May 31, 2018].

Lesman, A., Blinder, Y., and Levenberg, S. (2010). Modeling of flow-induced shear stress applied on 3D cellular scaffolds: Implications for vascular tissue engineering. *Biotechnol. Bioeng.* 105, 645–654. doi:10.1002/bit.22555.

Lombardo, M. E., Carfì Pavia, F., Vitrano, I., Ghersi, G., Brucato, V., Rosei, F., et al. (2019).

PLLA scaffolds with controlled architecture as potential microenvironment for in vitro tumor model. *Tissue Cell* 58, 33–41. doi:10.1016/j.tice.2019.04.004.

Maes, F., Van Ransbeeck, P., Van Oosterwyck, H., and Verdonck, P. (2009). Modeling fluid flow through irregular scaffolds for perfusion bioreactors. *Biotechnol. Bioeng.* 103, 621–630. doi:10.1002/BIT.22277.

Mannella, G. A., Carfì Pavia, F., Conoscenti, G., La Carrubba, V., and Brucato, V. (2014). Evidence of mechanisms occurring in thermally induced phase separation of polymeric systems. *J. Polym. Sci. Part B Polym. Phys.* 52, 979–983. doi:10.1002/polb.23518.

McCoy, R. J., and O'Brien, F. J. (2010). Influence of shear stress in perfusion bioreactor cultures for the development of three-dimensional bone tissue constructs: A review. *Tissue Eng. - Part B Rev.* 16, 587–601. doi:10.1089/ten.teb.2010.0370.

Mehrian, M., Lambrechts, T., Papantoniou, I., and Geris, L. (2020). Computational Modeling of Human Mesenchymal Stromal Cell Proliferation and Extra-Cellular Matrix Production in 3D Porous Scaffolds in a Perfusion Bioreactor: The Effect of Growth Factors. *Front. Bioeng. Biotechnol.* 8, 376. doi:10.3389/fbioe.2020.00376.

Muljadi, B. P., Blunt, M. J., Raeini, A. Q., and Bijeljic, B. (2016). The impact of porous media heterogeneity on non-Darcy flow behaviour from pore-scale simulation. *Adv. Water Resour.* 95, 329–340. doi:10.1016/j.advwatres.2015.05.019.

Pan, Z., and Ding, J. (2012). Poly(lactide-co-glycolide) porous scaffolds for tissue engineering and regenerative medicine. *Interface Focus* 2, 366–77. doi:10.1098/rsfs.2011.0123.

Paopo, I. (2014). Stem Cell Bioprocessing : Bioreactor Design and Characterisation By Computational Fluid Dynamics and the Differentiation of Murine Embryonic Stem Cells Into the Alveolar Progenitor Cells in Sparged.

Pasha Mahammod, B., Barua, E., Deoghare, A. B., and Pandey, K. M. (2019). Permeability quantification of porous polymer scaffold for bone tissue engineering. in *Materials Today: Proceedings* (Elsevier Ltd), 1687–1693. doi:10.1016/j.matpr.2020.02.186.

Podichetty, J. T., Bhaskar, P. R., Khalf, A., and Madihally, S. V. (2014). Modeling pressure drop using generalized scaffold characteristics in an axial-flow bioreactor for soft tissue regeneration. *Ann. Biomed. Eng.* 42, 1319–1330. doi:10.1007/S10439-014-1009-5/FIGURES/7.

Podichetty, J. T., and Madihally, S. V. (2014). Modeling of porous scaffold deformation induced by medium perfusion. *J. Biomed. Mater. Res. - Part B Appl. Biomater.* 102, 737–748. doi:10.1002/jbm.b.33054.

Pok, S., Dhane, D. V., and Madihally, S. V. (2013). Computational simulation modelling of bioreactor configurations for regenerating human bladder. *Comput. Methods Biomech. Biomed. Engin.* 16, 840–851. doi:10.1080/10255842.2011.641177.

Porter, B., Zauel, R., Stockman, H., Guldberg, R., and Fyhrie, D. (2005). 3-D computational modeling of media flow through scaffolds in a perfusion bioreactor. *J. Biomech.* 38, 543–549. doi:10.1016/j.jbiomech.2004.04.011.

Raeini, A. Q., Blunt, M. J., and Bijeljic, B. (2014). Direct simulations of two-phase flow on micro-CT images of porous media and upscaling of pore-scale forces. *Adv. Water Resour.* 74, 116–126. doi:10.1016/j.advwatres.2014.08.012.

Salah, N. A. (2018). In Vitro Bronchial Mucosa Model using Air-Liquid Interface culture on PLLA Electrospun Membrane.

Salehi-Nik, N., Amoabediny, G., Pouran, B., Tabesh, H., Shokrgozar, M. A., Haghighipour, N., et

al. (2013). Engineering parameters in bioreactor's design: A critical aspect in tissue engineering. *Biomed Res. Int.* 2013. doi:10.1155/2013/762132.

Salerno, A., and Domingo, C. (2015). Pore structure properties of scaffolds constituted by aggregated microparticles of PCL and PCL-HA processed by phase separation. *J. Porous Mater.* 22, 425–435. doi:10.1007/s10934-015-9911-2.

Sandino, C., and Lacroix, D. (2011). A dynamical study of the mechanical stimuli and tissue differentiation within a CaP scaffold based on micro-CT finite element models. *Biomech. Model. Mechanobiol.* 10, 565–576. doi:10.1007/s10237-010-0256-0.

Sibilio, S., De Gregorio, V., Urciuolo, F., Netti, P. A., and Imparato, G. (2019). Effect of peristaltic-like movement on bioengineered intestinal tube. *Mater. Today Bio* 4, 100027. doi:10.1016/j.mtbio.2019.100027.

Siddiqui, N., Asawa, S., Birru, B., Baadhe, R., and Rao, S. (2018). PCL-Based Composite Scaffold Matrices for Tissue Engineering Applications. *Mol. Biotechnol.* 60, 506–532. doi:10.1007/s12033-018-0084-5.

Truscello, S., Kerckhofs, G., Van Bael, S., Pyka, G., Schrooten, J., and Van Oosterwyck, H. (2012). Prediction of permeability of regular scaffolds for skeletal tissue engineering: A combined computational and experimental study. *Acta Biomater.* 8, 1648–1658. doi:10.1016/j.actbio.2011.12.021.

Tuan, H. S., and Hutmacher, D. W. (2005). Application of micro CT and computation modeling in bone tissue engineering. *CAD Comput. Aided Des.* 37, 1151–1161. doi:10.1016/j.cad.2005.02.006.

Vetsch, J. R., Betts, D. C., Müller, R., and Hofmann, S. (2017). Flow velocity-driven differentiation of human mesenchymal stromal cells in silk fibroin scaffolds: A combined experimental and computational approach. *PLoS One* 12, e0180781. doi:10.1371/journal.pone.0180781.

Vetsch, J. R., Müller, R., and Hofmann, S. (2015). The evolution of simulation techniques for dynamic bone tissue engineering in bioreactors. *J. Tissue Eng. Regen. Med.* 9, 903–917. doi:10.1002/term.1733.

Vissers, C. A. B., Harvestine, J. N., and Leach, J. K. (2015). Pore size regulates mesenchymal stem cell response to Bioglass-loaded composite scaffolds. *J. Mater. Chem. B* 3, 8650–8658. doi:10.1039/c5tb00947b.

Voronov, R. S., Vangordon, S. B., Sikavitsas, V. I., and Papavassiliou, D. V. (2010a). Distribution of flow-induced stresses in highly porous media. *Appl. Phys. Lett.* 97, 024101. doi:10.1063/1.3462071.

Voronov, R., VanGordon, S., Sikavitsas, V. I., and Papavassiliou, D. V. (2010b). Computational modeling of flow-induced shear stresses within 3D salt-leached porous scaffolds imaged via micro-CT. *J. Biomech.* 43, 1279–1286. doi:10.1016/j.jbiomech.2010.01.007.

Xue, R., Chung, B., Tamaddon, M., Carr, J., Liu, C., and Cartmell, S. H. (2019). Osteochondral tissue coculture: An in vitro and in silico approach. *Biotechnol. Bioeng.* 116, 3112–3123. doi:10.1002/bit.27127.

Yamada, S., Yassin, M. A., Schwarz, T., Hansmann, J., and Mustafa, K. (2021). Induction of osteogenic differentiation of bone marrow stromal cells on 3D polyester-based scaffolds solely by subphysiological fluidic stimulation in a laminar flow bioreactor: *https://doi.org/10.1177/20417314211019375* 12, 204173142110193. doi:10.1177/20417314211019375.

Zeinali, R., Del Valle, L. J., Torras, J., and Puiggalí, J. (2021). Recent progress on biodegradable tissue engineering scaffolds prepared by thermally-induced phase separation (Tips). *Int. J. Mol. Sci.* 22, 3504. doi:10.3390/ijms22073504.

Zermatten, E., Haussener, S., Schneebeli, M., and Steinfeld, A. (2011). Tomography-based determination of permeability and Dupuit–Forchheimer coefficient of characteristic snow samples. *J. Glaciol.* 57, 811–816. doi:10.3189/002214311798043799.

Zermatten, E., Vetsch, J. R., Ruffoni, D., Hofmann, S., Müller, R., and Steinfeld, A. (2014). Micro-Computed Tomography Based Computational Fluid Dynamics for the Determination of Shear Stresses in Scaffolds Within a Perfusion Bioreactor. *Ann. Biomed. Eng.* 42, 1085–1094. doi:10.1007/s10439-014-0981-0.

Zhao, F., Vaughan, T. J., and McNamara, L. M. (2016). Quantification of fluid shear stress in bone tissue engineering scaffolds with spherical and cubical pore architectures. *Biomech. Model. Mechanobiol.* 15, 561–577. doi:10.1007/s10237-015-0710-0.

Zhao, Y., Zhu, G., Zhang, C., Liu, S., Elsworth, D., and Zhang, T. (2018). Pore-Scale Reconstruction and Simulation of Non-Darcy Flow in Synthetic Porous Rocks. *J. Geophys. Res. Solid Earth* 123, 2770–2786. doi:10.1002/2017JB015296.

Chapter 8

General discussion, conclusions, and future directions

8.1 Final discussion

With a view to future application for in vitro tissue modeling, the original objective of this thesis was achieved by obtaining valid results on the design of specific perfusion bioreactors to perform dynamic cell culture. Experimental tests (Chapters 2, 5, 6, and 7) and mathematical and numerical models (Chapters 6 and 7) were analyzed and discussed to validate scaffold-cell or bioreactor-scaffold-cell systems.

As a scaffold-cell system, bone tissue engineering was chosen as the context of a case study in which the porosity and pore size of PLLA scaffolds produced by TIPS could regulate cell activity. Specifically, from morphological analysis techniques (micro-CT), high porosity (87-91%) was obtained in all groups tested, i.e., with pores similar to cancellous bone, trabecular bone, and bone in its overall structure. Total porosity showed no direct relationship with cellular response, which, on the contrary, changed with pore size. Scaffold pore size influenced the number of cells after 7 days of culture, with some scaffold groups having different proliferation rates (Fig. 2.11). The level of mineralization developed after 7 days also differed in the structures analyzed, showing a trend appropriate to the type of cells used. Overall, in this work, protocols for PLLA-based scaffold production were optimized to improve scaffold ability in eliciting an osteoblastic response in terms of adhesion, proliferation, and hydroxyapatite matrix production.

In Chapters 1, 3, and 4, an overview of tissue engineering, the use of perfusion bioreactors, and their mathematical and numerical modeling are presented, respectively. Such theoretical and literature analysis was crucial in assessing the types to be analyzed most appropriately and describing a specific experiment, resolving computational limitations and the difficulty in finding the correct equations to describe a given system. Two types of perfusion bioreactors are mainly described: the airlift and the dual flow, used in the present thesis work to model and test scaffolds in PLLA.

In Chapter 5, the fluid dynamics and efficacy of a dual-flow perfusion bioreactor were validated in the field of in vitro modeling for TE purposes. From the fluid dynamics analysis, the main objective of the device was confirmed, which is to provide independent control of two flows through a hollow cylindrical porous scaffold. This feature results in a radial flow

whose perfusion rate can be precisely adjusted, depending on the desired application. Thus, when testing the presented system, the latter could control fluid migration/diffusion through a hollow scaffold, mimicking flow conditions suitable for drug release from nano-carriers and nutrient delivery to cells seeded in the scaffold channel. In the latter context, the bioreactor proved to be a viable system for in vitro reproduction of tissues with an air-liquid interface, such as nasal mucosa.

As the objective of Chapter 6, the mathematical equations and numerical analyses proposed to characterize and optimize the design of a new airlift bioreactor was found to be correct for studying the system under different operating conditions, showing good agreement between modeling and experiments. Among the proposed methods, the computational simulation was the most effective tool to optimize the bioreactor design; on the other hand, biological experimentation was necessary to confirm the modeling results about the oxygen concentration profile inside the device to ensure the viability and proliferation of cells. Overall, the combination of validated mathematical equations, accurate computational simulation, and specific experimental techniques was a powerful tool for the characterization and optimization of complex systems.

Finally, in Chapter 7, the fluid-dynamic effect of perfusion on the pores of a complex scaffold was evaluated without simplifying the pore morphology, thus obtaining reliable and predictable results. This work is one of the few studies that could achieve this result on structures with high porosity, interconnection, and overall size. The combined computational method and experimental analysis demonstrated that the airlift system (presented in Chapter 6 and coupled with scaffold support) could elicit uniformly distributed flow over all cultured scaffolds. Thus, fluid-scaffold-cell interactions were studied to achieve the fundamental characteristics of long-term cell culture under perfusion conditions in an airlift bioreactor.

8.2 Conclusions and future directions

This PhD thesis research was addressed to the design of novel perfusion bioreactors and PLLA-based scaffolds and their combined use for prospective *in vitro* tissue engineering for nasal mucosa modelling, nasal tissue engineering and bone tissue engineering. PLLA is a biodegradable and biocompatible biomaterial widely used as a base material for three-dimensional polymer scaffolds that can accommodate cells. The TIPS technique has been exploited to fabricate these matrices, ensuring high interconnectivity and porosity and allowing the control of the pore size simply by changing the thermal protocol. This aspect has been used to develop porous foams with different morphologies regarding pore size

distribution via TIPS. Thus, scaffolds with a gradient pore size were produced either by a single operation or by bonding several layers with various controlled pore distributions. The obtained morphologies were analyzed using the non-invasive technique of micro-computed tomography, verifying the continuity between the glued layers or the effectiveness of the thermal path adopted. The porosity of the constructs was found to be more than 80% and uniformly distributed even in gradient scaffolds obtained in a single pass or by bonding. For bone TE applications, pore size has been varied in the range of 90-200 microns, according to bone morphology presenting two different pore sizes in the trabecular and cortical area. Biological tests with osteoblastic cells were performed on the morphologies presented in this thesis work. Hence, their degree of proliferation and mineralization were evaluated. By manipulating the pore size distribution of a scaffold, a very different degree of cell growth and hydroxyapatite production can be achieved. In principle, in addition to bone testing, scaffold morphologies with a pore gradient can be used to replicate various tissues that naturally exhibit pore size distribution, including osteochondral and vascular tissue.

When mimicking the environment surrounding the tissue to regenerate, static conditions are no longer sufficient. Indeed, tissues are continuously subject to mechanical, physical, and chemical stimuli. Dynamic systems, called bioreactors, have been developed to replicate these phenomena outside the body. Several types of bioreactors are used in the field of tissue engineering, improving cell activity compared with static conditions. Among these systems, perfusion bioreactors have shown the advantage of offering a continuous exchange of culture medium by exerting beneficial mechanical efforts for cells. In addition, an airlift perfusion bioreactor can ensure an optimal mass transfer within the dynamic system while oxygenating the cells and favoring the removal of metabolites. In this thesis work, two types of airlift bioreactor were modeled and tested for tissue growth in porous and interconnected structures.

A dual-flow bioreactor was developed to replicate *in vitro* physiological conditions *in vivo*, allowing separate control of the two external and internal environment streams, the latter relating to an internal channel in the scaffold. This system can allow the diffusion of fluid (with or without particles dispersed inside it) through the thickness of the scaffold, allowing both the screening of drugs and the reproduction of tissues surrounded by two different fluids. In this thesis, this bioreactor was used for both applications. In particular, its fluid dynamics was studied through a semi-empirical model combining mathematical equations and experimental data. This method also allowed to calculate the permeability of the scaffold without the use of more expensive devices such as pressure or flow meters. In addition, the

system was controllable in terms of diffusive flow in value and direction. Finally, a scaffold with a canal was flushed inside with air to mimic the physiology of the nasal mucosa. This structure was adapted to induce diffusion of the medium from outside the scaffold to its inner channel, where cells requiring nutrients are located.

The last part of this thesis was dedicated to the modeling and testing study of a bioreactor capable of dynamically culturing many scaffolds simultaneously and reproducing the hydrodynamic conditions suitable for tissue growth. The bioreactor was designed and modeled preliminarily, then tested with PLLA scaffolds fabricated through TIPS. As for modeling, both mathematical models and numerical simulations were used. The modeling analysis showed a good agreement between the various models and the experimental validation using a bioreactor-scaffold-cells system. In particular, parameters influencing cellular activity, such as gas velocity and holdup, bubble size, and oxygen-related mass transfer coefficient, were evaluated. Concerning the bioreactor configuration, numerical models initially showed that the flow was not uniformly distributed in the bioreactor geometry. In contrast, the addition of a liquid distributor at the top of the system interacted with the velocity of the liquid, generating a profile that can ensure a uniform flow stimulus on the scaffolds inserted into the bioreactor. Scaffolds grown in dynamic showed uniform and better cell growth than static controls. The insertion inside the bioreactor of a multi-grid support allowed testing of up to 24 scaffolds simultaneously. Through the CFD analysis, a uniform velocity profile was observed in the regions occupied by the scaffolds; the biological analysis carried out after 6 days showed that the cells are not subject to liquid velocities that are different along the height of the bioreactor. These results reinforce the possibility of successfully testing many scaffolds in a system whose fluid-dynamic is adequate for cellular growth in a dynamic system. Besides the characterization of the bioreactor, fluid-dynamic simulations were performed through porous scaffolds placed in the validated dynamic system. The simulations were implemented on virtual structures obtained from micro-computed tomography, with a morphology that strictly mimics that complex scaffold produced via TIPS. The results showed that the pores of the scaffold are subject to uniform shearing efforts and that they fall within the range not harmful to the cells. The influence of the fluid dynamics affecting the stresses acting on a matrix, along with its porosity and pore interconnection, had previously been reported. However, these involved either the result of unrealistic pore-level flow models or simulation on micro-computed scaffolds with less complex morphology than that reported in this paper. This is the first work that studies the influence of the fluid dynamics of a perfusion bioreactor on a scaffold with high porosity,

micropore, and high interconnection. The study reveals that the combination of scaffolds produced by TIPS, micro-CT analysis, and CFD simulation has determined the effects of perfusion on the pores of the structure that will host the cells, in particular, to optimize the dynamic system parameters that promote cell growth. Overall, the proposed system and the effective methodology applied showed very satisfactory outcomes for scaffold analysis at the pore-scale to study the fluid-scaffold-cells interactions.

In conclusion, several in vitro approaches and models have been adopted to assess which strategies work best to produce specific tissues, in static or dynamic conditions, on scaffolds in PLLA produced by the TIPS technique.

New future perspectives can be developed by the results shown in this thesis. As for scaffolds produced with different pore sizes and distribution, we focused on bone tissue and, therefore, on tests of osteoblastic cells. Further tests may be performed using mesenchymal cells to assess the intrinsic influence of scaffold morphology on cell differentiation. These tests can be done both in static and dynamic, using the bioreactor airlift with multi-grid support to test several scaffolds subjected to the same environmental conditions, thus evaluating the only effect of morphology. The dual-flow bioreactor developed here can be potentially applied to multiple systems. In addition, you can test different morphologies and thicknesses of the foam. The scaffold with the channel, only preliminarily tested statically, requires further investigation. A combination of bioreactor dynamics and scaffold structure should be perfect for mimicking the nasal mucosa considered here. Taking advantage of the fluid dynamics offered by this bioreactor, it is possible to test the diffusion of drugs as a model to analyze the cellular response in a customizable 3D system. In principle, the direction and amount of fluid that diffuses through the scaffold can be easily manipulated for various targets. In addition, concerning the perfusion airlift bioreactor with the support, once it has been assessed that the system is capable of exerting uniform stress along the entire geometry of the device, different conditions and/or experimental times can be easily analyzed to increase the efficiency of the experiment. The CFD simulation on the scaffold at the level of the pores showed the good vitality guaranteed within the dynamic system. However, to verify whether the morphology of the pores affects the cellular response, different porous structures must be compared. These simulations can provide crucial information to optimize scaffold design and performance for a specific application.